Red Blood Cell mechanics:
from membrane elasticity to blood rheology

Guillermo Rodríguez Lázaro

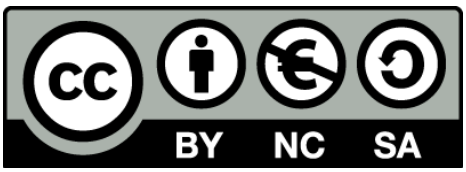

Red Blood Cell mechanics:

from membrane elasticity to blood rheology

Ph. D. Thesis

Guillermo Rodríguez Lázaro

Advisors:

Aurora Hernández-Machado
Ignacio Pagonabarraga

Programa de Doctorat en Física
Departament d'Estructura i Constituents de la Matèria

Acknowledgments

The results presented in this Thesis involve the work carried out during several years of research. During this time in Barcelona I have received the help of many people that have contributed in different ways, both scientifically and on a personal level, to make this Thesis possible. I would like to thank you all for your support and help.

En primer lugar, me gustaría agradecer a mis dos directores de tesis, Ignacio Pagonabarraga y Aurora Hernández-Machado, el ofrecerme la posibilidad de realizar el doctorado en un campo tan fascinante como la biofísica. Las muchas horas de reuniones, a veces en horarios intempestivos, los consejos y discusiones, sin duda han sido determinantes para mejorar mi formación.

I would like to acknowlegde Kathryn A. Melzak the time dedicated to discuss and show me a more biological and experimental perspective about the world of red blood cells.

Algunos de los compañeros de la Facultad han contribuído decisivamente con interesantes discusiones o aportaciones que muchas veces me han ayudado a resolver diferentes problemas. Destacar especialmente a Xavier Clotet, Clara B. Picallo, Claudia Trejo, Francisco Alarcón, Carles Blanc y David Palau.

También querría agradecer las discusiones, y especialmente los consejos, de Rodrigo Ledesma y Félix Campelo, quienes precedieron en parte mi trabajo y cuyas aportaciones han resultado en más de una ocasión decisivas para poder avanzar.

En el plano personal, quiero agradecer en primer lugar el apoyo incondicional prestado por mis padres, Belén y Miguel, especialmente cuando las cosas no han ido bien y más lo he necesitado. También a toda la familia en general, con mención especial para mi hermana Paula y mi tía Begoña por su cariño y atención.

Sin duda estar en un ambiente de trabajo en el que me he sentido tan a gusto ha contribuído a ir con alegría día tras día a la Facultad. Ahi han estado siempre Xavifú, Laura, Pau, Claudia, Paco, Xavier, Carles, Jordi, Marta, y otros muchos junto a los que he sufrido de innumerables tuppers, menús y *exquisitos* cafés.

Por supuesto, también agradecer al resto de amigos que me han rodeado estos años, y con los que tan buenos ratos he pasado. En especial a Manolo, Melchor y Pesquera, por aguantarme a todas horas y estar siempre ahí cuando lo he necesitado. Lara siempre me apoyó en los buenos momentos, pero especialmente en los malos. Martí, Alberto, Marce, Aida, Albert, Marcel, y todos los demás con los cuales he compartido alegrías, bien delante de unas cervezas o en Aiguamolls o Tarragona. A la gente de Santander, por acogerme las pocas veces que vuelvo, en especial a David, Jose y Coso. Finalmente, no quiero dejar de agradecer a todos con los que he compartido viajes durante estos años, con sus aventuras y desventuras, y que me han ayudado a mantener la dosis de adrenalina que tanto necesito. En especial a Dani y Manolo, que siempre se han ofrecido a acompañarme por estrambótico que fuese el plan.

Barcelona, 7 de Mayo de 2014.

Contents

General introduction

In recent years, the application of physical techniques and rapid technological development have driven biological research towards a more quantitative description. A wealth of new experimental data at the molecular and cellular scale has been obtained, allowing a more direct connection with physical models. Thereby, the closer connection between biologists and physicists has facilitated the emergence of biophysics as a new field, and research has benefitted from the profitable interplay between both disciplines.

Cell membranes are complex objects which involve biological processes spanning from the flip of the lipids they contain, on the length scale of tens of nanometers, to the overall response of the cell, at typically ten microns. Membranes have fascinated physicists since the earliest stages of development of the field, due to their very specific properties, which are not shown but any other material (such as non-classical elastic behaviour). Additionally, in spite of the membrane intrinsic complexity, physical models have explained an astounding number of phenomena observed experimentally, demonstrating that membranes invite to an extensive theoretical exploration. Furthermore, the recent access to the cellular and molecular scale in experiments has led to the discovery of new phenomena that must be both understood and explained.

At the scale in which the cell responds to mechanical pressures in the tissue, the study of the system generally requires a coarse-grained description. Macroscopic variables such as membrane shape geometry and elasticity become useful tools for the purposes of studying the system. This Thesis is framed in this biophysical context. We will study, from a theoretical perspective, the mechanics of membranes and cells at different situations of biological interest that cells may face during their life.

Elasticity of cell membranes

The membrane is a fundamental structure in all living organisms, as it defines the cell as an entity, the basic unit of life. Membranes separate the external environ-

ment from the cell inner region which contains all the organelles and molecular machinery that constitute the basic ingredients with which the whole organism is constructed. The formation of closed membranes from lipid aggregates represented a major step that allowed the development of life. In a parallel way to the evolution towards more complex organisms, such as vertebrates and specifically mammals, cell membranes have also increased their complexity, incorporating a huge quantity of larger molecules and microstructures that enable a complex functionality.

For all these reasons, cell membranes have attracted interest from biologists for a long time, and from the pioneer model of the fluid mosaic by Singer and Nicolson (1972), our knowledge about membrane molecular composition and functioning has continuously increased. In the last 40 years, membranes have also been studied by physicists, providing a complementary picture about membrane behaviour and properties. The subject was first approached by Canham (1970) and Helfrich (1973), and based on their seminal models an outstanding number of membrane phenomena have been understood and explained from a physical perspective. In particular, the characterization of the elastic properties of the membrane is the scope of many studies. Whereas we have achieved a considerable understanding about the mechanics of simple biomimetic membranes such as bilayers of homogeneous lipid composition, the elastic behaviour of more complex membranes, such as those present in mammalian cells, is still under lively debate in the literature.

In this context, most research has focused on the study of the human red blood cell as a model system, due to its structural simplicity. Red blood cells present a remarkable capability to deform and pass through very thin capillaries, and in microcirculation they acquire strange shapes whose benefits are still unknown. They also develop a number of different morphologies if their membrane is altered or damaged, as known from a number of anemias, malaria, or during blood storage. The delicate membrane equilibrium at the molecular scale ultimately affects mechanisms taking place in a much larger scale, such as cell shape and blood properties.

Blood rheology

Newtonian fluid dynamics has proven to be an accurate theory for describing the behaviour of gases and liquids containing small molecules (with a molecular weight of less than roughly 1000 uma). If, however, the liquid contains larger molecules, a number of mechanisms (such as molecule orientation, spatial organization or aggregation) become dominant, introducing a more complex internal physics in the liquid microstructure that affects to the macroscopic behaviour, which differs from

the classic Newtonian dynamics. These phenomena are usually shear- or time-dependent, and they also depend on other factors such as molecule concentration or system geometry. The variable response of these liquids under the action of different external stresses has led to the widely extended denomination of *complex fluids*. Classic examples of this kind of fluids are polymer melts, glass-forming liquids and micellar solutions.

It is known for a long time that the rheological behaviour of blood is largely determined by the deformability of red blood cells, as suggested by the abnormal properties of blood notized in experiments of macroscopic rheology with altered samples (*eg* spherocytes). However, the problem remains poorly understood, due to the difficulty of a controlled experimental approach at the single-cell microscale. In the theoretical frame, most studies are based on a simplified description of the cells, ignoring important details of their shape and elasticity, and hence neglecting the important aspect of cell elasticity. In this Thesis, we deal in depth with the deformability of red blood cells flowing in confined channels, paying special attention to the importance of membrane elasticity and its consequences in blood properties.

Thesis aims and structure

This Thesis deals with the physical properties of cell membranes, partially based on our background on simpler interfaces. Our starting point is the microstructure of the plasma cell membrane, and we devote special effort to the conciliation between the biological picture and the physical modeling. The next step is to connect the membrane physical properties with the cell morphology, and identify the role of each membrane ingredient in the overall response of the cell. Finally, we study how the elasticity and morphology of the cell affect the physical properties of the whole tissue. Our research is focused in the particular case of red blood cells and blood, a prime element of our organism.

The main aim of this Thesis is to understand and explain red blood cell deformability and dynamic behaviour from the elastic properties of its membrane, and connect this behaviour with the rheological properties of blood. For this purpose, we need to set the physical properties of the membrane that our model should account for, after applying this model to specific problems at the cell scale. Two different problems are studied: the development of stationary altered shapes when the physiologic membrane equilibrium is broken, and the deformations undergone by healthy cells when exposed to confined flows. The first case corresponds to a mechanical equilibrium problem, whereas the second is stricly a non-equilibrium problem in which the hydrodynamics of the external fluid plays a central role.

Attending to these objectives, the Thesis is structured in four separated parts. Part I contains two introductory chapters. In Chapter 1, the main aspects of the biological systems of interest are described, including an overview covering membrane composition and structure, red blood cell characteristics, and a brief description of the circulatory system and blood. In Chapter 2 we present the most relevant physical theories describing cell membranes. Based on the Helfrich theory framework, new and more depured models have been proposed, achieving a more realistic description that accounts for more complex phenomena than the initial Helfrich theory. We outline the main models in order to provide the physical framework necessary to understand the subsequent studies.

Once the biophysical frame has been stablished, we then present our original research. Part II is devoted to the study of the membrane elastic response during morphological transformations in the so-called disco-echinocyte transition of the red blood cell. It is known that alterations in the membrane molecular structure, such as lipid rearrangements or conformational changes in the proteins of the cytoskeleton, lead to the formation of spicules and bumps, in a sequence of increasingly crenated shapes. The purpose of this Part is to elucidate the role of both the lipid bilayer and the cytoskeleton during these morphological changes and generically understand the response of each membrane component during any kind of deformation. In a series of experiments performed by Kathryn A. Melzak and José Luis Toca-Herrera, perturbation of altered cells by an AFM tip is shown to induce a reverse morphological transformation towards the healthy discocyte. We develop a theoretical model, based on a Cassini ovals parametrization of the cell membrane, that allows us to study and understand the first stages of this transition. Thereby, Chapter 3 first presents the fundamental aspects of the disco-echinocyte transition and some of the molecular mechanisms running in the cell membrane that have been discovered in previous experiments. We then describe the AFM experiments and discuss the molecular mechanisms involved. These conclusions are based on the theoretical study, which is presented in Chapter 4. In this chapter, we analyze the main morphologies observed during the transition, identifying the key mechanisms that explain each cell shape. Our results show that the cytoskeleton is relevant for stabilizing the discocyte and opposes resistance to the formation of bumps, but it shows weak disturbance when cell shape is close to the initial discocyte. One of the main assumptions of our model is that the cytoskeleton is relaxed at the discocyte stage, based on numerous experimental observations. This point is, however, controversial and remains as one of the less understood aspects of cell elasticity, and we discuss the subject in detail throughtout the Thesis.

Afterwards, we drive our attention to the development of a phase-field method for membrane modeling, corresponding to Part III. The phase-field approach is

based on the Helfrich theoretical framework. In Chapter 5, we dedicate special effort to the formalization and rationalization of the model, showing its convergence to the Helfrich theory. We obtain the stress tensor of the membrane from which the membrane local force can be derived. This is used to incorporate the membrane phase-field model to a more general model in which membrane dynamics is coupled with an external fluid, whose hydrodynamics is dictated by the Navier-Stokes equation. The consideration of an external fluid is important as in many membrane-related problems the hydrodynamics plays a central role. From the complete phase-field Navier-Stokes model, we derive the macroscopic equilibrium equation of the membrane. Finally, we perform a linear stability analysis, studying the relaxation of flat membranes when subjected to a sinusoidal perturbation, in order to validate the model and test if it captures the correct membrane dynamics. In Chapter 6 we describe the numerical implementation of the model, based on a lattice-Boltzmann scheme.

The last piece of work, Part IV, focuses on the behaviour of red blood cells while flowing in confined channels. The rheological behaviour of blood in narrow conduits, in which the cell concentration is considerably lower than in the thickest arteries, is dominated by the elasticity and deformability of the red blood cells. However, the problem of non-linear rheology caused by deformable objects is still poorly understood. Red blood cells flowing in small channels are known to exhibit a complex morphological behaviour, often assuming asymmetric shapes termed *slippers*, whose advantages with respect to symmetric shapes are still unclear. The main aims of this Part are to link the rheological behaviour of red blood cell suspensions with the elasticity of the cells they contain, as well as to explore the cell morphological response. In Chapter 7, we present the main applications and interests of this subject, especially in the context of microfluidics and lab-on-a-chip devices, whose development is being conducted towards the field of pathology diagnosis and other medical applications. In this Chapter, we also outline some previous results about the behaviour of red blood cells in different flow conditions. In Chapter 8, we identify the morphological regimes of red blood cells flowing isolated in confined channels, characterizing the observed cell shapes and analyzing the elastic contributions to the membrane in each case. We also describe the effective viscosity of the cell suspension, discussing the shear-thinning behaviour that we obtain. In Chapter 9, we focus on the understanding of why red blood cells develop asymmetric (slipper) shapes, comparing these configurations with the symmetric shapes in order to identify the benefits of a lateral position in the channel, and to adress its implications in the suspension fluidity. In Chapter 10, we drive our attention to the control of red blood cell migration and lateral position in the channel by tuning the channel and flow properties, a subject of relevance for the improvement of chip devices to manipulate and separate single

cells.

We end with a separated part containing the conclusions of the Thesis, where we conciliate the three previous parts and provide an all-encompassing picture of the elasticity and deformability of red blood cells. Finally, we discuss future perspectives of the work presented in the Thesis.

Part I

Physical description of cell membranes

Chapter 1

Biological introduction

In order to set the proper biophysical context that allows us to identify the main features to be captured in our physical models, we start with a biological introduction of the systems of study. Thereby, this Chapter is organized in a sequence of increasingly complex structures. First, we cover the cell membrane composition and assembly, driving then our attention to the particular properties of the red blood cells. Besides, we describe the circulatory system which represents the biological frame in which red blood cells live.

1.1 Cell membrane

In this Section we present the most important biological characteristics of cell membranes necessary to understand their elastic and mechanic response. We will briefly outline the molecular composition of the membrane before identifying the main components that form its microstructure. Then, the importance of membrane properties will be analyzed in the case of human erythrocytes, a unique case among human cells because it lacks any organelle or internal structure, so that its overall shape and mechanical properties can be directly related to that of its membrane.

Cell membranes represent an essential element in the development of living organisms. They constitute the cells frontiers, separating the interior of the cell from the external environment. Membranes enclose the organelles and components that all together form the basic unit of life. However, membrane functionality is not limited to its simple structural role, but membranes are also responsible of the interactions of the cell with neighbour cells. These interactions are mediated by a certain type of transmembrane proteins that coordinate the cell signaling, enabling the cell response to environmental pressures. Additionally, membranes maintain

ion gradients which allow the synthesis of ATP, the basic energetic molecule. The plasma membrane is the most important membrane of the cell, but other types of membrane are present in organelles like the nucleus, the Golgi aparatus, the endoplasmic reticulum and the mitochondria. Considering all the membranes of the cell, they concentrate around 30% of the total proteinic activity (Alberts et al., 1994).

All biological membranes share a common structure and composition in spite of being part of different entities, and regardless of their function. Membranes are composed by different lipid molecules that assemble forming bilayers. Lipid bilayers are selectively permeable to the exchange of polar molecules and host a high density of transmembrane proteins, which essentially define the specific membrane functionality. Lipids are bound by relatively weak, non-covalent interactions that allow a rapid lateral interchange of positions, leading to a huge surface diffusion over the membrane plane. Typically, a lipid flips with neighbour molecules 10^7 times per second, exploring the whole cell surface in just a few seconds. The lipids practically behave as a fluid in the bilayer plane, a property with important implications for the cell activity. Transmembrane proteins waft in the fluid bilayer (Singer and Nicolson, 1972), and they are also able to diffuse laterally. The membrane is connected with the inner (cytosolic) cytoskeleton, a three-dimensional mesh formed by actin filaments which provides compactness and structural ordering, and determines the cell shape, which in turn depends on the type of cell and its function. In some cells, an exterior (cortical) cytoskeleton also exists, and it connects with neighbouring cells in order to facilitate a coordinate response of the tissue. The fragile membrane equilibrium is controlled by a number of active processes, including flip-flop rearrangement of the different lipid species of the bilayer, remodeling of the cytoskeleton, or the balance of lipid densities during vesiculation processes (*eg.* during endo and exocytosis), which is achieved by the existence of lipid reservoirs in the interior of the cell.

1.1.1 The lipid bilayer

Lipid composition

Lipids represent up to 50% of the total mass of the membrane in mammalian cells. They are amphiphilic molecules with a polar head (which prefers to contact and interact with other polar molecules, such as water) and a tail formed by two hydrocarbon chains which present a strong hydrophobicity, and therefore tails avoid the interaction with water. The term amphiphile, which means in greek *both lover*, derives from the ancient observation that amphiphilic molecules organize in the presence of oil and water due to their polar nature, as they assemble in the

surface separating these fluids, orienting their heads to the water region and the tails to the oil region. If lipids are immersed in water, they tend to self-assemble to avoid the hydrophobic interactions with the surrounding water. Two basic structures can be formed by these aggregates. Sometimes they assemble forming micelles, a closed structure, with all the tails in the inner, free-water region, and the lipid heads oriented to the exterior, in contact with water. Another possibility is the formation of bilayers, when two lipid monolayers fold in opposite directions, so that the heads form two parallel sheets whereas the tails are trapped in the intermediate region, without contact with the aqueous environment. Still, at the edges of the bilayer the tails of the boundary lipids do interact with water molecules. Lipids rearrange to avoid the presence of edges, forming closed surfaces in which the water is both at the inner and outer regions, but there is no direct interaction with the tails. The strong hydrophobicity causes that these closed structures are much energetically favourable, thus ensuring large stability under thermal fluctuations and other mechanical disruptions. The shape of the lipid favours the formation of one structure in detritment of the other. Conical shaped lipids (thus with a large head section compared to the tail), such as lysolipids, pack forming micelles, whereas cylindrical lipids, such as phospholipids, are more symmetric and form bilayers.

Despite their structural simplicity, bilayers are formed by an extensive variety of lipid species. An eukaryotic cell is typically composed by 500-1000 different species, although many occur just incidentally and the major components reduce to the phospholipids, with just a few species present in mammalian cells. All phospholipids have two fatty chains of variable length (ranging from 14 to 24 carbons), with the particularity that one of the chains is unsaturated (thus it contains a *cis* bond), and hence it is not completely straight but presents a kink, resembling a broken rod (see Figure 1.1), whereas the second chain is saturated. The presence of an unsaturated tail is crucial, since it breaks the symmetry of the molecule and reduces the packing capacity of the lipids, leading to an increase in the fluidity of the bilayer. In mammalian cells, the bilayer is basically composed by sphingomyelin, phosphatidycholine, phosphatidylethanolamine, and phosphatidylserine. They are asymmetrically distributed in the monoloyers: the first two are always present in the outer monoloyer whilst the later are restricted to the inner one (van Meer et al., 2008). This asymmetry responds to the presence of certain chemical groups (such as an amino group in the particular case of phosphatidylserine), that allows the cell to maintain a strict control of the membrane asymmetry.

In addition to the phospholipids, animal cell membranes also contain cholesterol and glycolipids (Yeagle, 1993). Cholesterol is a small molecule with a polar hydroxyl group and a short hydrocarbon chain. Cholesterol occupies the space

between phospholipid tails in the inner region of the bilayer, with its head oriented close to the phospholipid head. Mammalian cell membranes are rich in cholesterol and this molecule plays an important role in the control of bilayer fluidity, and it also affects the membrane rigidity when present at abnormal high densities. The glycolipids are found exclusively in the outer leaflet of the plasma membrane and, in spite of their usual low concentrations (roughly 2%), they are important in the control of bilayer asymmetry.

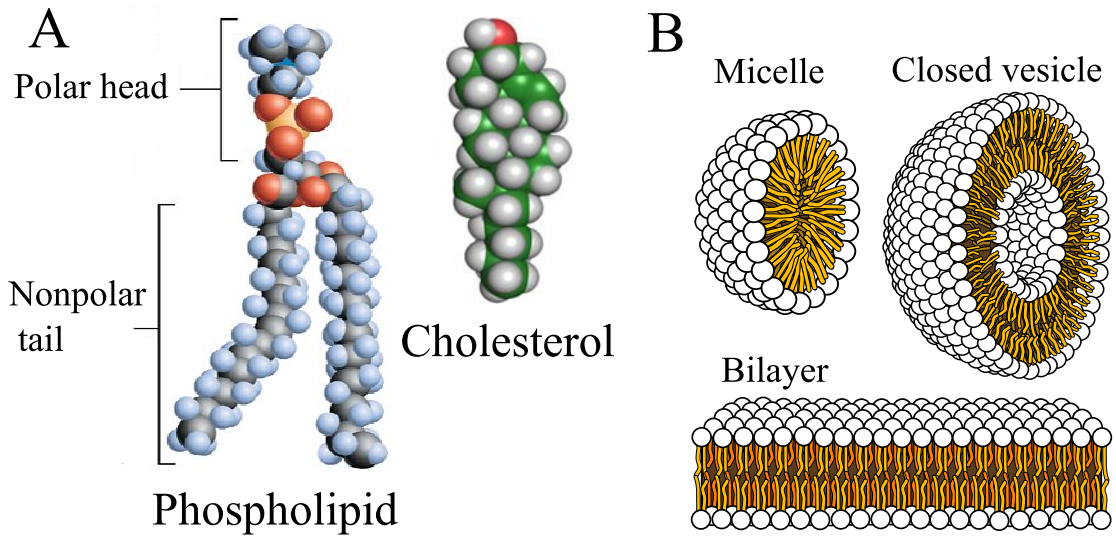

Figure 1.1: (A) Comparison between a phospholipid and the much smaller cholesterol molecule. Phospholipids are characterized by a typical structure with a polar head which interacts with the molecules of water and a non-polar tail of high hydrophobicity. The tail is composed by two carbon tails, one of which is unsaturated. This symmetry breaking reduces the packing capability of the lipids enabling a higher fluidity of the bilayer. Credits: (left) Biology Department at College of the Siskiyous, California; (right) Biochemistry Dictionary, Jeff D Cronk. (B) Different aggregates formed by lipids: micelles, bilayers, and closed bilayers forming vesicles or liposomes. The preference of the lipids to aggregate in one or other structure is determined by the shape of the lipid; phospholipids form bilayers. Credits: Mariana Ruiz Villareal.

Transmembrane proteins

Membrane proteins are responsible of the main processes that take place in the membrane and therefore they define the membrane functionality (Alberts et al., 1994). Depending on the membrane, proteins represent 25-75% of the total mass of the membrane. Membranes of bacteria, such as *E. coli*, characterized by a low protein activity, present protein concentrations below 20%. In the inner membrane of the mitochondria of eukariotic cells, however, proteins may represent as much as 80% of the total mass, reflecting the high concentration of ion gradients and catalytic activity of these structures (Cooper and Hausman, 2009). In the case

of plasma membranes, a typical value is 50%. Since proteins are much larger than lipids, this concentration corresponds to a protein per $\sim 50 - 100$ lipids. Transmembrane proteins are also amphiphilic and orient their polar groups to the aqueous environment (cytosol and exterior of the cell) whereas the hydrophobic groups interact with the lipid tails. Other molecules are located at either side of the membrane and interact externally with the bilayer; an example is the spectrin cytoskeleton that we will study in the subsequent section. Although the action of transmembrane proteins presents many fascinating aspects, for the purposes of this Thesis they are not especially important and we will not extend further on this subject. Still, it is remarkable that these molecules also suppose an important contribution to the membrane elasticity, but this contribution will be directly incorporated to the models by the effective parameters that capture the averaged membrane properties.

Bilayer properties

The bilayers of mammalian cells, as stated before, are complex structures with a bewildering number of proteins working on and through them. They have a typical thickness of 4nm, while most eukaryotic cells are $\sim 5\mu$m length. Thus, the membrane thickness is much smaller $\sim 10^{-3}$ than the overall cell length. Lipids can diffuse freely throughout their own monolayer, with diffusion coefficient $D \sim 10^{-12}\mathrm{m}^2/\mathrm{s}$, but the exchange of molecules between monolayers (the so-called *flip-flop*) is inhibited by the presence of a strong hydrophobic potential (Alberts et al., 1994). The time scale of spontaneous flip-flop is, roughly, several days. There are, however, explicit mechanisms to regulate this lipid rearrangement which control the appropriate bilayer asymmetry. Among others, the translocases are transmembrane proteins specialized in the flip-flop of certain lipids. Cells regulate their bilayer asymmetry to control shape and mechanical properties of the membrane, or to mediate in the interactions with the environment. For instance, since translocases action is ATP-driven, when this molecule is depleted or the cell undergoes apoptosis, lipids start to diffuse freely and the lipid composition of the external monolayer changes. This process is used for cell signaling, alerting especialized cells which detect the abnormality and phagocyte the dead cell (Devaux et al., 2008).

Although the bilayer is usually fluid, this property presents a strong dependence on the temperature and lipid composition. The high diffusivity of each lipid along the leaflets would suggest that they might be randomly distributed along the cell surface. However, in certain molecules, van der Waals interactions between the hydrocarbon tails are strong enough to form aggregates and inhibit the lateral diffusion. These aggregates are known as lipid rafts and are composed of

sphingomyeline, phosphatidylcholine and especially cholesterol (Jacobson et al., 2007). Experiments suggest that cholesterol are present in much higher densities in these rafts than in the surrounding areas of the bilayer. It seems that the organization in rafts has specific functions, since some signaling molecules are only assembled in these microdomains, and therefore rafts are important for regulation of neurotransmission, and receptor traffiking (Allen et al., 2007). The fluidity of the bilayer, presence and formation of rafts and generically the microstructure of the lipid bilayer are subjects of intense debate, and recent studies suggest that the current description represents just a rough picture of the actual bilayer structure (Engelman, 2005; Leslie, 2011).

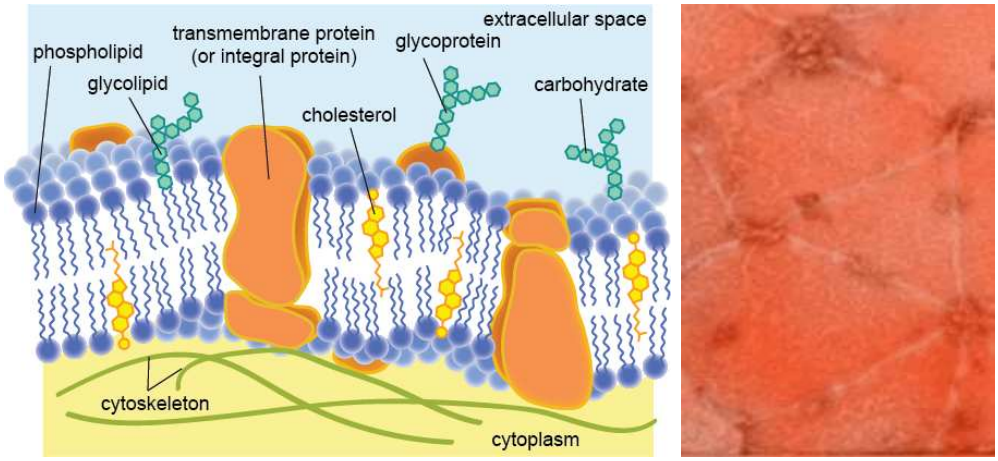

Figure 1.2: (A) Plasma membrane scheme. The plasma membrane is composed by a fluid lipid bilayer and a high concentration of transmembrane proteins that account for the enzymatic activity. The bilayer contains a rich composition of diverse lipid species, including cholesterol, a small molecule inserted in contact with the phospholipid tails. The underneath spectrin cytoskeleton is a two dimensional fold attached to the bilayer. Source: *www.shmoop.com/biology-cells/plasma-membrane.html* (B) Electron microscopy imaging of the cytoskeleton network. Note the 6-vertices links. Source: *www.lbl.gov/Science-Articles/Archive/LSD-single-gene.html*

1.1.2 The cytoskeleton

Most cells have a complex mesh formed by actin filaments which occupies most of the inner cytosolic volume, and connects the different organelles and microstructures of the cell. This structural element provides mechanical strength to the cell and it often participates in cell shape and cell mobility. This structure, known as cortical cytoskeleton, is connected with the membrane in order to coordinate the response to external perturbations. Despite its importance in several aspects of the cell mechanics, we concentrate here in other and much simpler cytoskeletal structure, the so-called *membrane* cytoskeleton which lies underneath the lipid bilayer.

The membrane cytoskeleton has a structural functionality, providing strenghten and preventing from certain shape deformations, such as vesiculation or pinch-off of the bilayer. Its presence also limits the transmembrane diffusion on the bilayer, defining small patches that effectively act as domains where the protein diffusion is restricted. The membrane cytoskeleton is a two-dimensional spectrin network anchored to the inner (cytosolic) monolayer of the plasma bilayer of certain cells (Bennett, 1989), such as the human erythrocyte. Spectrin is a long rod of around 75nm length. The spectrin molecules are crosslinked by vertices formed by actin, which can form different type of junctions, depending on the number of molecules that they connect (from 3 to 7). In healthy cells, the 6-vertices junction is dominant, with as low as 3% of 5-vertices and 8% of 7-vertices (Liu et al., 1990). The presence of these *defect* junctions is, however, important as it allows local relaxation of the network tension.

The spectrin cytoskeleton is an active tissue. The presence of ATP is crucial for maintaining the cytoskeleton properties, and when this molecule is depleted the cell experiences drastic shape changes. Although this phenomenon is not completely understood, the *fluid gel* hypothesis assumes that the network is subjected to continuous remodeling, which allows relaxation of the cytoskeleton tensions (Li et al., 2005). Hence, when active processes cease, the cytoskeleton loses its fluidic behaviour and stiffens.

1.1.3 Active processes in the membrane

The membrane description presented so far corresponds to a static picture. However, both the bilayer and the cytoskeleton are controlled by a sophisticated engineering maintained by active processes. Therefore, the membrane is not in thermodynamic equilibrium, but it is subjected to a continuous renewal of molecules that requires of an expensive energy consumption, in order to guarantee the delicate steady state of the membrane.

As previously mentioned, the lipid bilayer asymmetry is modulated by three main proteins that control the composition of each leaflet (Devaux et al., 2008). Flippases transport aminophospholipids from the outer to the inner leaflet, althouth it seems that incidentally they are capable of flipping other lipid molecules. Floppases transport amphiphilic drugs and phospholipids with little selectivity from the inner to the outer leaflet. Scramblases flip phosphatidylserine from the inner to the outer leaflet of the membrane. The presence of this lipid in the cell surface triggers platalet aggregation, so that the very specific function of scramblases relates with the response to certain abnormal environmental pressures. The fragile balance of membrane asymmetry is achieved by the coordinate action of these (among others) transmembrane proteins.

The presence of active processes affecting the cytoskeleton chemical composition is known for a long time ago (Pinder et al., 1977), but its molecular basis has been adressed in detail only recently. Several studies have identified the cytoskeletal proteins (mainly β-spectrin and protein 4.1R) that under phosphorylation can modify the network connectivity, affecting the mechanical stability of the membrane (Manno et al., 2005). However, it is still unclear whether these processes occur spontaneously and serve as a regulation system of the cytoskeletal mechanics. A different mechanism of control of the cytoskeleton structure has been proposed (Wong, 1999). The flux of anions mediated by the transmembrane protein Band 3 is used to fold and unfold the spectrin filaments, giving rise to a contraction or relaxation of the cytoskeleton. This may be used by the cell to control its shape in certain conditions. These and other active mechanisms will be discussed in detail in Chapter III.

1.2 The human Red Blood Cell

Eukaryotic cells present an extensive variety of shapes, as an adaptation to their specific function and location within the different tissues. The cortical cytoskeleton and the plasma membrane are the two main elements responsible of the cell shape and mechanic response. Still, the different organelles occupy an important portion of the cell volume, and their presence implies that the cell must accomodate them. Hence, while studying the mechanical properties of the cell it is difficult to discern between the different effects, obscuring the understanding of the specific properties of the membrane. Taking into account this problem, the erythrocyte or red blood cell (RBC hereafter) represents an interesting case. Mammalian RBCs are anucleated and lack any internal structure, so that their unique components are the plasma membrane with its underlaying cytoskeleton. Accordingly, the shape of the RBC can be directly understood as the result of its membrane properties. The RBC is therefore studied as a model system in order to understand plasma membrane properties and, indeed, many of the studies that have elucidated key insights in membrane biology focused on RBCs. Nevertheless, RBCs are interesting not only as a model system but also due to their crucial role in our lifes, as they are the main component of blood and the unique carriers of oxygen.

1.2.1 RBC properties

Mammalian RBCs have different shapes and sizes, depending on the animal physiological requirements (*eg* oxygen consumption in animals inhabiting high altitude

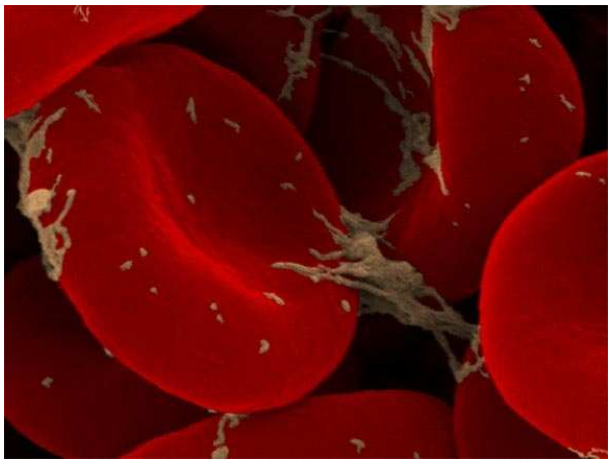

Figure 1.3: Healthy red blood cells present a distinct shape, the so-called discocyte, characterized by a discoidal shape with a concave region in the center. The disc has a typical diameter of 8μm and thickness 2μm. Credits: CDC / Janice Carr.

mountains). Very similar species have different RBC shapes, such as sheeps and goats. The human red blood cell has a disk shape of typical diameter 8μm, with a concave region in the center where the cell achieves its minimum thickness of 1μm, and a convex outer rim where it reaches a maximum thickness of 2μm. This particular shape is usually known as the biconcave discocyte, and it corresponds to the healthy state of the cell. Typical cell area and volume on a healthy individual are 140μm^2 and 90μm^3 (Zarda et al., 1977), respectively. Cells present specific regulatory systems to maintain their area and volume constant, and thus ensuring that their resting shape is fixed. In humans, RBCs exhibit a huge intraindividual variability, with strong correlation with sex and age. Cells of men are up to 20% larger than in women, and men also present higher hematocrit (*ie* the volume fraction of RBCs in blood) in the circulatory system. Ageing affects to the RBC membrane rigidity, so that old individuals present more rigid cells.

The biconcave discocyte, however, represents just one of the many morphologies exhibited by RBCs, and it responds to a very specific conditions of area to volume ratio, bilayer and cytoskeleton elastic properties, membrane internal asymmetry and pH of the surrounding aqueous environment, among others. Other well-known morphologies are the stomatocyte, when the cell acquires a cup-like shape, and the echynocyte, when the cell becomes spherical and it develops many spikes around its contour, resembling a sea urchin. The entire shape deformation comprises a sequence of different morphologies usually known as stomato-discoechynocyte (Besis, 1973), and it is triggered by disruption of the membrane microstructure which changes the membrane asymmetry. These phenomena will be studied in detail in the Part II of this Thesis.

RBCs are produced in the bone marrow, developed from stem cells. RBCs

mature during the subsequent 7 days in a process known as erythropoiesis, before they develop the healthy discocytic state and are released in the circulatory system. Approximately, 2.5 million cells per second are produced in adult humans. They have a 120 functional life span in which they complete a cycle each 20 seconds. During each cycle, RBCs pass through capillaries of 5μm that force the cell to undergo extreme deformations. Ageing reduces cell deformability, and eventually RBCs enter in eryptosis, in which they are removed from the circulatory system.

The origins of the peculiar discocyte shape have been subject of debate for decades. It seems reasonable that the large cell area compared to volume (comparing with that of a sphere, the so-called reduced volume $v_{red} = V/(4\pi R^2/3)$=0.6, where $R = \sqrt{(}A/4\pi)$ is the radius of a sphere with equal area to the cell; thus, for a sphere $v_{red} = 1$), responds to the necessity of optimizing the diffusion of oxygen across the membrane. Alternatively, it has been proposed that the disk has a low inertial momentum, so that it does not rotate when flowing in the main arteries, minimizing the formation of turbulent flows (Uzoigwe, 2006). Other hypothesis postulates that the discocyte is an appropiate shape to undergo strong deformations and pass through the smallest capillaries, after recovering the normal relaxed shape (Reinhart and Chien, 1986).

1.2.2 RBC disorders

The healthy running of RBC circulation and oxygen transport can be affected by different disorders. For instance, iron cell anemia, in which low concentrations of iron imply a reduced storage capacity of oxygen, is a regular and well-known disorder even in healthy individuals. However, most interesting disorders concern inherited pathologies which affect the RBC membrane, producing abnormalities in the RBC shape or deformability, which potentially reduce the healthy functioning of blood circulation. In addition, malaria (which does not have a genetic origin) is also known to impair the membrane microstructure leading to cell stiffening. These membrane alterations provide important information about the membrane structural balance, and their main causes and consequences are outlined below.

- **Sickle cell anemia (drepanocytosis).** This disease is characterized by the formation of sickle cells that lose their capability to deform and recover the discocyte shape, altering the oxygen delivery. The molecular basis is found in an abnormal phosphorilation of hemogoblin that promotes a massive aggregation of this molecule under low concentrations. The formation of these aggregates affects the concentration of the protein Band 3, and the cell

membrane is damaged in a process similar to ageing, becoming rigid. Patients affected by this pathology present a reduced life expectancy, although modern medical treatments allow a normal life.

- **Hereditary spherocytosis.** Patients present a high concentration of spheroidal shaped RBCs, as a consequence of defects in several proteins of the membrane (mainly from the bilayer-cytoskeleton links) which produce fragility of the membrane. The alteration of membrane properties allows vesiculation and loss of membrane surface, triggering the cell shape deformation. Spherocytes are rapidly retired from circulation by the spleenic system, leading to hemolysis. Patients must be treated with blood transfusions for critical levels of anemia (Gallagher, 2005).

- **Hereditary elliptocytosis.** This pathology is characterized by abnormalities in the spectrin dimers, producing weakness of the cytoskeleton which impairs the membrane stability. RBCs deform into ellipsoidal (or cigar-shaped) cells. The RBC functionality might not be severely affected, as most patients are asymptomatic and only 10% present anemia. Interestingly, elliptocytes are more resistant to malaria than normal RBCs, and presumably this fact explains why hereditary elliptocytosis presents a much higher incidence in Africa and Mediterranean Europe than any other regions (Gallagher, 2005).

- **Malaria.** Malaria is caused by the infection of a parasit of the genus *Plasmodium*. Malaria is currently the disease causing the highest number of deaths in the world, roughly 1-2 million per year (most of them in Africa), with up to 200 million documented cases each year. The parasit infects different cell species. Infected RBCs develop an advanced proteinic machinery, including the formation of organelles similar to the Golgi apparatus which serve for nutrient transport and storage, and allow enzimatic activity. The parasit is hosted in a vacuole, and during its maturation it reaches the size of a nucleus in a typical eukaryotic cell. Appart from this new internal structure, the parasit produces changes in the membrane proteins that affect the deformability of the cell. At least 50 protein abnormalities have been identified (Cooke et al., 2004). The RBC also adopts a more spherical shape, and proteins allocated in the external face of the membrane promote aggregation with other infected cells, avoiding the hemolysis in the spleen. All these conformational changes strongly affect the cell mechanical properties, modifying the rheological properties of blood (Dondorp et al., 2000).

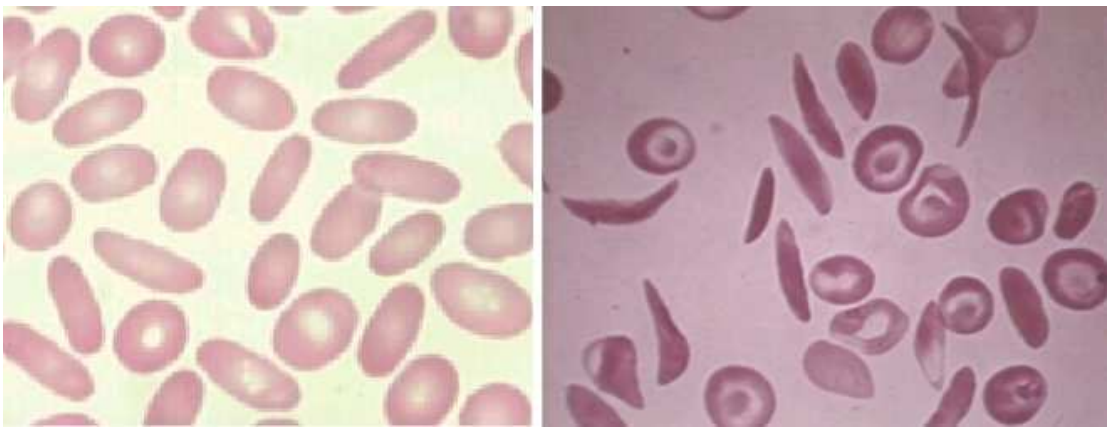

Figure 1.4: Red blood cell membrane disorders. Alterations in the membrane microstructure produce and imbalance in the membrane that lead to abnormal cell shapes. (*Left*) Elliptocyte. (*Right*) Drepanocyte (sickle cell anemia). Source: *http://www.mclno.org/WebResources/kbase/cellatlas/Ovalocyte.html*

	Cross-sectional area (cm^2)	Velocity(cm/s)	*Re*
Aorta	2.5	33	3000
Small arteries	20	4.12	80
Arterioles	40	2.05	0.5
Capillaries	2500	0.033	0.05
Small veins	80	1.03	0.2

Table 1.1: Values of the total cross-sectional area, flow velocity and Reynolds number for different conduits of the circulatory system. Adapted from Hall (2011).

1.3 Circulatory system and blood

The circulatory system is an organ system that circulates the blood along all the cells and tissues, facilitating the transport of oxygen and nutrients which allow the nourishment of the cells. It also serves as carrier of other molecules or matter, such as transport of waste products towards the excretory system, or a fast transport of hormones from one part of the body to another in response to a certain environmental condition. Generally, the main function of the circulatory system is to provide the molecules that the body tissues need at each moment. The circulatory system is divided into two main parts, the pulmonary circulation (which represents a closed circuit from the heart towards the lungs in order to oxigenate the blood, and back to the heart) and the systemic circulation (which corresponds to the network that distributes the blood all along the body). The circulatory system is coupled to the cardiovascular system, formed by the heart and adjacent venule circuits, which serves as the engine that pumps blood.

1.3.1 Functionality

The systemic circulation comprises a structured network in which the conduits are increasingly thinner, as they distance from the heart. The arteries transport oxygen-rich blood under high pressure to the different tissues. The aorta is the thickest conduit of the body as it collects all the blood from the heart, which is then distributed between the different arteries. These conduits have strong vascular walls, and blood flows at high velocities. The arterioles are small branches which release blood into the capillaries. Arterioles have strong muscular walls that control the conduit width, adapting to the specific tissue needs. The capillaries are the thinnest conduits of the system, with a cross section that can be considerably smaller than the surface of the RBC disk. When passing throughout the capillaries, the RBC membrane is largely in contact with the capillary wall. It is here where the oxygen delivery occurs, as well as diffusion of other molecules transported in the blood. Molecules pass through the capillary wall to the intersticial fluid, and from here they freely diffuse, reaching all the cells of the tissue. Capillary walls have numerous pores that facilitate the exchange of substances. Oxygen-depleted blood is returned to the heart by the vessel system. Veins transport blood under very low pressures. For this reason, they serve as blood reservoirs, controlling the volume of extra blood by muscular contraction.

The amount of blood hosted by veins and arterioles is inhomogeneously distributed. Of the 84% from the total body blood contained by the systemic circulation, 64% corresponds to veins, 13% to arteries, and 7% to capillaries (Hall, 2011). The total cross sectional area for each type of conduit is shown in Table 1.1. In spite of the reduced thickness of the capillaries, they form a very dense mesh and therefore the total area is enormous. Since the total blood flow Q is constant, an estimate of each conduit velocity can be obtained from $v = Q/A$, and it is shown in Table 1.1, in addition to the correspondent Reynolds number. The results show that highly turbulent flows are present in the aorta, but laminar flow is expected in most arterioles and venules and indeed Re is very low in the capillaries.

The heart pumps blood by periodic muscular contractions. Accordingly, the blood pressure is also periodic as the pulse wave travels through the circulatory system. In the large arteries, where the systolic pressure is usually measured, the periodic pulses are easily detected, and as it is widely known that this represents one of the main medical indicators of life. However, the pressure damping along the smaller arterioles and capillaries attenuates the amplitude of the pulse, and actually blood pressure is almost constant in capillaries, as shown in Figure 1.5.

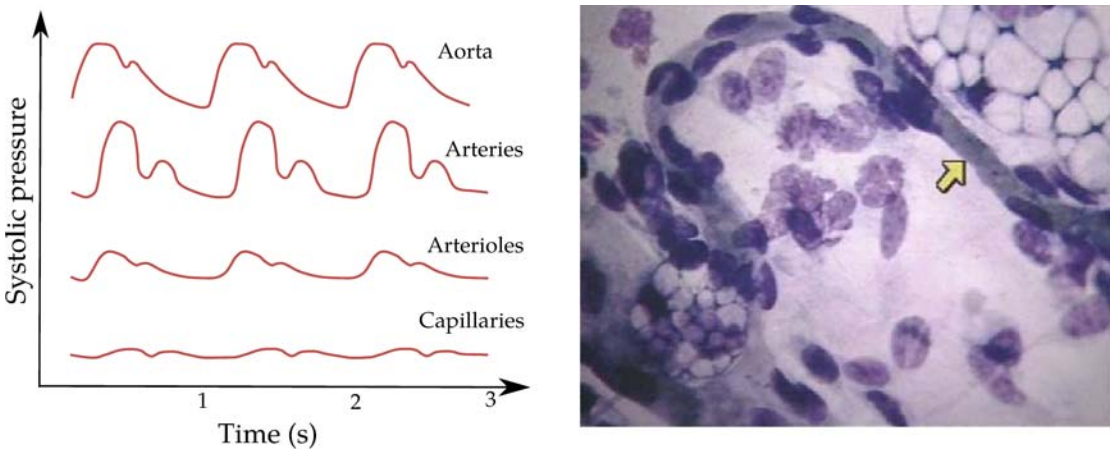

Figure 1.5: (*Left*) Blood pressure pulse for different conduits of the circulatory system. The periodic heart beats produce a periodic pulse of the blood pressure in arteries. However, the pressure damping in thinner conduits attenuates this pulse and pressure is almost constant in the thinnest capillaries. Adapted from Hall (2011). (*Right*) *In vivo* red blood cell flow in capillaries. To pass through the thinnest capillaries, RBCs are forced to undergo severe deformations, squeezing and adopting asymetric shapes. Source: *http://quizlet.com/4383143/circulatorylymph-quiz-flash-cards/*

1.3.2 Blood properties

Blood comprises a fluid known as plasma and a high concentration of immersed cells. Among them, three main species deserve mention: red blood cells, leukocytes, and platalets. RBCs are the major component of blood, representing up to 95% of the total number of cells. Leukocytes are large cells found in very low concentrations (around 0.1%), but with crucial functions in the immunity system. Platalets represent roughly 5% of cells and are responsible of blood coagulation to control blood loss when the circulatory system is damaged. In healthy humans, RBC concentration in blood is typically $5.2 \cdot 10^6$ cells per cubic milimeter in men and $4.7 \cdot 10^6$ in women. This represents a volume concentration (known as hematocrit) of approximately 40-45%. Nevertheless, RBC concentration is not uniform in the circulatory system, and it decays in the thinnest conduits. For instance, concentrations of 10-20% are found in the capillaries (Fung, 1997).

Blood plasma is a solution of diverse molecules (including proteins, mineral ions, hormones, and glucose) and 92% of water. It is characterized by a straw-yellow colour, an adult individuals contain roughly 3 litres of plasma. Blood plasma density is approximately 1025 kg/m^3, and cells density is around 1125kg/m^3, leading to a value for the whole blood of typically 1060 kg/m^3. Blood viscosity is, *at normal conditions*, $3 - 4 \cdot 10^{-3}$Pa s, but it strongly depends on the hematocrit and RBC mechanical properties, including RBC deformability and RBC aggregation, as we will study in Part IV of this Thesis. Alterations of blood

viscosity can be relevant in many disease processes, and hemorheology is an important area in a medical frame (Baskurt et al., 2007).

Chapter 2

Physical approach to membranes

The complexity of biological membranes constitutes a challenge for any theoretical description. In order to capture their rich behaviour, one needs to carefully consider the scales of interest of the system. If one is interested in the study of the overall membrane response at the cell scale, the atomic description is clearly unaffordable: the complexity of atomic interactions, even in simple molecules such as lipids, discards any treatment at this scale. Coarse-grained descriptions, which represent each lipid by a number of grains (typically 3-10) that encompass a region of the molecule with similar properties (Marrink et al., 2007; Shillcock and Lipowsky, 2006), offer a path for the study of small sized patches of membranes. The state-of-the-art numerical methods are able to describe the kinetics of typically 10^6 molecules (Marrink and Tieleman, 2013), involving membrane domains of roughly 100 x 100nm, but still far from the macroscopic cell scale, 10μm x 10 μm. It is clear that this scale is not feasible if one pretends to study the overall cell response. For this purpose, it is convenient to invoke mesoscopic theories (Deserno, 2009). By considering the membrane as locally homogeneous and introducing a continuum description, each small part of the membrane is characterized by some certain local properties. These properties must be consistent with the local molecular structure of the membrane, so that a connection between the micro and meso scales should be derived.

The molecular complexity of biological membranes only affects to a few essential aspects of relevance in a physical description of membranes. Namely, these main features can be summarize as follows

1. Length scale separation. The membrane thickness is of the molecular scale, $\sim$ 4nm, whereas the radii of curvature of typical objects of interest (such as cells, vesicles and vacuoles) are typically of microns. This difference ensures that in the cell scale the membrane can be considered a two-dimensional sheet.

2. Fluidity. At normal conditions (including lipid composition and physiological temperature), the lipid bilayer is fluid in the membrane plane. Thus, it does not present resistance to shear stresses.

3. Hydrophobicity of the lipid tails. The strong hydrophobicity of the nonpolar tails of the phospholipids implies two different considerations. First, that lipid molecules are insolube in water, so that the total amount of lipids in the membrane is constant (though this fact does not affect the distribution of lipids between leaflets). Second, that even when assembled in a bilayer, lipid tails are sensitive to the interaction with water molecules (*eg* if the bilayer is stretched and the distance between lipid increases, tails can be exposed to water). The hydrophobic repulsion forces that the bilayer is almost incompressible, with a very high resistance to stretch.

4. Bilayer architecture. Although by assertion 1 the membrane can be considered as a fold, the internal microstructure of the membrae must be taken into account. The bilayer is formed by two leaflets separated by a constant distance. However, the leaflets slide each other, accomodating the local lipid densities to the local shape and curvature of the membrane.

5. RBCs present a spectrin network beneath the bilayer, similar to a string mesh, whose mechanical properties can be important – or dominant – under certain conditions. In the typical size of a cytoskeleton patch, ~ 50 nm^2, the overall composition of the lipid bilayer is relatively homogeneous throught the cell membrane, and hence this invites to a continuous description.

6. Active processes. At resting conditions (*ie* in the absence of external hydrodynamic fluxes), RBCs are in a stable state given by the mechanical equilibrium of their membrane. This equilibrium is determined by the internal properties of the membrane, which actually are maintained by active processes. Thus, strictly speaking, cells are out of thermodynamic equilibrium, since energy is required to maintain the steady properties of the membrane, but these properties determine the mechanical dynamics and equilibrium of the cell. Unless otherwise specified, in this Thesis *equilibrium* refers to mechanical equilibrium.

In this context, the Helfrich bending energy represents the fundamental theory of membrane elasticity. Helfrich adapted the general theory of elasticity to the particular characteristics of membranes, accounting for the structural membrane properties. The theory has proven to be largely succesful, explaining an extensive phenomenology of membrane related problems. In this Chapter, we first outline some important results of the general theory of elasticity, focusing on the bending deformations which are of special interest within the membrane framework.

We then formally present the Helfrich theory, and briefly describe some of its main results regarding cell and vesicle morphology. Afterwards, we consider other alternative or complementary models that haven been proposed to explain new and more complex phenomena, such as the cytoskeleton elasticity or the bilayer-couple model. We end with an overview of the characterization of the material parameters of the model as measured by different experimental techniques.

2.1 Theory of elasticity

Membranes are elastic structures whose mechanical properties are usually described by the general theory of elasticity. The deformation of any object is described by the deformation vector $u_\alpha = x'_\alpha - x_\alpha$, where x are the coordinates in the relaxed state and x' represent the coordinates under deformation. For simplicity we shall assume an isotropic, homogeneous material. The strain tensor is defined as

$$u_{\alpha\beta} = \frac{1}{2}\left(\frac{\partial u_\alpha}{\partial x_\beta} + \frac{\partial u_\beta}{\partial x_\alpha}\right). \tag{2.1}$$

The energy of an elastic object subjected to a certain deformation, given by the tensor $u_{\alpha\beta}$, reads

$$\mathcal{F}_{el} = \int \left[\frac{\lambda}{2}(u_{\gamma\gamma})^2 + \mu\,(u_{\alpha\beta}u_{\alpha\beta})\right] dV, \tag{2.2}$$

where λ and μ are material parameters known as Lamé coefficients. $\mathcal{F}_{el}$ actually represents an excess energy with respect to the undeformed state. The interpretation of the diagonal terms of the deformation tensor $u_{\alpha\beta}$ is simple. Considering a stretching deformation $x' = \psi x$ (see Fig. 2.1A), a simple calculation shows that the non-diagonal terms of the strain tensor are zero, leading to an energy of deformation $\mathcal{F}_{el} = (\lambda + 2/3\mu)\psi^2 V$, where V is the volume of the underformed object. Conversely, in a shear deformation $x' = \alpha x, y' = \beta y$ (see Fig. 2.1B), which maintains constant surface, the trace of the tensor vanishes. Given that any planar deformation can be decomposed into a pure stretching and a pure shear, we rewrite the elastic energy,

$$\mathcal{F}_{el} = \int \left[\mu\left(u_{\alpha\beta} - \frac{1}{3}\delta_{\alpha\beta}u_{\gamma\gamma}\right)^2 + K(u_{\gamma\gamma})^2\right] dV, \tag{2.3}$$

where μ is renamed as shear modulus and $K = \lambda + (2/3)\mu$ is the bulk (or compression) modulus. Within the frame of biological membranes, often the elasticity

is described in terms of two new modulii, the Young modulus E and the Poisson ratio ν, and the expression for the elastic energy now reads

$$\mathcal{F}_{el} = \frac{E}{2(1+\nu)} \int \left[u_{\alpha\beta}^2 + \frac{\nu}{1-2\nu} u_{\gamma\gamma}^2 \right] dV, \tag{2.4}$$

where $E = 9K\mu/(3K+\mu)$ and $\nu = (3K-2\mu)/2(3K+\mu)$.

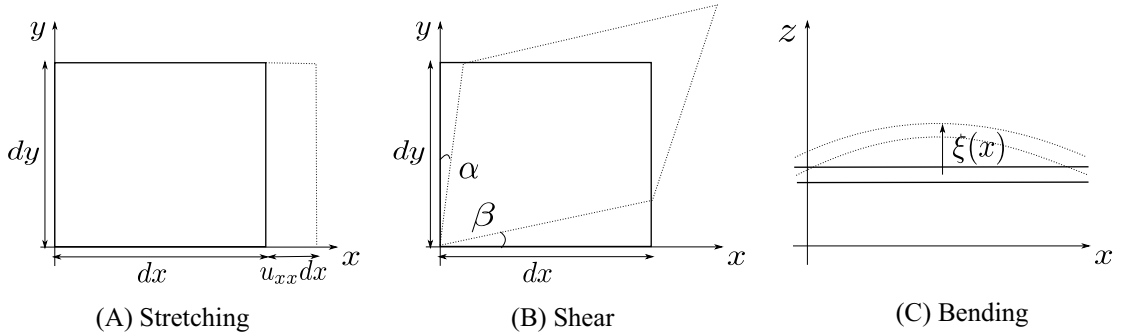

Figure 2.1: Scheme of the main deformations. Bold lines represent the underformed state and dashed lines the deformation. (A) Stretching, when the object increases its area; (B) shear, when the object deforms without a change on its area; and (C) bending, which represents a normal displacement ξ to the surface.

2.1.1 The bending mode

In order to comprehensively understand the elasticity of membranes, we explore here the elastic properties of plane objects of small thickness compared to their surface. Thus, we represent the membrane as a generic object, such as a plate, subjected to a pure bending deformation. Cell membranes have a typical thickness of 4nm, whereas the overall cell length is usually $5 - 10\mu$m. The separation in the length scales suggests that the approximation of the membrane as a two dimensional fold, as previously commented, is largely appropriate. After averaging the elastic parameters over the plate section and adopting the two-dimensional description, the Helfrich free energy is recovered.

Let us consider a flat plate of thickness h. Consider now the bending deformation shown in Figure 2.1C, with no in-plane deformation $u_x = u_y = 0$ but out-of-plane displacement $u_z = \xi(x, y)$ in the Monge representation (do Carmo, 1976). The stress tensor is given by the variations of the elastic energy with respect to the deformation,

$$\sigma_{\alpha\beta}(\vec{r}) = \frac{\partial \mathcal{F}_{el}}{\partial u_{\alpha\beta}(\vec{r})}. \tag{2.5}$$

The specific dependence on the strain tensor reads

$$\sigma_{\alpha\beta} = K(u_{\gamma\gamma}\delta_{\alpha\beta}) + 2\mu(u_{\alpha\beta} - \frac{1}{3}u_{\gamma\gamma}\delta_{\alpha\beta}). \tag{2.6}$$

And the force exerted by the object can be derived from

$$F_{\alpha}^{plate} = \frac{\partial\sigma_{\alpha\beta}}{\partial x_{\beta}}. \tag{2.7}$$

The deformation of the object may respond to the action of an external forcing, F_{α}^{ext}, on the object surface. This force is balanced by the internal stresses of the plate, which are given by the force $-\sigma_{\alpha\beta}n_{\beta}dA$. The equation of force balance on the object surface, where the external forces apply, reads

$$\sigma_{\alpha\beta}n_{\beta} = F_{\alpha}^{ext}, \tag{2.8}$$

where n is the normal vector to the object surface. We suppose that, given that the plate is very thin, the external forces required to bend it are small compared to the internal tensions across the membrane (Landau and Lifshitz, 1999), so that F^{ext} are neglected in (2.8). Note that this hypothesis is *a priori* not obvious, but still let us assume its validity under certain conditions. For a strictly flat plate, $n_z = 1$ and therefore $\sigma_{xz} = \sigma_{yz} = \sigma_{zz} = 0$. If the plate is only slightly bent, these components are strictly non-zero but remain small compared to the rest of components of $\sigma_{\alpha\beta}$, so we can equate them to zero and use the resulting equations to solve the strain tensor components. For this deformation, all the terms of the strain tensor can be calculated explicitly:

$$\begin{aligned} u_{xx} &= -z\partial_x^2\xi, \\ u_{yy} &= -z\partial_y^2\xi, \\ u_{zz} &= -(\nu/(1-\nu))z(\partial_x^2\xi + \partial_{yy}^2\xi), \\ u_{xy} = u_{yx} &= -z\partial_{xy}^2\xi, \\ u_{xz} = u_{zx} &= 0, \\ u_{yz} = u_{zy} &= 0. \end{aligned} \tag{2.9}$$

By introducing these expressions in (2.2), the elastic energy of the bent plate is

$$\mathcal{F}_{el,b} = \int z^2 \frac{E}{1+\nu}\left\{\frac{1}{2(1-\nu)}\left(\frac{\partial^2\xi}{\partial x^2} + \frac{\partial^2\xi}{\partial y^2}\right)^2 + 2(1-\nu)\left[\left(\frac{\partial^2\xi}{\partial x\partial y}\right)^2 - \frac{\partial^2\xi}{\partial x^2}\frac{\partial^2\xi}{\partial y^2}\right]\right\} dV. \tag{2.10}$$

Integrating across the plate thickness, from $-h/2$ to $h/2$, in the z-direction,

$$\mathcal{F}_{el,b} = \frac{h^3 E}{24(1-\nu^2)} \int \left\{ \left(\frac{\partial^2 \xi}{\partial x^2} + \frac{\partial^2 \xi}{\partial y^2} \right)^2 + 2(1-\nu) \left[\left(\frac{\partial^2 \xi}{\partial x \partial y} \right)^2 - \frac{\partial^2 \xi}{\partial x^2} \frac{\partial^2 \xi}{\partial y^2} \right] \right\} dS. \tag{2.11}$$

Some considerations are required to readily identify the ξ-dependent terms in (2.11). In the Monge parametrization, the normal vector to the surface can be obtained from $\hat{n} = \nabla\xi/|\nabla\xi|$. The total and Gaussian curvatures are defined in terms of the normal vector as $C = -\nabla \cdot \hat{n}$ and $G = 1/2[(\nabla_s \cdot \hat{n})^2 - \nabla_s \cdot \hat{n} : \nabla_s \cdot \hat{n}]$, respectively. Hence, straightforward calculations lead to (do Carmo, 1976)

$$C = -[(1 + (\partial_x \xi)^2)\partial^2_{yy}\xi + (1 + (\partial_y \xi)^2)\partial^2_{xx}\xi] - 2(\partial_x \xi)(\partial_y \xi)(\partial^2_{xy}\xi) \approx -[\partial^2_{xx}\xi + \partial^2_{yy}\xi] \tag{2.12}$$

,

$$G = \frac{(\partial^2_{xx}\xi)(\partial^2_{yy}\xi) - (\partial^2_{xy}\xi)^2}{(1 + ((\partial_x \xi)^2)^2 + ((\partial_y \xi)^2)^2)^2} \approx (\partial^2_{xx}\xi)(\partial^2_{yy}\xi) - (\partial^2_{xy}\xi)^2, \tag{2.13}$$

for the total (2.12) and Gaussian (2.13) curvatures. We have assumed that the out-of-plane displacement ξ is small relative to the lengthscale of the plate, so that the gradients are small $\partial\xi \ll 1$. By direct comparison of (2.11) with expressions (2.12) and (2.13), the elastic energy for the bending deformation can be rewriten as

$$\mathcal{F}_{el,b} = \int \left(\frac{\kappa}{2} C^2 + \kappa_G G \right) dS, \tag{2.14}$$

where we have introduced the bending rigidity $\kappa = Eh^3/12(1-\nu^2)$ and the saddle-splay modulus $\kappa_G = -\kappa(1-\nu)$. This derivation applies generically for objects such as plates or, in the present context, monolayers. However, a bilayer consists of two monolayers which glide each other, so cannot transmit shear stresses and the bending rigidity of the bilayer, κ^{bil} arises as the sum of the rigidities of the monolayers, κ^m. Considering monolayers of thickness $h = d/2$, the bilayer bending modulus is given by

$$\kappa^{bil} = \kappa^m_1 + \kappa^m_2 = \frac{d^3 E}{48(1-\nu^2)} = \frac{K_A}{24(1+\nu)}, \tag{2.15}$$

where we have introduced the area-compression modulus $K_A = dE/2(1+\nu)$, which represents the energetic cost of expand/compress the area of the plate, and it is

related with the volumetric bulk modulus K. Hence, assuming a homogeneous plate and considering a pure bending deformation, the general elastic energy (2.2) reduces to the bending contribution (2.14). The particular elastic modulii used to describe cell mechanics depend on the cell species. In the frame of RBC elasticity, it is usual to characterize the membrane mechanics with the bending and shear modulii. On the contrary, in cells with an inner structure (such as leucocytes or epithelial cells), especially in the framework of atomic force microscope experiments, most studies focus on the Young modulus (Kuznetsova et al., 2007). We hereafter concentrate on the elastic description based on the bending modulus, which is widely extended in the membrane mechanics field.

2.2 The Helfrich bending energy

The theoretical study of membranes at the cell scale was first performed by Canham (1970), Helfrich (1973), and Evans (1974). They concentrated on the identification of the relevant elastic properties of the RBC membrane by trying to reproduce its distinctive discocyte shape. The main assumption of their approach is that the cell membrane can be described as a two-dimensional fold, based on its minute thickness compared to the cell length. They initially focused on lipidic membranes, neglecting any contribution from the cytoskeleton. Helfrich proposed that from the three main type of deformations that a layer can undergo, shear, tilt and bending, only the last does play a relevant role in the membrane elasticity. Accordingly, he generalized the curvature energy (2.14) to describe the elasticity of lipid membranes, proposing the free energy

$$\mathcal{F}_b = \frac{\kappa}{2}\int (C - c_0)^2 dA + \kappa_G \int G dA + \int \gamma dA + \int \Delta p dV, \tag{2.16}$$

where c_0 is the so-called spontaneous curvature that accounts for any asymmetry in the membrane internal structure, whereas γ and Δp generically represent a surface tension and a pressure difference across the membrane. In the Helfrich initial description, these two components are Lagrange multipliers to ensure that cell area and volume, respectively, are conserved. It is remarkable that in part of the literature there is a misleading use of the mean curvature $H = 1/2(c_1 + c_2)$, instead of the total curvature $C = c_1 + c_2$, in (2.16). Although the factor 2 does not obviously affect to the geometrical description of the shape, it is relevant for the value of the associated material parameters, κ and c_0, which depending on the specific notation will deviate in a factor of 4 and 2, respectively. In this Thesis we use the total curvature C (sometimes also represented as K in the literature). The Gaussian curvature is a topologic invariant, as known from the Gauss-Bonnet

theorem,

$$\int GdA = 4\pi(1-g), \tag{2.17}$$

where g is the topological genus, *eg* number of holes or handles. Consequently, the Gaussian curvature only plays a role in the membrane elasticity in processes involving topological transformations. For the case of closed membranes, such as cells, the Gaussian term remains constant and for simplicity it can be ignored.

The minimization of (2.16) for an ellipsoidic shape under the appropriate values of area and volume leads to the biconcave discocyte of the RBC as the equilibrium shape. Ensuing studies investigated the properties and minimal shapes of this energy and the theory has been refined in order to incorporate other mechanisms, as explained later on. In the last years, the model has been incorporated to different dynamic theories, offering the possibility of studying new and more complicate phenomena. Many of the results of this theory have proven good agreement with experiments; nice examples include the theoretical prediction of shapes of the stomatocyte-echynocyte transition (Lim et al., 2002), the study of tubulation when polymers are attached to a lipidic vesicle and effectively induce a spontaneous curvature (Campelo and Hernández-Machado, 2008), or the experiments of stretching of red blood cells with optical tweezers (Li et al., 2005).

2.2.1 Microscopic realization

The mesoscopic description assumes that there exist domains of small size compared to the length scale of the system, considered homogeneous, so that the variables at the mesoscale effectively capture the relevant properties of the microscale. With the objective of explaining this fundamental assumption, and validate the mesoscopic membrane description of Helfrich, we present here the simple model proposed by Petrov and Bivas (1984) which, in spite of being highly non realistic, is useful to naively illustrate the connection between both scales. The model assumes a rough description of the interactions between lipids, and from this simple basis the Helfrich free energy (2.16) for a bilayer is derived.

The model assumes a harmonic approximation of the free energy per molecule,

$$f_m = \frac{1}{2}k_H\left(\frac{A_H}{A_H^0}-1\right)^2 + \frac{1}{2}k_T\left(\frac{A_T}{A_T^0}-1\right)^2 \tag{2.18}$$

where $A_{H/T}$ are the areas per molecule of the head/tail, respectively, and $k_{H/T}$ are the harmonic constants related to the respective interactions between each group. A^0 are the *preferent* areas, related with the equilibrium intermolecular distance

in the relaxed monolayer. Still, the effective constants $k_{H/T}$ should be related with the specific bonds between molecules, but this is difficult to address at this simple level of description. If one defines the neutral surface as the point of the lipid where the forces are balanced, and we call A the lipid section at this point, the head and tail areas can be expanded in terms of the curvature at this neutral point as

$$A_{H/T} = A[1 + \delta_{H/T} C + \delta_{H/T}^2 G]. \tag{2.19}$$

where $\delta_{H/T}$ are the respective distances to the neutral surface. In the case of a flat interface ($C = G = 0$), when the areas per lipid at the head, tail and neutral points are the same, the energy density reduces to

$$f_m = \frac{1}{2} K_m \left(\frac{A}{A^0} - 1 \right)^2 \tag{2.20}$$

where $K_m = k_H/A_H^0 + k_T/A_T^0$ is the stretching modulus per molecule. On the contrary, for a positively curved membrane, the head and tail areas are expanded and contracted, respectively, with respect to the neutral one. Thus, introducing (2.18) in (2.19), the density energy of the deformation leads to the Helfrich energy (2.16), with the elastic parameters

$$\begin{aligned} \kappa^m &= \delta^2 K_m \frac{\psi_H \psi_T}{(\psi_H + \psi_T)^2} = \delta_H \delta_T K_m, \\ \kappa_G^m &= (A_H^0 - A_T^0)(\psi_H - \psi_T) \frac{\psi_H \psi_T}{(\psi_H + \psi_T)^2}, \\ c_0^m &= \frac{\kappa_G^m}{\kappa} \frac{1}{\delta_H - \delta_T}. \end{aligned} \tag{2.21}$$

where $\psi_{H/T} = k_{H/T}/A_{H/T}^0$, and the superscript m indicates that it refers to one of the monolayers. Some properties of the elastic parameters can be infered from these expressions. First, the bending parameter is always positive, as opposed to the Gaussian modulus which depends on the specific properties of the lipid. Analogously, the sign of the spontaneous curvature depends on the relative position of the neutral surface with respect to the head and chain. Thus far we have just considered a monoloyer. For a bilayer, the elastic parameters depend on whether the monolayers are connected or not. For simplicity, we suppose that there is no interaction and then

$$\kappa = 2\kappa^m, \qquad \kappa_G = 2(\kappa_G^m - 2\kappa^m c_0^m \Delta_N), \qquad c_0 = 0. \tag{2.22}$$

where Δ_N is the distance between neutral surfaces. In spite of the enormous

simplifications considered in this model, it shows how the Helfrich energy can be derived from a simple harmonic description of the lipid-lipid interactions.

2.2.2 Equilibrium equation and membrane fluctuations

The membrane equilibrium equation was first derived by Ou-Yang and Helfrich (1987) for a spherical shape. They considered the free energy (2.16) and use a variational argument to solve the equation $\delta\mathcal{F}/\delta A = 0$. The resulting equation reads

$$\Delta p = \gamma C - \frac{1}{2}\kappa(C - c_0)[C(C - c_0) - 2C^2 + 4G] - \kappa\Delta_s C. \tag{2.23}$$

This expression can be understood as a generalization of the Young-Laplace equation for contributions of higher orders in the curvature $\mathcal{O}(C^2)$. This general equation has a major limitation, as it is only valid in the limit of low curvatures. The general equations have also been derived (Capovilla and Guven, 2002; Kozlov, 2006).

Out-of-equilibrium, expression (2.23) relates with the force exerted by the membrane, $f_{mem} = \delta\mathcal{F}/\delta A$, which corresponds to the right hand side of equation (2.23). This expression can be used to obtain the undulation modes of the membrane. We show here a simplified derivation, though more strict and complicate procedures have been developed (Kuriabova and Levine, 2008). Suppose an almost flat membrane whose height with respect to the equilibrium plane is given by $y = h(x,t)$. We shall assume that the surrounding fluid is important in the membrane dynamics, so that the hydrodynamic effects must be considered. The Langevin equation describing the membrane dynamics is

$$\frac{\partial h(x,t)}{\partial t} = -\int dx \Lambda(|x - x'|) f_{mem} + \xi(x,t), \tag{2.24}$$

where ξ is a white noise and Λ is the Oseen tensor accounting for the hydrodynamics,

$$\Lambda(x) = \frac{1}{8\pi\eta x}. \tag{2.25}$$

Assuming that the membrane profile can be decomposed in a Fourier series, $h = \sum_k h_{k,0} e^{iqx}$, the membrane force in Fourier space to linear order $\mathcal{O}(h_0^2)$ is given by $f_{mem} = \Delta p + \gamma q^2 + \kappa q^4$. Therefore, equation (2.24) reads

$$\frac{\partial h_q(t)}{\partial t} = -\omega(q) h_q(t) + \xi_q(t) \tag{2.26}$$

where the relaxation frequency is given by

$$\omega(q) = \frac{\Delta p q^{-1} + \gamma q + \kappa q^3}{4\eta}. \tag{2.27}$$

The terms associated to q^1 and q^3 are the surface tension and bending, respectively, whereas q^{-1} is a chemical term related with the volume conservation. Using the equipartition theorem, the equilibrium spectrum of undulations is obtained,

$$< h_q h_{-q} >= \frac{k_B T}{\Delta p + \gamma q^2 + \kappa q^4} a. \tag{2.28}$$

where a is the area of the membrane patch considered. This expression provides an important pathway to measure membrane elastic parameters by analyzing the fluctuation spectrum of the membrane in locally flat regions of the cell, such as the main disk of the RBC (Brochard and Lennon, 1975; Park et al., 2010b).

2.2.3 Shapes of vesicles

Once the free energy of the membrane has been determined, the first step is to obtain the minimal shapes for this energy. This minimization is, however, generally complex and in many cases requires of advanced numerical methods. Still, if one limits the search to axisymmetric shapes, a few cases are analytically affordable or, at most, require of simple numerical integrations. We overview here some of the first results obtained based on the Helfrich theory, as they provide intuition and key insights for the understanding of more complex morphologies in the subsequent studies.

Unduloids

It is obvious that for a bilayer of spontaneous curvature c_0, minimal shapes include a sphere of radius $1/c_0$ or a cylinder of radius $2/c_0$, as both have zero curvature energy. Interestingly, there is a family of axisymmetric surfaces with curvature $C = 1/c_0$, called unduloids. This family comprises from a cylinder to an undulated tube and eventually a necklace of spheres, as shown in Figure 2.2. These shapes naively remind phenomena of tubulation and pearling (Tsafrir et al., 2001, 2003) that are observed when a spontaneous curvature is artificially induced in vesicle membranes. Likewise, the formation of pearls connected by fine necks can be associated with the budding and vesiculation phenomena that is known to occur during the formation of spherocytes.

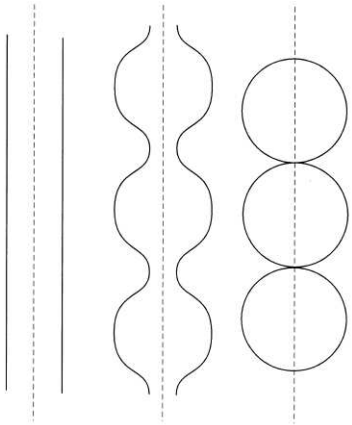

Figure 2.2: Different unduloids: cylinder, undulated tube and necklace of sphere. These family of shapes, of strictly zero curvature energy, reminds the shapes observed in vesicles when subjected to prompt changes in their membrane asymmetry, as observed when vesicles are exposed amphiphilic proteins that anchor to the bilayer and introduce and spontaneous curvature. Figure from Seifert and Lipowsky (1995).

Shape diagrams for axisymmetric vesicles

The determination of the minimal shapes for closed vesicles is more complicate, even considering axisymetric shapes. The procedure is as follows. From the complete free energy for the membrane (2.16), the Euler-Lagrange equation is obtained in the appropriate parametrization of the vesicle contour. Stationary of this equation is imposed, and (usually numerically) solving this relatively simple equation provides the equilibrium shape. For symmetric bilayers ($c_0 = 0$), three different type of shapes are found (Seifert et al., 1991), depending on the specific area and volume of the vesicle: stomatocytes, oblates and prolates. The relation between vesicle area A and volume V is captured by the reduced volume, as defined in Chapter 1. Stomatocytes are found for low $v_{red} < 0.592$. The vesicle accomodates its area bending and acquiring a cup-like shape. For $0.592 \leq v_{red} \leq 0.651$, oblates become minimal shapes. It is remarkable that the discocyte belongs to this subfamily of shapes. For $v_{red} > 0.591$, vesicles present prolate shapes.

If asymmetric bilayers are considered, a complex shape diagram in the parameter space (v_{red}, c_0) is obtained. However, the three family of shapes commented before are invariably present at low values of c_0. Negative spontaneous curvature favours the development of stomatocytes, and in general the transitions are swifted towards this shape. Interestingly, at high c_0 a new branch of shapes is found: pears and buds. Budding phenomena is therefore necessarily associated to high asymmetries of the membrane.

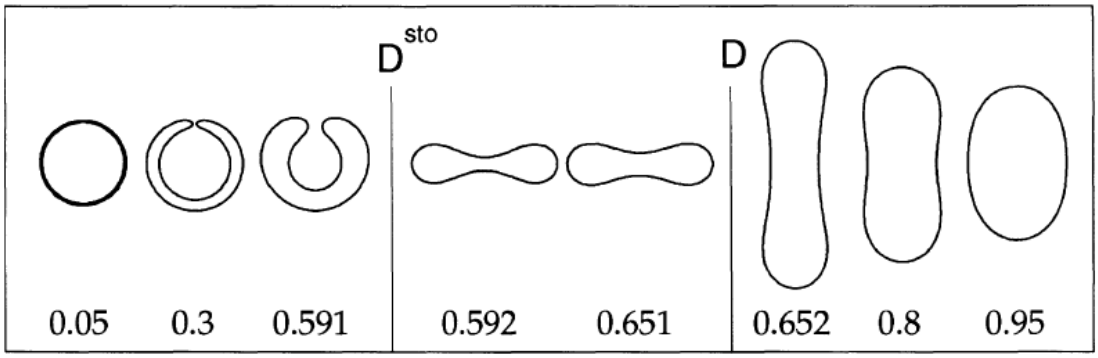

Figure 2.3: Axisymmetric vesicle shapes of lowest bending energy with $c_0 = 0$ as a function of the reduced volume ν. Stomatocytes, oblates and prolates are found for increasing ν. The transition between each subfamily of minimal shapes is discontinuous. Figure from Seifert et al. (1991).

2.3 Other membrane models

The Helfrich model has been extended to incorporate other structural properties of membranes. Specifically, the Helfrich theory assumes that the membrane can be considered as a two-dimensional layer, neglecting the internal architecture of the bilayer. The area-difference elasticity accounts for the coupling between leaflets. In addition, different descriptions have been proposed to model the elasticity of the spectrin cytoskeleton, which is not included in the Helfrich theory.

2.3.1 Area-difference elasticity

The Helfrich theory does not consider any internal structure of the bilayer, such as the coupling between leaflets when both try to accomodate their lipid densities to the local shape, gliding each other. This effect is incorporated in the so-called area-difference model, closely related to the bilayer-coupled model. Although the theoretical basis of these models was adressed by Sheetz and Singer (1974) and Evans (1974), it was formally proposed by different independent groups in 1991 (Seifert et al., 1991; Waugh et al., 1992) .

The area-difference model can be derived by introducing two densities $\phi^{\pm}$ for the two leaflets at their own neutral surface. In order to rationalize this description with the single-fold scheme, these densities are expressed as projected densities onto the neutral surface of the bilayer,

$$\phi^{\pm} = \phi^{\pm}_{proj}(1 \mp dC), \tag{2.29}$$

where we have neglected higher order contributions (C^2, G, etc). Assuming a

harmonic free energy for each monolayer, in the spirit of the microscopic model presented in Section 2.2.1,

$$f^{(m)} = (k^{(m)}/2)(\phi^{\pm}/\phi_0 - 1)^2 \approx (k^{(m)}/2)(\rho^{\pm} \mp dC)^2, \tag{2.30}$$

where $k^{(m)}$ is the compression modulus of the monolayer and $\rho^{\pm}(\phi^{\pm}_{proj}/\phi_0 - 1)$ is the deviation of the projected density from the equilibrium value for a relaxed membrane. The total membrane for the bilayer reads

$$f^{(b)} = (k^{(m)}/2)[(\rho^{+} - dC)^2 + (\rho^{-} + dC)^2]. \tag{2.31}$$

For simplicity, we have assumed a symmetric bilayer, $d^{+} = d^{-} = d$ and $k^{+} = k^{-} = k^{(m)}$. Introducing the average density $\bar{\rho} = (\rho^{+} + \rho^{-})/2$ and the density difference $\rho = (\rho^{+} - \rho^{-})/2$, the local free energy of the bilayer is rewritten as

$$f^{(b)} = k^{(m)}[\bar{\rho}^2 + (\rho - dC)^2]. \tag{2.32}$$

From this relation it can be seen that $\bar{\rho}$ does not couple to the local shape, and thus $\bar{\rho} = 0$ minimizes the total free energy of the membrane. ρ, however, is inhomogeneous as it adapts to the local surface. The minimization of the total free energy of the membrane leads to

$$\rho(s) = d[C(s) - M/A] + (N^{+} - N^{-})/(2A\phi_0), \tag{2.33}$$

where A is the total membrane area, M is the averaged total curvature, and we have made use of the relation

$$\int dA\rho = (N^{+} - N^{-})/\phi_0, \tag{2.34}$$

which fixes the total number of lipids and relates it with the surface membrane area. By introducing expression (2.33) into the free energy of the membrane (2.32), and integrating over the membrane surface,

$$F^{(b)} = \frac{k^{(m)}}{2A_0}(\Delta A - \Delta A_0)^2, \tag{2.35}$$

where $A_0 = A$ is introduced to avoid confusion with the area-difference ΔA, calculated from

$$\Delta A = 2d \int C dA. \tag{2.36}$$

ΔA and ΔA_0 represent the differences in area between the two leaflets, for the actual and preferent (relaxed) shapes, respectively. Adding this non-local bending contribution to the Helfrich free energy, we obtain the complete area-difference model (ADE),

$$F = \frac{\kappa}{2}\int (C - c_0)^2 dA + \frac{\kappa_{NL}\pi}{A_0 d^2}(\Delta A - \Delta A_0)^2, \tag{2.37}$$

where we have introduced the non-local bending rigidity, $\kappa_{NL}d^2/\pi$. This parameter can be related with the bending rigidity, $\kappa_{NL} = \alpha\kappa$. The theoretical prediction provides the value $\alpha = 3/\pi$, but this parameter is best left free (Seifert and Lipowsky, 1995). For large α, the non-local term is dominant and this approximation is usually known as bilayer-couple model. The interpretation of c_0 and ΔA_0 responds to the framework in which each model is derived. The area-difference specifically refers to the change in area of each leaflet, typically associated to a translocation of lipids from leaflet to the other, or a chemical change in the lipids that lead to a reduction of the relaxed area per lipid. The spontaneous curvature is however more general, and it can account for different imbalances such as insertion of proteins in the bilayer, among others. Both parameters are, however, undoubtedly connected and indeed it is easy to prove that any $c_0 \neq 0$ can be mapped on a renormalization of the effective area difference.

2.3.2 Cytoskeleton elasticity

The cytoskeleton is a triangulated mesh of spectrin rods. The elasticity of the cytoskeleton has been studied by many different techniques, but much insight is still required to completely understand its basic mechanics. The cytoskeleton presents a low resistance to bend, with a bending modulus at least two orders of magnitude lower than that of the bilayer (Mukhopadhyay et al., 2002). It does present, however, resistance to shear and compression in the membrane plane, and it is known to play a fundamental role in inhibiting budding and vesiculation processes.

Different models have been formulated to model the cytoskeleton elasticity. A simple way is to represent it as a spring mesh, relating the spring constant with the elastic modulii. In the same spirit, a more refined model was propposed by Li et al. (2005), based on previous studies (Discher et al., 1997; Lee et al., 1999). The membrane surface is organized in a triangle tessellation, with 6-vertices junctions that can be flipped, mimicking an adaptative connectivity. The cytoskeleton free energy is given by a worm-like chain model (Marko and Siggia, 1995), which provides the elastic force for each spectrin rod

$$f_{WLC}(L) = -\frac{k_B T}{p}\left(\frac{1}{4(1-x)^2} - \frac{1}{4} + x\right), \quad x \equiv \frac{L}{L_{max}}, \tag{2.38}$$

where p, the persistence length of the chain, and L_{max}, the maximum length of each chain, are parameters of the model related to the spectrin properties. The total free energy of the cytoskeleton is given by

$$F_{cyt} = -\sum_i \int_0^{L_i} d\xi\, f_{WLC}(\xi). \tag{2.39}$$

where i runs over all the spectrin links of the network. The results of this model fit well with experimental results of optical tweezers elasticity, among others. However, it requires of a fine tuning of the model parameters and a considerable computational cost.

A different approach is to recover the continuum mechanics description and consider the finite strain theory . It can be shown that the contributions of shear and stretching for a 2D fold are given by (Evans and Skalak, 1980)

$$F_{in-plane} = \int dS_0 \left(\frac{K}{2}(1-\lambda_1\lambda_2)^2 + \mu(\lambda_1-\lambda_2)/4\lambda_1^2\lambda_2^2\right). \tag{2.40}$$

where λ_i are the principal extension ratios, defined as $\lambda_i = \sqrt{2\epsilon_i + 1}$, where ϵ_i are the eigenvalues of the Green's strain tensor,

$$\epsilon_{\alpha\beta} = \frac{1}{2}\left(\frac{\partial x_\gamma}{\partial x^0_\alpha}\frac{\partial x_\gamma}{\partial x^0_\beta} - \delta_{\alpha\beta}\right). \tag{2.41}$$

In these expressions, x are the coordinates of the actual membrane surface, S, whereas x^0 are the coordinates of the reference surface S_0, in which the cytoskeleton is relaxed. The relaxed state of the cytoskeleton is one of the remaining fundamental questions about the cytoskeleton elasticity (Hoffman, 2001). Different experiments and theoretical predictions have pointed towards a relaxed cytoskeleton with an elliptic shape (Svodoba et al., 1992; Lim et al., 2002), a spherical shape (Fischer, 2004), or a discocyte shape (Yu et al., 1973; Stokke et al., 1986; Li et al., 2005), and to date there is no agreement about the subject.

One important aspect considering the cytoskeleton elasticity and relaxed shape is the presence of active processes affecting to the spectrin scaffold properties. Gov and Safran (2005) were the first to theoretically approach this problem, based on the experimental observation that after ATP-depletion, RBCs exhibit membrane undulations of lower amplitude than at physiological conditions (Zeman et al.,

1990). This surprising observation was explained postulating that the cytoskeleton is subjected to continuous phosphorylation of the spectrin-actin links, so that the bilayer undergoes local detachments of the cytoskeleton that allow larger thermal fluctuations. The active remodelling of the network represents a relaxation of the structural and elastic resistance of the cytoskeleton. Gov and Safran (2005) proposed a simple model to explain the abnormal membrane undulations observed in RBCs with normal ATP concentrations, which we briefly explain here. They define the occupation probability of an actin link, from standard thermodynamics

$$n_d = \frac{n_{ATP} e^{\epsilon}}{1 + n_{ATP} e^{\epsilon}}. \tag{2.42}$$

In this expression, n_{ATP} is the ATP concentration and $\epsilon = (\Delta E_{ATP} - \Delta E_{sa} - k_B S_f - \Delta E_{mec})/k_B T$. ΔE_{ATP} is the energy gain per ATP molecule, ΔE_{sa} is the cost of detaching a spectrin-actin link, S_f is the entropy of the spectrin filaments and $\Delta E_{mec} = \mu(R - R_0)$ is the mechanical energy released by the molecule dissociation, where μ is the shear modulus and R and R_0 are the typical and relaxed length of the spectrin filaments. Considering the regimes in which the bending modes are dominant, the fluctuation spectrum when active processes are present is given by,

$$< h^2 >_{ATP} \simeq \frac{\Delta E_{mec} \mu a}{\kappa^2} \frac{n_d}{1 + (\tau \omega_b)^{-1}}. \tag{2.43}$$

where $\omega_b = \kappa / 4\eta a^{3/2}$ is the static fluctuation frequency and τ is the characteristic time of filament diffusion that enable the actin-spectrin re-attachment. The model by Gov and Safran (2005) quantitatively explains the large ATP-driven membrane fluctuations, and highlight the importance of active processes in the cytoskeleton elasticity.

2.4 Elastic parameters values

The elastic properties of the RBC membrane are highly dependent on the specific bilayer lipid composition, ATP concentration, age of the cell, and temperature. They are also known to vary with the morphogolical state of the cell, and echinocytes or spherocytes are considerably more rigid than discocytes (Park et al., 2010b). Bearing in mind this huge variability, we provide below typical values for the elastic parameters as measured in experiments.

The bending rigidity has been measured by different experimental techniques, for instance flicker spectroscopy and phase contrast microscopy, analyzing the

membrane amplitude oscillations due to thermal fluctuations, or disturbing techniques such as micropipette aspiration and by optical tweezers (see Seifert and Lipowsky (1995) and references therein). Typical values fall between 10-50k_BT with slight deviations depending on the specific technique. The shear modulus of the bilayer is negligible due to its fluidic nature in the membrane plane, given that that any shear stress is instantaneously relaxed by the rapid lateral rearrangement of lipids. The area-compression modulus of flat bilayers has been measured for different lipid species, with typical values of 100-250 mJ/m^2 (Evans and Needham, 1987; Rawicz et al., 2000). Note that, for the given values $\kappa = 2.0 \cdot 10^{-19}$J, $K_A = 10^{-1}$J/m^2 and cell radius $R = 8 \cdot 10^{-6}$m, the energy scale of stretching is much larger than that of the bending $K_A R^2/\kappa = 3 \cdot 10^8$. This huge energetic penalty imposed to the expansion of area implies that any membrane deformation driven by bending is required to effectively maintain a constant area. For practical purposes, it is usual to remove the elastic contribution of the area-compression and strictly impose the constraint of constant area, for instance by introducing a Lagrange multiplier, as proposed by Canham and Helfrich and shown in (2.16). The molecular basis of this phenomenon is found in the strong hydrophobicity of the lipid tails. An expansion of the membrane area implies that the area per molecule increases from its relaxed state and the lipid tails are therefore exposed to the water molecules. To avoid this situation, the attractive interaction between molecules enforces the bilayer incompressibility. Finally, it is important to remark that whereas membranes are permeable to transfer of nutrients and other molecules, they do not allow water exchange. This imply that for closed membranes (*ie* cells, vesicles), the amount of enclosed water remains constant. Assuming incompressibility, this condition can be translated into a constant volume, and accordingly another Lagrange multiplier, accounting for this volume conservation, is incorporated to the elastic membrane energy. Hence, the addition of the bilayer incompressibility and constant volume to the bending contributions of (2.14) allow to recover the complete Helfrich free energy (2.16).

The cell spectrin cytoskeleton, which plays a fundamental role in the cell response under certain deformations (such as morphological changes during crenation (Melzak et al., 2013) or squeezing during optical tweezers experiments (Li et al., 2005)) adds a shear contribution to the membrane elasticity. Although the value of the cytoskeleton shear modulus has been under debate until recently, typically measurements agree around μ=50mJ/m^2 (Dimitrakopoulos, 2012).

Part II

Membrane elasticity and RBC morphological transitions

Chapter 3

The disco-echinocyte transition

It has long been realized that healthy RBCs deform from the discocyte shape when exposed to the action of a number of agents, adopting different morphologies that can be divided into stomatocytes (cup-like shapes), and echinocytes (crenated shapes) (Besis, 1973). The first agents to be identified included ATP-depletion (Nakao et al., 1960), Ca^{2+} loading (White, 1974), and incubation in the presence of certain amphiphilics (Sheetz and Singer, 1974), but the list was extended in subsequent research. In particular, the pioneer studies by Sheetz and Singer (1974) demonstrated that the conversion into stomatocytes or echinocytes is actually dictated by the chemical nature of the amphipatic compound that triggers the shape deformation: *crenator* molecules are those that equilibrate in the outer leaflet, whereas cup formers are incorporated to the outer leaflet. The morphologies observed are virtually independent of the agent, suggesting that the alteration affects to a very specific and basic elements that determine membrane stability. These observations provide an important insight about the bilayer leaflets coupling that gave rise to the bilayer-couple and area-difference models that were presented in Chapter 2.

The complete morphological sequence is usually known as stomato - disco - echinocyte, and has attracted interest from biologists, and subsequently from physicists, for many years as it provides a wealth of information about the membrane molecular balance and functioning. Among many other reasons, echinocytes can be easily obtained in any laboratory, and actually RBCs spontaneously transform into echinocytes if not properly treated during blood storage. Additionally, the fact that the shape deformation responds to the action of several agents offers different ways to understand the problem.

In this Chapter, we present the main characteristics of the disco-echinocyte transition and some of the hypotheses and explanations that have been proposed to understand this phenomenon. We then concentrate on the experiments realized

by Kathryn A. Melzak and José Luis Toca-Herrera of shape transformations induced by AFM perturbation, which allow to induce shape transitions between the different morphologies in a controlled manner, offering new information about the deformations of the cells. A proper characterization of the morphological transition is required to understand the theoretical study of Chapter 4, in which we focus on the identification of the physical mechanisms controlling the transition.

3.1 Morphological sequence

The RBC morphologies observed can be divided into three main groups: stomatocytes, discocytes and echinocytes. The later group, however, is subdivided into different stages (Besis, 1973). The shapes are developed sequentially for increasing intensity of the agent acting, forming an ordered sequence. Typically, the morphologies are classified following a criteria that accounts for the degree of crenation and sphericity of the cell. The *morphological index* (MI) characterizes the deformation state of each cell, associating a number to each morphology. Given that the discocyte is the healthy morphology, its MI is asigned to 0 (ground state); crenated shapes are associated to positive numbers, of increasing value for larger number of spicules and bumps; and cup-shapes are associated to negative values of the MI. Hence, a high MI implies a very deformed cell from the discocyte, with a considerable degree of membrane damage due to the strong and prolonged action of the agent. These shapes are usually referred as advanced stages of the morphological transition, whereas slightly deformed shapes, closer to the healthy discocyte, are referred as lower stages. The transition can be understood in two different but relatively equivalent ways: *(i)* as a sequence of stable shapes for increasing intensity in the action of the agent; *(ii)* as the temporal evolution of the cell shape, if the time scale of shape deformation is much shorter than that of the agent effects. For instance, the absorption of lipid molecules occurs in a very fast time scale, and discocytes deform directly towards the corresponding morphological stage (specified by the amount of lipids incorporated to the membrane) in seconds or minutes. ATP-depletion, however, induces changes in the membrane composition in typically hours or days, and the cells sequentially develop the different morphologies, covering the entire transition during their temporal evolution. The MI of a cell is, by definition, an integer number (see below specific values for each morphology). In experiments, however, the MI is usually averaged over the entire RBC population of the blood sample, leading to a decimal value. Given that RBCs are relatively inhomogeneous both in their geometrical and elastic properties, the morphological response of some cells is faster than in others, and in a blood sample it is usual to simultaneously observe discocytes and different types of echinocytes.

The complete transition is thereby divided into (see examples of each morphology in Figure 3.1)

- Stomatocyte (MI=-1). The cell bends towards a cup-like shape, with a variable degree of curvature.

- Discocyte (MI=0). As extensively commented before, the discocyte is a disc with a biconcave profile, with a concave central region and a convex outer rim.

- Discoechinocyte I (MI=+1). The first stage of the echinocyte region is characterized by the presence of some undulations in the contour of the cell disk. These undulations are relatively smooth, and the cell maintains a flat shape though they are appreciably less biconcave than discocytic cells.

- Discoechinocyte II (MI=+2). This stage is characterized by the development of bumps normal to the disc plane, often known as out-of-plane bumps, maintaining the overall shape of the Discoechinocyte I. The number of bumps is typically low, $\sim$1-5.

- Echinocyte III (MI=+3). The cell adopts a more compact shape, close to an ellipsoid, with numerous bumps (~ 20) that are increasingly sharp.

- Echinocyte IV (MI=+4). The cell is nearly spherical and its surface presents a high density of small, spiky bumps. Budding and vesiculation lead to a loss of membrane area.

- Spherocyte. The cell equilibrates in a small spherical shape when it achieves the appropriate area to volume ratio.

Once the action of the external agent ceases, the membrane eventually reaches an internal balance and the cell stabilizes in one of the morphologies. The specific morphology depends on the final properties of the membrane. At these conditions, the final morphology is usually very stable and no shape changes are observed for days. The transition is, however, reversible for those agents whose action can be driven in the opposite direction; for instance, echinocytes formed by ATP-depletion return to discocytes if the physiological ATP concentration is restored. The reversibility is limited to typically MI$\leq$3, since more advanced stages are usually accompanied by severe membrane damage and surface loss.

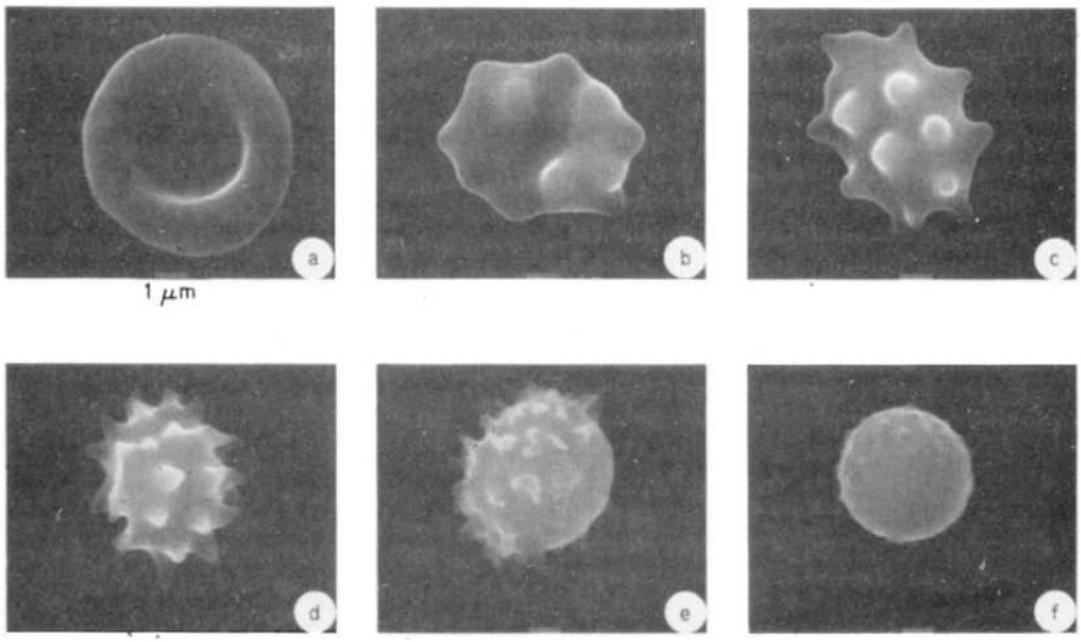

Figure 3.1: Scanning electron micrographs of different stages of the disco-echinocyte transition: (a) discocyte; (b) discoechinocyte I; (c) discoechinocyte II; (d) echinocyte III; (e) echinocyte IV; and (f) spherocyte. Figure reproduced from Ferrell et al. (1985).

3.2 Agents inducing echinocytosis

The biological processes associated to echinocytosis affect both the bilayer and the cytoskeleton, and the different experimental techniques can selectively alter one or the other, offering an interesting tool to understand the interplay and balance between both structures.

The first subset of studies group those agents that affect the bilayer structure. The first agent studied in detail was the effect of incubation with amphiphilic molecules. Lipid molecules exposed close to the RBC surface are incorporated to the cell membrane and equilibrate at their natural position (inner or outer leaflet). Direct observations of the process by fluorescent markers (Matayoshi, 1980) confirm the initial hypothesis of Sheetz and Singer (1974). The imbalance induced by the different amount of lipids between leaflets force the cell to expand (echinocytosis) or contract (stomatocytosis) the outer leaflet with respect to the inner one, depending on the preference of the lipid to occupy the outer or inner leaflet, respectively. A similar effect is observed when RBCs are exposed to high concentrations of Ca^{2+}, which activate the phospholipase C that is able to degradate some specific phospholipid species of the inner leaflet into simpler molecules of smaller effective area (Ferrell et al., 1985). Hence, although the amount of lipids remains constant, the mean area per molecule decreases in the inner leaflet and the total area of the outer leaflet expands with respect to the inner one. ATP-

depletion and the addition of vanadate are also known to trigger echinocytosis by means of the inhibition of the lipid translocases action. The lipids spontaneously flip towards a non-physiological membrane asymmetry, and this imbalance leads to crenation. This process is generally much slower and more reversible than others described here, but it is of great relevance in blood handling and storage, since echinocytosis occurs if blood is not suitably preserved. Finally, lipid balance can be also modified by mechanical disruption of the membrane, as demonstrated by micropipette aspiration (Artmann et al., 1997). Micropipette aspiration is a widely extended technique for measuring the RBC elastic modulii, but in these experiments aspiration pressures are typical low, and after aspiration the cell rapidly recovers the discocytic shape. If, however, one applies a high pressure, inducing a severe aspiration of typically $\sim 1.5\mu$m, the cell adopts a echinocytic shape after being released. Apparently, the extremely high curvatures that the membrane adopts inside the pipette force lipid translocation. The degree of crenation of the cell correlates with the duration of the aspiration experiment, supporting this hypothesis. Moreover, shape recovery was studied both for normal cells and for cells in presence of vanadate. The later shows much larger time scales for recovering the discocyte shape, as expected since in normal cells lipid translocases rapidly regulate the bilayer asymmetry, restoring the initial conditions.

The second group of techniques involves those agents that alter the stability of the cytoskeleton. For instance, if urea is added to crenated cells, spicules disappear and the cells deform towards the discocyte (Khairy et al., 2010). On the contrary, if urea is added to discocytic cells, they assume a elliptocytic shape (Khairy et al., 2010). These observations have been rationalized by the hypothesis that urea weakens the cytoskeleton scaffold as it is known to denature spectrin. However, this hypothesis should be confirmed by other techniques since urea is an aggresive agent that could potentially affect other molecules of the membrane. Wong (1999) proposed a mechanism for echinocytosis in which the lipids play a secondary role, and cell shape change is entirely controlled by the proteins of the cytoskeleton that attach to the bilayer. The cytoskeleton is attached to the bilayer by ankyrin molecules, which in turn are bound to Band 3, the protein that mediates influx and efflux of anions and cations. Depending on the ion concentration, Band 3 assumes an inward or outward position in the membrane, and thus it modulates the cytoskeleton tension, inducing relaxation or contraction of the network. Thereby, alterations in the pH or addition of Ca^{2+} affect to the normal anion equilibrium, thus modifying the cytoskeleton state and leading to echinocytosis. Likewise, amphiphilic drugs and detergents inhibit the Band 3 anion transport, inducing a similar response of the cell. This hypothesis, however, fails to explain other phenomena such as the mechanical induction of echinocytosis.

The experiments explained so far focused on the formation of echinocytes by

manipulation of discocytes, but the reverse process has also been investigated in a few studies. Additional experiments have reversed echinocytosis by affecting the bilayer balance, though their interpretation in terms of the bilayer-couple model is less direct. For instance, it has been shown that hemolyzed echinocytes produce discocytic ghosts (Lange and Slayton, 1982), and that electroporation is able to avoid shape changes triggered by one of the different crenator agents (Schwarz et al., 1999). The interpretation of these effects is based on the perforation of the membrane and formation of pores, which allow an easier flip of lipids between lipids.

Although many different agents capable of inducing echinocytosis have been identified, allowing the description of several new mechanisms of shape control, our knowledge on quantitative aspects of the transition is very limited. Experimentally, only Ferrell et al. (1985) were able to provide accurate measurements of the area expansion required to induce shape transformations. Theoretical studies based on physical membrane models (Mukhopadhyay et al., 2002; Khairy and Howard, 2011) have described the basic physics behind these phenomena, recovering a number of shapes with nice agreement with those observed in experiments, but a quantitative characterization of the transition is still lacked.

3.3 AFM-induced RBC shape change

Atomic force microscope (AFM) has been used in different ways to characterize mechanical properties of cells and membranes (Alcaraz et al., 2003; Kuznetsova et al., 2007). Although many of the techniques are conceived for determining the properties of the cell (or material, depending on the context), AFM has numerous biomedical applications as an active tool to manipulate or disrupt very specific regions of the cells, *eg* in plasmid delivery to viable cells, which then express the encoded proteins, through a pore formed by the AFM tip (Lamontagne et al., 2008). Other examples include the extraction of membrane lipids and proteins (Ikai and Afrin, 2003), and localized disruptions of the cytoskeleton (Lamontagne et al., 2008). Therefore, AFM offers a pathway for RBC shape manipulation by mechanical alteration of the membrane properties, and the experiments by Kathryn A. Melzak and José-Luis Toca-Herrera exploit this technique to explore RBC membrane response to an external mechanical disruption. The study is based on the observation that echinocytes pushed by the AFM tip deform into other morphologies, implying that conformational changes in the membrane structure are involved. The link between the disruption of the AFM and the membrane balance is not direct. In order to clarify the principles driving these shape transformations which could help us to understand the effect of the AFM on the membrane

structure, we perform a theoretical study (presented in Chapter 4), providing a quantitative explanation and description of the these transitions. The theoretical results allow us to interpret and understand the experiments described below.

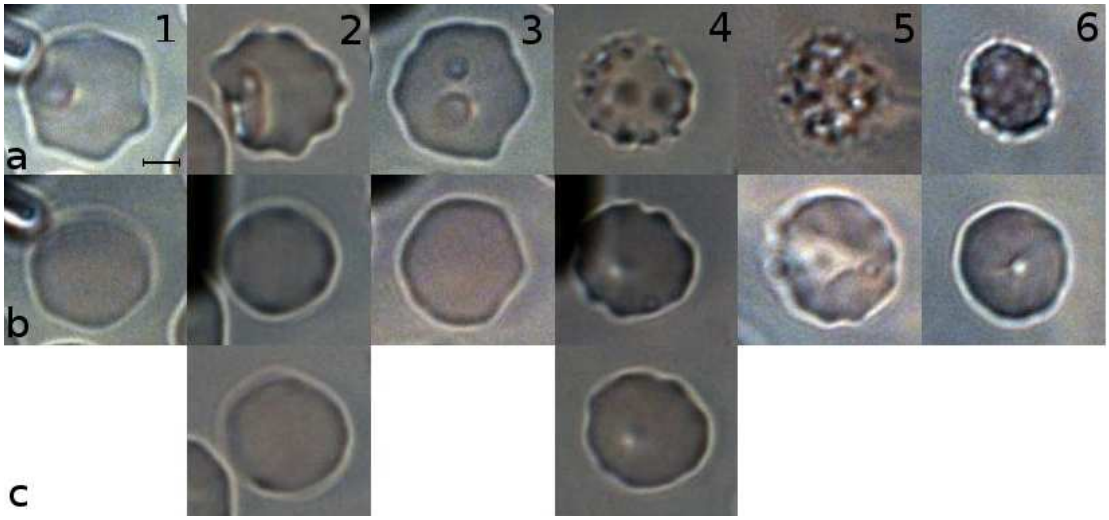

Figure 3.2: Shape changes for different initial RBC morphologies after puncturing with the AFM tip. Cells are shown (a) before the interaction with the tip, (c) after the measurements, and (c) after a period of 2.1, 2.5 and 2 hours after the measurement, for the cells 2, 4, and 5 respectively, in order to demonstrate the stability of the obtained shape. For cells 1-3 the puncture produced the disappereance of the out-of-plane bumps placed in the central region, characterizing a transition from the discoechinocyte II to the discoechinocyte I (1,3), or to the discocyte (2).

3.3.1 Experimental results

The study focuses on the morphological response of crenated RBCs distorted by the tip of an AFM. The series of experiments described here presents two main novelties with respect to the methods explained in the previous section: *(i)* only a mechanical disruption is induced, so that chemical processes such as anion fluxes are not involved; and *(ii)* experiments focus on the recovery of discocytes from damaged cells, instead of inducing echinocytosis.

The details of the experimental setup are not described here, but we outline briefly the main features of the experiments (for further information see Melzak et al. (2012)). RBCs from a single individual were washed and preserved in buffer. RBCs are known to undergo echinocytosis during storage due to partial depletion of ATP. After one day, most cells were seen to transform into echinocytes, and vanadate was added at a concentration of 200μM to ensure that lipid translocators were inhibited. Discoechinocytes II (thus, disregarding echinocytes IV and spherocytes which had potentially undergone vesiculation) were selected visually,

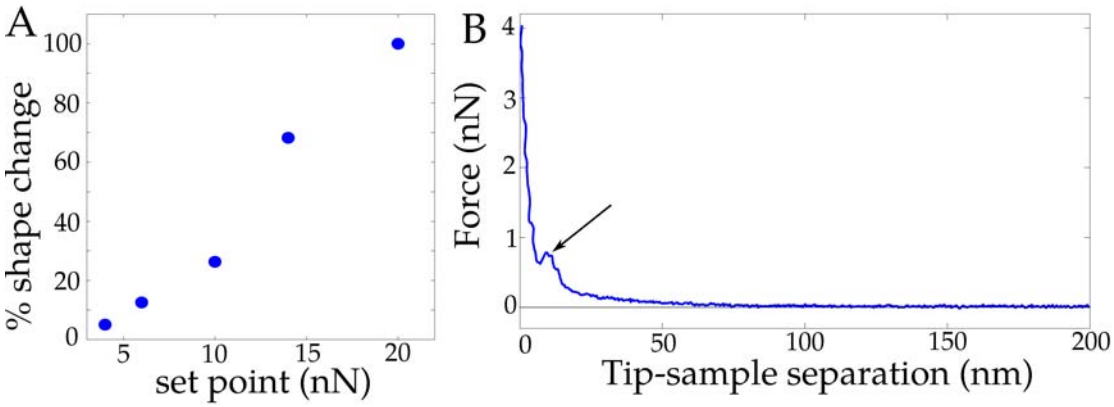

Figure 3.3: (A) Percentage of shape change after the AFM measurements, as a function of the maximum force exerted by the cantilever. The percentage of shape change increases with the force up to nearly 100% for the maximum load 20nN. This curve is expected to depend on the particular properties of the AFM tip. (B) Force-distance curve of the AFM. The discontinuity marked with an arrow coincides with the typical membrane width, suggesting that the membrane was punctured at that point.

focusing on cells with flat main body but with 1-5 spicules in the central region of the cell. The loading rate at which the tip approaches the membrane was maintained constant at 1 μm/s, before maintaining a constant force for 10 s. AFM measurements of the force exerted by the membrane during the interaction with the AFM cantilever were performed. Force-distance curves were recorded at maximum loads of 2 to 20 nN. After the measurement, a considerable proportion of cells were observed to transform into discocytes or lower stages of the transition than the initial one. Shape response was systematically recorded for 390 cells.

Echinocytes with a range of different initial shapes were shown to recover less advanced shapes of the transition, as shown in Figure 3.2. In the case of echinocytes IV it is difficult to identify the final morphology, although they clearly transform into a smoother shape. Dischoechinocytes II and I, however, clearly recover a previous stage, either discoechinocyte I or discocytes. The shape obtained after the interaction with the AFM tip was largely stable, and no perceptible shape changes were observed after 2 hours. The proportion of cells that changed shape increased with the applied force, as shown in Figure 3.3 A, in a set of experiments with the same AFM tip. The results show that at weak loads $\sim$ 5nN, the percentage of cells exhibiting shape changes remains low, but it increases linearly reaching $\sim$ 100% for a 20nN load. This curve is expected to depend on the AFM tip geometry and size, but it reflects the general trend regardless of these factors.

Many of the force-distance curves showed a discontinuity of 5nm lenght, as shown in Figure 3.3 B. This length scale corresponds to the typical membrane width, suggesting that the AFM tip was puncturing the membrane at this point. There is no apparent correlation between punctures and shape change, since mem-

brane puncture was sometimes not accompanied by shape change, whereas some cells deformed even if the curve-distance curve did not indicate any puncture. However, it is remarkable that this discontinuity cannot be recorded during the 10 s period that the force was held constant, so that the percentage of punctures recorded from the force-distance curves does not necessarily correspond to the total of punctures performed, and likely capture just a low proportion of the total punctures. During the constant force loading, direct observation showed that the cell maintained its echinocytic shape, suggesting that the force was not strong enough to disrupt the cytoskeleton.

Other rare events deserve mention. When the AFM tip was dried in air after a series of experiments, subsequent experiments showed a low percentage of shape changes. If, however, the tip was cleaned, it recover its ability to induce shape changes. Finally, ghosts were rarely observed after the AFM measurement and they were likely produced due to the formation of large pores.

3.3.2 Interpretations and discussion

The experiments described in the previous Section evidence that mechanical disruption of the membrane drives shape changes in RBCs, in this case from crenated to discocytic shapes. However, there is no direct observation of which kind of disruption that the AFM tip induces. Possible mechanisms that explain this phenomenon include distortion of the cytoskeleton, the bilayer, or both.

Given that chemical conditions are held constant (*ie* there is no anion increase and ATP is depleted in the entire series of experiments), the only explanation concerning the cytoskeleton is direct mechanical disruption of the network. In this hypothesis, weakness of the cytoskeleton would lead to a solely lipid membrane, whose minimal shape corresponds to the discocyte, explaining the observed echinocyte - discocyte transition. This picture requires, however, that the formation of echinocytes after ATP-depletion is driven by conformational changes in the cytoskeleton, a process that has not been described and seems unlikely. Large disruptions in the cytoskeleton are expected to produce cell deformation into elliptocytes or pear shapes, as occurs in lipid vesicles under high membrane asymmetries (Seifert et al., 1991). Very local perturbations of the network should be accompanied by budding or the formation of very thin necks at the bump base. In addition, many echinocytes were seen to be stable after the AFM tip disruption if puncture did not occur, suggesting that the force exerted by the tip was not sufficient to disrupt the network. This phenomenology indicates that the cytoskeleton remained largely unperturbed during the experiments.

The most plausible explanation is the alteration of the bilayer microstructure when the AFM tip punctures the membrane. Within this scenario, echinocytes are

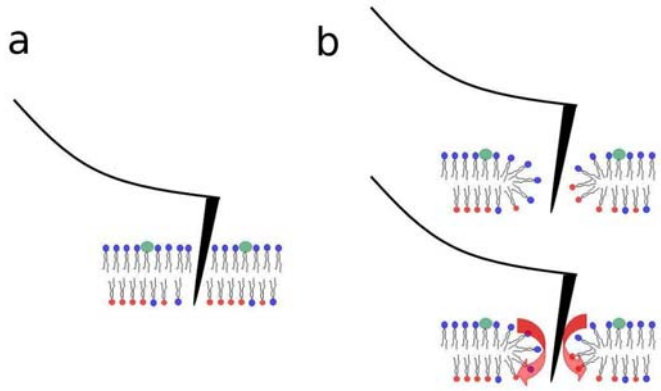

Figure 3.4: Sketch of the mechanism proposed for shape change when the AFM tip interacts with the echinocyte membrane. The temporal breaking of the hydrophobicity barrier by the formation of a pore allows flip flop of lipids, and the natural balance between lipid densities of the leaflets can be restored.

formed after ATP-depletion by an increase in area of the outer leaflet, which can be due to either an imbalance in the lipid densities between leaflets, due to inhibition of lipid translocases, or to degradation of some lipid species. ATP depletion also avoids remodelling of the cytoskeleton. The AFM disruption would affect this imbalance between the monolayer areas, allowing the recovery of the initial state. We propose that the puncturing of the membrane forms a pore, which is open during the maximum load of the AFM (pores at normal conditions are rapidly self-healing). The pore induces a temporary breaking of the hydrophobic barrier and hence it permits flip flop of lipids between leaflets during roughly 10 s, allowing a relaxation of the lipid density imbalance and recovery of the healthy discocyte shape, as shown in Figure 3.4. The hypothesis is consistent with the experimental observation of membrane puncturing and the fact that cells return to previous stages of the transition; as commented before, disruptions of the cytoskeleton are associated to a different class of shapes. Other possible explanations, such as mechanically induced degradation of ceramids that would balance the membrane asymmetry (López-Montero et al., 2005) are unlikely as the time scale of this process (minutes) is much larger than the prompt shape changes observed in the experiments.

Chapter 4

Membrane elasticity and RBC morphology

The altered shapes of the disco-echinocyte transition, unless until budding occurs, can be explained from conformational changes in the microscopic structure of the cell membrane. This has attracted the interest of physicists, as the prediction of crenated shapes serves to test physical membrane models. Many of the key insights achieved recently about membrane elasticity relate with the interpretation of echinocytes. However, the shape at which the cytoskeleton is relaxed remains under debate. As commented in different sections of this Thesis, recent approaches to the microstructure of the cell membrane have shown strong evidence of ATP-dependent active remodelling of the network, both theoretically (Gov, 2007; Li et al., 2007) and experimentally (Pinder et al., 1977; Park et al., 2010b). Accordingly, as postulated by Stokke et al. (1986) and Li et al. (2005), the cytoskeleton could be able to relax its stress energy over long timescales by remodelling of the actin vertices of the network, but acting as an elastic mesh if subjected to prompt perturbations. With this assumption, on healthy cells the resting shape of the network would be identified as the discocyte. Conversely, macroscopic models focusing on the cell morphologies have assumed a static scenario, with spherical or ellipsoidal shapes fixed as resting configurations of the cytoskeleton, and indeed they succesfully predicted some of the morphologies observed in the discoechinocyte transition (Mukhopadhyay et al., 2002; Peng et al., 2010; Khairy and Howard, 2011). Nevertheless, a global picture, encompassing all the experimental evidence, is still lacked.

In this Chapter, we perform a theoretical study of the membrane elasticity during the disco-echinocyte transition, paying attention to the minimal shapes observed and characterizing the transition in terms of the energetic contributions of the membrane components. The study has two main objectives. First, to

provide a quantitative description of the morphological sequence, facilitating the understanding of the elastic and structural role of each membrane component. Afterwards, the identification of the physics behind the shape transitions will allow to interpret the AFM experiments presented in Chapter 3 in terms of membrane internal balance between the cytoskeleton and the bilayer.

We focus on the first three stages of the disco-echinocyte transition, the discocyte, the discoechinocyte I and the discoechinocyte II. The characteristics of the spicules and the elastic properties of the crenated shapes have been studied in the later stages of the transition (Ferrell et al., 1985; Lim et al., 2002), within the regime of the spheroechinocyte, but little is known about its first stages. We will study the shape transformations driven by the increase in the preferred asymmetry and how it affects to the energy landscapes.

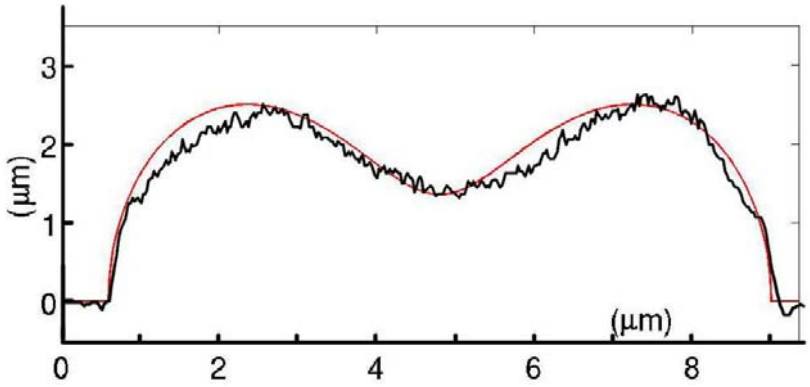

Figure 4.1: Comparison between the minimal shape obtained in the Cassini ovals parametrization, at zero asymmetry $c_0 = \Delta A_0 = 0$, and a RBC profile experimentally estimated from a picture takken by high-resolution camera C2, and assuming Beer's law. Adapted from Lewalle and Parker (2011).

4.1 The model

4.1.1 Membrane elastic energy

We consider the area-difference elasticity (ADE) model for describing the bilayer and the finite strain theory description for modeling the cytoskeleton, both presented in Chapter 2, but outlined here again for the sake of clarity. Therefore, the RBC membrane elastic energy, E_{mem}, arises from the interplay between the lipid bilayer, E_{bil}, and the spectrin cytoskeleton, E_{cyt},

$$E_{mem} = E_{bil} + E_{cyt}. \tag{4.1}$$

where the ADE model includes the Helfrich bending energy, and a non-local term that penalizes any deviation from a preferred area difference between the two leaflets ΔA_0,

$$E_{bil} = \frac{\kappa}{2}\int_S (C - c_0)^2 dS + \frac{\kappa_{NL}\pi}{A_{RBC}d^2}\left(\Delta A - \Delta A_0\right)^2, \tag{4.2}$$

The integration of expression (4.2) is performed over the current surface of the cell S. Both contributions to the membrane asymmetry are grouped in a unique dimensionless parameter,

$$\Delta a_0 = \Delta A_0/A_{RBC} + \kappa_{NL} d c_0/\kappa. \tag{4.3}$$

The cytoskeleton elastic contribution is represented by two terms corresponding to shear and stretching:

$$E_{cyt} = \int_{S_0}\left[\frac{K}{2}(\lambda_1\lambda_2 - 1)^2 + \mu\frac{(\lambda_1 - \lambda_2)^2}{2\lambda_1\lambda_2}\right] dS_0, \tag{4.4}$$

The integration is performed over S_0, the resting shape of the cytoskeleton at which its stress energy vanishes. We assume a fluid cytoskeleton with an initially relaxed network for a discocyte shape (the minimal shape of the membrane free energy (4.2)); the discocyte is therefore a ground state of the morphological transition, in the sense that it does not present a constant storage of membrane stress energy. When the asymmetry is increased, the timescales of shape change are shorter than those of network remodelling, and hence the cytoskeleton displays memory, acting as an elastic layer. Since we will focus on the early stages of the transition, we have not included non-linear terms (Lim et al., 2002) as they are only relevant when the protrusions are very spiky, in the latest echinocyte regimes.

4.1.2 Shape description

We perform a parametrization of the cell surface based on the Cassini ovals curves for the cell profile, but specific treatment is required to describe the spicules and bumps developed by the cell during echinocytosis. We therefore introduce two specific parametrizations for the in-plane and out-of-plane bumps.

The modified Cassini ovals.

The minimization of the Helfrich free energy (corresponding to the first term in equation (4.2)) requires numerical methods, since to date no analytical solution

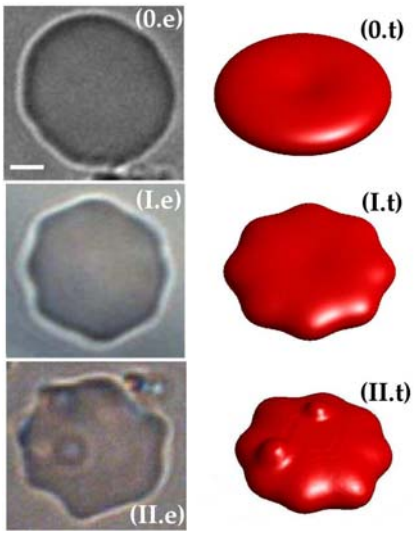

Figure 4.2: Different RBC morphologies: (0) discocyte, (I) discoechinocyte I, and (II) discoechinocyte II. (e) In vitro cells as observed by optical microscopy. The white bar corresponds to 2μm. Images were acquired with a transmission optical microscope (Axio Observer D1 Zeiss, Germany), using a 100x oil immersion objective lens (NA 1.3). (t) Theoretical shapes obtained by the model under constraints of total area 140 μm^2 and volume 90μm^2, at Δa_0= 0.001, 0.017 and 0.024 (defined in equation (4.3)), respectively. The increase in the asymmetry forces the discocyte to develop in plane undulations. After the undulations have acquired a considerable height, bumps appear in the central flat region of the disk. Even at this state, the cell remains as a nearly flat disk. The following stages, characterized by a spherical central body with numerous conical spikes, are known as echinocytes.

has been found. In an attempt to obtain an analytical description as close as possible to the exact solution, different expressions have been proposed (Evans and Skalak, 1980). Among them, the Cassini ovals represent an elegant parametrization of the cell profile, ranging from the critical lemniscate of Bernoulli to a circle, in a shape transformation controlled by just one parameter. Even if these curves do not represent an exact solution of the minimal shape of the Helfrich free energy, they offer a consistent basis for an analytical study of the properties of the curvature energy. They have been previously used as a parametrization of the cell profile, e.g. to study spherocytosis of the cell (Martino and Zampirollo, 1978), or for fitting data from neutron interferometry of the RBC resting shape (Hellmers et al., 2006). In our model, we make use of the Cassini oval family to parametrize the cell surface, in the spirit of Canham's original paper. A comparison between the minimal shape obtained from a Cassini oval parametrization at zero asymmetry and an experimental profile of a RBC is shown in Figure 4.1.

The geometrical properties of the Cassini ovals have been studied in detail (Angelov and Mladenov, 2000). This plane curve obeys the expression:

$$(x^2 + z^2 + a^2)^2 - 4a^2x^2 = c^4. \tag{4.5}$$

To obtain a discocyte shape (see Figure 4.2 0) the curve must be rotated around the polar axis, leading to an axisymmetric surface. Thus, expressed in cylindrical coordinates, the cell surface is characterized by

$$z(r) = \sqrt{\sqrt{4a^2r^2 + c^4} - a^2 - r^2}, \tag{4.6}$$

where the ratio $\epsilon \equiv a/c$, usually known as *biconcavity*, describes the shape of the profile. In the limit $\epsilon \to 0$ it reduces to a circle, but in the range $0.7 < \epsilon < 1$ the curve presents a concave region in the center, increasing the ratio between the maximum and minimum heights with ϵ. The radius of the disk is defined by $R = c\sqrt{1+\epsilon^2}$. In the case of the RBC, both volume and area are conserved, and then another parameter must be introduced (Canham, 1970), reading

$$z(r) = B\sqrt{\sqrt{4a^2r^2 + c^4} - a^2 - r^2}, \tag{4.7}$$

where B fixes the height of the profile and the parameter set (ϵ, R, B) entirely determines the shape and the size of the manifold subject to the constraints of constant area and volume (A_{RBC}, V_{RBC}).

In-plane bumps.

To study the in-plane undulations that appear in the discoechinocyte I (Figure 4.2 I), the radial contour is modified introducing an angular dependence,

$$R(\theta) = R_d(1 + \mathcal{Y}(\theta)), \tag{4.8}$$

where R_d represents the radius of the central disk. The function $\mathcal{Y}(\theta) = \sum_m a_m(1+\sin(m\theta))$, expressed in terms of sinusoidal functions, will determine the shape of the undulation. It is also necessary to allow for an angular dependence of the parameter $B = B(\theta)$, to smooth the undulated surface in the central region. We found that over extensive ranges of Δa_0, there is a specific mode l which assumes the main contribution to the sequence, typically $(\sum_{m\neq l} a_m)/a_l < 0.1$. Thus, the undulation is basically specified by just one mode and the rest of modes define details of the shape. We use this fact to introduce a simplification of the model: each virtual configuration is generated with a fixed l, separating the different modes as different configurations. This method also allows for an interesting direct comparison between modes, as well as an easier identification of the competition between

modes in spite of the obvious loss of degree of freedoms. The undulation height can be identified as $2\delta R_d$, where we have defined $\delta \equiv a_l$ for the specific mode l.

Out-of-plane bumps.

The out-of-plane bumps that characterize the discoechinocyte II grow on the flat central region of the disc, presenting an apparent random distribution over the surface, as opposed to the in-plane bumps which present a more regular spacing (Besis, 1973) along the contour (see Figure 4.2 II). Following Waugh (1996) and Lim et al. (2002), we parametrize these bumps as modified gaussians modulated by a smooth truncation function. The algebraic expression for the cell height at the bump region takes the form:

$$z_{bump}(r) = z(r) + s(r_b)\left[he^{-((r_b-R_b)/c)^\alpha}\right], \tag{4.9}$$

where $z(r)$ is the height (4.7), R_b is the central position from where the bump grows (thus $R_b < R_d$), h is the bump height, α fixes the shape of the bump and c is related with the bump diameter at its base, $c(D_b)$. We introduce the function $s(r) = \exp(-A^2/(D_b - r_b)^2)$ to ensure that the bump contribution vanishes at $r_b = D_b$. Note that in this expression, r_b is the radial variable with respect to the center of the bump, $\vec{r} = \vec{R_b} + \vec{r_b}$. Thus, we explore the size (h, D_b, c), shape (α, A) and location in the cell (R_b) of the bump.

4.1.3 Minimal shapes of the model

The expansion of the outer area with respect to the inner one forces the cell to deform, leading to morphological changes as previously described. To reproduce this shape transition, we increase the preferred area-difference Δa_0, obtaining the shapes which minimize the membrane energy, (4.1), for each value of the asymmetry. Given that the preferred area-difference is time-dependent as it increases gradually with the action of the damaging agent, the sequence of minimal shapes obtained mimics the temporal evolution of the cell. The rate of change of Δa_0 is, however, not properly controlled and it is defined by the timescale in which the agent impairs the membrane structure, typically minutes (López-Montero et al., 2005) to hours (Ferrell et al., 1985), but we will not enter into a dynamic characterization of the transition.

Elastic parameters

We choose typical values for the elastic modulii $\bar{\kappa}_{NL} = \kappa_{NL}/\kappa = 1/\pi$, $\bar{K} = KA_{RBC}/\kappa = 3.3 \cdot 10^3$, and $\bar{\mu} = 2\bar{K}$. This corresponds to $K = 2.0 \cdot 10^{-6}$ J/m^2, a

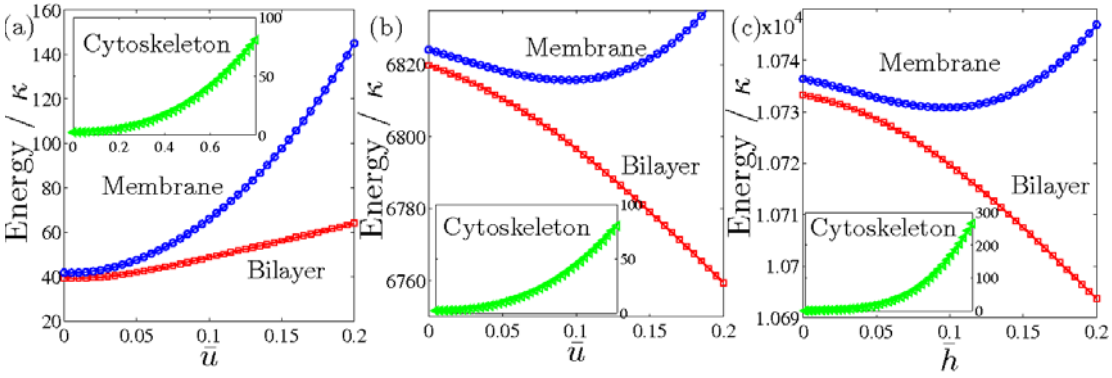

Figure 4.3: Energy for a sequence of RBC shapes with increasing degree of crenation, corresponding to the shapes shown in Fig. 1. The competition between the bilayer and the cytoskeleton, which opposes resistance to the undulation growth, defines the position and depth of the energetic well. The heights of the protrusions are rewritten in a dimensionless form $\bar{u} = 2\delta R_d/R_0$ and $\bar{h} = h/R_0$, where R_0 is the radius of the initial discocyte. In (a), the low asymmetry $\Delta a_0 = 0.0024$ implies a relaxed bilayer for a discocyte morphology. (b) When the asymmetry is increased, the presence of membrane protrusions involves an important bilayer relaxation that favours crenation; at $\Delta a_0 = 0.017$, a minimal shape is found at $\bar{u} = 0.095$, corresponding to an undulation height of 0.39 μm (in (a) and (b), $\bar{h}$ is found to be zero). (c) At higher $\Delta a_0 = 0.024$, the out-of-plane bumps appear and the energy minimum moves to $\bar{h} = 0.1$, corresponding to 0.41μm; in this plot the minimal $\bar{u}$ ranges from 0.096 to 0.13.

typical value found in experimental measurements (Dimitrakopoulos, 2012). The energetic scale of the system is therefore defined by the bending modulus κ, with a typical value of $\sim 50 k_B T$. The energy is expressed in a dimensionless form, $\bar{E} = E/\kappa$.

We fix the RBC area and volume at A_{RBC} =140 μm^2 and V_{RBC} =90μm^3 respectively, and they are maintained constant during the transition. This is imposed by exploring a wide range of values of $\{R_d, B\}$ for a specific set of the rest of parameters, and selecting those which fulfill the constraints (Canham, 1970).

Geometrical parameters are rewritten in units of the radius of the discocyte at physiological conditions, R_0. We define the height of the undulations with the new variable $\bar{u} = 2\delta R_d/R_0$, and analogously the dimensionless form of the bumps height reads $\bar{h} = h/R_0$.

Energy minimizations

Since the integrals of expressions (4.2) and (4.4) over the resulting surface is not generally analytical, we perform numerical integrations by means of the following procedure. We discretize the space, and at each point the local energy densities

of the bilayer and the cytoskeleton can be analytically calculated for the elastic parameters given previously (*ie* the problem reduces to compute the surface element, mean curvature, and extension ratio at each grid node; for further details see Appendix A). The integration is then straightforward, obtaining the desired total energy for a specific set of the geometrical parameters $(\epsilon, \delta, h, B, \alpha)$. We perform integrations over domains of 500x500 nodes, achieving a high precision in the energy calculation (*eg* errors in the case of a sphere, which can be calculated analytically, of order $\Delta E/E \approx 10^{-4}$).

The energy minimization is performed as follows. The parameter space is discretized in a grid of roughly 50 points for each parameter (with some differences between parameters). For each Δa_0, the energy is evaluated for all the configurations of the parameter set. To obtain the absolute energy minimum at the relevant asymmetry, the parameter grid is explored sequentially. The parameters are ordered, and the whole parameter space is explored by successive sweeps of the one-dimensional subspace corresponding to each parameter. For example, fixing all the parameters except the last one α, the minimization problem is reduced to the one-dimensional case. After sweeping the entire range for the rest of parameters, the new energy landscape involves only the parameters (ϵ, δ, h, B) and each new configuration is minimal for α. The absolute minimum for the complete parameter space is reached once the minimization process has been carried out for the whole sequence. The elastic energy has two contributions (bilayer and cytoskeleton), each one displaying a simple monotonic behavior over the whole parameter range. The global minimum strongly dominates the whole space. This has been tested by permutations in the order of the sequence, in order to check if the minimization procedure is trapped in a metastable state related to local minima. We find that, regardless of the order of the sequence, the minima obtained fall in a range with variations below 0.5%. These results point out that the minimization method is robust and the minima obtained can be safely identified as the absolute minima of the system. Hence, given a Δa_0, an energy minimum $E_{min}(\Delta a_0)$ is found for some specific values of the geometrical parameters. The morphology state of the cell can then be identified: the discocyte is obtained at biconcavities $\epsilon > 0.7$ and no protrusions $\{\delta = 0, h = 0\}$; the discoechinocyte I is characterized by the in plane undulations, but it still lacks out-of plane bumps $\{h = 0\}$; and finally, the discoechinocyte II, in which both bumps and undulations are simultaneously present $\{\delta \neq 0, h \neq 0\}$.

Parameter	Interpretation	Value
κ	Bending modulus	1.0
$\bar{\kappa}_{NL}$	Non-local bending modulus	$1/\pi$
$\bar{K}$	Shear modulus	$3.3\ 10^3$
$\bar{\mu}$	Stretching modulus	$2\bar{K}$
R_0	Discocyte radius	4.08μm
d	Bilayer width	$3 \cdot 10^{-3}\mu$m
R_d	Disk radius	A,V constraints (*)
B	Disk height	A,V constraints (*)
l	Number of undulations	2-15
δ	Undulation height	0.0-2.0 μm
h	Bump height	0.0-2.0 μm
α	Bump shape	1.0-8.0
D_b	Bump diameter	0.4-4.0 μm
R_b	Bump position	$0.0\text{-}0.8R_{RBC}$

Table 4.1: Parameters of the model an their numerical values. The elastic modulii are expressed relative to the bending modulus κ. The geometrical parameters are expressed in dimensions, for typical values for RBCs (μm) to facilitate an intuitive understanding. In the text, morphological parameters are expressed in units of the discocyte radius R_0. For the parameters that are varied, the table indicates the range explored in the different minimizations. Parameters marked with (*) are directly fixed by applying the constraints of constant RBC area and volume.

4.2 Results

4.2.1 Energy contributions

When the membrane asymmetry is increased, cell shape transformations can be understood from the interplay between its two main components, the bilayer and the cytoskeleton. The bilayer, with an increasing excess of area in the outer layer, forces the cell to deform and curves the membrane. The growth of spicules and protrusions represents a natural way to favour the expansion of the outer leaflet. In contrast, the cytoskeleton offers resistance to spiculated shapes, preserving the discocyte morphology of its resting shape. The competition between the expanding bilayer and the resistance of the cytoskeleton defines the morphological response of the cell to Δa_0, as shown in Figure 4.3. Let us consider the case (a) of the Figure in the context of the previous section. The energy is represented here as a function of $\bar{u}$, which depends on δ, and the membrane energy of each configuration has been obtained as a minimum of the subspace (ϵ, h, B, α). From the plot, the energy minimum is attained at $\bar{u} = 0$, representing the minimal shape at the given asymmetry that is identified as the shape observed in the experiments.

In Figure 4.3, the energy of both the bilayer and the cytoskeleton is plotted for a sequence of shapes with increasing degree of crenation (given by $\bar{u}$ and $\bar{h}$). The cytoskeleton (which does not depend on the value of Δa_0) is distorted when deformed from its reference state, and hence its elastic energy rapidly grows with the undulation height. At low asymmetries, Figure 4.3 (a), the bilayer is relaxed and the minimal shape corresponds to the discocyte. When the preferred area-difference is increased, Figure 4.3 (b), the bilayer is stressed by its intrinsic asymmetry, and therefore prefers undulations with large mean curvatures. An energy minimum of the total membrane arises as a compromise between an undulation high enough to considerably relax the bilayer, but implying a limited elastic penalization by the cytoskeleton. If we consider the dependence on $\bar{h}$, we see that the presence of out-of-plane bumps, Figure 4.3 (c), require of further increase in Δa_0, as the cytoskeleton distortion of these structures is considerable larger than in the previous case. This can be tested comparing insets in Figure 4.3 (a) and Figure 4.3 (b), where the energy barrier of the out-of-plane bump is several times larger than that of the undulations. The energy wells of these protrusions, of several hundreds of k_BT, ensure a large stability of the shapes, in agreement with RBCs that do not exhibit visible fluctuations when observed through an optical microscope.

4.2.2 Shape diagram

From the energy minimizations, for each preferred area-difference a unique minimal shape is found, allowing to build up the sequence of real shapes and identifying the stability range for each morphology. In Figure 4.4, the energy difference between the three configurations of interest is presented for each membrane component (bilayer, cytoskeleton and total membrane). In our formalism, the discocyte represents a subfamily of shapes of the discoechinocyte I. Similarly, both stages are particular cases of the discoechinocyte II. Thus, within the range of stability of the discocyte, minimal discoechinocytes I and II degenerate into the discocyte. Dashed lines represent the minimal energies for the bilayer contribution (4.2), whilst bold lines represent the evolution of the shapes minimizing the total energy, (4.1). The transition to positive energy differences defines the shape change from one configuration into the other. To attain an undulated shape, the bilayer needs to store enough energy to beat the cytoskeleton resistance to gain curvature. In the case of the first in-plane undulations, the bilayer is favoured by crenation at low asymmetries $\Delta a_0 \approx 0.003$. However, the negative effect in the cytoskeleton, presented in Figure 4.4 (a), delays the developement of undulations until a considerable increase in the preferred area-difference, $\Delta a_0 = 0.0063$. Discoechinocytes I are then energetically favourable for the total membrane in detritment of dis-

cocytes, which are no longer the stable shapes. At this asymmetry, the energy difference for the bilayer is $\sim 12\kappa \sim 500 k_B T$, consistent with the elastic energy of deformation of the cytoskeleton. A similar process is observed in the transition between discoechinocytes, from I to II, in Figure 4.4 (b). In this case, the growth of the out-of-plane bumps characteristic of the later is again triggered by the bilayer at low asymmetries. The action of the cytoskeleton shifts the shape transition up to $\Delta a_0 \approx 0.0175$. Bumps therefore require of larger asymmetries to grow up than in-plane undulations, in agreement with the experimentally observed sequence.

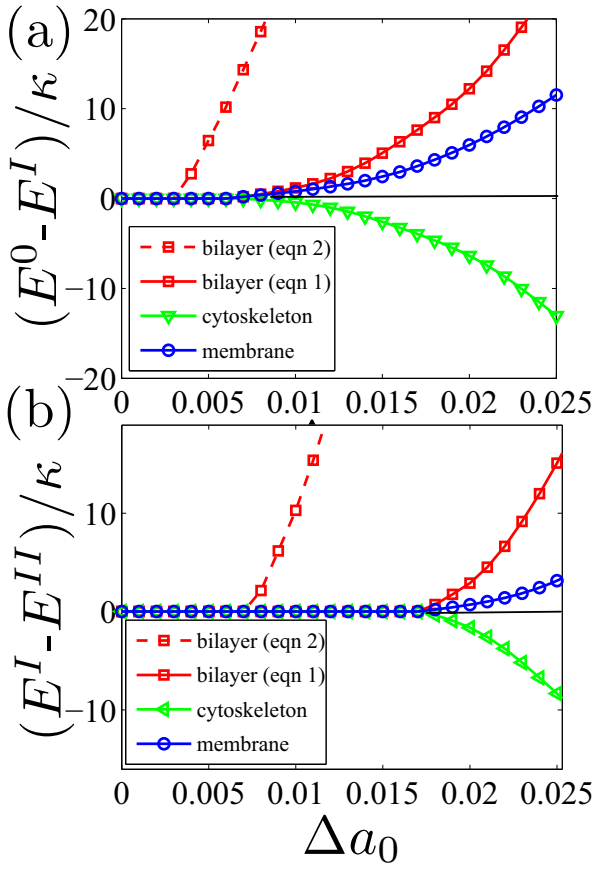

Figure 4.4: Energy differences between RBC stages as a function of Δa_0. Each configuration is labeled as discocyte (0), discoechinocyte I (I) and discoechinocyte II (II). (a) The discoechinocyte is favourable with respect to the discocyte at 0.0063, though the bilayer would prefer to undulate at lower asymmetries. (b) The energy barrier of the cytoskeleton resistance to the growth of bumps of the discoechinocyte II is considerably larger than the discoechinocyte I. The transition occurs at 0.0175.

In RBCs, out-of-plane bumps are rarely present before the discocyte has developed undulations. The order of appearence of the configurations is very strict, as a consequence of the enormous differences in energy between configurations. From the minimal shapes for the bilayer, dashed lines in Figure 4.4, it can be inferred that out-of-plane bumps and in-plane undulations achieve a similar benefit

in terms of bilayer relaxation. However, the larger energy gap that the bumps induce due to a higher distortion of the cytoskeleton derives in a delayed appearence of these structures in the total membrane energy.

The discocyte is found to be the minimal shape of the curvature energy for a symmetric membrane, but the cell shape is highly sensitive to the variation of the asymmetry in the absence of a cytoskeleton. In this case, the discocyte destabilizes into a prolate ellipsoid already for $\Delta a_0 \sim 0.0001$ (Khairy and Howard, 2011). In lipid vesicles –in which the cytoskeleton is absent, thus only the bilayer contribution is considered –, systematic studies on the dependence of the vesicle shape with the asymmetry lead to a different sequence of shapes (Svetina et al., 2004): discocytes, elliptocytes, dumbbells and eventually pearling are found for increasing asymmetries, but crenated shapes are not recovered. Therefore, the cytoskeleton arises as an essential ingredient to understand the appearence of protrusions. Although we have not directly analyzed this transition, different indirect evidence also supports the importance of the cytoskeleton. The presence of the cytoskeleton implies a high energy storage, with energy barriers of typically $> 10^3 k_B T$, consistent with experimental observations which show that undulations and bumps are long-term structures with a well-defined shape. In contrast, in the absence of a network, the discocyte becomes unstable at $\Delta a_0 = 0.003$ –when undulated shapes become minimal over a short range of preferred area-difference– but the energy barriers between configurations are typically of $\sim 5 k_B T$, and hence crenated shapes would be highly unstable under thermal fluctuations. A structural component is required to explain the large stability of these structures. Accordingly, the cytoskeleton plays a fundamental role in the stabilization of the different RBC morphologies.

The energy landscapes of Figure 4.3 allow to identify the different stages that are sequencially found as energy minima when the asymmetry is increased. To make a clear connection with the observed transition, a purely morphological description is obviously more appropiate. The shape diagram defining the presence of undulations and bumps, and their height, is presented in Figure 4.5. Each point of the diagram represents a minimal shape, and the energy corresponding to each configuration can be directly obtained from Figure 4.4. Only when the energy difference in Figure 4.4 (a) is positive, and discoechinocytes I are favourable with respect to discocytes, the undulation height $\bar{u}$ is non-zero and increases with the membrane asymmetry. Analogously, out-of-plane bumps appear when the energy difference between discoechinocyte I and II is non-zero. A comprehensive description of the morphologies found is presented in the subsequent section.

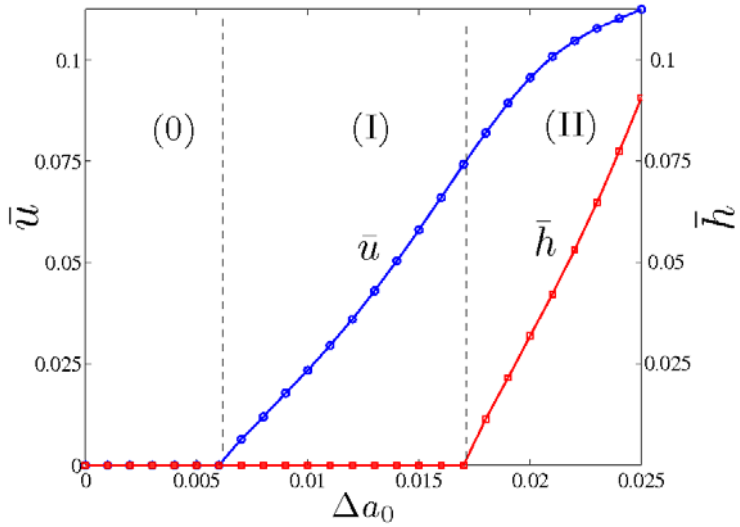

Figure 4.5: Shape diagram of the first stages of the RBC shape transition: (0) discocyte, (I) discoechinocyte I, and (II) discoechinocyte II. The number of undulations is fixed at $l = 5$ (the first to appear after the desestabilization of the discocyte), although it does not correspond with the minimal configuration for the entire range of Δa_0 (see Fig. 4.7). The growth of in-plane undulations saturates when out-of-plane bumps appear. The later grow much faster and rapidly acquire similar heights.

4.2.3 Morphological characterization

The discocyte.

Assuming a discocytic-relaxed cytoskeleton (where $E_{cyt} = 0$, and the shape is determined only by the bending contribution of the bilayer), the minimal shape obtained at zero asymmetry corresponds to $\epsilon = 0.98$ and $R_0 = 4.08\mu$m, shown in Figure 4.2 (0.t). The thickness of the cell is 2.11μm at its maximum and 1.03μm at the center, giving a ratio of 2.05, consistent with results for the discocyte found in previous Cassini-based calculations (Canham, 1970; Angelov and Mladenov, 2000; Eremina et al., 2006). This shape remains minimal over a small range of positive asymmetry, but its energy decreases until reaching an absolute minimum at $\Delta a_0 = 0.00089$. This is consistent with previous theoretical works (Liu et al., 1999) that also found global energy minima for discocytes with small positive asymmetries. This discocyte is fixed as S_0, mimicking the relaxation of the cytoskeleton over the bilayer, and the cytoskeleton will hereafter present resistance to deformations from this reference shape.

Transition to discoechinocyte I.

When Δa_0 is increased from the initial discocyte, the biconcavity shows a slow decay to less biconcave profiles, forced to reduce the negative curvature of the

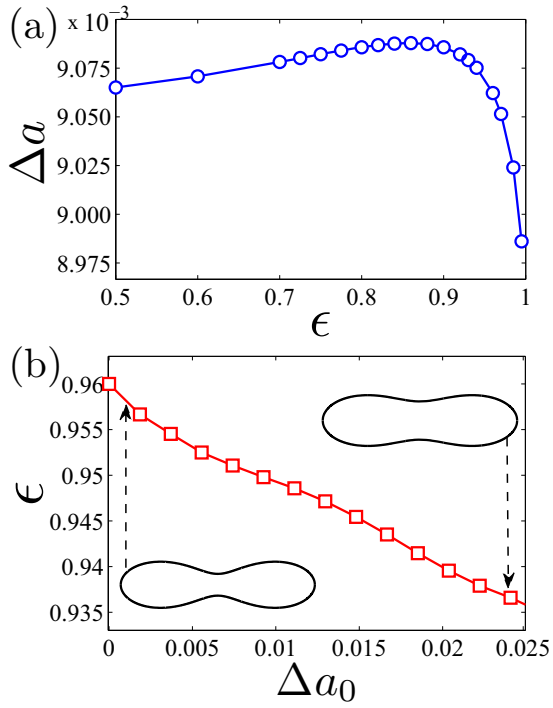

Figure 4.6: (a) Total area-difference of RBC shapes as a function of the biconcavity in the discocyte regime. The area-difference is lower at small biconcavities because the large area-to-volume ratio implies very flat disks. (b) Rate of thickening of the cell when Δa_0 is increased. Even at high asymmetries the shape remains slightly biconcave.

center of the disk. But the area difference does not increase monotonously when the biconcavity is reduced, and it actually achieves a maximum at $\epsilon = 0.88$, as shown in Figure 4.6 (a). Convex profiles do not imply a net benefit in the outer area, because shapes fulfilling the high area to volume ratio of the RBC demand large radius and low thickness, close to a very flat disk. Instead of losing biconcavity as a mechanism to increase its curvature, the cell can also break its axisymmetry and it develops undulations along its in-plane contour. This shape transformation leads not only to an explicit gain of curvature, but also to an increase of the surface area of the contour, allowing for an overall thickening of the central body of the cell whilst the total area remains constant. Therefore, these undulations allow the cell to deform into more spherical shapes. The rate at which the cell becomes thicker with Δa_0 seems to be slightly low compared with previous works (Lim et al., 2002), in which the cell is markedly ellipsoidal for $\Delta a_0 \sim 0.02$, whereas in our case at this point the shape remains considerably flat (typically $\epsilon \approx 0.9$, see Figure 4.6 (b)). Discocytes become unstable earlier ($\Delta a_0 = 0.0063$) than predicted with resting cytoskeletons in an oblate ellipsoid ($\Delta a_0 = 0.0082$) (Khairy and Howard, 2011). This delay in the transition might be related to the more compact resting shape of the cytoskeleton, as the ellipsoid would provide

more resistance to the undulations than a discocytic relaxed network.

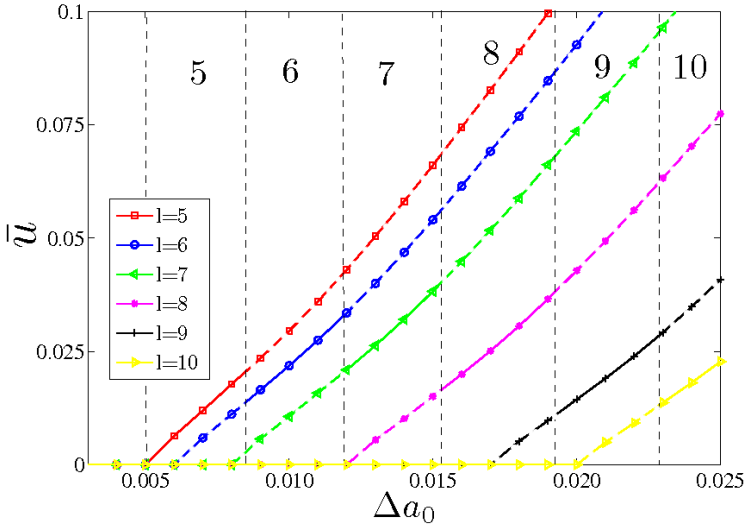

Figure 4.7: Dependence of the number of undulations l and their height with the preferred area-difference in a RBC within the discoechinocyte regime. Each l represents a minimal shape only over the range in which the line is bold; vertical dashed lines limit the range in which each mode is dominant. Contours with more undulations present lower heights and appear later in the transition.

The discoechinocyte I.

An example of a typical discoechinocyte I obtained is shown in Fig. 4.2 (I.t). The diagram of stable shapes within the discoechinocyte I regime predicted by the model is presented in Figure 4.7. A sequence of minimal shapes with increasing number of undulations is found, from $l = 5$ at low asymmetries up to $l = 10$ at the end of the discoechinocyte I regime, when the cell first develops out-of-plane bumps. $l = 1-4$ are sequentially found as minimal shapes over a very short range right before $l = 5$ becomes dominant,and for this reason are not shown here. The height of the undulation is very sensitive to the current overall number of undulations; for low numbers, the protrusions are considerably larger than those found for more undulated cells, giving a more spiky appearence to the cell, in accordance with experimental observations (Khairy et al., 2010). For instance, cells with 5 undulations show protrusions up to $\bar{u} \sim 0.15$, reduced to ~ 0.1 for 8 undulations and ~ 0.75 for 10; these values correspond to undulation heights of 0.6, 0.4 and 0.3 μm, respectively. This dependence can be explained on the basis of the stretching that the undulation undergoes. For high l, the base of the undulation is small and reaching large heights involves large stretchings, which disappear for sufficiently large bases associated to low-l. As previously explained, each mode has been analyzed here separately (as a single shape), which allows

an easier comparison between modes and identification of the dominant one at each Δa_0, but the curve in Figure 4.7 would be actually continuous if the entire combination of modes is considered.

Transition to discoechinocyte II.

The cell develops in-plane undulations in an earlier stage than out-of-plane bumps in spite of being, a priori, similar ways to increase the outer area. In-plane undulations grow on a curved surface, and the network disruption from the reference state is limited, involving only a smooth deformation of the contour. In contrast, out-of-plane bumps are drastic events which grow on an almost flat surface, and the local perturbation of the network is considerably larger. In Figure 4.8 (a), the dimensionless energy density map $f_{cyt}(\vec{x}) = (R_d^2/\kappa)\delta E_{cyt}/\delta A$ of the cytoskeleton for a discoechinocyte II is presented. The stress energy is largely localized in the out-of-plane bump, whilst the in-plane undulations bear a much less severe penalization. Figure 4.8 (b) shows the local area-difference for the same configuration. Both kind of protrusions achieve an area-difference benefit of the same order of magnitude, albeit slightly larger for the out-of-plane bump. Accordingly, the more stressed cytoskeleton inhibits the appearence of bumps in favour of the in-plane undulations, which imply a similar bilayer relaxation to the former.

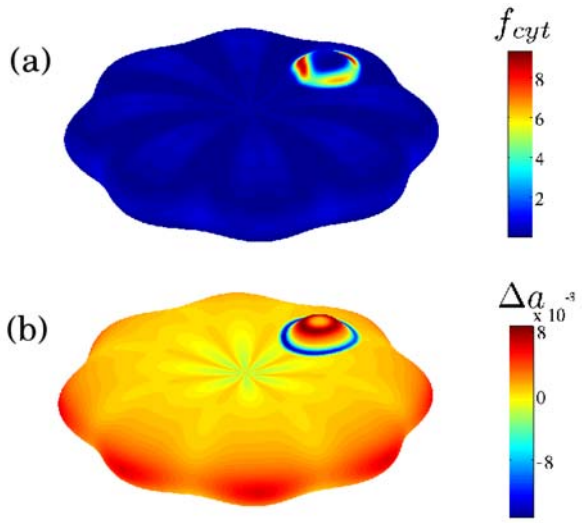

Figure 4.8: (a) Stress-energy density of the cytoskeleton $f_{cyt}(\vec{x}) = (R_d^2/\kappa)\delta E_{cyt}/\delta A$ in the discoechinocyte II stage. (b) Local area-difference Δa between layers for a discoechinocyte II. The out-of-plane bumps are highly penalized for a limited area-difference benefit, and consequently they appear when the bilayer has stored more energy than the in-plane undulations.

In-plane undulations induce a limited cytoskeleton distortion as far as their height is $\bar{u} \lesssim 0.125$; from this point onwards, the cytoskeleton perturbation affects

to significantly large regions of the entire network, and the rate of increase with Δa_0 of the undulations height decays. The cell develops new protusions in the central area of the disk, the so-called out-of-plane bumps, which characterize a new stage of the transition. As shown in Figure 4.5, the rate of growth of the undulations saturates coinciding with the development of the bumps, and the undulation stabilizes at $\bar{u} \sim 0.13$ (around 0.5 μm). The energy to relax the bilayer is now concentrated in the bump rather than continue with the growth of undulations.

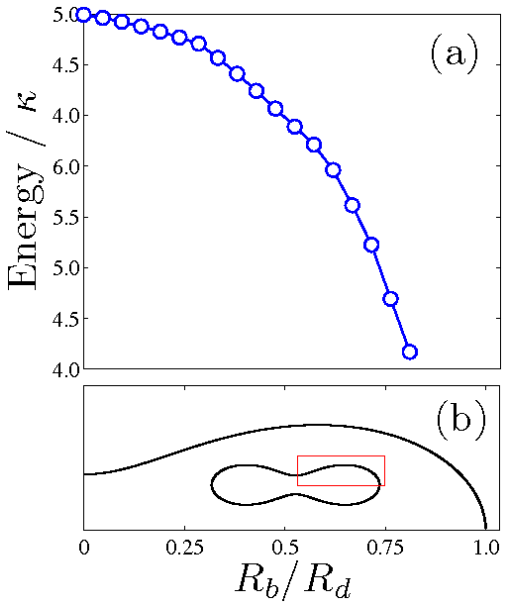

Figure 4.9: (a) Energetic cost associated with the growth of a bump as a function of the position of the bump in the cell (the resting shape of the cytoskeleton is shown in (b) for comparison). Bumps avoid the center of the cell, where the distortion of the concave cytoskeleton is around 15% larger (see main text), prefering the outer convex ring.

The discoechinocyte II.

Figure 4.2 (II.t) shows a typical example of discoechinocyte II. At this stage, the cell develops out-of-plane bumps which grow faster than the undulations, as shown in Figure 4.5. The model predicts bumps with a fairly rounded profile and typical base diameter $D_b \approx 0.9\mu$m. This is in good agreement with experimental observations, Figure 4.2 (II). The bumps maintain a nearly constant base, increasing their height and becoming thicker with Δa_0. Bump growth is limited by the constraints of area and volume, since a large bump size implies a considerable deformation of the overall cell shape, leading to typical heights of $\bar{h} \sim 0.2$. The bumps, even if they imply a locally large disruption of the cytoskeleton, are isolated events with a limited global impact over the network. The area and volume occupied by the

bump also allows the cell to reduce its radius and become thicker. Interestingly, bumps growing over convex profiles require less energy storage of the bilayer to obtain a similar shape than those appearing at concave surfaces. For this reason, it is found that out-of-plane bumps preferably grow over the convex ring, close to the contour, and avoiding the central concave region, as shown in Figure 4.9. The energy necessary to grow a bump in the center is higher than close to the rim, $(E_{center} - E_{ring})/E_{ring} \approx 0.15$. This implies that the out-of-plane bump might show a distribution pattern over the disk. Studies on the membrane fluctuations of the RBC showed that the amplitude of the fluctuations are also larger at this convex region (Park et al., 2010a). It may be feasible that the larger fluctuation amplitudes and the tendency of bumps to grow on the convex ring are related and due to geometrical restrictions, but further study is required in this direction. However, it has been suggested (Lim et al., 2002; Gov and Safran, 2005) that the development of the bumps is highly sensitive to isolated defects of the network implying local weakening of the cytoskeleton, which could facilitate the growth in the surrounding region. Such a dependence on the network defects could affect the predictions on the asymmetries required for the bump development and it would obscure any pattern in the bump distribution.

4.3 Discussion

The results presented show that a simple description of the cell shape via a Cassini oval parametrization provides a good account of the shape transformation in response to an increase of the membrane asymmetry. The analytical description allows a clearer interpretation and identification of the main ingredients determining the RBC morphological evolution, in spite of the limitations of the model in comparison with numerical free minimizations. Eremina et al. (2006) compared the minimal profile based on a Cassini ovals parametrization with the curve proposed by Evans and Skalak (1980), showing similar results. In spite of the variability shown by a population of RBCs, including size, cell profile, physiological membrane asymmetry and elastic modulii, most cells exhibit all the morphologies of the sequence in the correct order, suggesting that the transition presents a certain lack of sensitivity to variations in these parameters. The restriction of the cell profile being subject to a predetermined curve such as the Cassini oval is therefore expected to introduce small quantitative deviations with respect to the exact solution, but the overall process should be reasonable robust to profile differences.

The increase in the bilayer asymmetry triggers the formation of crenated shapes, driven by a stressed bilayer that tries to expand its outer leaflet to acco-

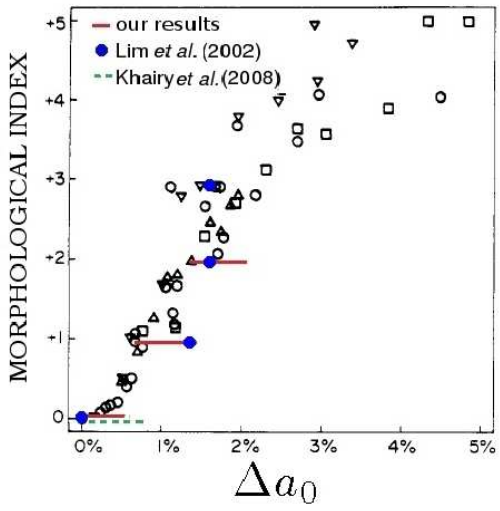

Figure 4.10: Comparison between the experimental results from Ferrell et al. (1985) (black symbols; the different types of symbols correspond to different lipid species), and theoretical results from Mukhopadhyay et al. (2002), Khairy and Howard (2011) (from which only the range of stability of the discocyte can be extracted because they do not distinguish between different types of echinocytes) and the results presented in this Thesis. The morphological index refers to the shape stage; 0-5 correspond to the discocyte, discoechinotes I and II and echinocytes I, II and III, respectively. The morphological index is a continuous quantity only when it is averaged over a population of cells; hence the theoretical results are expressed as a stepped curve. The measured magnitude in experiments is the preferred area difference, Δa, whereas the parameter from simulations is the preferred area-difference Δa_0, which tends to be slightly larger. All models show a qualitative agreement with experimental results, but the model of Lim *et al.* develops the most spiculated morphologies over a short range around $\Delta a_0 \sim 0.017 - 0.020$; in contrast, our results predict a more gradual transition. These divergences are already present in the discocyte regime, as our model predicts a shorter range of stability for this shape (the lines at morphological index equal to zero have been intentionally shifted in order to discern the exact range predicted by each model). Adapted with permission from Ferrell et al. (1985). Copyright 1985 American Chemical Society.

modate the excess area. It has been shown that the presence of the cytoskeleton is required to explain the whole transition, as a stabilizing component which favours compact axisymmetric shapes against vesiculation. The growth of protrusions has two direct implications in the shape transformation: *(i)* the gain of positive curvature allows a relaxation of the bilayer; *(ii)* the presence of undulations and bumps entails a relaxation of the large area to volume ratio, as they locally involve large surfaces enclosing small volumes. This allows the central body of the cell to become more spherical, and eventually protrusions will undergo vesiculation and the cell derives in a small spherocyte, with a considerably reduced area. The energy differences between configurations are large, ensuring a huge stability and explaining the marked hierarchy of the transition. Discoechinocytes I are therefore

necessarily found earlier along the transition than discoechinocytes II.

The reference state of the cytoskeleton was fixed as a discocyte shape. The present results support this assumption as a valid option. As with previous theoretical studies in which the resting shape was fixed as a prolate ellipsoid, we sequentially recover shapes in nice agreement with the RBC shapes observed in experiments. The quantitative analysis highlights the differences in the rate of development of the crenated morphologies. The shape diagram in Figure 4.5 shows a gradual shape transformation when the preferred area-difference is increased. The discocyte remains as a minimal shape up to $\Delta a_0 = 0.0063$, when the cell develops in-plane undulations. These structures grow up smoothly, increasing sequentially their number, and its stability range expands up to $\Delta a_0 \sim 0.02$, when out-of-plane bumps appear in the central region, defining the transition to discoechinocyte II. The bumps grow up over a short range of Δa_0 compared with the undulations, thus requiring a small amount of excess area in the outer leaflet. A typical discoechinocyte II such as that shown in Figure 4.2 (II.t) is attained at $\Delta a_0 = 0.0024$. In Figure 4.10, these results are compared with the experimental results of Ferrell et al. (1985), as well as with the theoretical results found by Lim et al. (2002) and Khairy and Howard (2011). All the models predict a similar order of magnitude in the preferred area difference to induce the transition. Nevertheless, studies which assumed an ellipsoidic relaxed cytoskeleton found a markedly steep transition; for instance, the discocyte, discoechinocyte I and echinocyte I and II are found at $\Delta a_0 = 0.00143, 0.01717$, 0.01788 and 0.02003 respectively. Whilst a considerably increase in Δa_0 is required to convert a discocyte into a discoechinocyte, the subsequent stages appear for a proportionally very reduced increase of Δa_0, and actually the transition saturates around a preferred area-difference of 0.02. These discrepancies might concern the different resting shape of the cytoskeleton. In-plane undulations represent a lower distortion for a discocyte than for an ellipsoid relaxed cytoskeleton, and thus lower Δa_0 are required to destabilize the discocyte in the former case. Conversely, when the cell is more spherical, the cytoskeleton is more stressed for a discocytic-reference state than for the ellipsoidal case, explaining why discocytic-relaxed shapes present more gradual transitions. Experimental evidence supports a regular transition; discoechinocytes I and II require an increase in Δa of ~ 0.008 and 0.014 from the discocyte, whilst an echinocyte II is not found up to $\sim$0.03. Thus, they found a similar increase in Δa_0 to induce both transitions, in accordance with our results, but at lower values than what our findings suggest. However, the magnitude of the outer monolayer expansion associated with these shapes has not been properly clarified, and significant divergences have been found; in comparison with the results in Figure 4.10, Lange and Slayton (1982) reported an increase of ~ 0.015 necessary to obtain a echinocyte II, whilst Matayoshi (1980) suggested that this quantity must be exceeded several

times. Therefore, more accurate results are necessary to determine the actual shape (the discocyte or the ellipsoid) at which the cytoskeleton is relaxed.

It has been shown that both the rigidity of the bilayer and the tension of the cytoskeleton are modified when ATP is depleted (Betz et al., 2009). Typically, the elastic modulii increase during morphological transformations in the absence of ATP (Park et al., 2010b), producing stiffening of the cell membrane. The rate of shape change with the bilayer asymmetry depends on the specific values of the elastic parameters. If $\bar{K}$ and $\bar{\mu}$ decrease from their normal values (which would correspond to a relative increase in the bilayer rigidity with respect to the cytoskeleton stiffness), the ranges of stability of the discocyte and discoechinocytes are reduced and the asymmetries required to induce the shape transformation are lower. The order in the shape sequence is maintained, but undulations and bumps develop earlier. If the cytoskeleton is weakened enough, we found that eventually out-of-plane bumps can appear at very early stages, even before the in-plane undulations have been developed. Future studies may explicitly incorporate the ATP-dependent mechanisms of cytoskeleton relaxation and how it affects to the cell morphologies, though a comprehensive understanding and description of this change in the elastic response is still required.

4.4 Discussion of the AFM experiments

The theoretical results show a considerable separation in the energy scale between each morphology. Accordingly, weak reductions of the membrane asymmetry may be accompanied by a strong relaxation of the deformation energy of the cell membrane, and therefore cells will change their shape even if minute changes in their membrane conformation are induced. The fact that the discocyte represents the ground state of the entire transition also explains the strong directionality of the shape recovery, as nearly in all cases cells were observed to deform into lower stages of the transition (towards the discocyte).

The stable shapes show an exteme sensitivity to the internal balance between the cytoskeleton and the bilayer. This fact, as well as the observation that cells invariably return to discocytic shapes, indicate that the AFM disruption does not affect the cytoskeleton equilibrium, or at least the potential damage is not important for shape stability. The effect induced by the AFM disruption must be then associated to the bilayer. The internal processes taking place in the bilayer cannot be identified in this model, altough we provide a measure of the area-expansion necessary to induce each shape transformation. The hypothesis presented in Section 3.3.2, in which we propose that the puncture of the membrane

by the AFM tip allows the flip of lipids due to a breaking of the hydrophobic potential, is plausible and consistent with the present results.

Finally, in the experiments it is shown that when crenated shapes (regardless of their morphological index) are punctured, they return to lower stages of the transition but showing a certain dispersion in the final stage induced. For instance, echinocytes IV are observed to deform into either echinocytes III, II or I. This observation supports a gradual shape transition with respect to an increase in the asymmetry. During each puncture, the amount of lipids transferred to the inner leaflet is likely different, giving rise to a dispersion in the induced change of the asymmetry. For a sharp transition, the final shape will be strongly dominated by the stable configuration for a wider range of Δa_0, and hence the transition towards discoechinocytes III (which, in this scenario, are stable only for a very reduced range of Δa_0) would be very unlikely.

4.5 Conclusions

The mechanisms driving cell deformations and the role of each structural component of the RBC membrane have been identified. The reported results highlight the relevance of understanding the process of membrane asymmetry control, and how it interplays with the cytoskeleton remodelling, in order to stablish the time-dependent behaviour of the shape transformation. The theoretical results support the hypothesis of lipid rearrangement induced by AFM puncturing proposed in the previous section.

The spectrin cytoskeleton has been shown to play an important role in the stabilization of the discocyte shape. The results presented here agree with other theoretical and experimental studies that indicate an (at least partially) relaxed cytoskeleton in the discocytic state. The cytoskeleton is highly stressed when the membrane deforms and bumps and spicules develop, though its energetic storage is very low when the cell remains weakly deformed from the initial discocyte. This may imply that even if the cytoskeleton is relevant in some kind of deformations, opposing resistance to crenation and confiring stability under budding and vesiculation, it could have a secondary contribution to RBC elasticity when cell shape remains close to the discocyte, such as during blood flow.

Active processes seem fundamental to clarify the kinetic behaviour of the cell morphology and elasticity; whereas recent theories have incorporated the effect of ATP in several mechanisms affecting membrane elasticity, the approach to study cell morphology still assumes a static picture, with active processes been considered negligible or of little importance. In that regard, more studies are required to elucidate the resting shape of the cytoskeleton, ideally including local

relaxation, as it seems realistic that the network is able to conveniently change its connectivity at certain regions depending on the enviromental conditions (Li et al., 2007). All these questions are crucial to throw additional light into the issue of how active processes modulate membrane elasticity and achieve a deeper understanding of RBCs mechanics.

Part III

A phase-field method for membrane modeling

Chapter 5

Phase-field modeling of biological membranes

In Chapter 2, we have presented the main physical models describing membrane elastic behaviour. One of these theories, the ADE model, has been used in Chapter 4 to gain a deeper understanding of the role of each membrane component in the membrane elasticity, and we have predicted some equilibrium morphologies of the cell on the basis of an analytic parametrization of the membrane. However, when more complex problems are faced, such as any dynamic instability or out-of-equilibrium process, a more flexible framework is usually required. Given that the representation of the membrane as a two-dimensional layer is reasonably accurate, the simplest and most direct formulation consists in defining a mesh of points which represents the membrane neutral surface, and from here extract the local mean curvature or deformation tensor necessary to compute the elastic energy. This must be combined with a minimization procedure (such as a Monte Carlo free minimization (Lim et al., 2002)) to obtain equilibrium shapes, or introducing the elastic mesh in a dynamic theory if one is interested in membrane kinetics. Most important examples include the immersed boundary methods (Peskin, 2002; Kaoui et al., 2012), integral boundary methods (Pozrikidis, 1992, 1995) or multiparticle collision dynamics (Malevanets and Kapral, 1999; McWhirter et al., 2008). Methods in this direction have been succesfully applied to the study of many membrane related topics (Li et al., 2005; Peng et al., 2013). All these methods require of a explicit tracking of the membrane position and the calculation of the deformation variables, *ie* the curvature. A different approach, based on an Eulerian rather than a Lagrangian description, are the phase-field models. The membrane is identified from an auxiliary scalar field defined in the entire space, and the method details the dynamics of the field, instead of specifically deal with the evolution of the interface. This formulation also avoids the problematic of defining the boundary conditions at the membrane surface.

This Part of the Thesis is devoted to the characterization, rationalization and study of a phase-field method for membrane modeling. We connect the phase-field model with the theory of elasticity, explaining how the elastic properties of the membrane can be controlled. The macroscopic equations that define the membrane dynamics, including the general membrane equilibrium equation, are derived. Finally, we numerically perform a linear stability analysis in order to test the reliability of the model. The phase-field method presented here corresponds to a bending membrane, based on the Helfrich theory, and thus it represents a purely lipidic description of the membrane. The method does not incorporate any shear contribution characteristic of the cytoskeleton. Accordingly, this method can be applied to study phenomena associated with vesicles and cells (Campelo and Hernández-Machado, 2007a, 2008; Campelo et al., 2012; Wang and Du, 2008) in which the cytoskeleton plays a subdominant role, as we will see in the Part VI of this Thesis.

5.1 Phase-field method

Phase field models have been widely applied in the study of different phenomena of phase transitions, such as superconductivity and solidification (Steinbach, 2009), due to their universality as well as their utility as a mathematical tool in the numerical and analytical fields. Although the application of phase-field methods to amphiphilic systems was extensively investigated in the past (Gompper and Schick, 1994), it has not been until recently that these models have been used in the study of cell morphology and dynamic response. One of the main advantages of the phase-field modeling is that the evolution and shape of the membrane does not need to be tracked, as in the explicit methods, but it spontaneously evolves with the phase field dynamics. Phase-field methods also invite to a deep analytical exploration as they have a robust physical basis.

Ginzburg-Landau free energy

The origins of phase-field models are found in the mean-field approach to phase transitions. The Landau theory consists in a free energy which is expanded in powers of a scalar field, called order parameter ϕ, which receives different interpretations depending on the system, as we will see below, but, for instance, in a ferromagnetic system it is readily identified as the magnetization. The symmetries of the system specify the value of the coefficients of the expansion. However, this model does not account for the presence of interfaces which could have an energetic cost associated with the interaction between the components of each phase.

Ginzburg and Landau generalized this expression in their studies about superconductors and they incorporate to the free energy of the system, $\mathcal{F}[\phi]$, powers of the gradients of the order parameter,

$$\mathcal{F}[\phi] = \int \mathcal{L}(\phi, \nabla\phi, \nabla^2\phi)dV = \int \left[f(\phi) + g(\phi)\epsilon^2(\nabla\phi)^2 + c\epsilon^4(\nabla^2\phi)^2\right] dV. \quad (5.1)$$

where $\mathcal{L}$ is the energy density, $f(\phi)$ is the bulk potential, so that in equilibrium $f'(\phi_{eq}) = 0$ and ϕ_{eq} are the stable bulk phases. The coefficients associated to the order parameter gradients, $g(\phi)$ and c, represent the energetic cost of having an interface. Typically, $f(\phi)$ is chosen to form a symmetric double-well potential, and hence two phases are present, $\phi_{eq} = \pm 1$. The interface is characterized by a smooth profile characterized by a width ϵ, and it is usual to fix the interface position at the isosurface $\phi = 0$. The method does not necessarily need that ϵ operates on the same scale of the width of the real interface, which in some systems can be the atomic scale, but it is sufficiently to require that *(i)* ϵ is much smaller than any other length of the system; and *(ii)* the interface incorporates the relevant information from the microscale trought the effective constants of the model.

The construction of a Ginzburg-Landau free energy often responds to a purely phenomenological basis and it generally attends to the symmetries of the system. The order parameter is related to a characteristic physical property depending on the specific system; in the particular case of a membrane, it can be described as a function of the concentration of lipids, $\phi(x) = 1 \mp \rho_{lip}(x)/\rho_0$, where ρ_0 is the reference concentration of maximum package and the $\mp$ corresponds to the equilibrium phase, -1 and +1, in the inner or outer regions of the membrane, respectively. It is noteworthy that ϕ is defined in a spatial scale sufficiently large to have a statistically good average of the molecular densities, but yet small enough to capture the mesoscopic spatial variations of the density.

5.1.1 Thermodynamics of phase-field models

In thermodynamics, the chemical potential of a species in a mixture is defined as the free energy change for deviations in the concentration from the reference value. Analogously, within the phase-field framework the chemical potential is obtained from the free energy (5.1),

$$\mu[\phi] = \frac{\delta\mathcal{F}}{\delta\phi} = \frac{\partial\mathcal{L}}{\partial\phi} - \nabla_\beta \frac{\partial\mathcal{L}}{\partial(\nabla_\beta\phi)} + \nabla^2 \frac{\partial\mathcal{L}}{\partial(\nabla^2\phi)}. \quad (5.2)$$

In equilibrium, the chemical potential is constant and in addition to the boundary conditions in the bulk phase $\phi(x \to \pm\infty) = \pm 1$, this equation can be solved obtaining the equilibrium profile of the interface. Typically, the relaxed profile is a smooth tanh-like function with interface width ϵ. As we will see later on, the chemical potential is a relevant variable as it governs the diffusion of the order parameter (Section 5.3). In the presence of a non-uniform phase field, there is a thermodynamic local force at each point (*eg* this force can be naively understood in the case in which ϕ is a concentration, and then gradients of concentration force diffusive fluxes towards a uniform concentration). Given that in the bulk $\mu = const.$, the force density is localized at the interface.

The stress tensor is an important magnitude to characterize the deformation of membranes, though it is not obvious how to compute this tensor from a phase-field free energy of the form (5.1). The work required to deform an object by a small displacement δx_α is given by (Landau and Lifshitz, 1999)

$$\delta\mathcal{F} = -\int \nabla_\beta \sigma_{\alpha\beta} \delta x_\alpha dV = \int \sigma_{\alpha\beta} \nabla_\beta \delta x_\alpha dV. \tag{5.3}$$

In the phase-field framework, we need to specify the variations in the order parameter due to the deformation δx. Assuming that these small variations only correspond to convective fluxes, *ie* diffusion is subdominant (Brannick et al., 2014),

$$\partial_t \phi + \nabla \cdot (\phi \mathbf{v}) = 0, \tag{5.4}$$

and writing $v_\alpha = \delta x_\alpha / \delta t$, we obtain the variation of the order parameter and, after differentiation, its derivatives

$$\begin{aligned}
&\delta\phi = -\phi\nabla_\alpha \delta x_\alpha - \nabla_\alpha \phi \delta x_\alpha. \\
&\delta\nabla_\beta\phi = -\nabla_\beta\phi\nabla_\alpha\delta x_\alpha - \phi\nabla_\beta\nabla_\alpha\delta x_\alpha - \nabla_\beta\nabla_\alpha\phi\delta x_\alpha - \nabla_\alpha\phi\nabla_\beta\delta x_\alpha. \\
&\delta\nabla^2\phi = -\nabla^2\phi\nabla_\alpha\delta x_\alpha - 2\nabla_\beta\phi\nabla_\beta\nabla_\alpha\delta x_\alpha - \phi\nabla_\alpha\nabla^2\delta x_\alpha - \nabla_\alpha\nabla^2\phi\delta x_\alpha \\
&\qquad -2\nabla_\beta\nabla_\alpha\phi\nabla_\beta\delta x_\alpha - \nabla_\alpha\phi\nabla^2\delta x_\alpha.
\end{aligned} \tag{5.5}$$

The work necessary to induce a general deformation δx_α of an interface with free energy (5.1) reads

$$\delta\mathcal{F} = \int \delta\mathcal{L} dV = \int \left(\frac{\partial\mathcal{L}}{\partial\phi}\delta\phi + \frac{\partial\mathcal{L}}{\partial\nabla_\beta\phi}\delta\nabla_\beta\phi + \frac{\partial\mathcal{L}}{\partial\nabla^2\phi}\delta\nabla^2\phi \right) dV. \tag{5.6}$$

Introducing expressions (5.5) in (5.6), and after several straightforward integrations of those terms containing second and third gradients of δx_α, one finds

$$\begin{aligned}\delta\mathcal{F} = &-\int\left[\frac{\partial\mathcal{L}}{\partial\phi}+\frac{\partial\mathcal{L}}{\partial(\nabla_\alpha\phi)}\nabla_\alpha\phi+\frac{\partial\mathcal{L}}{\partial(\nabla^2\phi)}\nabla_\alpha\nabla^2\phi\right]\delta x_\alpha dV\\ &-\int\left[\frac{\partial\mathcal{L}}{\partial\phi}-\nabla_\beta\frac{\partial\mathcal{L}}{\partial(\nabla_\beta\phi)}+\nabla^2\frac{\partial\mathcal{L}}{\partial(\nabla^2\phi)}\right]\phi\nabla_\alpha\delta x_\alpha dV\\ &-\int\left[\frac{\partial\mathcal{L}}{\partial\nabla_\beta\phi}\nabla_\alpha\phi+\frac{\partial\mathcal{L}}{\partial\nabla^2\phi}\nabla_\alpha\nabla_\beta\phi-\nabla_\beta\frac{\partial\mathcal{L}}{\partial\nabla^2\phi}\nabla_\alpha\phi\right]\nabla_\beta\delta x_\alpha dV.\end{aligned} \tag{5.7}$$

In the first term of the right hand side of (5.7) the divergence $\nabla_\alpha\mathcal{L}$ can be recognized. Analogously, the second term contains the expression of the functional derivative of $\mathcal{L}$, given by (5.2). Hence, comparing with (5.3), the stress tensor is identified,

$$\sigma_{\alpha\beta} = \left(\mathcal{L}-\phi\frac{\delta\mathcal{L}}{\delta\phi}\right)\delta_{\alpha\beta}-\frac{\partial\mathcal{L}}{\partial(\nabla_\beta\phi)}\nabla_\alpha\phi-\nabla_\beta\frac{\partial\mathcal{L}}{\partial(\nabla^2\phi)}\nabla_\alpha\phi+\frac{\partial\mathcal{L}}{\partial(\nabla^2\phi)}\nabla_\alpha\nabla_\beta\phi. \tag{5.8}$$

From (5.8), it can be shown that the divergence of the stress tensor reduces to

$$\nabla_\beta\sigma_{\alpha\beta} = -\phi\nabla_\alpha\mu, \tag{5.9}$$

which provides an expression for the local force density of the interface in terms of the chemical potential. The expressions obtained so far are valid for any free energy of the form (5.1), so that the elastic properties of the interface are solely determined by this free energy.

The dependence of the force density on the chemical potential can be understood from a thermodynamic perspective, taking into account that the stress represents the internal reaction to an external pressure (strictly speaking, the pressure and stress tensor are related by $P_{\alpha\beta} = -\sigma_{\alpha\beta}$). Hence, equation (5.9) may be related with the Gibbs-Duhem equation, which reads

$$VdP = \sum_i N_i d\mu_i \tag{5.10}$$

where N_i is the amount of matter of the species i and taking into account that $\phi \sim N/V$, leads to $dP = \phi d\mu$. The force density arise as the free energy change per unit volume, $\phi\delta\mu$, due to the transport of matter concentration ϕ for a change in the chemical potential $\delta\mu$.

5.2 Elastic properties of the phase-field interface

In the Helfrich theory, the physical meaning of each elastic modulii is clear, as each modulus is explicitly associated to the elastic deformation that penalizes (*ie* in (5.1), the surface tension represents the energetic cost of having an interface of surface dA, and the bending modulus corresponds to the cost of an interfacial bending given by the curvature C). In the phase-field representation of the interface free energy, however, the information about the geometrical properties of the interface deformation is implicitly contained in the gradients of the order parameter, and the elastic properties of the interface cannot be directly identified. It is therefore necessary to establish a connection between the phase-field coefficients, g and c, of the phase-field free energy (5.1), and the interface elastic parameters expressed in the Helfrich energy (2.16). The comparison between both free energies for simple geometries, such as spheres or cylinders, is a useful method for obtaining a mapping between the Helfrich and phase-field representations. In this Section, we derive the expressions of the elastic coefficients of (2.16) from the parameters of the free energy (5.1), as first proposed by Gompper and Zschocke (1991), and Gompper and Zsckocke (1992). Thereby, the method allows to specify the elastic properties of the phase-field free energy and conciliate this expression with the classic elastic description.

Let us suppose a generic interface with free energy (2.16), with contributions of surface tension and bending, but disregard the pressure difference term assuming that the interfacial surface is open. Note that this free energy can be locally understood as an expansion in terms of the radius of curvature $1/R$, since $C \sim 1/R$ and $G \sim 1/R^2$. Hence, the surface tension is associated to the zeroth order, $1/R^0$; the spontaneous curvature corresponds to the first order of the expansion, $1/R^1$; and the bending and saddle splay modulii are associated with the second order, $1/R^2$. The elastic energy per area (2.16) for a sphere of radius R is given by

$$\frac{\mathcal{F}_e^{(s)}}{A} = \left(\gamma + \frac{\kappa}{2}c_0^2\right) - \frac{\kappa}{R}c_0 + \frac{2\kappa + \kappa_G}{R^2}. \tag{5.11}$$

For simplicity, the first term is rewritten $\bar{\gamma} = \gamma + \kappa c_0^2/2$. For a cylinder, the Gaussian curvature vanishes and then the free energy reduces to

$$\frac{\mathcal{F}_e^{(c)}}{A} = \bar{\gamma} - \frac{\kappa}{R}c_0 + \frac{\kappa}{2R^2}. \tag{5.12}$$

The inclusion of the cylinder is important to identify the bending modulus, which appears coupled to the saddle-splay modulus in the spherical geometry.

The equilibrium condition for the free energy (5.1) determines the relaxed planar interface profile $\phi_0(z)$ in the normal direction z,

$$\frac{\delta\mathcal{F}[\phi]}{\delta\phi} = f' - 2g(\phi_0)\partial_z^2\phi_0 - g'(\partial_z\phi_0)^2 + 2c\partial_z^2\phi_0 = 0, \tag{5.13}$$

where $g' = \partial g/\partial\phi$ and $f' = \partial f/\partial\phi$. Multipliying by $\partial_z\phi_0$, and integrating across the interface,

$$f(\phi) = \int_{-\infty}^{\infty}[2g\partial_z^2\phi_0\partial_z\phi_0 + g'(\partial_z\phi_0)^3 + 2c\partial_z^2\phi_0\partial_z\phi_0]dz. \tag{5.14}$$

Note that, formally, (5.13) is the stationary condition of the Euler-Lagrange equation and then (5.14) is its first integral. For the specific geometry of spheres and cylinders, the free energy (5.1) reads

$$\frac{\mathcal{F}^{(c,s)}[\phi]}{A} = \frac{1}{R^{d+1}}\int_0^{\infty} drr^d\left[f(\phi_R) + g(\phi_R)(\partial_r\phi_R)^2 + c\left(\partial_r^2\phi_R + \frac{d}{r}\partial_r\phi_R\right)^2\right], \tag{5.15}$$

where $d = 1$ and 2 for cylinders and spheres, respectively, and ϕ_R is the phase-field profile for these two configurations. If the radius R is large, the phase-field profile ϕ_R can be expressed in terms of the relaxed planar solution, $\phi_0(z)$, by identifying the position of the interface at $z = r - R$. This approximation, known as *locally flat* interface, allows to expand the profile in powers of $1/R$,

$$\phi_R(r-R) = \phi_0(r-R) + \frac{\phi_1(r-R)}{R} + ... \tag{5.16}$$

By introducing this expression in (5.14), and using this to remove $f(\phi_R)$ from (5.15), to leading order the free energy for spheres and membranes now reads,

$$\frac{\mathcal{F}^{(c,s)}[\phi]}{A} = \int_0^{\infty} dr\left(1+\frac{r}{R}\right)^d\left[2g(\phi_0)(\partial_r\phi_0)^2 + 3c(\partial_r\phi_0)^2 + c\left(\partial_r^2\phi_0 + \frac{d}{r+R}\partial_r\phi_0\right)^2\right.$$
$$\left. - \frac{1}{R^2}\delta(d-2)2c\int_0^{\infty} dr(\partial_r\phi_0)^2.\right. \tag{5.17}$$

The expansion of this expression in powers of $1/R$ leads to

$$\frac{\mathcal{F}^{(c,s)}[\phi]}{A} = \int_0^\infty dr[2g(\phi_0)(\partial_r\phi_0)^2 + 4c(\partial_r^2\phi_0)^2] + \int_0^\infty dr\frac{2r}{R}[2g(\phi_0)(\partial_r\phi_0)^2 + 4c(\partial_r^2\phi_0)^2]$$
$$+ \int_0^\infty \frac{r^2}{R^2}[2g(\phi_0)(\partial_r\phi_0)^2 + 4c(\partial_r^2\phi_0)^2] + \delta(d-1)\int_0^\infty dr\frac{2c}{R^2}(\partial_r\phi_0)^2. \tag{5.18}$$

Comparing this expression with the free energy of cylinders (5.12) and spheres (5.11), and identifying the coefficients of the corresponding terms of the expansion, one obtains

$$\begin{aligned} \bar{\gamma} &= \int_{-\infty}^{+\infty} s(z)dz, \\ -\kappa c_0 &= 2\int_{-\infty}^{+\infty} zs(z)dz, \\ \kappa &= \int_{-\infty}^{+\infty} 2c(\partial_z\phi_0)^2 dz, \\ \kappa_G &= \int_{-\infty}^{+\infty} (z^2 s(z) - 4c(\partial_z\phi_0)^2)dz, \end{aligned} \tag{5.19}$$

where we have recovered the planar profile notation as a function of the normal coordinate z and we have introduced the function

$$s(z) = 2g(\phi_0)(\partial_z\phi_0)^2 + 4c(\partial_z^2\phi_0)^2. \tag{5.20}$$

The interpretation of this expression is found in the elasticity theory framework. The lateral stress profile of an object is calculated from the stress tensor via

$$s_e(z) = \sigma_t(z) - \sigma_n(z), \tag{5.21}$$

where σ_n and σ_t are the projections of the stress tensor in the normal and tangential directions to the interface, respectively. By computing the stress tensor (5.8) of an interface normal to the direction $\hat{z}$ and characterized by a free energy (5.1), it is found that (5.20) represents the phase-field representation of the lateral stress profile of the interface. Accordingly, the elastic modulii arise as moments of the lateral stress profile, as stablished in the Helfrich theory (Helfrich, 1973).

The particular microstructure and chemical composition of the interface dictate the interactions and internal tensions of the interface, ultimately determining its elastic behaviour. For instance, in the case of two inmiscible fluids, such as the water-oil coexistence, the unique contribution to the free energy corresponds to the surface tension, associated solely to the cost of having a surface in

which both species of molecules interact. The benefit of homotypic interactions when a molecule is surrounded by others of the same species is lost in the interface, where the van de Waals interactions between oil and water molecules are weaker. Accordingly, the system tries to minimize this contact surface, but the bending of the surface does not have any energetic cost. Other systems, such as monoloyers formed by amphiphilics, present a more complicated interface internal physics, reflected in an extremely rich phenomenology. In the presence of water and oil, amphiphiles form several different structures ranging from micelles to lamellar (plane) arrays of amphiphiles separating regions of each fluid (Gompper and Schick, 1994). The principles driving this kind of organization respond to the polar nature of the amphiphile, with a hydrofilic head, which prefers to interact with water, and the hydrophobic tail, which prefers the oil. The system evolves to minimize the contact between the hydrophobic tail and water. In these systems, the lateral tensions between the amphiphiles induce a more complex elastic behaviour, and all the terms in (2.16) contribute to the interface elasticity. Still, in the low curvature regime (when the interface thickness ξ is much smaller than the typical radius of curvature, $\xi/R \ll 1$; this regime applies to most systems, since ξ is of the order of the lipid length), the dynamics of the interface is generally dominated by the surface tension term, since it corresponds to the leading term of (2.16).

Lipid bilayers present an even more complex internal structure than monolayers, and are known to induce a strong reduction in the surface tension of the interface, sometimes of up to 5 orders of magnitude (Gompper and Schick, 1994), as a result of the internal balance of the lateral stresses between lipids. Accordingly, the dynamics of the membrane is driven by bending (the subsequent non-vanishing term in the curvature expansion of the Helfrich energy (2.16), assuming membrane symmetry). Since the scope of this Chapter is the modeling of biological lipid membranes, hereafter we focus on tensionless interfaces. It is noteworthy that the elimination of the surface tension contribution in phase-field models is highly non-trivial, as it requires of a subtle balance of the lateral tensions of the interface.

5.2.1 Cell membrane model

The theory presented thus far offers the necessary ingredients to build a model for cell membranes. The simplest approach to describe the cell is to follow the Ginzburg-Landau spirit, considering two domains, the inner fluid (*eg* cytosol) and the outer aqueus environment (*eg* plasma), and associate each medium to one of the equilibrium phases of the order parameter. The coefficients associated to the order parameter gradients determine the elastic properties of the interface, and

hence they must be chosen to capture the two main characteristics of membranes: resistance to bend and vanishing surface tension. The first condition is achieved by $c > 0$, given that a second derivative is necessary to introduce a bending contribution. The second condition requires a negative constant value of g, or alternatively an inhomogeneous function $g = g(\phi)$. However, the choice of the free energy coefficients to obtain a vanishing surface tension is delicate. The coefficients determine the equilibrium profile of the order parameter, and in general its solution requires of numerical integrations. The profile enters in the elastic parameters calculation, (5.19). Thus, the elastic properties depend on the coefficients via the equilibrium profile which in turn can be very sensitive to the values of the coefficients. A priori, there is not a unique solution for g and c that produces the prescribed elastic properties of the membrane.

We consider the particular case $f_b(\phi) = \phi^2 - 2\phi^4 + \phi^6$, $g_b(\phi) = 2(3\phi^2 - 1)$, and $c_b = 1$, which is of particular interest because its equilibrium equation has analytical solution and therefore it allows a more fine control of the interfacial behaviour. The interface free energy reads (Du et al., 2004; Campelo and Hernández-Machado, 2006)

$$\mathcal{F}_b[\phi] = \frac{\kappa^*}{2} \int (\phi^2 - 2\phi^4 + \phi^6 + (3\phi^2 - 1)\epsilon^2(\nabla\phi)^2 + \epsilon^4(\nabla^2\phi)^2)dV, \tag{5.22}$$

where the subscript b indicates that this model corresponds to a bending free energy. The free energy can be rewritten as

$$\mathcal{F}_b[\phi] = \frac{\kappa^*}{2} \int (\psi[\phi])^2 dV, \tag{5.23}$$

where we have introduced the functional $\psi = -\phi + \phi^2 - \epsilon^2\nabla^2\phi$ and additionally the parameter κ^* is incorporated to control the bending rigidity of the interface.. From this expression the chemical potential as defined in (5.2) reads

$$\mu_b = \delta\mathcal{F}_b[\phi]/\delta\phi = \kappa^*[(3\phi^2 - 1)\psi - \epsilon^2\nabla^2\psi]. \tag{5.24}$$

The relaxed profile is obtained by solving the equilibrium condition, $\mu_b = 0$. Although this equation does not have a unique solution, the trivial one $\psi = 0$ represents the minimal energy solution, given that the bending energy is always positive. Other potential solutions may arise as metastable solutions. This equilibrium profile of the model (5.22), $\psi = 0$, can be analytically integrated, leading to $\phi_0 = \tanh(z/\sqrt{2}\epsilon)$, connecting the bulk phase -1 with the phase +1. If this expression is introduced in (5.19) with the energy coefficients from (5.22), the

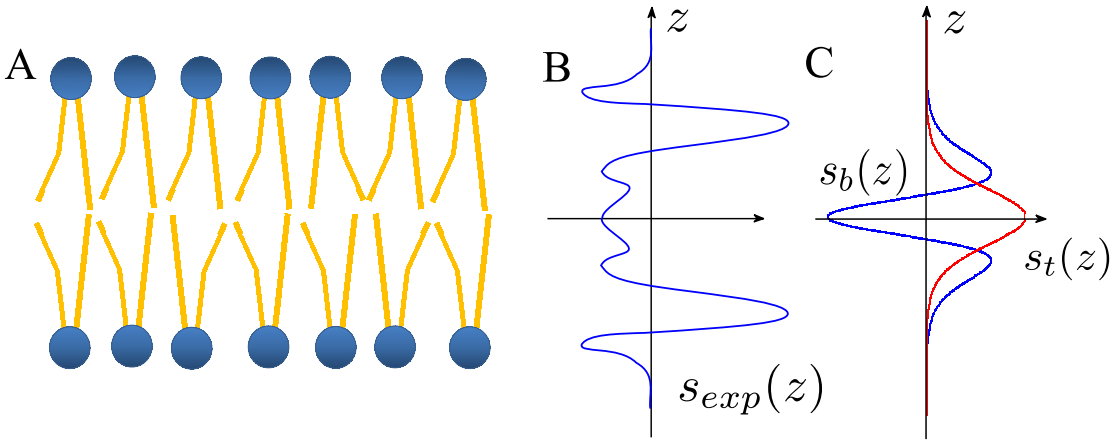

Figure 5.1: (A) Scheme of a lipid bilayer. The multiple interactions between the different chemical groups of the bilayer (including repulsion between polar groups, hydrophobic attraction, cohesive and repulsive effects between tails, etc) leads to a complicate stress profile in real cell membranes. However, they are characterized by a balance between internal tensions, so that the surface tension vanishes in this system. (B) Example of lateral stress profile $s_{exp}(z)$ for a lipid bilayer, based on the results of Hu et al. (2013) obtained from MARTINI simulations of DMPC bilayers. (C) Lateral stress profile of the membrane phase field model, $s_b(z)$ (blue line), and for a tension interface, $s_t(z)$ (red line). The phase-field model for membranes does not reproduce the exact lateral stress profile of a realistic membrane but effectively concentrates the interactions in two contributions, a central term of repulsion and two symmetric attractions, and their balance recovers the tensionless nature of the membrane. A physical interpretation of this simple profile is that the central term corresponds to the entropic repulsion between the lipid tails, whereas the the lateral attractions would represent the attractions between head and tails, following the spirit of the model of Petrov and Bivas (1984). In comparison, the lateral stress profile of a tension interface, involves a single term at the frontier between the two phases, penalizing the presence of the interface.

resulting elastic parameters are $\gamma = c_0 = 0$, $\kappa = (2\epsilon^3/3\sqrt{2})\kappa^*$ and $\kappa_G = 0$, consistent with a symmetric membrane. Hence, the model describes the cell as two fluid domains separated by an interface with the elastic properties characteristic of membranes.

From the bending free energy (5.22) we can study the interface properties that determine its elastic response. The stress tensor is computed from (5.8), obtaining

$$\sigma^b_{\alpha\beta} = -(\kappa^*/2)\{[-\phi^2 + 6\phi^4 - 5\phi^6 - 2\epsilon^2(3\phi^3 - \phi)\nabla^2\phi - (3\phi^2 - 1)\epsilon^2(\nabla\phi)^2 - 6\epsilon^2\phi^2(\nabla\phi)^2 + 2\epsilon^2\phi\nabla^2\nabla^2\phi - \epsilon^2(\nabla^2\phi)^2]\delta_{\alpha\beta} + 2\epsilon^2(3\phi^2 - 1)\partial_\alpha\phi\partial_\beta\phi - 2\epsilon^4\partial_\alpha\partial_\gamma\phi\partial_\beta\partial_\gamma\phi - 2\epsilon^4[\partial_\alpha\phi\partial_\beta\nabla^2\phi + \partial_\beta\phi\partial_\alpha\nabla^2\phi] + 2\epsilon^4\partial_\alpha\partial_\beta\partial_\gamma\phi\partial_\gamma\phi + 4\epsilon^4\partial_\alpha\partial_\beta\nabla^2\phi\}. \tag{5.25}$$

In Figure 5.1 C, the lateral stress profile $s_b(z)$ for the membrane free energy (5.22) is shown, in addition to the stress profile $s_t(z)$ for the classic surface tension

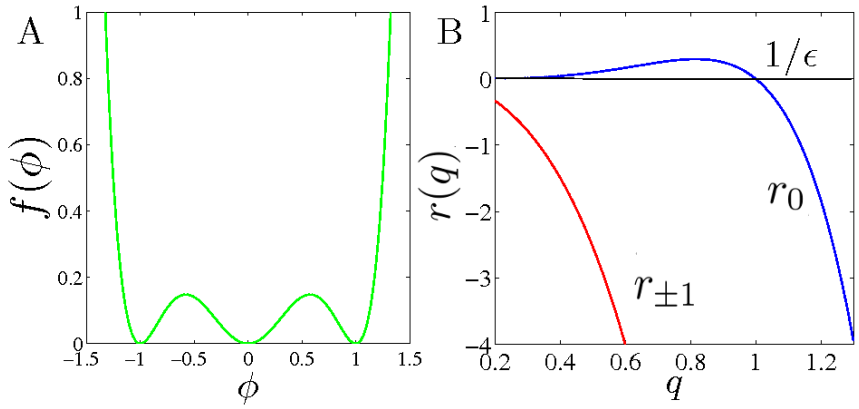

Figure 5.2: (A) Bulk potential of the curvature free energy (5.22), with three phases of equal energy. (B) Linear dispersion of the decay of a phase when subjected to a weak sinusoidal perturbation. The $\phi_{\pm 1}$ phases are stable, whereas the ϕ_0 phase is only stable for small domains of length $< \epsilon$.

interface which applies, for instance, for a water-oil phase separation, given by the coefficients $c = 0$ (not bending penalization) and $g(\phi) = g_0 > 0$. In this last case, the model includes an energetic cost for the existence of the interface. This area penalty is the surface tension. The stress through the interface are represented by a unique positive term, implying that the pressure is negative and thus the interfacial molecules are compressed, trying to minimize the surface area. In the case of the membrane, the lateral stress of the phase-field model does not capture a realistic profile, such as the one shown in Figure 5.1 B, but it condensates the information in two terms of repulsion and attraction. One could interpret the forces at the middle of the interface as the entropic repulsion between tails, whereas the two lateral attractive regions may correspond to the attraction between lipid and heads. In general terms, the profile recovers the behaviour proposed in the simple microscopic model studied in Section 2.2.1. In this approach, the balance between attractive and repulsive interactions means that the interface is not energetically penalized for having a certain surface (*ie*, it has zero surface tension) but instead it is penalized for having a non zero curvature, as the first non-vanishing term in the expanded free-energy corresponds to $1/R^2$. The parameter that determines this energetic cost is identified as the bending rigidity of the membrane.

The membrane model should include both the bending contribution and the compression of the membrane. The area-compression effect is modeled by directly imposing a constant surface area, as first proposed by Helfrich. This is done by adding a Lagrange multiplier in the bending free-energy, so that the complete membrane free energy is

$$\mathcal{F}_{mem}[\phi] = \mathcal{F}_b[\phi] + \frac{3}{2\sqrt{2}\epsilon}\int \gamma_A \epsilon^2 (\nabla\phi)^2 dV. \tag{5.26}$$

where γ_A represents the Lagrange multiplier for the area conservation. If the interface is small, then $|\nabla^2\phi_0|$ behaves as a δ-function,

$$\lim_{\epsilon\to 0} \frac{3}{4\sqrt{2}\epsilon}\text{sech}^4\left(\frac{x}{\epsilon\sqrt{2}}\right) = \delta(x), \tag{5.27}$$

and the volume integral converges to a surface integral over the interface, given by the coordinates x',

$$\frac{3}{2\sqrt{2}\epsilon}\int |\nabla\phi|^2 dV \xrightarrow{\epsilon\to 0} \int \delta(x-x')dV = \int dS. \tag{5.28}$$

Although the last term in (5.26) has the expression of a surface tension, note that γ_A is shape dependent and it varies with the deformation. The expressions of the chemical potential μ_{mem} and stress tensor σ^{mem} for the complete membrane model must be obtained.

Finally, it should be noted that a term ϕ^6 is present in (5.22). The system actually presents three equilibrium phases, $\phi_{eq} = 0, \pm 1$, evoking the case of amphiphilic systems, where often a third phase is introduced accounting for the presence of the lipid-rich domain (Gompper and Schick, 1994). Although the three phase description is actually more realistic (since it considers explicitly the presence of lipids), the two phase model described above is more consistent with the Helfrich theory, in the sense that it treats the membrane as a sheet characterized by its local curvature, disregarding the microstructure of the membrane. By means of a linear stability analysis, it can be shown that the phase $\phi_{eq} = 0$ is not macroscopically stable. Figure 6.3 A shows the form of the bulk potential f_b, with three equilibrium phases. The stability analysis reveals that the phase $\phi_{eq} = 0$ presents a different behaviour with respect to $\phi_{eq} = \pm 1$. The exact derivation requires of a detailed description, but we briefly outline the main steps here. Let us suppose a planar interface separating two of the stable phases. A sinusoidal small perturbation is introduced, $\phi_0 = \phi_{eq} + \xi e^{iqx}$, and one assumes that it will decay as $\phi = \phi_0 e^{rt}$, an ansatz generally valid in the linear regime $\xi q \ll 1$. Introducing these expressions in the model, the growth rate $r(q)$ is obtained, as shown Figure 6.3 B. If $r < 0$ the interface is stable and the system will decay to the initial planar interface. For $r > 0$ the system is unstable. Note that in these calculations an explicit time dependence is required, though it has not been presented yet. The time evolution is discussed in section 5.3 and we do not make here further comments on this, but let us concentrate on the stability of the system for each

equilibrium phase. The phases ± 1 are both stable for the entire range of wavelengths of the perturbation, $\lambda = 2\pi/q$. The phase $\phi_0 = 0$ is, however, stable for a short range $\lambda < \epsilon$. Thus, $\phi_{eq} = 0$ is not a thermodynamic stable phase and it can only be present as a microemulsion, and thus being irrelevant in our membrane description.

5.2.2 Generalized membrane model

The model presented in this Section corresponds to a symmetric homogeneous membrane. However, the phase-field methodology allows to extend the model to cover more complex membranes. Two cases are considered here: asymmetric membranes with a non zero spontaneous curvature that affects to the membrane balance, and multicomponent membranes in which the elastic properties vary along the membrane surface due to an inhomogeneous composition.

Asymmetric membranes

Cells often present asymmetric membrane composition, and benefit from the control of this property in a number of ways, such as the case of pearling and tubulation in the Golgi apparatus (Campelo and Hernández-Machado, 2007a, 2008). The phase-field free energy (5.22) can be modified in order to account for a membrane asymmetry, effectively captured in the Helfrich model by a positive spontaneous curvature, c_0. The resultant free-energy reads (Campelo and Hernández-Machado, 2007b)

$$\mathcal{F}_{SC} = \frac{\kappa^*}{2} \int \left[(-\phi + \phi^3 - \nabla^2 \phi) - \epsilon c_0^{\phi} (1 - \phi^2) \right]^2 dV. \tag{5.29}$$

The term $(1 - \phi^2)$ represents a δ-function centered at the interface position, so that the interface is forced to accomodate its surface to the spontaneous curvature $c_0 = c_0^{\phi}/\sqrt{2}$. In principle, this spontaneous curvature can be spatially inhomogeneous, $c_0(x)$.

Multicomponent vesicles

The different lipid species present in the membrane often pack forming monospecific aggregates, with important implications in the cell functioning as they are related with membrane trafficking and signaling (Simons and Vaz, 2004). The experiments carried out by Baumgart et al. (2003) with lipidic vesicles showed that the bilayer lipid composition can be controlled to form these aggregates, and

modulate the vesicle shape. Depending on the specific lipids of the domain, the vesicle presents inhomogeneous membrane properties. The morphology assumed by the vesicle responds to the balance of this particular membrane composition. The problem was theoretically approached by Wang and Du (2008), who developed a model in which both the bending rigidity and the spontaneous curvature depend on the local domain,

$$\mathcal{F}_{\Updownarrow\rfloor} = \int \frac{\kappa_i}{2}(C - c_{0,i})^2 dA + \oint \Gamma_i dl, \tag{5.30}$$

where i refers to the lipid species of the domain. The last term in (5.30) represents a line tension term accounting for the border between the different lipid domains. Wang and Du (2008) considered the problem of two coexistent species and introduced a phase field formulation based on two coupled order parameters, ϕ and η. The main field ϕ represented the vesicle surface, whilst the auxiliary field η formed a perpendicular surface to the vesicle, so that the regions where both surfaces superpose define the domain of one of the species. Furthermore, the parameter coefficients of the free energy of ϕ depend on the the field, $\kappa(\eta)$ and $c_0(\eta)$, with two constant values at $\eta = +1$ and $\eta = -1$ and a smooth transition in the interface. Thus, they propose a free energy of the form

$$\mathcal{F}^{\phi}_{mc} = \int \frac{\kappa(\eta)}{2}\left[(-\phi + \phi^3 - \nabla^2\phi) - \epsilon c_0(\eta)(1-\phi^2)\right]^2 dV + \Gamma \int l(\phi,\eta) dV, \tag{5.31}$$

and added the usual constraints of constant total area and volume for the order parameter ϕ. The functional $l(\phi, \eta)$ accounts for the line element of the frontiers of the lipid domains,

$$l(\phi,\eta) = L|\nabla\phi|^2|\nabla\eta|^2, \tag{5.32}$$

with normalization constant L. Minimization of (5.31) leads to the minimal shapes of the vesicle. The model nicely reproduces the shapes obtained in Baumgart et al. (2003), and highlights the subtle control of membrane shape mediated by the formation of local aggregates with suitable elastic properties.

Alternative membrane models

The model presented here exploits the balance of stresses along the smooth interface in order to obtain a tensionless membrane, whose only elastic contribution is then the bending. The goal of this approach is that the information of the

interface geometry (*eg* the local curvature) is intrinsically contained in the gradients of the order parameter, so that we only need to specify the dynamics of the order parameter and forget any other treatment of the surface membrane. A different approach has been proposed by Biben et al (Biben and Misbah, 2003; Biben et al., 2005). The basis of this model can be conceived as intermediate between phase-field and explicit methods. They proposed a bending free enegy of the form

$$\mathcal{F} = \frac{\kappa}{2} \int dV (\hat{C} - C_0)^2 \frac{|\nabla \phi|}{2}, \tag{5.33}$$

where $\hat{C}$ is the total curvature of each isosurface of constant ϕ. Thus, $\hat{C}$ is defined in the entire volume rather than in the membrane surface, albeit the presence of the delta-like function $|\nabla\phi|$ reduces the volume integral to a surface integral in the limit of thin interface, so that in this limit $\hat{C}(x)\delta(x - x_m) \to C$ at the membrane position x_m . The mean curvature is numerically computed from the normal vector to the isosurface, $\hat{C} = -\nabla \cdot \hat{n}$, where $\hat{n} = \nabla\phi/|\nabla\phi|$. Hence, although in this scheme the interface is not tracked either, the mean curvature must be specifically computed, implying a number of stability numerical problems that require of a very fine tuning of the model. For instance, $\nabla\phi \to 0$ in the bulk, given rise to numerical divergences of the normal vector far from the interface. This model of specific curvature calculation reproduces the desired elastic behaviour of the membrane, but it deviates from the original spirit of phase-field models.

5.3 Membrane dynamics and hydrodynamic coupling

The theory of Ginzburg-Landau provides a basis for the energetic characterization of membranes. However, the time dependence of the interface is obviously a critical ingredient in the modeling of the membrane phenomenology. In non-equilibrium dynamics it is usual to assume that, in absence of external forces, each small volume element is locally in thermodynamic equilibrium so that the whole system evolves towards a global equilibrium. In the case of membranes, the separation in time scales between the rearrangement and diffusion of lipids, $\sim 10^{-9}$s, and typical cell deformation times and mechanic response, $\sim 10^{-3}$s, ensures that the so-called local equilibrium approach applies correctly.

In the framework of the Cahn-Hilliard theory (Cahn and Hilliard, 1959), the dynamic evolution of the order parameters is dictated by a diffusive equation,

$$\frac{\partial \phi}{\partial t} = \nabla \cdot \left(M \nabla \frac{\delta \mathcal{F}_{mem}}{\delta \phi} \right). \tag{5.34}$$

It is not difficult to show that the total amount of order parameter is constant in the system. We will call this dynamic model simply phase-field model (PF). If the interface is locally in equilibrium, this implies that the total amount of each equilibrium phase is also constant. This remark is specially relevant in the present context, given that most membranes are impermeable (there is no transport of water through them) so, for closed systems such as cells, the conserved evolution ensures that the amount of fluid both inside and outside the cell frontiers remains constant, and the volume constraint of the Helfrich free energy (2.16) is directly fulfilled. Alternative models which consider a non-conserved dynamics, such as an Allen-Cahn dynamic equation (Du et al., 2004, 2005), explicitly introduce the volume conservation by adding the correspondent Lagrange multiplier.

The Cahn-Hilliard equation (5.34) dictates the dynamics of the interface but, in many systems, hydrodynamical effects of the aqueous enviroment are also crucial in the membrane evolution. A paradigmatic example is the study of red blood cells and lipid vesicles while flowing along capillaries forced by an external flow. To model the interaction of the membrane with the surrounding fluid, it is usual to incorporate the Navier-Stokes equation to describe the dynamics of the fluid, and both equations are coupled describing the interaction membrane-fluid. The complete Navier-Stokes phase-field model (NS-PF) is

$$\frac{\partial \phi}{\partial t} + \mathbf{v} \cdot \nabla \phi = M \nabla^2 \mu_{mem}. \tag{5.35}$$

$$\rho \left[\frac{\partial \mathbf{v}}{\partial t} + (\mathbf{v} \cdot \nabla \mathbf{v}) \right] = -\nabla P + \mathbf{f_{mem}} + \eta \nabla^2 \mathbf{v} + \mathbf{f_{ext}}. \tag{5.36}$$

where $\mathbf{f_{ext}}$ is an external forcing driving the flow, such as a pressure difference $(\Delta P)/L$ between the edges of a channel of length L, or a gravity force $\rho \mathbf{g}$. The advection term $\mathbf{v} \cdot \nabla \phi$ in (5.35) describes how the fluid pushes the membrane, and the response exerted by the membrane is given by the force density $\mathbf{f_{mem}}$, which affects to the surrounding fluid. The elastic force density $\mathbf{f_{mem}}$ is obtained from the divergence of the stress tensor (5.8),

$$\mathbf{f_{mem}} = \nabla \cdot \sigma_{\mathbf{mem}} = -\phi \nabla \mu_{mem}. \tag{5.37}$$

The complexity of these equations and the geometries that are usually studied in membrane problems avoid an analytic integration of the model, and thefore numerical methods are required. The Navier-Stokes equation can be integrated by

different methods which must incorporate the coupling with the order parameter. Among others, new hybrid formulations have been developed for immerse boundary methods (Du and Li, 2011; Shao et al., 2013) and lattice-Boltzman method (Kendon et al., 2001).

5.4 Macroscopic equations

The validity of a diffuse-interface mesoscopic model is justified as long as it recovers the correct macroscopic equations in the limit $\epsilon \to 0$, the so-called sharp-interface limit. This procedure has been extensively applied in phase-field models to obtain the set of equations that describe the dynamics of the interface (Folch et al., 1999; Biben et al., 2005), allowing the study of some important interfacial behaviour such as the Saffman-Taylor instability (Hernández-Machado et al., 2003). The scope of this Section is to characterize the macroscopic equations of the model that enable us to study of membrane elasticity by means of a linear stability analysis.

5.4.1 Sharp-interface limit

The sharp-interface limit consists in considering a macroscopic length scale, much larger than ϵ, and derive the equations dependent of the macroscopic variables, such as the total curvature of the interface, from the mesoscopic dynamic equation for the order parameter. It is a singular limit, as ϵ must be small but strictly nonzero. We first focus on the dynamic equation of the order parameter without hydrodynamic coupling, (5.34), which accounts for the dynamics of a membrane immersed in a diffusive medium, such as gel. We then discuss the application to the complete NS-PF model in which membrane dynamics is critically influenced by the hydrodynamics of the flows generated around the membrane.

We only outline the sharp-interface limit here, but further details of the method can be found in Appendix B. The space is separated into two regions, the (macroscopic) outer region, and the (microscopic) inner region of the interface. Both regions are described by the coordinates r and ω, respectively, related by $r = \omega/\epsilon$. Thus, the *fast* coordinate in the inner region allows to resolve the details of the interface. In the macroscopic scale, the interface is sharp and then $\epsilon \to 0$. The starting point is a flat interface in equilibrium, subjected to a weak perturbation. The interface is characterized by the general interface (5.1). The interface must be symmetric, $c_0 = 0$, so that the flat interface represents an equilibrium configuration; for strictly nonsymmetric interfaces the method should perturb an equilibrium configuration, such as a spherical membrane of radius $1/c_0$, requiring

a more complex analytical treatment. Once the fast coordinates are introduced, as explained in Appendix B, the dynamic equation reads

$$\epsilon\partial_\tau\phi - \frac{1}{\epsilon}v\partial_\omega\phi = M\left(\frac{1}{\epsilon^2}\partial_\omega^2 - \frac{C}{\epsilon}\partial_\omega + \partial_s^2 + \partial_u^2\right)\mu. \tag{5.38}$$

Membrane equilibrium equation

The sharp-interface limit allows the derivation of the macroscopic equilibrium equation for the membrane, imposing the condition $\mu = const.$ (Note that this condition directly gives $v = 0$ in (5.38). The problem reduces then to the determination of this constant in terms of the macroscopic variables. The starting point is a flat interface in equilibrium subjected to a weak perturbation. The phase-field profile of the perturbed interface can be expanded, $\phi = \phi_0 + \epsilon\phi_1 + \epsilon^2\phi_2 + ...$, where ϕ_0 is the equilibrium profile. The chemical potential can be analogously expanded, accounting for the expanded differential operators (see Appendix B), leading to

$$\begin{gathered}\mu_0 = f_0^{'} - g_0^{'}(\partial_\omega\phi_0)^2 - 2g_0\partial_\omega^2\phi_0 + 2c\partial_\omega^2\phi_0. \\ \mu_1 = f_1^{'} - g_1^{'}(\partial_\omega\phi_0)^2 - 2g_1\partial_\omega^2\phi_0 + 2Cg_0\partial_\omega\phi_0 - 2g_0\partial_\omega^2\phi_1 \\ +2c\partial_\omega^4\phi_1 - 4cC\partial_\omega^3\phi_0. \\ ...\end{gathered} \tag{5.39}$$

where $f' = \partial f/\partial\phi$ and $f_0 = f(\phi_0)$. The equilibrium value, $\mu_0 = 0$ provides the equilibrium phases ϕ_{eq} and defines the equation for ϕ_0. The next contribution μ_1 is non zero, and its value is evaluated by multiplying by $\partial_\omega\phi_0$ and integrating over the normal direction,

$$\begin{aligned}\mu_1\int_{-\infty}^{+\infty} d\omega\partial_\omega\phi_0 = \int_{-\infty}^{+\infty} d\omega[f_1^{'} - g_1^{'}(\partial_\omega\phi_0)^2 - 2g_1\partial_\omega^2\phi_0 + 2Cg_0\partial_\omega\phi_0 - 2g_0\partial_\omega^2\phi_1 \\ + 2c\partial_\omega^4\phi_1 - 4cC\partial_\omega^3\phi_0]\partial_\omega\phi_0.\end{aligned} \tag{5.40}$$

The right hand side of this expression includes terms depending solely on ϕ_0 whereas others also depend on ϕ_1. We focus first on the later. By using the relation $m_1^{'} = m_0^{''}\phi_1$ for any polinomial function m, (5.40) can be rewritten into

$$\mu_1 \int_{-\infty}^{+\infty} d\omega \partial_\omega \phi_0 = \int_{-\infty}^{+\infty} d\omega \partial_\omega \phi_0 [f_0'' - g_0''(\partial_\omega \phi_0)^2 - 2g_0'' \partial_\omega^2 \phi_0 - 2g_0' \partial_\omega^2 + 2c\partial_\omega^4]\phi_1 + \int_{-\infty}^{+\infty} d\omega \partial_\omega \phi_0 [2Cg_0 \partial_\omega \phi_0 - 4cC\partial_\omega^3 \phi_0]. \tag{5.41}$$

Let us consider now the expression for μ_0. Applying the operator ∂_ω, we obtain the equation

$$[f_0'' - g_0''(\partial_\omega \phi_0) - 2g_0'' \partial_\omega - 2g_0' \partial_\omega + 2c\partial_\omega^3] \partial_\omega \phi_0 = 0. \tag{5.42}$$

Thus, $\partial_\omega \phi_0$, known as Goldstone mode and related to the translational invariance of the interface, is an eigenvector of the linear operator in brackets in (5.42). Integrating by parts (5.41) and introducing (5.42), the term associated to ϕ_1 vanishes and then (5.40) reduces to

$$\mu_1 \int_{-\infty}^{+\infty} d\omega \partial_\omega \phi_0 = \int_{-\infty}^{+\infty} d\omega [2Cg_0 (\partial_\omega \phi_0)^2 - 4cC\partial_\omega^3 \phi_0 \partial_\omega \phi_0]. \tag{5.43}$$

Integrating by parts, this equation reads

$$\mu_1 \Delta\phi_{eq} = C \int_{-\infty}^{+\infty} d\omega s_\phi(\omega), \tag{5.44}$$

where we have introduced the lateral stress profile (5.20), and $\Delta\phi_{eq}$ is the gap between the two bulk phases. The left hand side of this equation can be rewritten in terms of the pressure, given that in the macroscopic scale $p_1(0) = \phi_{eq}\mu_1(0)$. In the right hand side, the expression of the surface tension (5.19) can be identified, leading to

$$\Delta p_1 = \gamma C, \tag{5.45}$$

which corresponds to the Young-Laplace equation that provides the pressure difference sustained across the interface.

By means of this procedure, the subsequent terms of the chemical potential can be evaluated, providing high-order contributions to the pressure difference. The explicit calculations are simple but long, and only the main steps are shown here. By using the equation $\partial_w \mu_1 = 0$ as with the Goldstone mode, evaluation of μ_2 reduces to:

$$\mu_2 \int_{-\infty}^{+\infty} d\omega \partial_\omega \phi_0 = (C^2 - 2G) \int_{-\infty}^{+\infty} d\omega \omega [2g_0 (\partial_\omega \phi_0)^2 - 4c \partial_\omega^3 \phi_0 \partial_\omega \phi_0]. \tag{5.46}$$

The term of the right hand side of this expression vanishes, since $s(\omega)$ is stricly symmetric. The term Δp_2 corresponds to the pressure contribution of the spontaneous curvature and accordingly it vanishes for a symmetric membrane. From the algebraic calculations shown in Appendix B, and considering the final expression (B.20), the subsequent term is given by

$$\begin{aligned} \mu_3 \int_{-\infty}^{+\infty} d\omega \partial_\omega \phi_0 = (C^3 - 3GC) \int_{-\infty}^{+\infty} d\omega \omega^2 [2g_0 (\partial_\omega \phi_0)^2 - 4c \partial_\omega^3 \phi_0 \partial_\omega \phi_0] \\ - \Delta_s C \int_{-\infty}^{+\infty} d\omega 2c (\partial_\omega \phi_0)^2 - \frac{1}{2} C (C^2 - 4G) \int_{-\infty}^{+\infty} d\omega 2c (\partial_\omega \phi_0)^2. \end{aligned} \tag{5.47}$$

The first term in the right hand side of (5.47) vanishes due to the symmetry of the equilibrium profile, and identifying the bending rigidity from (5.19), we obtain

$$\Delta p_3 = -\frac{1}{2} \kappa C (C^2 - 4G) - \kappa \Delta_s C. \tag{5.48}$$

Considering all the contributions and disregarding for simplicity the term associated to the Gaussian curvature modulus, the macroscopic equation is

$$\Delta p = \Delta p_0 + \epsilon \Delta p_1 + ... = \gamma C - \frac{1}{2} \kappa C (C^2 - 4G) - \kappa \Delta_s C. \tag{5.49}$$

This equation corresponds to the equilibrium equation for a symmetric membrane, as first derived by Ou-Yang and Helfrich (1987).

Dynamic equations

In the previous section we restrict our analysis to the situation of equilibrium, without considering the dynamics described by equation (5.34). The sharp-interface limit can be extended to this more general case, providing the macroscopic equations that describe the dynamic behaviour of the interface. The derivation of the complete dynamic model is necessary to study, among others, the stability and relaxational properties of the interface.

Following the formalism presented in the previous section, the space is separated in two domains, the inner corresponding to the interfacial region and the

outer, which corresponds to the bulk. The variables of equation (5.34) are expanded in terms of ϵ. In the **inner region**, the order ϵ^{-2} is given by $\partial_\omega^2 \mu_0 = 0$, and hence $\mu_0 = m_0 + n_0\omega$. Since μ_0 must be finite in the limit $\omega \to \pm\infty$, n_0 vanishes and we fix $\mu_0 = 0$. The dynamic equation at order ϵ^{-1} reads

$$-v_0 \partial_\omega \phi_0 = M \partial_\omega^2 \mu_1. \tag{5.50}$$

Integrating this equation accross the interface profile,

$$\partial_\omega \mu_1(+\infty) - \partial_\omega \mu_1(-\infty) = -v_0 \Delta\phi_{eq}. \tag{5.51}$$

Note that v represents the interface velocity, so that in the inner region it is constant by definition. Introducing the matching condition $\partial_\omega \mu_1(\pm\infty) = \partial_r \mu_0(\pm 0) = 0$ and we obtain $v_0 = 0$. We found that μ_1 is a constant that can be evaluated in the same manner than in the previous section. The subsequent order, ϵ^0, is given by

$$-v_1 \partial_\omega \phi_0 = M(\partial_\omega^2 \mu_2 - C \partial_\omega \mu_1 \partial_s^2 \mu_0). \tag{5.52}$$

Integration by parts and application of the matching conditions lead to

$$-\Delta\phi_{eq} v_1 = M(\partial_\omega \mu_2(+\infty) - \partial_\omega \mu_2(-\infty)) = M(\partial_\omega \mu_1(+0) - \partial_\omega \mu_1(-0)). \tag{5.53}$$

Considering $|\phi_{eq}| = 1$ and introducing the permeability $B = M/(2|\phi_{eq}|^2)$, this expression can be rewritten,

$$v = -B(\nabla p^+ + \nabla p^-). \tag{5.54}$$

This is the continuity equation that describes the interface velocity as a function of the pressure gradients at the interface.

In the **outer region**, at first order $\mu_0 = 0$ due to the matching conditions with the inner region. The subsequent order, however, is given by $\nabla^2 \mu_1 = 0$ which can be rewritten us $\nabla^2 p = 0$. This expression represents the Laplace equation in the bulk.

Taking into account the three equations obtained, the complete macroscopic model reads

$$\begin{aligned} \Delta p &= \gamma C - (1/2)\kappa C(C^2 - 4G) - \kappa \Delta_s C, \\ v &= -B(\nabla p^+ + \nabla p^-), \\ \nabla^2 p &= 0. \end{aligned} \tag{5.55}$$

Some remarks should be pointed out here. Although we have included the equilibrium equation (5.49) for completeness, the sharp interface limit specifies that the dynamics is dominated by the first contribution to the pressure difference. Thus, if the interface has a nonzero surface tension, its dynamics will be generally dictated by surface tension. For tensionless interfaces, in which the first non-vanishing term is Δp_3, bending governs the dynamics of the interface.

5.5 Linear stability analysis

The macroscopic model (5.55) describes the dynamics of the membrane for the PF model. In deterministic dynamics, a linear stability analysis can be performed to obtain information of the properties and relaxational behaviour of the membrane, analogous to the study of the fluctuation spectrum in stochastic systems, as stated by the Onsager's theory of linear relaxation processes. We perform a linear stability analysis to study the response of a flat interface in equilibrium when subjected to a sinusoidal perturbation (Hernández-Machado and Jasnow, 1988). The relaxational time of the membrane is calculated, and the method is applied to measure the elastic properties of the membrane. The flat interface is weakly perturbed, and the membrane position is then given by $y = h(x,t) = \xi_0 e^{iqx+\omega t}$, where h is the distance of the membrane with respect to the equilibrium position, q is the wavelength of the perturbation and ω is the relaxation rate. If $\omega > 0$, the perturbation will grow and the membrane is unstable; if $\omega < 0$, the membrane is stable and it recovers the initial configuration in a typical relaxation time $1/\omega$. For the pressure field we assume the ansatz $p = p_0 + Ae^{iqx+ky+\omega t}$, where $1/k$ is the distance from the interface in which the pressure converges to the bulk value. For sufficiently small amplitudes, the curvature of the interface can expressed as $C \approx -\partial_x^2 \xi = q^2 \xi$. Finally, the velocity of the interface is given by $v = \partial_t h$. Introducing all these considerations into equation (5.55), we find

$$\begin{aligned} A &= (\gamma q^2 + \kappa q^4)\xi, \\ \omega \xi &= -BA2k, \\ 0 &= -q^2 + k^2. \end{aligned} \tag{5.56}$$

And from here, the dispersion relation is obtained

$$\omega_\phi(q) = -2B|q|(\gamma q^2 + \kappa q^4). \tag{5.57}$$

where we have introduced $\omega_\phi = \omega$ to specify that this result corresponds to the PF model, (5.34). This represents the relaxational rate for a membrane in a diffusive medium, such as a gel. In the case of a membrane surrounded by a liquid, when the fluxes generated by the membrane movement affect the dynamics of the own membrane, we must solve the complete NS-PF model. The derivation of the macroscopic model of the NS-PF model is complex, but we can assume that the dispersion relation in this case should correspond to the general expression (2.27) (Theissen et al., 1998). For a flat membrane the term associated to volume conservation is not present and the relaxation rate, ω_η, reads

$$\omega_\eta(q) = -\frac{1}{4\eta}(\gamma q + \kappa q^3). \tag{5.58}$$

In order to validate the complete NS-PF model, and confirm that it captures the correct membrane dynamics given by expression (5.58), we numerically study the relaxation of an interface. The numerical method is described in detail in Chapter 6, but we include this Section here for completeness. The procedure is analogous to the derivation outlined above. A flat interface is perturbed with an initial sinusoidal profile $h(x, 0)$. The interface position $h(x, t)$ is tracked during the evolution and, from here, the relaxation rate ω_η can be easily obtained. The initial amplitude must be small compared to the wavelength of the perturbation, $q\xi \ll 1$. In Figure 5.3 we show the dispersion relation for interfaces dominated by surface tension and bending (membranes), comparing the results for the PF model, given by (5.57), and the NS-PF model, (5.58). In these simulations, the size of the box is maintained constant but sweeping along and extensive range of q; we fix the reference mode q_0 as that corresponding to the domain length (*ie* the minimum q studied). The relaxation rates are normalized by the relevant relaxation rate w_0 of the mode q_0; for instance, for the PF model of surface tension, $\omega_0 = 2B\gamma q_0^3$, and analogously for the other three cases. The dimensionless curves obtained are therefore universal for each model and type of interface. The models reproduce the expected behaviour, though we observe a certain deviation from the theoretical prediction for the longest modes. This is likely related with the penetration length of the perturbation, $1/k$, which scales linearly with the wavelength $\lambda = 2\pi/q$, so that the interface effectively interacts with the boundaries of the system in the limit of low q. By fitting the numerical results to the relaxation rate predicted by the linear theory, the effective elastic modulii of each interface can be obtained. Our results show a relatively good accuracy, considering that finite-system effects are present, obtaining $\gamma_\phi/\gamma_{th} = 1.02$ and $\kappa_\eta/\kappa_{th} = 0.88$ for the PF model, and $\gamma_\eta/\gamma_{th} = 1.17$ and $\kappa_\eta/\kappa_{th} = 0.85$ for the NS-PF model. In these expressions the subscript th indicates the theoretical value of the elastic modulus.

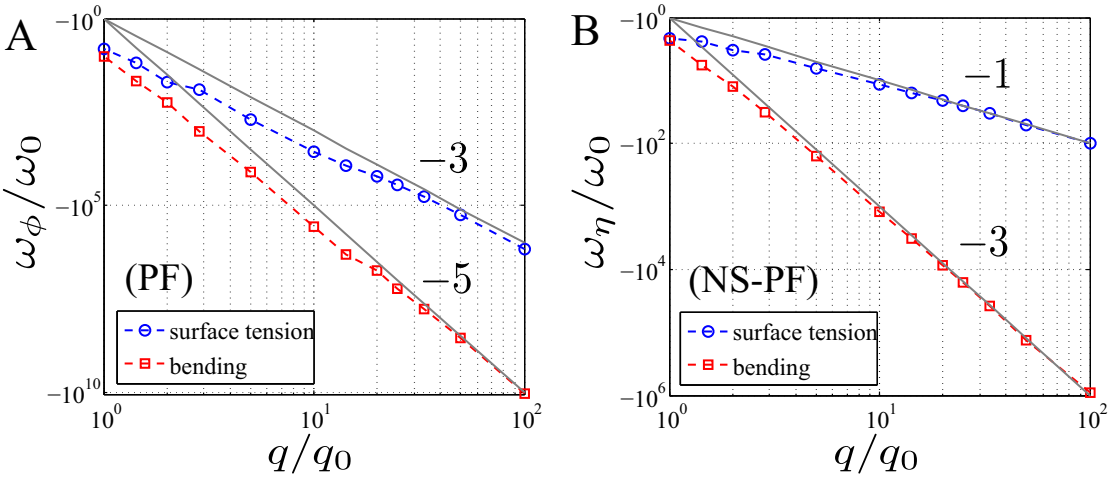

Figure 5.3: Dispersion relation for interfaces dominated by surface tension and bending (membranes), in the PF (A) and NS-PF (B) models. The simulations are perfomed in a box of constant dimensions, and hence q_0 represents the lowest mode. w_0 corresponds to the relaxation rate of the mode q_0 for each case; *eg* for the PF model of surface tension, $\omega_0 = 2B\gamma q_0^3$, and analogously for the other three cases. Bold grey lines correspond to the theoretical prediction for the relaxation rate given by expressions (5.57) and (5.58), respectively. Both models agree with the theoretical prediction, though the curves deviate at low q, probably as a consequence of a finite-system effect (see main text). The fitting of the numerical results to the theoretical curves provides a measure of the effective value of the elastic parameters. We obtain $\gamma_\phi/\gamma_{th} = 1.02$ and $\kappa_\eta/\kappa_{th} = 0.88$ for the PF model, and $\gamma_\eta/\gamma_{th} = 1.17$ and $\kappa_\eta/\kappa_{th} = 0.85$ for the NS-PF model.

5.6 Conclusions

Based on the Helfrich theoretical framework, we have presented the phase-field formalism as a powerful tool for approaching complex phenomena related with dynamics and morphology of biological membranes. Phase field models have been applied to the study of different interface problems, but only recently for membrane modeling. The phase-field theory makes use of an order parameter which has two stable phases, and the interface connects both phase domains by a smooth profile. Thereby, one needs to solve the dynamics of the field, avoiding the complex treatment of the moving boundary condition of the interface.

We have shown the link of the phase-field model with the elastic theory of membranes, providing a flexible methodology for the study of membranes with different properties. The membrane model presented here effectively describes the internal stresses of the membrane, which in turn determine their elastic properties. Phase-field methods allow a fine tuning of the interface properties, as demonstrated in this Chapter, a basic property when dealing with membranes given the particular elastic characteristics of these structures. The phase-field can be coupled to a velocity field describing the hydrodynamics of the surrounding

fluid, since in many situations hydrodynamics plays a critical role in membrane dynamics.

The robust physical basis of the method allows to derive the general equilibrium equation of lipidic membranes. The study of the relaxational behaviour of a flat membrane, analogous to the study of the fluctuation spectrum in real membranes, serves to validate the model. This procedure can be applied in the future to study membrane fluctuations in more complex geometries, offering an interesting method for exploring the interplay between geometry and elasticity.

Chapter 6

Numerical scheme

In the previous Chapter we have introduced the basis of the phase-field methods for the physical representation of amphiphilic membranes. Equations (5.35) and (5.36) are generally impossible to solve analytically and numerical methods must be invoked. Since, in general, at the membrane and cell scale the Reynolds member is usually $\sim 10^{-3} - 10^{-2}$, models often consider the Stokes equation. In our case, however, we integrate the complete Navier-Stokes equation by means of a lattice-Bolztmann method (LBM), a discretized version of the Bolztmann equation. It is well known that in the hydrodynamic limit, the macroscopic equations derived from the Bolztmann equation recover the conservation equations for the continuous hydrodynamic fields. The convergence of the Bolztmann equation to the Navier-Stokes equation can be proven by a Chapman-Enskog expansion (Duenweg and Ladd, 2009). The LBM makes use of this fact to perform numerical integrations of the discretized Bolztmann equation, and then the macroscopic fields are recovered. LBM is a fast and robust numerical method for fluid dynamics (Ladd and Verberg, 2001) which has been used in many soft matter systems and complex fluids (Cates et al., 2009, 2005; Benzi et al., 2009; Gonnella et al., 1997). Our model extends the classic LBM to incorporate the phase-field method (Kendon et al., 2001).

6.1 Lattice-Boltzmann method

The Bolztmann theory assumes that the hydrodynamic variables like the density or the momentum depend on a set of distribution functions of the velocity. The dynamics of these distribution functions is dictated by the Boltzmann equation, and they should obey the conservation laws of the system such as mass or momentum conservation. Hereafter, we concentrate on the discrete formulation of this theory, the lattice-Boltzmann method (Succi, 2001).

6.1.1 Single-relaxation time lattice-Boltzmann

In the lattice-Bolztmann scheme, the space is discretized in a lattice, and the nodes are connected by the velocity vectors c_i. The time is also discretized, so that the velocity distribution functions are $f_i(\mathbf{x}, t)$. The evolution of this function is given by the single relaxation time (Bhatnagar et al., 1954) model,

$$f_i(\mathbf{x} + \mathbf{c_i}, t + 1) - f_i(\mathbf{x}, t) = -\frac{1}{\tau}(f_i - f_i^{eq}) + F_i. \tag{6.1}$$

The dynamics of the distribution function f can be separated in two steps. The right hand side of the equation represents a collision step in which the function relaxes to the equilibrium one, in a time scale given by τ. The left hand side of (6.1) represents the propagation of the distribution function to the neighbour nodes. The term F_i represents an external forcing, such as a pressure difference or the gravity. The hydrodynamic variables (density and momentum) are recovered from the distribution functions by

$$\begin{array}{c} \sum_i f_i = \rho. \\ \sum_i f_i \mathbf{c_i} = \rho \mathbf{v}. \end{array} \tag{6.2}$$

The conservation laws enforce that the equilibrium distributions should obey

$$\begin{array}{c} \sum_i f_i^{eq} = \rho. \\ \sum_i f_i^{eq} \mathbf{c_i} = \rho \mathbf{v}. \end{array} \tag{6.3}$$

And the stress tensor $\bar{\bar{\sigma}}$, where we use this notation here for the sake of clarity, is defined from the equilibrium distributions as

$$\sum_i f_i^{eq} \mathbf{c_i} \mathbf{c_i} = \rho \mathbf{v}\mathbf{v} + \bar{\bar{\sigma}}. \tag{6.4}$$

The velocities c_i connect with the neighbour nodes but we need to specify the particular velocity subset. We use the D3Q19 model (Desplat et al., 2001) which includes 1 velocity of modulus $c = 0$, 6 of velocity $c = 1$ and 12 of $c = \sqrt{2}$. So far, the expression of the distribution function has not been specified. They are calculated as a expansion in terms of $\mathbf{v}$,

$$f_i^{eq} = \rho \omega_\nu \left(\mathbf{1} + \frac{1}{c_s^2} \mathbf{v} \cdot \mathbf{c_i} + \frac{1}{2c_s^4} \bar{\mathbf{v}\mathbf{v}} : \mathbf{c_i} \mathbf{c_i} \right), \tag{6.5}$$

where we have introduced the tensor $\bar{\mathbf{v}\mathbf{v}} = \mathbf{v}\mathbf{v} - (u^2/3)\mathbf{v}$, ν specifies the velocity subset and the weights ω_ν are constants of the model. For the D3Q19 model ν=0,

1, and $\sqrt{2}$, and $\omega_\nu = 12/36, 2/36$, and $1/36$, respectively, and $c_s = 1/3$ is the speed of sound. Analogously, the external forcing term,

$$F_i = 4\omega_\nu \left(1 - \frac{1}{2\tau}\right) [\mathbf{f_{ext}} \cdot \mathbf{c_i} + \mathbf{v} \cdot \mathbf{c_i} - \mathbf{v} \cdot \mathbf{f_{ext}}], \tag{6.6}$$

where $\mathbf{f_{ext}}$ is the external forcing vector. Finally, the viscosity is related with the relaxational time by $\eta = (2\tau - 1)/6$.

6.1.2 Boundary conditions

It is obvious that boundaries are crucial if one is studying the behaviour of RBCs and vesicles while flowing through thin capillaries. We impose the stick condition (*ie* zero fluid velocity at the interface) by means of the bounce-back method developed by Ladd (1994). The method consists in reflecting the distribution functions on the solid nodes that come from the fluid after each propagation step. This formulation implies that the distribution function is bounce backed to the fluid node instead of been absorbed by the solid (wall) node, and the zero velocity condition is achieved at the middle point between the fluid and solid nodes (Stratford and Pagonabarraga, 2008).

In this Thesis, we perform two-dimensional simulations, fixing $L_y = 1$. The solid boundaries are placed in the $\hat{x}$ direction, so that the principal fluid direction is $\hat{z}$. We thus apply periodic boundary conditions in the $\hat{z}$ direction.

6.2 Phase-field integration

The advection-diffusion equation that dictates the dynamics of the order parameter is solved by a simple finite-element method,

$$(\phi(\mathbf{x}, t+1) - \phi(\mathbf{x}, t))/\Delta t = -\mathbf{v}(\mathbf{x}, t) \cdot \nabla\phi + M\nabla^2\mu(\mathbf{x}, t). \tag{6.7}$$

Both the implementation of the advective term and the discrete calculation of the different derivatives are detailed below.

6.2.1 Advection

The advection term propagates the order parameter with the fluid fluxes. In a discrete scheme, this propagation is however affected by numerical dissipation, which occurs for wavelengths q lower than $2\pi/\Delta x$, where Δx is the spatial grid

unit. For this reason, it is convenient to use a specific technique to minimize numerical dissipation, such as the upwind-biased schemes which haven proven to be very robust (Li, 1997). The advection term $v \cdot \nabla\phi$ is calculated from the gradients of ϕ given by

$$\begin{aligned} \partial_j\phi &= \frac{1}{\Delta x}\left(\sum_{n=1}^{N} a_{-n}\phi_{j-n} + a_0\phi_j + \sum_{n=1}^{N} a_n\phi_{j-n}\right); \quad v_j > 0. \\ \partial_j\phi &= \frac{1}{\Delta x}\left(\sum_{n=1}^{N} a_{n}\phi_{j-n} + a_0\phi_j + \sum_{n=1}^{N} a_{-n}\phi_{j-n}\right); \quad v_j < 0. \end{aligned} \tag{6.8}$$

N is the order of the scheme, depending on the precission required. We use a third-order upwind sheme, N=2. The parameters $a_{N=2}$ are then adjusted to minimize the dissipation, $a_0 = 0.927865, a_2 = -0.213933$ and $a_{-2} = 0.286067$.

6.2.2 Derivative calculations

For computing the different derivatives of the order parameter and the chemical potential, we make use of the velocity set geometry c_i instead of the usual discrete expressions. Let us consider the order parameter at some node of the lattice at the position $\mathbf{x}$. Assuming smooth spatial variations in ϕ, it can be expanded in a Fourier series

$$\phi(\mathbf{x}+\mathbf{c_i}) = \phi(\mathbf{x}) + \nabla_\alpha\phi(\mathbf{x})\mathbf{c_i}^\alpha + \frac{1}{2}\nabla_\alpha\nabla_\beta\phi(\mathbf{x})\mathbf{c_i}^\alpha\mathbf{c_i}^\beta + \mathcal{O}(\nabla^3\phi). \tag{6.9}$$

Multipliying this expression by c_i^α and suming over all the neighbours,

$$\sum_i \phi(\mathbf{x}+\mathbf{c_i})\mathbf{c_i}^\alpha = \nabla_\alpha\phi(\mathbf{x})\sum_i \mathbf{c_i}^\alpha\mathbf{c_i}^\alpha + \mathcal{O}(\nabla^3\phi). \tag{6.10}$$

where we have made use of the symmetry conditions

$$\begin{aligned} \textstyle\sum_i \mathbf{c_i}^\alpha &= 0, \\ \textstyle\sum_i \mathbf{c_i}^\alpha\mathbf{c_i}^\alpha\mathbf{c_i}^\beta &= 0. \end{aligned} \tag{6.11}$$

The expression of the gradients yields

$$\nabla_\alpha\phi(\mathbf{x}) = \frac{\sum_i \phi(\mathbf{x}+\mathbf{c_i})\mathbf{c_i}^\alpha}{\sum_i \mathbf{c_i}^\alpha\mathbf{c_i}^\alpha}. \tag{6.12}$$

Applying the same symmetry argument, if equation (6.9) is directly sumed over all the neighbours, the laplacian reads

$$\nabla^2\phi(\mathbf{x}) = \frac{2\left(\sum_i \phi(\mathbf{x}+\mathbf{c_i}) - N_i\phi(\mathbf{x})\right)}{\sum_i \mathbf{c_i^\alpha c_i^\alpha}}. \tag{6.13}$$

where N_i is the number of velocities, *eg.* $N_i = 19$ in the D3Q19 model.

6.2.3 Area conservation

In the previous Chapter, we explained that the area conservation can be modelled by introducing a Lagrange multiplier in the free-energy. The area is computed from the square of the gradient of the order parameter,

$$A = \frac{3}{4\sqrt{2}\epsilon}\int |\nabla\phi|^2 dV. \tag{6.14}$$

However, one needs to calculate the value of the multiplier that ensures that the area will be maintained constant. This problem can be solved by several methods but here we study two: (1) the strictly imposed condition in the phase-field equation; (2) an effective method which penalyzes deviations from a reference area.

Strict constraint

We shall consider the dynamic equation of the order parameter,

$$\partial_t\phi = \mathbf{v}\cdot\nabla\phi + M\nabla^2[\mu_0 - \gamma\nabla^2\phi] \tag{6.15}$$

where μ_0 is the chemical potential of bending, (5.24). Applying the gradient operator over both sides of the equation and multiplying by $\nabla\phi$,

$$\nabla\phi\cdot\partial_t(\nabla\phi) = \nabla\phi\cdot\nabla(\mathbf{v}\cdot\nabla\phi) + M\nabla\phi\cdot\nabla\nabla^2[\mu_0 - \gamma\nabla^2\phi] \tag{6.16}$$

But, in this expression the first term can be rewritten as $\nabla\phi\cdot\partial_t(\nabla\phi) = (1/2)\partial_t|\nabla\phi|^2$. Hence, given that we want to maintain a constant area $\partial_t A = 0$, integrating over the complete domain and introducing the last relation, one directly obtains

$$\gamma = \frac{\int\left(-\nabla\phi\cdot\nabla(\mathbf{v}\cdot\nabla\phi) + M\nabla\phi\cdot\nabla\nabla^2\mu_0\right)dV}{M\int\nabla\phi\cdot\nabla\nabla^4\phi dV}. \tag{6.17}$$

This method ensures minute deviations from the initial one, $\Delta A/A_0 < 10^{-7}$, but it has an expensive numerical cost as it requires computations of high order derivatives.

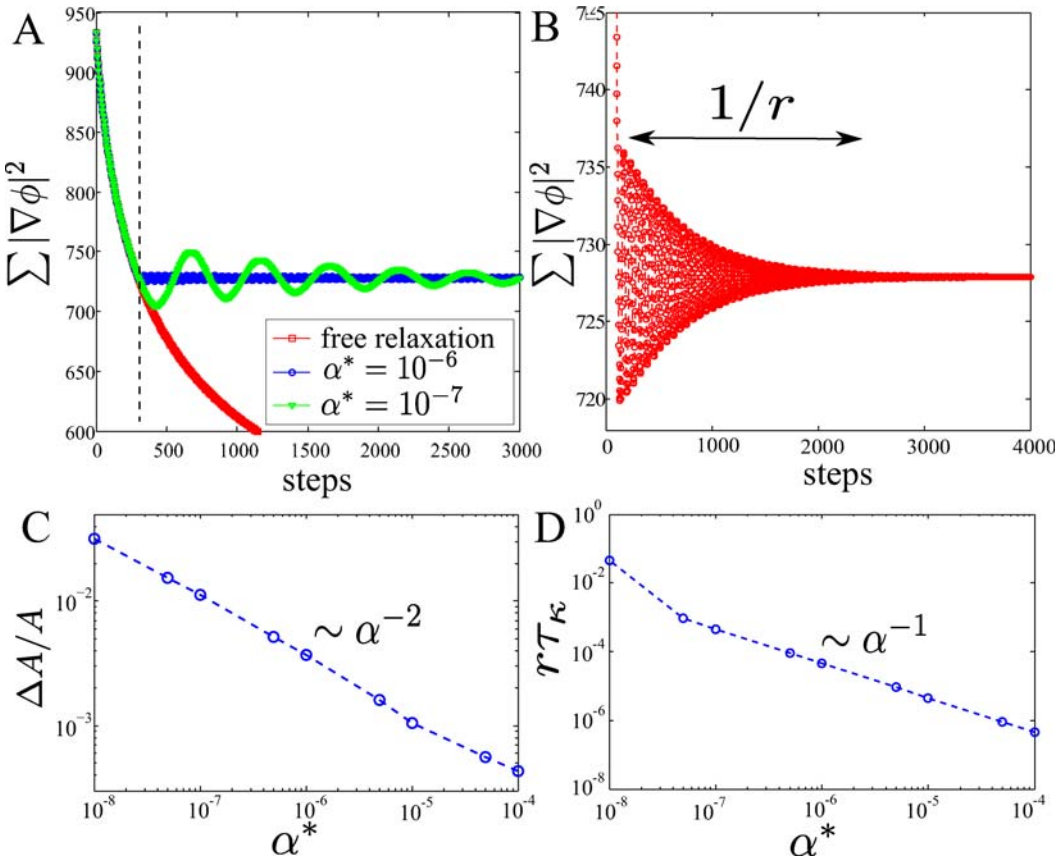

Figure 6.1: (A) Evolution of the total gradient square of order parameter for two values of α, the parameter that defines the dynamics of the Lagrange multiplier. The initial condition is a rectangle and it is allowed to relax during the first 300 steps before the Lagrange multiplier is switched on. α controls the amplitude of the oscilations around the reference value, as well as the timescale of the oscillations decay. The profile can be fitted to a curve of the form $\Delta A(t) = A(t) - A_0 = (\Delta A_0)e^{-rt+i\omega t}$, where we use A because the $|\nabla\phi|^2$ is related to the surface area, as given by (5.28). Here, A_0 is proportional to the desired area reference value. (B) Example of the oscillation decay, in a timescale given by $1/r$. (C) Dependence of the oscillation amplitude ΔA with α. Oscillations are attenuated by higher values of this parameter, showing a exponential dependence of the form $\sim \alpha^2$. (D) Dependence of the decay rate k with α, showing a $\sim \alpha^{-1}$ behaviour. The curve demonstrates that $1/\alpha$ represents the time scale in which the area converges to the reference value.

Penalty approach

An effective way of conserving area is by penalizing the deviations from a certain reference area A_0. This can be performed by introducing the following dynamic equation for the multiplier evolution:

$$\frac{\partial \gamma}{\partial t} = \alpha(A(t) - A_0) \tag{6.18}$$

The parameter α controls the dynamics of the Lagrange multiplier and the precision of the fixed constraint. We perform a simple test in order to understand its behaviour and comparison with the strict constraint, as shown in Figure 6.1. The initial condition is a square domain Ω in two dimensions, so that we initialize $\phi(x) = 1$ if $x \in \Omega$ and $\phi(x) = -1$ otherwise. The order parameter evolves freely during the first t_0 =300 steps, and afterwards the Lagrange multiplier is switched on. We analyze the evolution of the magnitude $|\nabla\phi|^2$, integrated over the whole domain, which is the conserved quantity in our scheme as it is proportional to the area of the $\phi = 0$ isosurface, as given by (6.14). For the sake of simplicity we refer here directly to the area A. The first plot (A) in Figure 6.1 shows that once the mutiplier is activated at t_0, the actual area oscillates around the desired value $A_0 = A(t_0)$, and the amplitude of the oscillation is damped, as can be seen in plot (B). This amplitude is clearly controlled by $\alpha^* = \alpha\Delta t$, and we perform a systematic study over an extensive range of this parameter to set its precision and time scale. The oscillation amplitudes are fitted to a curve $\Delta A(t) = A(t) - A_0 = (\Delta A_0)e^{-rt+i\omega t}$. Hence, $1/r$ represents the timescale in which the actual area converges to the desired one, A_0. The minimization of the oscillations in the actual area, ΔA, is important even if they take place in a very short timescale, since if large area variations are allowed the cell could deform into prohibitted shapes. In plots (C) and (D) of Figure 6.1 we show the dependence of the area amplitude ΔA and decay rate r with the control parameter α^*. Both magnitudes decrease for higher values of α, although eventually higher α lead to numerical instabilities. The time scale in which the area converges to the reference value must be much smaller than the other time scales of the system, such as the elastic time τ_κ and the viscous time $\tau_\eta = l/v$, where l and v are a typical lenth and velocity of the system. The results show that for high values of α^* there is a clear separation in the timescales of the Lagrange multiplier and the cell deformation, ensuring that at the cell time scale the area is conserved with high precision. In our simulations we fix $\alpha^* = 10^{-4}$, which fulfills the requirements of low area oscilations, fast time convergence to the reference area and it proves numerical stability over the entire range of parameters studied.

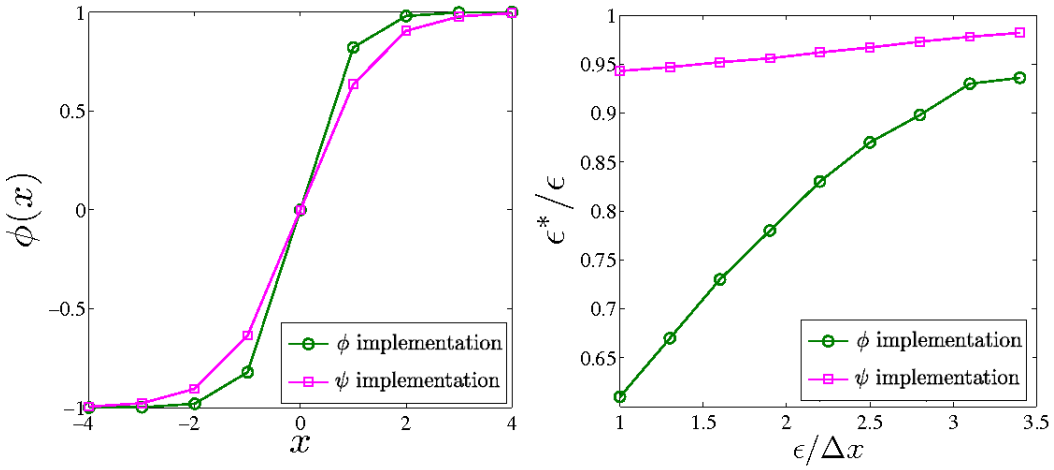

Figure 6.2: *(Left)* Equilibrium profiles of the ϕ (red) and ψ (blue) implementations of a flat interface, for $\epsilon = 1$ and $\Delta x = 1$. The resulting profiles are different, $\epsilon^*_\phi = 0.6$ and $\epsilon^*_\phi = 0.93$. *(Right)* Dependence of the effective width ϵ^* with the spatial mesh resolution $\epsilon/\Delta x$. In the continuum limit, the ϕ-implementation recovers the analytic solution and converges to the ψ-implementation.

6.3 Numerical realization of tensionless interfaces

The simulation of cell membranes requires of an exquisite control of the elastic properties of the interface. Interfaces show an extreme sensitivity to the value of the surface tension. Interfaces with low but finite value of the surface tension, such as lipid monolayers, are still dominated by this contribution rather than bending. Only in the case of bilayers, characterized by a strong decrease of the surface tension with respect to monolayers, membrane dynamics is controlled by bending. Accordingly, within the phase-field framework the elimination of any potential tension contribution is crucial to describe the appropriate membrane behaviour. In Chapter 5, the phase-field free energy (5.22) has been shown to present a stricly zero surface tension. However, the precision lose when the model is discretized introduces certain problems in the control of the interface properties that must be adressed.

The minimization in a discrete mesh of the free energy (5.22) for a flat interface leads to an equilibrium profile of effective width $\epsilon^* = 0.6\epsilon$, when fitted to $\phi_0 = \tanh(x/\sqrt{2}\epsilon^*)$, thus the actual and desired interfacial widths do not match. If this profile is introduced into expressions (5.19), it is straightforward to find that the resulting interface has nonzero surface tension. As explained in the Chapter 5, only the solution $\epsilon^* = \epsilon$ entails a tensionless interface. For obtaining this equilibrium profile, we introduce the field $\psi = -\phi + \phi^2 - \epsilon^2\nabla^2\phi$ and express the chemical potential (5.24) in terms of this field. The ψ-implementation forces the solution $\psi = 0$ which corresponds to the required equilibrium profile (see Figure

6.2A). In the continuum limit, $\Delta x/\epsilon \to 0$, the ϕ-implementation must recover the tensionless interface. This is tested in Figure 6.2B, where the dependence of the interface width ϵ^* with the spatial resolution of the mesh is shown for increasing widths ϵ. Only for $\epsilon \approx 3\Delta x$ (which corresponds to roughly 11 nodes within the range $-0.9 < \phi < 0.9$, in comparison with the 3 nodes for $\epsilon = 1$) both implementations lead to a similar equilibrium profile.

The implications of the profile precision in the elastic properties of the interface can be inferred from Figure 6.3, where we plot the energetic contributions of surface tension and bending for different interfacial widths. The effective value of the effective modulii is obtained from the integration in the grid of the expressions (5.19). For $\epsilon/\Delta x = 1$, the ϕ-implementation corresponds to an interface dominated by surface tension whereas the ψ-implementation leads to an interface dominated by bending, though still a small tension is present. A considerable increase in the interfacial width is required to recover the tensionless interface in the ϕ-implementation. Given that phase-field models require of an interface as thin as possible, we conveniently adopt the ψ implementation and set $\epsilon = 1$. Note also that the remnant surface tension might be partially controlled by the Lagrange multiplier, as changes in area will be corrected by this last contribution.

6.4 Several cells

The presence of several cells in the domain has two main consequences concerning the numerical implementation of the model. First, the area conservation condition, as imposed by the Lagrange multiplier, (6.18), must be modified to restrict the integration of $|\nabla\phi|^2$ to a local domain of the cell, so that the areas of each cell can be identified. Second, when flowing freely in a channel, cells can potentially collide. In the phase-field scheme, collision between two cells will lead to fussion, obtaining a large vesicle. To avoid this effect, we introduce a short-range repulsion which prohibits fussion. We have introduced a new field, $c(x)$, which takes the value i if $\phi(x) > -0.98$ for the i-cell of the suspension, and 0 otherwise. The field c follows the field ϕ, and it is updated just after the later. From this field, both the area calculation and the repulsion between cells can be introduced.

Individual area calculation.

The scheme is exactly the same as presented before, though the integral for computing the area of the i cell, A_i, given by (6.14), is restricted to the domain $x \in \{c = i\}$. Each cell has then a specific Lagrange multiplier associated, γ_i.

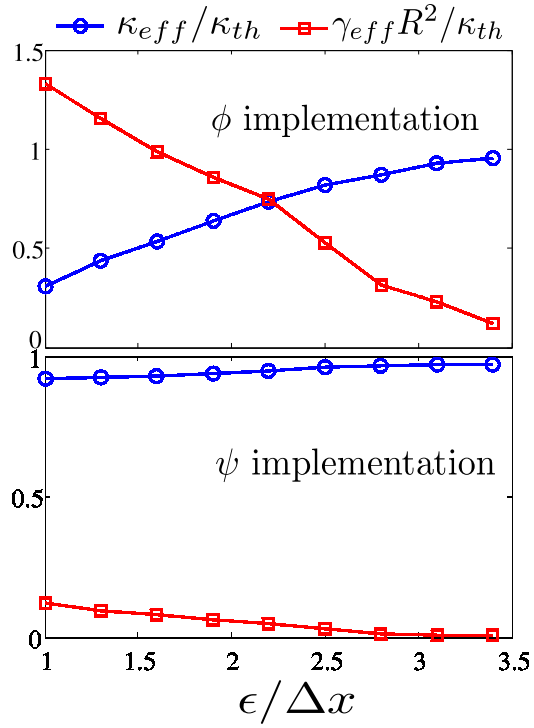

Figure 6.3: Effective bending and surface contributions for an interface in the ϕ and ψ-implementation, expressed relatives to the expected theoretical value in the continuum limit. The tension term is expressed in units of energy by multiplying by a typical drop radius, $R = 15$ in code units. The elastic modulii are measured as the discrete version of expressions (5.19). The plot shows that in the ψ a low spatial resolution is required to obtain a negligible surface tension, and therefore this scheme is much more convenient than the ϕ-implementation.

Repulsion between cells.

We introduce a weak repulsion to avoid cell fussion when two cells are too close. The repulsion is incorporated as a new term to the free energy, and it takes the form

$$E_{rep}(x_i) = \sum_j W e^{-|x_i - x_j|/l} \delta(c(x_i) - c(x_j))[1 - \delta(c(x_i))]. \tag{6.19}$$

where j runs over the two closest neighbour nodes, and we fix $W = 0.2\kappa$ and $l = 1.5\Delta x$. We check the dependence of the cell behaviour with respect to these parameters, ensuring that the repulsion avoids the fussion but does not introduce a spureous interaction that pushes the cells away.

6.5 Parameter steering

The simulations performed in this Thesis are based on LUDWIG (Desplat et al., 2001), an implementation of the lattice-Boltzmann scheme presented in this Chapter. The parameter steering is determined by both physical requirements and numerical stability restrictions. As commented in Section 6.3, simulation of membranes requires of a subtle control of the interface elasticity. Thus, ϵ must be sufficiently large to resolve correctly the gradients of ϕ in the interface. We have shown that $\epsilon = 1$ is a reasonable choice. Hence, the scale of the cell length l is fixed, since there must be a clear separation, $l/\epsilon \gg 1$. We use $l = 50\epsilon$, which represents a compromise between the previous condition and a sufficiently small domain so that the simulation time is reasonably short.

We are interested in the viscous (or Stokes) regime, in which inertial effects are negligible. The Reynolds number must be small,

$$Re = \frac{\rho v L}{\eta} \ll 1 \tag{6.20}$$

and in particular we fix $Re < 0.05$, ensuring that our results do not depend on the particular value of Re. This condition fixes that the value of η must be high, and we set $\eta = 1$ in code units (this is the highest value in LUDWIG, as larger values could potentially lead to problems of numerical stability). The low Reynolds condition fixes a value of the maximum flow velocity, in turn determining the maximum external forcing f which is our actual control paramenter. Since we are interested in capturing a realistic elastic response of the cell membrane with respect to the surrounding flow, from the maximum velocity the value of the bending rigidity κ is also fixed. We then obtain a typical relaxation time of the cell shape $\tau_\kappa = \eta l^3/\kappa$. We need to impose that the dynamics of the interface, controlled by the order parameter mobility M, is much faster than the dynamics of shape change. Hence, the time of interface relaxation, $\tau_\epsilon = \epsilon^2/M$, must follow $\tau_\kappa/\tau_\epsilon \gg 1$. This provides a condition for the mobility value, which we fix at $M = 0.1$ obtaining the desired separation between both dynamics, $\tau_\kappa/\tau_\epsilon = 10^5$.

Part IV

Red Blood Cells flow in confined systems

Chapter 7

Blood circulation

The recent development of microfluidics has allowed an important improvement in our understanding of blood circulation and rheological properties. The study of blood flow at the single-cell scale enables the identification of the individual elastic mechanisms driving blood behaviour, which formerly should be infered from macroscopic observations of the whole blood (Thurston, 1972). The dynamics and elastic mechanics of RBCs in confined systems is a subject of fundamental interest due to its enormous applications in biomedical engineering, as it affects to the hemorheology during blood handling and storage, or to cell manipulation in pathology diagnosis. It also represents an interesting problem from a theoretical perspective, as the highly non-linear rheology of suspensions of deformable objects is still poorly understood. In this Chapter, we first study the main applications and current state of the microfluidic technology in order to identify the problems of interest within this field. We then overview our current knowledge, both from experiments and theory, about the behaviour of RBC flow.

7.1 Motivation

7.1.1 Blood properties

The proper functionality of blood is very sensitive to the mechanic properties of the fluid, as perfusion only occurs when blood shows certain rheological properties (Baskurt et al., 2007). Altered blood, for instance by abnormal RBC concentrations or stiffening of the cells, can lead to a reduction in the oxygen delivered. The control of these properties is therefore important for the organism functioning. For these reasons, among many others, the study of blood properties has been a subject of prime interest for a long time (Thurston, 1996).

Rheology

Rheology is the field that studies the flow behaviour and deformability of different materials. Fluids show a continuous deformation when externally forced, and they do not recover the initial state once the force is removed. On the contrary, solids respond to external forces by a certain deformation, after recovering the initial shape when the forces do not apply. Elastic solids are those which their deformation is proportional to the applied force. Some materials present an intermediate behaviour, combining solid-like and liquid-like response depending on the type or intensity of external forcing. These materials are especially interesting within the rheology frame, since their rheological properties usually show a strong sensitivity to this forcing.

The external force that deforms the material, expressed per unit area, is usually called stress and involves several components, most relevants being the shear stress (which acts parallel to the material surface) and the normal stress (which in a fluid is recognized as the pressure). If we consider the rate at which the shear deformation is applied, a definition for the viscosity of the liquid arises from the ratio between shear rate and shear stress. Most macroscopic viscometers use the local relation between shear stress and rate to measure the viscosity (Degré et al., 2006). However, although this standard procedure provides important information about the bulk behaviour of the fluid, it is of limited interest for understanding the flow in very confined systems, when the rheological behaviour can be severely affected.

Viscosity is constant in Newtonian fluids, but it depends on the applied stresses and tube geometry in non-Newtonian (or complex) fluids. In the case of blood, it is known that blood viscosity decreases for high shear rates, presenting a shear-thinning behaviour.

Hemorheology

Hemorheology is the study of the flow and deformation properties of blood. In vivo, blood flow is determined by a multitude of factors, including RBC deformability, hematocrit, elasticity of venules and arteries, blood pressure, etc. Clinical and experimental evidence suggest that blood fluidity is strongly related to tissue perfusion, and thus processes affecting the properties of blood, such as damage of the RBC membrane by a particular disease or ageing, impair the normal rate of oxygen received by the body cells. Thereby, understanding blood flow is determinant in medicine for identifying symptoms of many diseases associated with the deficient functioning of circulation.

The rheological behaviour of blood is dictated by a complex combination of different coupled effects (Baskurt et al., 2007). The hematocrit is critical to increase blood viscosity with respect to plasma viscosity. The degree of disturbance of flow streamlines, and thus the resistance to flow of blood, is severely increased for high hematocrits. Many mammals are able to specifically regulate their hematocrit in response to physical requirements (*eg* a well known example is horses during demanding exercise), due to the existance of RBC reservoirs in the spleenic system, but this mechanism is largely absent in humans. The elasticity of the capillar walls permits the modulation of the blood pressure, regulating the external forcing driving the flow. The rigidity and deformability of RBCs is also known to alter blood properties, and blood with high concentrations of echinocytes or spherocytes show a much higher resistance to flow, impairing perfusion capability. Blood viscosity also increases if RBCs form aggregates. RBC aggregation is promoted by certain molecules allocated at the cell surface, and aggregation is of importance in certain diseases, such as malaria, which benefits from alterations in normal blood viscosity. Hemorheology is likewise important ex vivo, especially in the improvement of blood handling and storage for blood transfusion or renal dialysis, among others. Designing and optimization of pipe devices used for blood manipulation are based on a detailed knowledge of blood behaviour.

Hemorheology is mainly based on experiments performed in laboratories, and the importance of the rheological parameters for in vivo flow conditions is still uncertain. For instance, most viscosity measurements make use of cylindric rotational viscometer, which certainly differs from the geometries found in the circulatory system. It has been suggested that alterations in the rheological properties of in vivo blood do not correspond to the predictions based on ex vivo studies (Baskurt and Meiselman, 2003). Accordingly, a better understanding of the fundamental mechanisms dictating hemodynamics in pressure-driven flows is fundamental to characterize and predict the correct rheological behaviour of blood in the human circulatory system.

7.1.2 Cell manipulation

The central role of blood in the body running has been exploited from the beginnings of the medicine to detect abnormalities in the state of health. Quoting Toner and Irimia (2005): “Blood is a treasure of information about the functioning of the whole body. Every minute, the entire blood volume is recirculated throughout the body. [...] Cells of the immune system are transported quickly and efficiently through blood, to and from every place in the body. As a result, blood harbors a massive amount of information about the functioning of all tissues and organs in the body. Consequently, blood sampling and analysis are of prime interest for both

medical and science applications, and hold a central role in the diagnosis of many physiologic and pathologic conditions, localized or systemic. However, tapping into this wealth of information, for clinical and scientific applications, requires not only the understanding of the biology involved but also adequate technologies".

In the last ten years, the microfluidic technology has undergone an important and rapid development, especially in the designing of fine lab-on-a-chips. These devices represent an exquisite toolbox for blood handling at the microscale, allowing single-cell distinction and manipulation (see Figure 7.1). The technology can be used both for scientific research, to improve our understanding about blood properties, or for applications in medicine. The insights gained from scientific studies are, in turn, necessary to improve devices design, and thus medicine benefits from this interplay between science and engineering.

The main applications of this technology concern cell manipulation for pathology diagnosis and blood preparation for different uses, such as plasma-cell separation (Dimov et al., 2011). Ideally, specific chips of basic functioning could provide instantaneous diagnostics and prognostics at the doctor office, avoiding the tedious process of blood test which usually takes several days (mainly spent in the transport to the laboratory) and requires large blood samples. It also will be extremely useful for medical development in regions lacking a suitable medical infrastructure, such as many areas of Africa where malaria has a catastrophic effect.

Typically, microfluidic devices take advantage of the different properties of RBCs, platalers and leukocytes, including size, deformability, density, and membrane electric properties. Both RBCs and leykocytes are target cells in pathology tests. Devices are designed to exploit the different response of each cell species (as well as the plasma) to a number of physical fields, and select the object of interest. Among others, mechanical forces, electric and magnetic fields, biochemical interactions, and optical trapping have been incorporated to chip devices, often combining more than one technique (Li et al., 2013). However, regardless of the nature of the field, lab-on-a-chips require of a fine microscale control of the flow.

The most relevant *active* methods include (Toner and Irimia, 2005)

- **Dielectrophoresis (DEP).** This technique benefits from the sensitivity of the membrane to changes in the charge of the environment. When cells are exposed to non-uniform electric fields, they polarize and their translational motion or orientation can be driven by control of the external field. The typical strategy is to create electric traps in which target cells are attracted. The induced polarization strongly depends on the electric properties and composition of the external surface of the membrane, so that DEP provides a very high selectivity in the cell separation, not only at species level

but also it can distinguish between different states of activation of similar cells. Nonetheless, the multiple variables affecting to the output of DEP experiments represents an important drawback for this technique, as it difficults the interpretation of the results and comparison between experiments. Moreover, even if weak electric fields in principle do not affect to the membrane balance, DEP represents a (weakly) invasive technique and potential conformational changes in the cell membrane must be considered.

- **Magnetic interactions.** RBCs contain a high density of hemogoblin in their cytosolic volume. Hemoglobin is an iron-bearing molecule whose ferromagnetic properties could be exploited to differentiate RBCs from other cells. However, RBCs in oxygenated blood present a similar diamagnetic behaviour to leukocytes, and only in oxygen-depleted blood a weak paramagnetic behaviour has been detected. High magnetic fields are required to achieve a good accuracy in cell separation.

- **Optical traps.** Laser tweezers devices can be incorporated to chips, for instance creating an optical lattice in which cells are trapped. This technique offers many possibilities for cell manipulation as it achieves a very high precision, but devices capable of dealing with millions of cells (as required in small blood samples) would be really challenging.

- **Biomarkers.** The addition of certain bioagents at specific points of the chip can be used to selectively destroy subpopulations of target cells, if exposed to a toxinc enviroment, or attach them to the surface. For instance, leukocytes are more resistant to solutions of ammonium chloride than RBCs, and therefore the lysis of the later can be used to separate both cells. Although these methods also achieve a high precision, agents usually act over all the cells and the method could affect the healthy state of the target cells.

On the other hand, the use of **mechanical forces**, such as filters and junctions of channels, represents a *passive* method. The size is the most direct observable for differentiating cells, and the designing of filters that selectively permit the pass of RBCs, whereas they are thin enough to hold back leukocytes, is the simplest device that can be fabricated for cell separation. However, separation based on mechanical restriction has a limited efficiency and low purity of the sample. Still, methods in this direction have been able to separate small tumor cells (Mohamed et al., 2004). A different method consists in taking advantage of the lateral translation that cells show depending on their specific size and shape. Although with limited examples in cells yet, the method has proven good accuracy for separating particles of a few microns difference, analogous to the RBC and leukocytes case. This method uses the interactions of the cells with the channel geometry, so that

complex geometries such as unduloids have been fabricated (Carlo et al., 2007), combined with passages through thin bottlenecks (Abkarian et al., 2008).

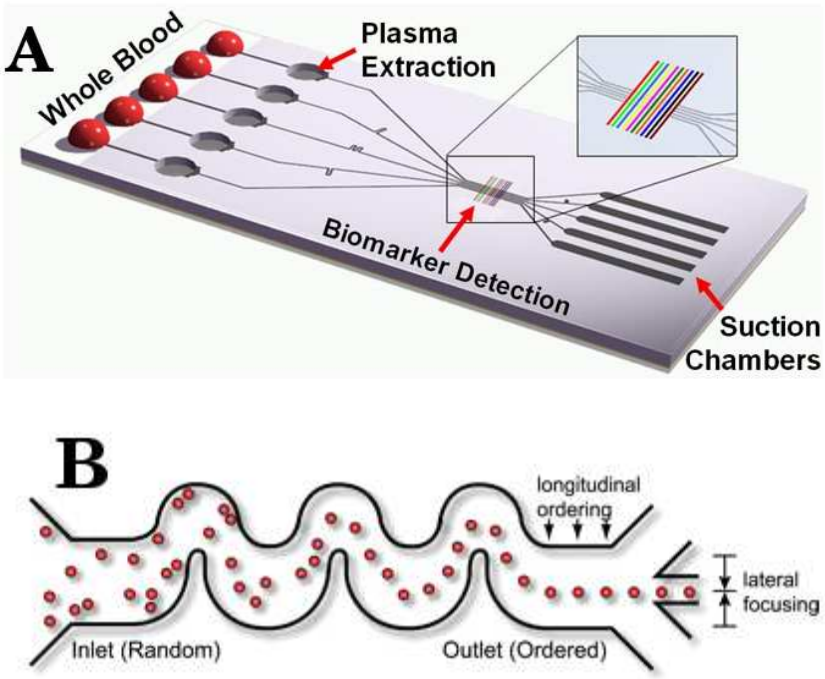

Figure 7.1: (A) Example of lab-on-a-chip for RBC handling. The chip is designed to exploit the channels geometry that permit the cells/plasma separation. Then specific biomarkers act over the target cells and the outcome sample is collected. Credits: Ivan Dimov. (B) Sketch of use of channel geometry to manipulate RBCs. In this example, the channel is designed to focus the cells to a very specific position in the channel. Reproduced from Carlo et al. (2007).

7.2 RBC behaviour in shear and parabolic flows

RBCs and vesicles present a rich phenomenology when flowing in thin tubes. The problem has been especially studied for giant unilamelar vesicles (GUVs), enclosed bilayers of typically 10-30μm size and circular or elliptical shape, since it has been generally accepted that these simple structures capture the basic physics of RBCs and serve as model systems (Dimova et al., 2007). The use of GUVs offers many advantages as they are more stable under chemical changes of the environment, and a number of features, such as their internal viscosity, can be manipulated without affecting their stability. Conversely, RBCs require of a delicate treatment and the number and range of the parameters studied decreases. However, recent studies have highlighted the importance of the differences between RBCs and GUVs in terms of shape and membrane elasticity in blood flow (Abkarian et al.,

2007). Theoretical studies have concentrated on the dynamics of an isolated RBC or vesicle in linear shear flow, as it represents a simpler problem and invites to a more extensive analytical treatment than the Poiseuille (or parabolic) flow, which presents a non uniform stress profile.

7.2.1 Shear flow

Membrane motion

RBCs and vesicles in unbounded shear flows present three main regimes of motion, determined by two or three basic parameters (Vlahovska et al., 2009). Since most experiments performed are based on the study of vesicles, here we use this term to refer equally to vesicles an RBCs. Namely, these regimes are: *(i)* tank-treading (TT), when the vesicle deforms into a prolate shape and mantain a fixed position and orientation, though its membrane is subjected to continuous rotation; *(ii)* tumbling (TB), when the vesicle performs a periodic rotation, and *(iii)* vacillating breathing (VB), when the vesicle shows oscillations on its inclination with respect to the flow, also known as trembling.

The dynamics is controlled by two main parameters, the viscosity ratio between the inner and outer region of the vesicle, $\lambda = \eta_{in}/\eta_{out}$, and the capillary number which characterizes the shear rate of the force relative to the membrane rigidity, $Ca = \eta\dot{\gamma}R^3/\kappa$. Additionally, the deformability of the vesicle is also relevant, as rigid vesicles only present TT and TB motions (Keller and Skalak, 1982). A phase diagram for a deformable vesicle in an unbounded flow, obtained by Kaoui et al. (2009), is shown in Figure 7.2. At low viscosity ratios, typically $\lambda < 5$, only TT is observed. Vesicles exhibit VB motion at a reduced range $5 < \lambda < 6$, whereas for higher viscosity ratios only TB is observed. The transition between each motion regime depend on the capillary number, as at low capillaries VB dissapears and TB is observed at lower viscosity ratios $\lambda > 4$. The TB behaviour at high λ is not surprising, as it is known that solid rods in shear flows rotate with a constant frequency (Jeffrey and Pearson, 1965). Therefore, the *solid* limit ($\kappa \to \infty, \lambda \to \infty$) is seemingly governed by the viscosity contrast, whilst membrane rigidity plays a secondary role. This phase diagram is drifted towards higher values of λ when the confinement is increased. These results have been predicted by analytic models (Keller and Skalak, 1982) and numerical simulations (Kaoui et al., 2009; Noguchi and Gompper, 2005), showing a nice agreement with experimental results (Deschamps et al., 2009).

Experiments dealing directly with RBCs have shown the particularities of these entities. RBCs exhibit a new motion, known as swinging (SW) (Abkarian et al., 2007), which can be described as a combination of tank treading motion with a

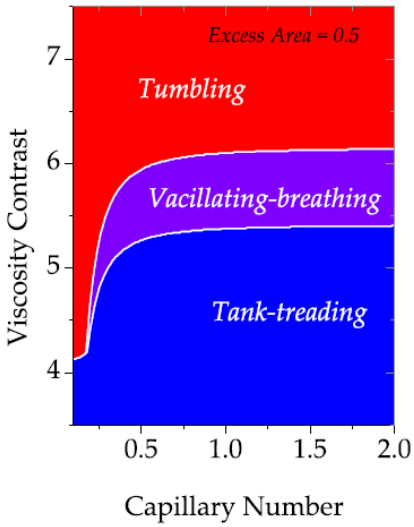

Figure 7.2: Phase diagram of the dynamic motion of vesicles in simple shear flow. At intermediate and high capillary number, tank treading, vacillating-breathing and tumbling are sequentially found for increasing viscosity contrasts. At low capillary number, VB disappears and TB is observed at lower λ. For $\lambda = 1$, the motion is dominated by TT regardless of the value of the other control parameters. Reproduced from Kaoui et al. (2009).

periodic change in the inclination of its major axis. SW is observed at low viscosity ratios $\lambda \sim 4$, in the intermediate regime between TB and TT. The mechanism dictating this motion is still unclear and both the presence of the spectrin network (and thus the existance of resistance to shear), and the particular biconcave shape of RBCs have been identified as important features with respect to GUVs.

It has been recently demonstrated that in confined systems, vesicles require of a larger viscosity ratio to recover the TB motion (Kaoui et al., 2012). This is likely related with the presence of walls, which confine the motion and reduce the freedom to rotate.

Wall-induced migration

It is well known that neutrally buoyant particles perform crosstream migrations in the inertial regime ($Re \gg 1$), driven by both wall repulsions or shear-gradients (Wang and Skalak, 1969). This result explains the classic observation that particles flowing in tubes are located at an off-center position, the so-called Segré-Silverberg effect. The lateral position in the tube is determined by the balance between the shear-driven shift from the axis and the repulsion from the wall. In the viscous regime ($Re \ll 1$), however, the linearity of the Stokes equation determines a symmetry under flow-reversal that inhibits this crosstream migration.

To break this symmetry, the objects must be deformable or of asymmetric shape (Olla, 1999).

The migration of vesicles when placed close to a wall in shear flows has attracted interest from theoricists. The problem can be analyzed by the method of images: the flow driven by the vesicle towards the wall is reversed by its image vesicle at the symmetric position. By this method an analytic expression for the repulsion velocity can be obtained (Olla, 1997, 1999), dependent on the distance to the wall, size of the particle, and capability to deform. It is also expected that high viscosity ratios promote migration. The models show good agreement with the experimental data (Abkarian et al., 2002).

7.2.2 Parabolic flow

Single-cell behaviour

In spite of its prime interest for the understanding of microcirculation, the behaviour of RBCs in parabolic flow has received limited attention in comparison with shear flow, at least from a theoretical perspective. At low confinements (when the channel width is much larger than the RBC diameter, and thus at the cell scale RBCs effectively interact with a constant gradient velocity profile) RBCs are known to maintain their discocytic shape, exhibiting little or no deformations. In thinner channels, when both the width of the channel and the cell diameter are comparable, RBCs present a complex and fascinating behaviour (Abkarian et al., 2007). While flowing in channels of $< 30\mu$m, RBCs exhibit an asymmetric morphology known as *slipper*. Additionally, they can also assume a symmetric shape, termed *parachute*, situated at the center of the channel. Whilst both configurations are often seen during experiments in microchannels (sometimes simultaneously, see Figure 7.3 A), the conditions necessary to observe one or the other shape have not been properly determined (Abkarian et al., 2008; Tomaioulo et al., 2009). Actually, why RBCs remains an asymmetric (slipper) shapes when flowing in symmetric flows remains as an unresolved question (Noguchi and Gompper, 2005; Kaoui et al., 2009), despite its importance to understand its implications in the capability of RBCs to flow along very thin conduits. Some authors argue that the slipper configuration enhances flow efficiency, reducing the lag in speed between RBC and the flow (Kaoui et al., 2009), whereas others defend that slippers do not serve any specific purpose and they just represent a consequence of the increasing flow (Secomb et al., 2007).

It is remarkable that, whereas RBCs are usually observed at off-center positions, spherical vesicles present a considerably different behaviour. The deformability of the lipidic membrane allows vesicles to perform crosstream migrations,

but they stabilize at axial positions in the tube (Coupier et al., 2008), instead of the lateral position observed in RBCs.

Collective flow

The flow of RBCs in tubes and channels is critically controlled by the hematocrit, as RBCs show a very different behaviour at low and high concentrations. The interactions between RBCs, involving hydrodynamic interactions, purely geometrical constraints, or aggregation, play a fundamental role in the collevtive dynamics of the RBC suspension.

At low concentrations, vesicles and hard spheres flowing in thick tubes migrate from the center line and reach a stable trajectory at $\sim 0.6R$ from the axis, forming an annulus of high density at this radial distance, the so-called Segrè-Silverberg effect (Segré and Silberberg, 1962). At high concentrations, however, RBCs distribute along the tube core, avoiding the region close to the wall (see Figure 7.3 D). The transition from the single-cell to the high hematocrit behaviour is still poorly understood (Narsimhan et al., 2013), in spite of its important in the rheological behaviour of the fluid. The Faehreus-Lindqvist effect (Fahraeus and Lindqvist, 1931), characterized by a dependence of the blood viscosity with the channel thickness, is perhaps the most important example. In the range between roughly 300μm and 10μm of tube diameter, the effective viscosity decreases up to 4-5 times. The effect occurs as a consequence of the strong repulsions from the walls that force the blood cells to concentrate on the central region of the channel. The formation of layers free of cells close to the walls allows a rapid flow in these regions, enhancing the overall fluidity. At high confinements, the walls proximity enforces a more concentrated distribution of cells in the center and consequently broader layers of free flow are present. In larger channels the free layers are proportionally thinner until their effect becomes eventually negligible.

Although in the narrowest channels ($<10\mu$m) RBCs flow ordered in a single row at low concentrations, and thus interactions between cells are disregardable, at intermediate channels ($\sim 20\mu$m) RBCs present a more complex behaviour and collective effects must be considered.

7.3 Scope of Part IV

This Part of the thesis is devoted to the study of RBC and vesicle suspensions. We concentrate on parabolic flows, the relevant ones in blood circulation, and in the limit of highly confined microchannels, which has been scarcely studied by theoretical models. We focus on the understanding and identification of some of

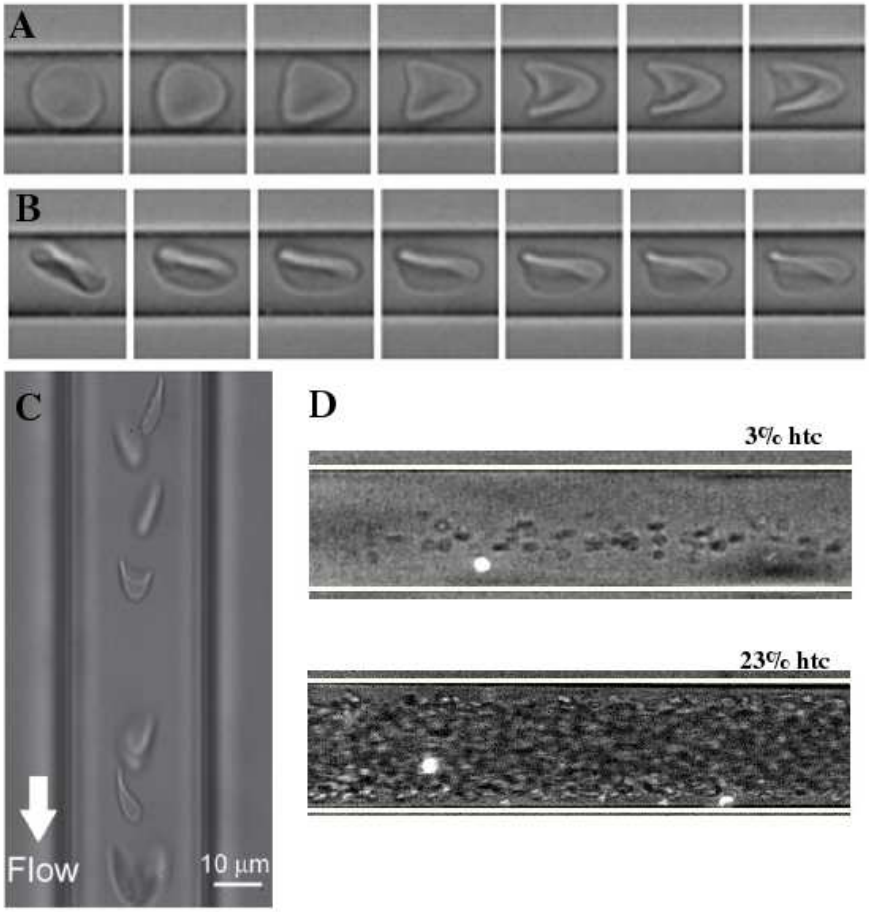

Figure 7.3: (A) and (B) Shape evolution of a single RBC during downstream flow, for a channel width of 10μm. At similar flow conditions, both a parachute (A), and a slipper (B), are developed. Reproduced from Tomaiuolo and Guido (2011). (C) Flow of RBCs at low concentrations for a slightly thicker channel. Both parachutes and slippers are observed simultaneously. Reproduced from Oishi et al. (2012) (D) Collective flow of RBCs. Even at relatively low concentrations (top image; 3% hematocrit), if cells flow separated by short distances they interact and their behaviour changes, focusing towards the core of the channel. At higher concentrations (bottom image; 23% hematocrit), cells are concentrated on the central region and a layer free of cells is formed close to the walls, the so-called Faehereus-Lindqvist effect. Reproduced from Lima et al. (2009).

the most basic and fundamental aspects driving the dynamics of RBC flow, dealing with some of the most relevant questions that arised in the previous sections. Thereby, the main aims of this part are:

- characterization of the interplay between membrane elasticity, cell deformability and flow properties as the basis to explain the complex rheological behaviour of the suspension. Specifically, we focus on how the stiffening of the membrane affects RBC deformability and suspension viscosity,

- identification of the control parameters of RBC flow at the microscale. In particular, we concentrate on RBC focusing, due to its relevance in the designing of chip devices, as shown in Figure 7.1,
- comparison between the single-cell behaviour and the collective properties when several cells interact, and the identification of the mechanisms driving the different behaviour at these conditions.

The subsequent Chapters, 8, 9, 10 and 11, are dedicated to elucidate these important questions, and perform a systematic study of the different problems, exploring wide range of the parameters space.

Chapter 8

Rheology and deformability of RBCs

Blood is a typical example of complex fluid, in which the non-linear rheological behaviour is introduced by the presence of RBCs. However, compared to classic complex fluids, blood is a singular case because its compounds are considerably large (typical polymers and micelles are of a few hundred of nanometers, compared to 8 microns of RBCs) and characterized by a remarkable deformability. For these reasons, two main sources of non-linearity can be identified, the *collective* effect induced by the interaction between cells, and the purely *elastic* effect intrisinc of each cell. As explained in Chapter 1, changes in the elastic properties of the RBC membrane is a common consequence of a number of pathologies, and its impact on the affected blood is still unclear. In macroscopic rheology, however, it is difficult to separate the collective and the elastic effects. Thereby, the main aim of this Chapter is to identify the rheological properties of blood that can be solely associated to the deformability of RBCs, and explore the role of membrane elasticity in blood fluidity.

In this Chapter, we study the behaviour of a RBC flowing in a thin tube at fixed confinement, sweeping over a wide range of capillary number. The main morphological regimes are identified, and we discuss the relevance of the RBC capability to deform and orient in the suspension fluidity. Before these results are presented, we first describe the main characteristics and specific values of the system and parameters of the simulations we have carried out. These conditions likewise apply to the results of Chapters 9, 10 and 11.

8.1 Simulation of RBC and vesicle flow

In Part III of this Thesis we present a phase-field model which provides the technology necessary to simulate cell membranes. In the subsequent chapters of this Part IV we make use of this model to study different aspects of the elastic response of RBCs in channel flow. Some preliminar considerations, concerning the relevant physical aspects on the modelization of blood, must be highlighted here.

RBCs properties

Stricly speaking, RBCs elasticity results from the interplay between the bilayer and the cytoskeleton. Thus, a complete model accounting for RBC elastic properties should include the terms of shear and compression. The purely lipidic description of Helfrich is often associated to vesicles, and the term RBC is applied to models which include resistance to shear (Noguchi and Gompper, 2005). In Part II of this Thesis we have shown that the cytoskeleton is severely stressed under certain high-curvature deformations such as spicules, but its contribution is subdominant for cell deformations close to the discocyte. We consider that during blood flow RBC deformations are weak enough (involving low curvatures) to disregard the cytoskeleton contribution, and accordingly the Helfrich description accurately describes the RBC elastic behaviour.

RBCs and vesicles are enclosed membranes characterized by their fixed volume and area, and the bending rigidity of their membrane, κ. Since the density of the cytosol and the blood plasma is similar to that of water, we consider that the density is homogeneous. The viscosity of the cytosol is roughly ~ 5 times larger than that of the plasma, but studies have proven that the viscosity contrast does not play a relevant role in the cell dynamics at confined systems (Tahiri et al., 2013), and for simplicity we assume a homogeneous viscosity, which we express relative to that of plasma, $\eta_{in} = \eta_{out} = \eta_0$. Therefore, $\lambda = 1$ and only tank-treading motion is expected. Blood plasma is known to present a slightly viscoelastic behaviour, but we disregard this contribution for simplicity. The viscosity of the lipid membrane is known to be considerably higher than that of plasma $\sim 10^2\eta_0$, but the volume fraction of lipids in the system is small enough to consider that the hydrodynamic dissipation in the bulk is prevalent, and membrane viscosity does not play a relevant role in the aspects of the dynamics we focus on (Vlahovska et al., 2009).

In order to compare the role of shape, and distinguish the particularities of RBCs with respect with classic vesicles (GUVs), we generate a set of shapes of the same diameter a, including a nearly spherical shape, of reduced volume $v_{red} = 0.97$, and three deflated vesicles of 0.69, 0.55 and 0.48 (note that, in spite of the 2D

approach, we maintain the nomenclature *reduced volume* for consistency with the literature). The last one corresponds to the usual discocyte shape of RBCs. The shapes are obtained from the minimization of an initial ellipsoid with the desired area and perimeter, by switching off the flow $v = 0$ in equation (5.35). During the first steps, the Lagrange multiplier is set to zero, while the equilibrium profile is formed. We then restore the multiplier in order to conserve the perimeter. Since the time scales of the interface dynamics and shape deformation are very different, we assume that the lose in perimeter during the first steps is disregardable, though we check the actual values of the area and perimeter at the final state. Once the system reaches the steady state, the equilibrium shape of the cell is obtained. The vesicles used as equilibrium configurations in this Thesis are depicted in Figure 8.1.

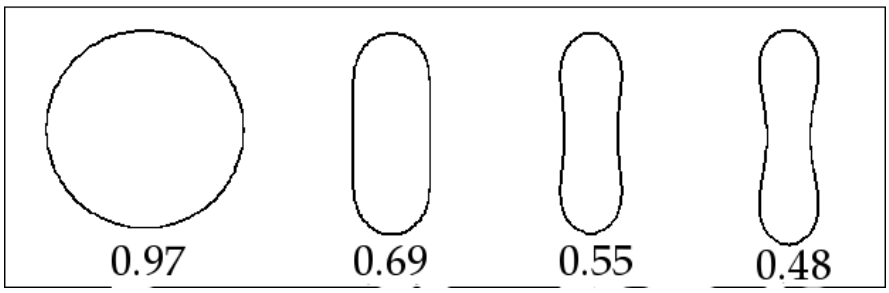

Figure 8.1: Morphologies studied in this Thesis, for decreasing ν_{red}=0.97, 0.69, 0.55 and 0.48, from left to right. The last one corresponds to the 2D profile of the discocyte morphology, representative of the healthy RBC shape. The shapes are obtained by minimizing the bending energy (5.22) for an initial ellipsoid, maintaining constant volume and area.

Flow characteristics

In Part I, we show that the periodic nature of blood flow dictated by the heart is attenuated along the circulatory system due to pressure damping. The blood pressure in the capillaries is nearly constant, and we consider a flow driven by a time-independent and homogeneous pressure gradient.

We carry out simulations in a two dimensional domain, which qualitatively capture the actual RBC behaviour (Kaoui et al., 2009) and enable a more extensive sweep of the capillary number avoiding the constraints of the computational time for tree dimensional domains. The fluid is forced in the channel axis direction, z, and periodic boundary conditions are applied in this direction. Strictly speaking, this situation corresponds to a regular array of RBCs, but we keep the cell to cell distance sufficiently large so that the cell does not interact with its images. This flow might be understood as the section of a rectangular flow in 3D, with walls

$L_y \gg L_x$ (often known as plane Poiseuille). We consider that the coupling of the shape in the normal direction, y, is subdominant with that induced by the close walls in $\hat{x}$.

At narrow capillaries and channels, the concentration of cells reduces down to $\sim 10\%$ Fung (1997). The interactions between RBCs consequently decrease and the dynamics of the cells is dominated by the interactions with the walls. The RBC effectively behaves as hydrodynamically isolated from its neighbours cells. This effect requires tubes of similar width b to that of the cell, roughly $b \sim 10\mu$m, which includes a large proportion of the microvessels that compound the circulatory system, as well as many of the typical widths of the channels currently used in microfluidic devices. We explore the range of confinements $a/b = 0.8 - 0.3$. In addition, consistent with Table 1.1, the Reynolds number is maintained below $Re < 0.05$, corresponding to the viscous regime present in the thinnest capillaries.

The interplay between RBC elasticity and flow is captured by the capillary number, C_κ, defined as the ratio between the elastic (2.27) and viscous $\tau_\eta = b/\bar{v}_z$ relaxational times,

$$C_\kappa = \frac{\tau_\kappa}{\tau_\eta} = \frac{\eta_0 \bar{v}_z a^2}{\kappa} \left(\frac{a}{b}\right). \tag{8.1}$$

where $\bar{v}_z$ is the mean velocity in the direction of the flow. This new definition relates with the previous one by $C_\kappa = Ca(a/b)$, containing more information of the confinement of the system, given by (a/b). Hereafter we only use this definition of capillary number, C_κ. The change in the capillary value can be understood as the different response of a specific cell under different flow velocities or, alternatively, the behaviour of cells of different softness under the same flow conditions. We will explore the range $0.2 < C_\kappa < 120$. For RBCs, typical values for the bending rigidity and cell diameter can be fixed at $\kappa = 2 \cdot 10^{-19} J$ and $a = 8\mu$m.

Rheological measures

Traditionally, the rheological properties of complex fluids have been experimentally determined by means of rotational viscometers (Thurston, 1972). These devices, characterized by a cylinder-in-cylinder or cone-plate geometry, operate maintaining a constant shear rate (fixed by the rotational speed) or a constant stress, and thus the effective viscosity is extracted from the response of the fluid in terms of the measured shear stress or plate velocity. However, the behaviour of complex fluids is highly sensitive to the flow properties, and hence the fluid response in pressure-driven flows in narrow channels and tubes may substantially

differ from that observed in rotational viscometers at larger scales (Baskurt and Meiselman, 2003). In order to study the rheological behaviour of complex fluids below the microscale, an alternative procedure consists in using micro-PIV techniques, in which small beads are added to the flow, and the tracking of these beads allows the reconstruction of the velocity field. The shear stress and rate can be then computed, and the shear viscosity arises from the ratio of shear stress to rate (Degré et al., 2006). However, in very narrow channels, the resolution necessary requires of a high control of the flow conditions (Pommer and Meinhart, 2005), making the previous approach inappropriate. An alternative measure of the viscosity, usually termed effective (or apparent) viscosity, is obtained from the ratio of the pressure drop to the flow rate in a channel. Chip viscometers based on this idea have been increasingly used in microfluidics (Guillot et al., 2006; Srivastava et al., 2005; Nghe et al., 2010; Gachelin et al., 2013), due to their simplicity, low-cost and fast measure processing. For practical purposes, we base our rheological study in the latter approach to obtain the effective viscosity, facilitating a direct comparison with these new chip viscometers.

The effective (or apparent) viscosity of the whole suspension (*ie* liquid and cells) is computed from the relation of the applied force and the outcome flow given by the mean velocity $\bar{v}_z$,

$$\eta_{eff} = \frac{f_0}{12\bar{v}_z} b^2. \tag{8.2}$$

This expression arises as the viscosity necessary to, assuming a Poiseuille flow and given the imposed forcing f_0, obtain a mean velocity $\bar{v}_z$. The high inhomogeneity of the suspension of study (originated on the large length of the object that introduces the elasticity relative to the channel width) suggests to deal with averaged quantities.

8.2 RBC behaviour

The sequence of RBCs flowing in a parabolic flow at steady state, for confinement $a/b = 0.71$, is shown in Figure 8.2. We maintain fixed κ, the bending rigidity, and increase the intensity of the external forcing (and therefore the mean flow velocity also increases). In all cases the RBC was initially placed symmetrical at the channel center, with its main axis normal to the flow direction. At low C_κ the RBC flows pushed by the fluid with slight or no deformation from the initial discocytic shape due to its relative rigidity. This initial stage is called discocyte regime. As fluid forces become important, the RBC starts to deform coupling its shape with the flow. It simultaneously acquires an asymmetric shape and

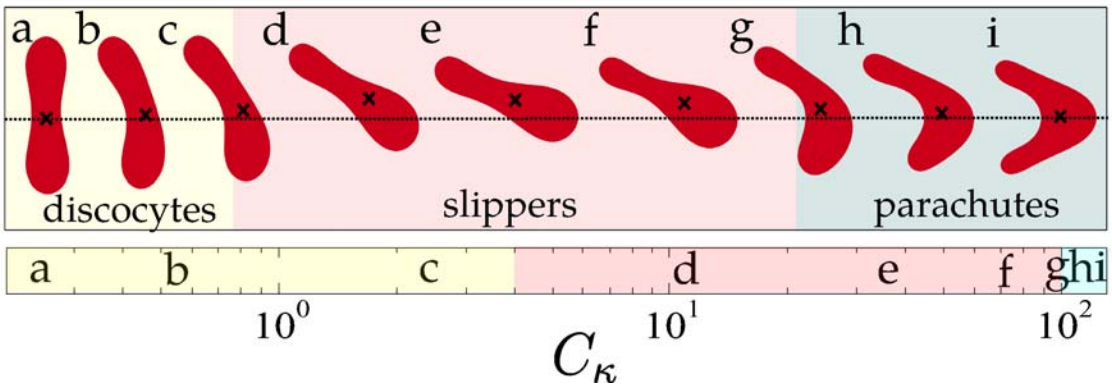

Figure 8.2: Red blood cell morphologies in a Poiseuille flow, with $v_{red} = 0.48$ and confinement $a/b = 0.71$, for increasing capillary number, C_κ. The coloured regions represent the three main morphological regimes, namely the discocyte (yellow), the slipper (red), and the parachute (blue); this convention will be used all along the Thesis. The dotted line represents the channel axis, and the crosses are the center of mass of each RBC. At low capillaries, RBCs maintain a discocytic shape. For increasing capillary, they start to deform and rotate, migrating from the channel axis. The lateral positioning in the channel is accompanied by an allignement with the flow profile, exhibiting the slipper shape. The center of mass of the cell moves towards a forward position, and the leading part of the cell becomes thicker. Further increasing C_κ, this configuration becomes unstable and the RBC moves back to the axis, now acquiring a parachute like shape.

eventually migrates from the center line, displaced to a lateral position in the channel. Cells initially placed close to the wall migrate in the opposite direction, stabilizing at a close but outer (closer to the wall) position than those starting from the center, forming a band of stable lateral positions where cells are localized. This band narrows for increasing C_κ. In this intermediate regime, the so-called slipper morphology, the RBC is characterized by an asymmetric shape and orientation with respect to the local flow profile, with the leading lobe of the cell being bulkier than the trailing one, leading to the usual denomination of slipper or slipper-bowl shape. At high capillaries, the off center positions become unstable and the RBC returns to its axial position, but the strong fluid flow forces it to bend and to acquire the parachute like shape, in which the RBC is again normal to the flow direction but both edges of the cell are bent, coupled to the parabolic profile of the flow.

Energetic contributions

The three morphological regimes previously introduced can be understood in terms of the RBC deformation energy, as shown in Figure 8.3A, where the dimensionless bending energy $\mathcal{F}_b/\kappa$, expression (5.22), is plotted as a function of C_κ. The deformation energy is expressed as the excess energy with respect to the reference state,

the equilibrium discocyte. In the discocyte regime, the bending energy gradually increases from the equilibrium one, as the cell is forced to bend and couple its surface to the incoming flow. The bending energy peaks before the RBC shows a marked migration towards an off center position, where it aligns its axis with the local flow profile and this configuration allows a relaxation of the bending energy by a recovery of a more planar shape, the slipper-bowl. We define the limit between the discocyte and slipper regimes at the maximum bending energy that preludes the migration of the cell, $C_\kappa = 4$. Slippers are characterized by a low deformation energy, especially at $C_\kappa < 40$. For higher C_κ, the RBC develops a thicker leading lobe to stabilize the horizontal inclination, and this asymmetric deformation is increasingly penalized by the elastic energy. Parachutes are highly distorted shapes, penalized by a high deformation energy. The transition between typical slipper and parachute energies is sharp, and we place the limit of the parachute regime just before the first high-energy configuration found, corresponding to the cell g in Figure 8.2, at $C_\kappa \sim 98$. Cells g and h of Figure 8.5 could be arbitrarily identified as slippers attending to morphological criteria, given that they still maintain an important asymmetry. A classic symmetric parachute, cell i, is found at $C_\kappa = 111$.

Figure 8.3B shows the ratio between the bending energy and the surface incompressibility contributions to the membrane elastic energy (5.26). At low C_κ, the RBC deformation induced by the flow is weak and the stretching imposed to the membrane is negligible. The RBC elastic energy is therefore dominated by the bending contribution. At intermediate C_κ, RBCs undergo larger deformations and the incompressibility contribution becomes comparable to the bending one. The formation of slippers far from the axis roughly defines when the incompressibility becomes dominant. For higher C_κ, the incompressibility plays a relevant role in the cell dynamics. If it is removed (effectively performed in our simulations by setting the Lagrange multiplier to zero), the object lengthens and undergoes extreme deformations. The incrompressibility arises as a crucial ingredient in the preservation of a compact shape, and as a consequence, RBCs flowing are high confinement are subjected to strong membrane tensions.

RBC morphologies

In this section we deal in detail with the morphological characterization of each regime. The parameters studied to describe each morphology are the shape distance to the discocyte, and the shape asymmetry with respect to the cell axis. The shape distance provides a measure of the amplitude of the deformation from the reference shape, fixed here as the relaxed RBC discocyte. It is defined as $\Delta_s = \sum_i |\vec{r}_i - \vec{r}_i^0|/\Delta_s^0$, where $i = 1, .., N$ are the sequence of N points of the cell

contour, and $\vec{r}$ and $\vec{r}^0$ represent the position vector of the deformed and relaxed shapes, respectively (see Figure 8.4A, inset). Δ_s^0 corresponds to a reference value of the distance between the equilibrium shape and the ellipse with equivalent perimeter and area. The shape asymmetry $\Lambda_A = (A_1 - A_2)/(A_1 + A_2)$, where A_1 and A_2 are the areas of the regions separated by the cell axis, measures the asymmetry of the deformed shape. Two asymmetries can be calculated, either with respect to the major (disk diameter in 3D) or the minor (disk thickness in 3D) axis (see Figure 8.4B, inset).

Discocytes .– RBCs maintain a discocytic shape close to its equilibrium morphology for capillaries $C_\kappa \lesssim 5$. For $C_\kappa > 2$ the RBC deforms into a slightly asymmetric shape, bending and coupling its shape to the external flow. RBCs maintain, however, a symmetric position in the channel and remain moving normal to the flow direction (see Figure 8.2). The effective viscosity in this regime is high compared to that of the solvent, corresponding to the plateau when RBCs are close to the rigid limit. RBCs occupy a large proportion of the channel section and thus force the solvent to flow through thin layers between the RBC and the walls. Part of the shear-thinning behaviour, corresponding to the region when the RBC deforms and curves, also takes place within the discocyte regime. The range of C_κ characteristic of this regime requires velocities $< 5\mu$m/s, below the typical ones affordable in experiments, and therefore these shapes are rarely observed in experiments at high confinement.

Slippers .– By gradually increasing the flow velocity, the fluid pressure is large enough to force the RBC to deform and bend, adapting its shape to the flow profile, and losing its symmetric discoid shape. Eventually, RBCs focus to a lateral position, and depending on the initial height their flowing within a band of permitted trajectories, at roughly $h_{cm}/R \approx 0.22$. In the capillary range $C_\kappa \approx 10-90$, the RBC stays off-center adopting the slipper morphology with very limited changes on its shape. Although the term slipper has been applied for different morphologies in the literature, the energetic criteria used here corresponds to the slipper-bowl shape that RBCs adopt when laterally displaced. The asymmetric position is accompanied by a tank-treading motion, characterized by a continuous rotation of the membrane while flowing. The switch from the axial to the stable lateral position requires of a small increase in the capillary, from $C_\kappa \sim 7$ to ~ 12. Far from the central region, where the curvature of the flow profile is lower, the RBC recovers a symmetric shape, closer to the equilibrium one (Figure 8.4 A), similar to a bowl. It gradually aligns its main axis with the flow, reaching a nearly horizontal orientation at high capillaries. In the 3D analogy, the RBC will flow with its disk parallel to the walls. In the slipper regime, the asymmetry along the major axis reduces to nearly zero (Figure 8.4 B). However, the center of mass is gradually displaced to a forward position as the leading lobe becomes thicker for

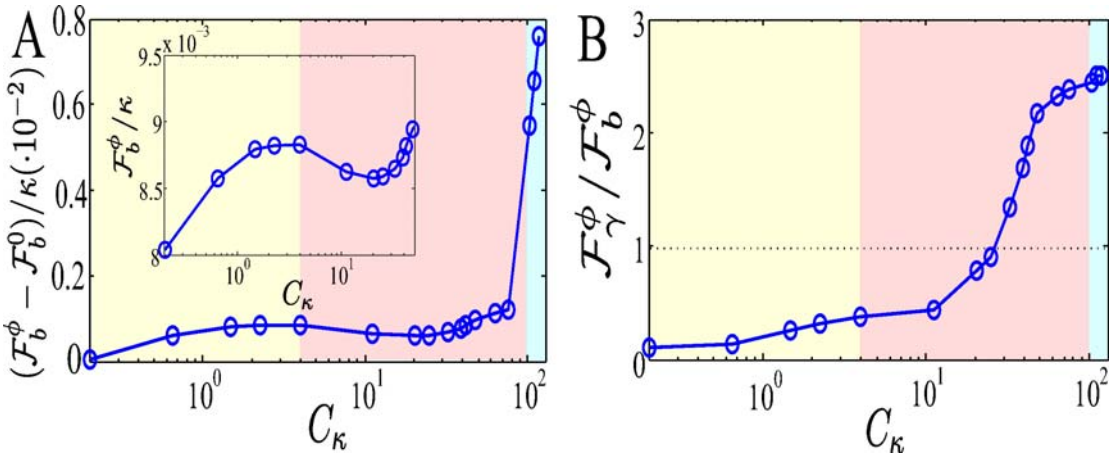

Figure 8.3: (A) Bending energy of representative morphologies of RBCs in parabolic flow (first term in expression (5.26)), expressed as excess energy from the equilibrium discocyte, $\mathcal{F}_b^0$. Discocytes are obviousy the shapes with less energy (as they are the closest to the equilibrium shape). However, when they start to deform their energy considerably increases. In this sense, the lateral migration allows relaxation of the elastic energy as the RBC recovers more symmetric, discocytic-like shapes (see below). Parachutes are much severely penalized shapes. The inset shows a zoom up of the energy curve at low C_κ, where the relaxation of the bending energy when the cell assumes a slipper shape can be observed. (B) Ratio between the incompressibility contribution (second term in eqn 4.4, associated to the Lagrange multiplier that ensures membrane inextensibility), and the bending energy. At low capillaries, the cell is nearly rigid and the membrane does not undertake relevant stretching. At higher capillaries, when the bending forces are much weaker than the fluid forces, the incompressibility represents the dominant contribution to the elastic deformation.

increasing capillary number, as shown in Figure 8.4 B, where the asymmetry along the minor axis increases whereas the asymmetry along the major axis remains at low values. The effective viscosity in this regime continues decreasing with the migration and it reaches a value $\sim 1.05\eta_0$ when the RBC is already on its lateral position deformed in a slipper-bowl shape. Experimentally, isolated slippers are observed at higher values of C_κ, close to the transition to the parachute (Abkarian et al., 2008).

Parachutes .– For $C_\kappa > 90$, the increasing asymmetry along the minor axis leads to a shape in which the leading lobe is much thicker than the trailing one, and eventually this configuration becomes unstable and the RBC returns to a centered position. The RBC acquires the symmetric parachute shape, a severely deformed morphology with respect to the equilibrium discocyte. The transition from slippers to parachutes is rather abrupt and we find parachutes similar to that observed in experiments (centered and highly curved, *eg* cell *i* in Figure 8.2) at $C_\kappa > 105$, in good agreement with previous numerical ($C_\kappa \sim 112$ in Kaoui et al. (2009)) and experimental results ($C_\kappa \sim 110$ in Tomaioulo et al. (2009)), assuming

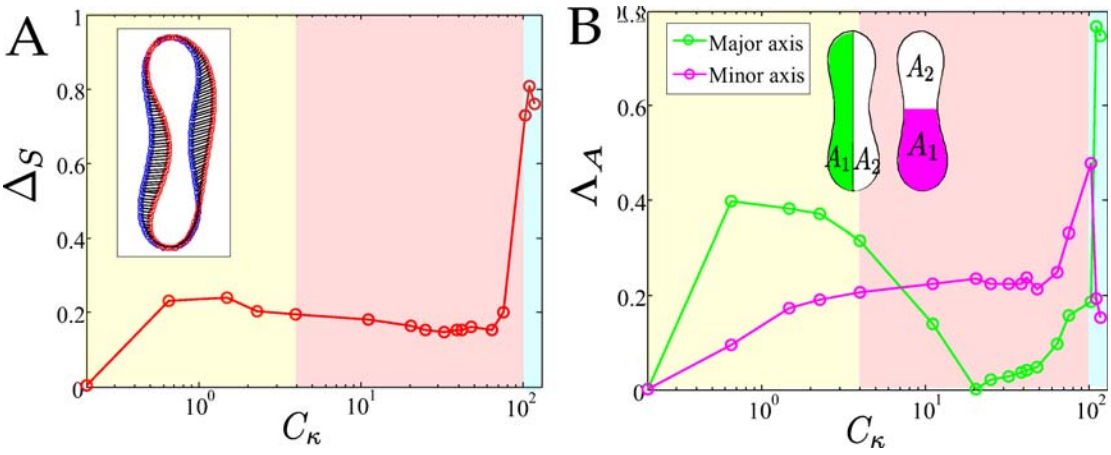

Figure 8.4: Morphological characterization of RBCs in a parabolic flow. (A) Shape distance $\Delta_s = \sum_i |\vec{r}_i - \vec{r}_i^0|/\Delta_s^0$, where $i = 1, .., N$ are the sequence of N points of the cell contour, $\vec{r}$ is the position vector and the 0 refers to the equiblibrium configuration. This parameter is normalized with the shape distance to the ellipse of same area and perimeter, Δ_s^0. The shape distance between slippers and the equilibrium discocyte is lower than discocytic shapes that remain more centered and are forced to bend. Parachutes represent, as suggested by the previous plot, large deformations from the equilibrium shape. (B) Asymmetry of each shape, defined as $\Lambda_A = (A_1 - A_2)/(A_1 + A_2)$ where A_1 and A_2 are the areas at both sides of the minor or major axis. The axis is defined as the segment between the two most distant points of the cell contour (major axis) and the normal to this segment (minor axis). Interestingly, the asymmetry along the major axis of the RBC almost vanishes in the slippers. However, the asymmetry along the minor axis increases as the cell becomes thicker in the leading edge, until it eventually transforms into a parachute.

a typical value of the bending rigidity $\kappa \sim 2{\cdot}10^{-19}$J). The effective viscosity within this regime is very close to that of the solvent, as viscous forces are much larger than elastic ones and the RBC is not able to significantly perturb the surrounding flow.

8.3 Effective viscosity of RBC suspensions

The effective viscosity for an isolated RBC is shown in Figure 8.5. At low C_κ, the system presents a certain memory of the initial conditions and the steady shape will depend on its initial configuration. This effect implies that for each C_κ, there is a set of possible shapes, orientations and positions of the RBC flowing in the channel. We plot in Figure 8.5 an average, effective viscosity, which we obtain from averaging over a set of 21 different initial configurations, including 3 different heights along the channel section and 7 different RBC inclinations. Further details on this phenomena are provided in Chapter 10.

At low C_κ, the viscosity presents a newtonian behaviour, in which the RBC behaves as a rigid object (without deformation) pushed by the flow. When the external forcing becomes comparable with respect to the elastic membrane forces, the RBC starts to deform and the fluid viscosity decreases, showing a strong shear-thinning behaviour. The viscosity continues decreasing with the focusing of RBCs to a thin lateral band, but its decay gradually decreases when this band narrows, and eventually the cells are localized at a unique position. The effect of the flow reduces to a increasing orientation of the cell, entering in the asymptotic region in which the viscosity converges to that of the solvent. For higher C_κ the elastic forces of the RBC are largely exceeded by the flow forcing and the elastic contribution to the viscosity is small. The off center position permits the cell to align with the flow profile, acquiring gradually an horizontal inclination, minimizing the cell cross-section exposed to the incoming flow and thus reducing the dissipation. Centered cells present a normal orientation which is less favourable. Thereby, the alignment of the cell requires a previous migration towards a lateral position, and both mechanisms play an important role to explain the shear-thinning behaviour of the suspension.

In Figure 8.5 (inset), the effective viscosity is shown for different bending rigidities, to test if C_κ represents an appropriate parameter to characterize the rheology of the fluid. For each bending rigidity, we sweep the external forcing f_0 covering in all the cases the same range of C_κ. Thus, for each capillary number analyzed, the ratio f_0/κ is constant. Accordingly, the curves should collapse indicating that C_κ captures the relevant mechanisms controlling blood viscosity, as shown in Figure 8.5.

8.4 Flow description

In this section, we describe in detail the flow characteristics and stress profile for the three main regimes. In Figure 8.6 A, we show the colormap of the velocity field in the flow direction, v_z, from which we have substracted the contribution of the unperturbed Poiseuille v_z^0 in the absence of cell. The velocity is normalized by the maximum velocity of the unperturbed flow, $v_z^{0,max}$. Within the slipper regime, the flow is considerably disrupted, and at the region occupied by the cell the velocity reduces down to a 50% of the imposed value. Only close enough to the walls the velocity converges to the reference one, forced by the stick condition at the boundary. The velocity profile is therefore more planar (compared to the parabolic profile of the unperturbed Poseuille) at the center region. In the slipper regime, flow disruption is weaker, roughly 20% in the region occupied by the cell, and the perturbation induced by the cell is obviously asymmetric. In the parachute regime,

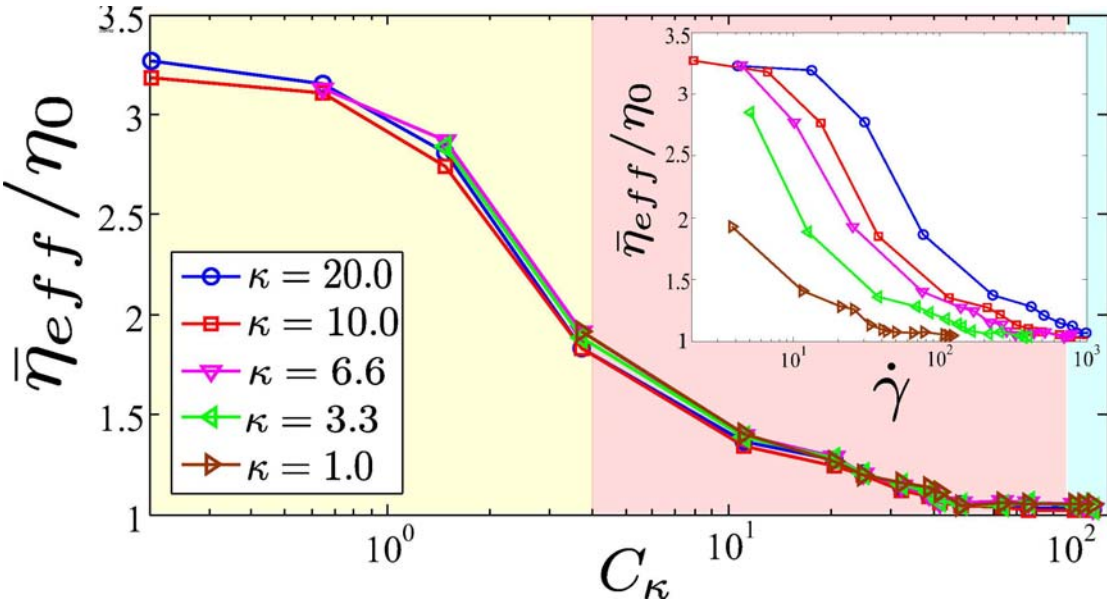

Figure 8.5: Effective viscosity of a RBC suspension as a function of the capillary number for different bending rigidities, κ. The value presented here, $\bar{\eta}_{eff}$, is averaged for different initial conditions of the RBC, see main text for details. The coloured regions correspond to the three morphological regimes (see Figure 8.2). The curves for different rigidities as a function of the shear rate show the sensitivity of the viscosity and RBC morphology to the rigidity of its membrane (inset); however, the curves collapse when the relative effect between the viscous and elastic forces is considered. The curve presents three regions: *(i)* a newtonian plateau at low capillaries when it achieves a value ~ 3.5 (which depends on the volume fraction; in these simulations, $\phi_{ves} = 0.012$). *(ii)* a region of strong shear thinning decay, converging to the solvent viscosity; and *(iii)* an assymptotic region in which the viscosity converges to that of the solvent. Both the shear rate and the bending rigidity, which are subsequentially incorporated to the dimensionless number C_κ, are normalized here with respect to their lowest value used in the simulations.

the flow recovers a more symmetric profile, and the velocity decrease at the central region is $25-30\%$, higher than in the slipper. This fact agrees with the general observation that centered cells flow slower than those situated at the lateral, as we study in Chapter 9. The length of the perturbation is also important as it determines the range of the hydrodynamics interactions present. For instance, if a cell is situated close to the discocyte shown in Figure 8.6 A, it will interact with a very perturbed flow, attenuated by the original cell. Thus, the second cell will be subjected to a effective lower C_κ than the actual imposed, and a different deformations (such as lower deformations) are likely expected. This effect, called termed here as *screening*, will be studied in detail in Chapter 11, when several cells are interacting. Figure 8.6 A intuitively shows that the length of the perturbed flow can be associated with an interaction distance, which reduces with C_κ. The dependence of the hydrodynamic interactions with the flow will be also adressed in Chapter 11.

The vorticity map for the different regimes is shown in Figure 8.6 B. The vorticity here corresponds to the normal component, $\omega = \omega_y$, and we also extract the contribution of the unperturbed Poiseuille and normalize with respect to its maximum value. In the discocyte regime, the vorticity is homogeneously distributed, with maximum values at the edges of the cell closer to the walls. In the slipper regime, however, the velocity is extremely localized at the trailing lobe of the cell, and the rest of the domain presents neglible vorticity. The pattern contrasts with that obtained for parachutes, in which the vorticity is extensively distributed in the regions surrounding the cell. Accordingly, the development of slippers seems to reduce the formation of vortices with respect to the centered configurations.

From the viscous stress tensor, $\sigma^\eta_{\alpha\beta} = -\eta[(\nabla_\alpha v_\beta)+(\nabla_\beta v_\alpha)^T]$, we can obtain the shear stress profile, in our geometry given by the component σ^η_{xz}. This magnitude relates with the viscosity of the suspension, as explained in Section 8.1. The distribution of shear stresses for the three main regimes is shown in Figure 8.7 A, for the same conditions as in Figure 8.6. Analogously to the previous plots, we extract the contribution from the unperturbed Poiseuille and normalize with the maximum value at each configuration. In the discocyte regime, shear stresses concentrate on the inner region of the cell, and in the region between the cell and the wall where the fluid is pushed by both the membrane and the wall. In the slipper regime, the stress reduces considerably and it is concentrated around the trailing lobe of the cell, being of relative low value in the rest of inner region of the cell. In contrast, the centered parachute presents high shear stresses in the interior fluid, particularly at both cell lobes.

Finally, in Figure 8.7 the map of normal membrane force, $f^{mem}_n = \hat{n}_\alpha f^{mem}_\alpha$, is shown, normalized by the external forcing f_0. $\hat{n}$ is the normal vector to the membrane surface, computed from $\hat{n} = \nabla\phi/|\nabla\phi|$. The results show that in the

symmetric configurations, discocyte and parachute, the membrane presents an homogeneous tension distributed along their contour, whereas in the case of the slipper, the membrane force is concentrated on the two extremes of the cell, whereas the lateral edges parallel to the major axis are exposed to very reduced forces. The magnitude of the force is high compared to that of the external forcing, roughly 50 times higher. It is also interesting that maximum forces in the parachute are slightly higher than those found in the slipper, in spite of the increase in the external forcing by a factor of 2. This fact suggests that cell membrane at the slipper regime presents lower elastic stresses than the parachute, in accordance with the results from the deformation energy obtained in Section 8.2.

8.5 Discussion

The sequence of RBC morphologies depicted here has been also found in experimental studies with RBCs (Abkarian et al., 2008; Tomaioulo et al., 2009), with qualitative good agreement between the shapes found in our simulations and those observed in the laboratory, as shown in Figure 8.8. Likewise, our results agree with the shapes found in previous numerical studies in which the membrane elasticity incorporates an in-plane contribution (Noguchi and Gompper, 2005; Shi et al., 2012), *ie* both shear and area-compression, suggesting that the importance of these contributions is limited in this system and the cell dynamics is effectively dominated by the bending elasticity and area incompressibility. This hypothesis is in good agreement with some recent results, in which the dynamic behaviour of RBC flow has been analyzed for healthy cells, and for others in which the cytoskeleton was severely stiffened by addition of aminade (Forsyth et al., 2011). Aminade produces rigidity of the spectrin mesh, but it does not affects the properties of the bilayer. Healthy and stiffened cells were shown to present virtually the same behaviour, concluding that the influence of the cytoskeleton in this system is limited.

The relative softness of RBCs, which for typical *in vitro* flow velocities at highly confined channels lie in the advanced slipper and parachute regimes, implies that their resistance to flow at normal conditions is reduced. However, in vivo flow is usually characterized by lower velocities and then the fluidity of blood is drastically dependent on the cell deformability. A potential stiffening of their membrane, as occurs in several pathologies (including malaria) or during the development of echinocytes, could lead to severe alterations in their morphology and rheology. For instance, measurements of the bending rigidity during morphological changes have reported increases of roughly 2 and 5 times in the bending rigidity of echinocytes and spherocytes, respectively (Park et al., 2010b). This change could cause the

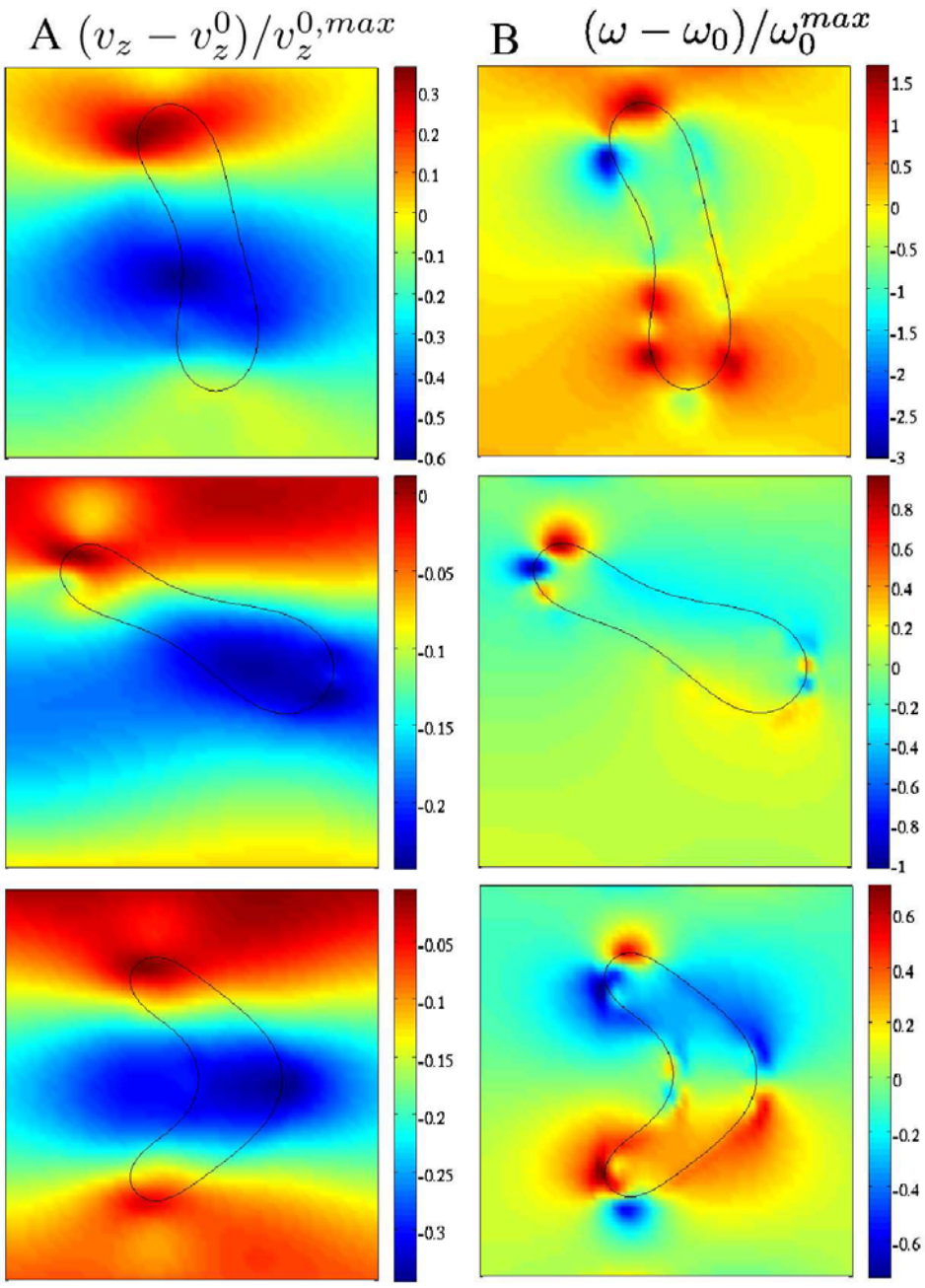

Figure 8.6: (A) Velocity of a RBC flowing in a channel; from top to bottom, in the discocyte, slipper, and parachute regimes, for $C_\kappa =$, respectively. The contribution of the original Poiseuille in the absence of cell, v_z^0, has been substracted, and it has been normalized with respect to the maximum velocity. (B) Vorticity field, corresponding to the only non zero component in this geometry, $\omega = \omega_0$. The contribution of the unperturbed Poiseuille has been removed.

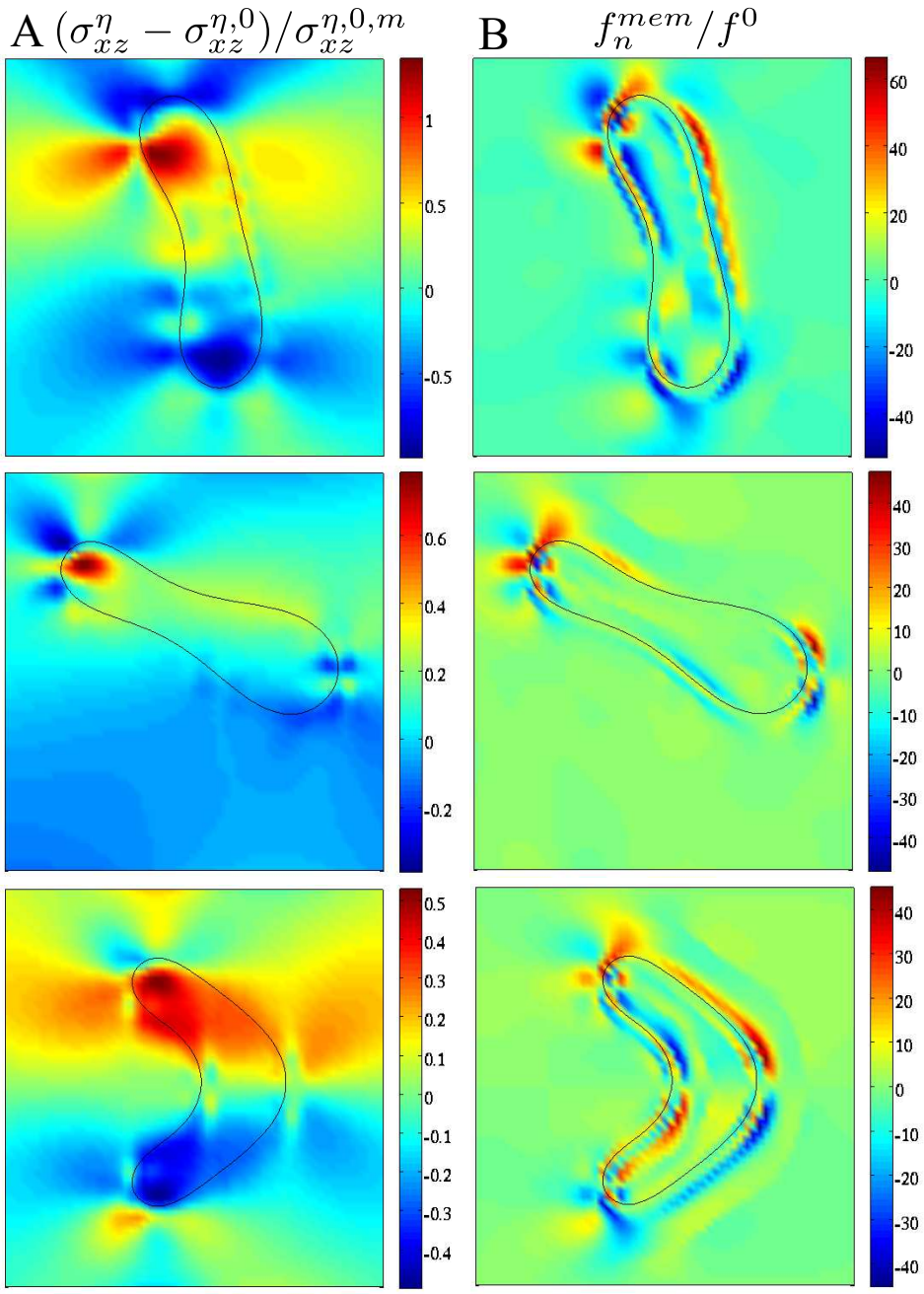

Figure 8.7: (A) Viscous shears stress, σ^{η}_{xz} of a RBC flowing in a channel; from top to bottom, in the discocyte, slipper, and parachute regimes, for $C_\kappa =$, respectively. The contribution of the original Poiseuille in the absence of cell, σ^0_{xz}, has been substracted, and it has been normalized with respect to its maximum value. (B) Normal contribution of the membrane force, $f^{mem}_n = \hat{n}_\alpha f^{mem}_\alpha$, for the different configurations. The force is normalized with the external forcing f_0 that drives the flow.

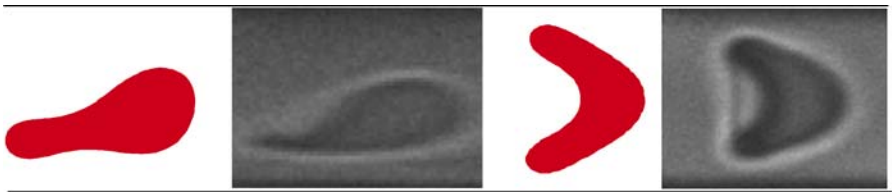

Figure 8.8: Comparison between slippers (left) and parachutes (right) observed in experiments and found in our simulations, for the same confinement $a/b = 0.8$. Experimental snapshots reproduced from Tomaioulo et al. (2009).

shift from parachute to slipper or from slipper to discocyte, affecting to the overall rheology of the suspension. Experimentally, the effect of RBC rigidity has been studied in the macroscopic rheology of RBC suspensions (Thurston, 1972), but it has received little attention in the case of single RBCs at high confinement, in spite of its importance in the development of new devices for cell targeting. Although the suitable experiments are complex, hopefully future experiments could through some light into this issue.

The three morphologies exhibited by RBCs when flowing isolated along a thin channel are also found for higher concentrations, where RBCs are closely placed each other and they present collective behaviour. McWhirter et al. (2009) studied the aggregation of several RBCs at similar conditions to the ones used here. They identified three phases, namely *(i)* the disordered-discocyte, in which the cells maintain the discocyte shape with random orientation; *(ii)* the zigzag slipper, where cells cluster in two stripes in the center of the channel, accomodating their shape to the neighbour cells; and *(iii)* the alligned parachute, formed by an array of centered parachutes. The random orientation of the cells in the disordered-discocyte phase, found at low flow velocities, might relate with the dependence we observe with the initial conditions in the discocyte regime. This disordered phase is stable for rather high capillaries; this may respond to the screening effect between cells, which atenuates the effect of the flow perturbation on each cell. The zigzag-slipper phase, in which the observed slippers present an horizontal inclination, is a highly stable configuration observed for an extensive range of capillaries, even for values in which parachutes are also found if the cell-to-cell distance is increased. One could speculate that, being a lower energy configuration with respect to the parachute, the collective effect favour a longer life span of the slipper configuration, whereas when RBCs flow isolated this shape eventually becomes unstable. The alligned parachute forms at high shear rates and large distances between cells; the shapes observed are similar to the isolated case, although they are not forced to deform as much severely.

8.6 Conclusions

An isolated RBC is found to present a non-linear rheological behaviour, characterized by a shear-thinning decay at high shear rates due to a combined effect of cell deformation and orientation with the flow. For a given flow, the effective viscosity is entirely determined by the membrane rigidity.

RBCs present three main morphologies, strongly dependent on the rigidity of their membrane. In our model the rigidity is expressed relative to the incoming flow. Very rigid cells maintain their relaxed shape, with weak deformations from the discocyte. For intermediate rigidities the cell acquires an asymmetric slipper shape, orienting its axis with the flow. For soft cells return to an axial position and acquire a parachute shape. Why cells develop this sequence and the advantages of the lateral position of the slipper is discussed in the ensuing Chapter.

Chapter 9

On the mechanisms of RBC deformation and migration

In Chapter 8 we find that RBCs flowing in confined channels assume asymmetric shapes, called slipper or slipper-bowl, at intermediate values of the capillary number. However, why RBCs adopt this morphology in detritment of a symmetric shape remains as an intriguing phenomenon, in spite of the numerous studies that have faced the problem. The lateral position of the cell can be exploited in microfluidics to separate different type of cells or particles, as we will see in Chapter 10, and the understanding of the mechanisms driving RBC deformation is therefore important.

The asymmetric position of RBCs when flowing in symmetric flows, even if their initial configuration was symmetric, indicates that there exists some kind of instability. In order to adress this question, we perform simulations comparing the behaviour of axisymmetric RBCs, which are limited to a centered position in the channel, with unconstrained RBCS (that can move freely along the channel profile), which adopt the slipper morphology, identifying the benefits and drawbacks of each configuration.

Axisymmetry is introduced imposing reflective boundary conditions at the channel axis, and therefore the dynamics of the phase and velocity fields is symmetric with respect to the axis. Accordingly, the cell must be initiliazed obeying this symmetry, with its center of mass strictly located at the axis. The imposed dynamics ensures that when the external forcing is applied, the cell will remain centered. By sweeping over a range of capillary number, we compare this configuration with the free cell, imposing that both share the same initial configuration. We explore the differencess between symmetric and asymmetric cells in the viscosity, the absolute elastic energy and dissipated energy.

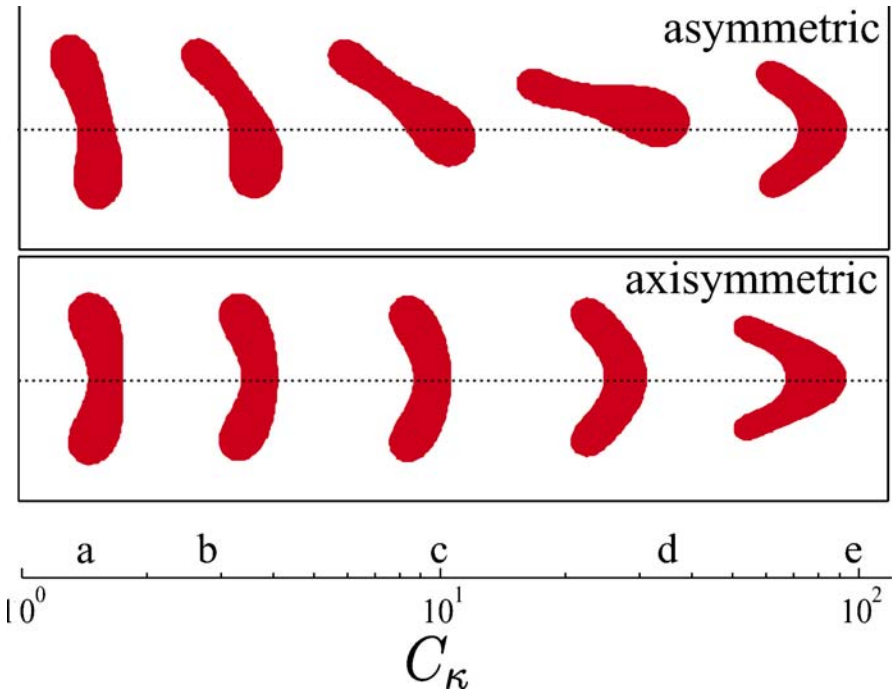

Figure 9.1: Morphologies of RBCs flowing in a confined channel, $a/b = 0.70$, for free cells that can assume asymetric shapes *(up)* and strictly axisymmetric shapes *(bottom)*. Each shape correspond to a letter $a, b, .., e$, from left to right. The respective C_κ for each configuration is shown in the bottom scale.

For convenience, we fix a system with slightly lower confinement than in Chapter 8, $a/b = 0.70$, and lower volume fraction. In Figure 9.1 some examples of the morphologies for each case are shown. The case of the asymmetric RBC is similar to the results found in Chapter 8: at low C_κ, cells remain centered but already showing a certain asymmetry. At intermediate C_κ RBCs assume the slipper shape at a lateral position in the channel, and they orient their axis with the flow. At high C_κ, the cell returns to the axis and assumes a parachute shape. The sequence of axisymmetric shapes is, as expected, considerably different. During an extensive range of C_κ, RBCs exhibit a very similar shape, with and increasingly bent profile for higher values of C_κ, but maintaing both edges of the cell parallel. Only for $C_\kappa > 50$ cells assume parachute shapes, with a cup-like profile in which the edges of the cell are uncoupled.

9.1 Effective viscosity

The effective viscosity for both the symmetric and asymmetric cells is shown in Figure 9.2, measured from the expression provided in Chapter 8, (8.2). The shear-thinning behaviour is recovered in both cases, although asymmetric cells present

lower resistance to flow along the entire range of C_κ explored, only converging at very high capillaries when both configurations are similar. The shear-thinning is more pronounced in asymmetric RBCs when the cell displaces from the center, at the beginning of the slipper regime, and reduces slowly when the cell is situated far from the center. On the contrary, axisymmetric shapes show a smoother decay, converging to the solvent viscosity only at very high capillaries. Largest deviations in the effective viscosity are observed at the slipper regime, demonstrating that the lateral position and orientation of the slipper actually enhance the suspension fluidity with respect to symmetric configurations. Nonetheless, even at low capillary number there is a considerable difference in the viscosity, suggesting that asymmetry, even if weak deformations or migrations are involved, is an important mechanism to decrease the viscosity.

The velocity of the RBC center of mass for each configuration reveals that asymmetric cells not only enable a higher flow rate of the suspension but also move faster than centered cells, especially in the advanced slipper regime, as shown in Figure 9.2 (inset), where we have expressed the velocities in the co-moving frame of the suspension. This agrees with the well-known fact that particles flowing off-center lead the flow whereas those situated close to the axis lag the flow (Matas et al., 2004). At low C_κ, the velocity of both configurations is virtually the same, suggesting that fast RBC velocities are only achieved when cells are situated far from the axis.

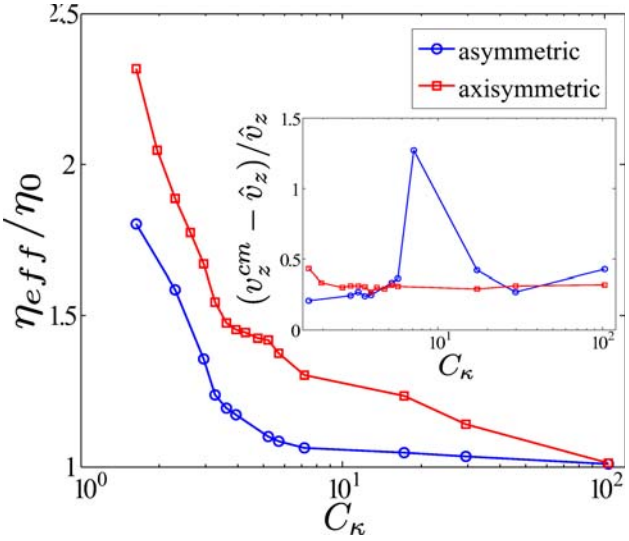

Figure 9.2: Effective viscosity of a RBC suspension as a function of C_κ for asymmetric and axisymmetric cells. (Inset) Velocity of the RBC center of mass with respect to the mean velocity of the whole suspension. The velocity is normalized by $\hat{v}_z$.

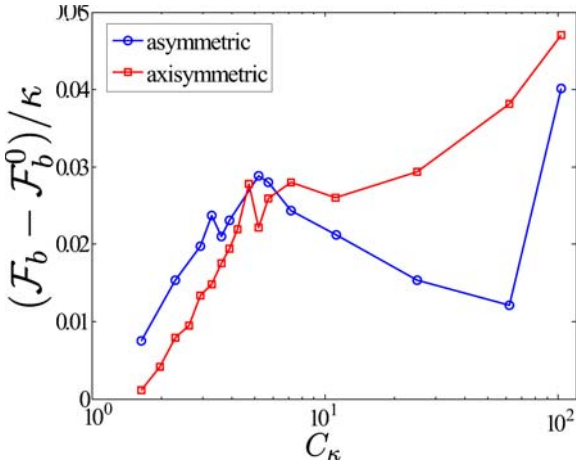

Figure 9.3: Bending energy of a RBC as a function of C_κ for axisymmetric and symmetric cases, expressed as excess energy from the relaxed discocyte shape.

9.2 Elastic energy

In Chapter 8 we have observed that the lateral position of the cell within the slipper regime allows the cell to recover a symmetric shape, closer to the resting discocyte, and this implies a relaxation of the deformation energy stored. In Figure 9.3 this behaviour is compared with the energy landscape of an axisymmetric cell. Centered cells bend and deviate from the original discocyte monotonously. At low C_κ, the deformation energy increases similarly to the asymmetric case, being slightly lower as a consequence of the penalization to the asymmetry. However, the energy relaxation found for slippers at intermediate C_κ is not observed in the axisymmetric case as the centered position forces a bent profile of the cell, inhibiting any mechanism of shape recovery. Hence, the elastic energy of axisymmetric cells increases monotonously with C_κ. Only when free cells return to a center position at high capillary, within the parachute regime, the deformation energy of both configurations is similar. Asymmetric cells strongly benefit from their capability to deform and adopt symmetric shapes by a low deformation energy, in contrast to axisymmetric cells, which are severely penalized by their more curved shape.

9.3 Energy dissipation

The flow is driven by an external forcing analogous to a pressure gradient. The energetic cost of maintaining this forcing can be calculated from the Navier-Stokes equation. At low Re, the equations reads,

$$\rho \frac{\partial v_\beta}{\partial t} = \nabla_\alpha [\eta \nabla_\alpha v_\beta + \sigma^{mem}_{\alpha\beta}] + \rho f^{ext}_\beta. \tag{9.1}$$

Under conditions of mechanical equilibrium the left hand side vanishes, and after multiplying by the velocity field v_β and integrating over the whole volume,

$$\rho \int v_\beta f^{ext}_\beta dV = -\eta \int v_\beta \nabla_\alpha \nabla_\alpha v_\beta dV - \int v_\beta \nabla_\alpha \sigma^{mem}_{\alpha\beta} dV. \tag{9.2}$$

The left hand side can be readily identified as the power introduced to the system which maintains the fluid flow,

$$W_{ext} = \rho \int v_\beta f^{ext}_\beta dV, \tag{9.3}$$

The first term on the right side of (9.2) can be integrated by parts, obtaining the viscous dissipation,

$$W_\eta = \eta_0 \int (\nabla_\alpha v_\beta)^2 dV. \tag{9.4}$$

The remaining term can be rewritten in terms of the force exerted by the membrane, obtaining the elastic power of the membrane,

$$W_{mem} = \int v_\beta f^{mem}_\beta dV. \tag{9.5}$$

Hence, equation (9.2) is formulated as

$$W_{ext} = W_\eta - W_{mem}. \tag{9.6}$$

Note the that we use the term dissipation and power according to the sign of each term on the left relative to the sign of the external power. However, W_{mem} is computed from the force exerted by the membrane, and thus it represents a reactive term; it is therefore expected to be negative.

The formal equivalence between (9.4) and (9.5) is proven by introducing the hydrodynamic stress tensor $\sigma^\eta_{\alpha\beta} = -\eta \nabla_\alpha v_\beta$. Although W_{mem} is calculated from the integral over the whole domain, f_{mem} vanishes far from the interface. Hence, whereas W_η and W_{ext} are extensive variables that depend on the size of the system, W_{mem} only depends on the membrane, regardless of the domain size. We therefore rescale the former with the volume fraction in order to obtain comparable variables. In this Section we analyze how the external energy is distributed in

the asymmetric and axisymmetric case. All the powers are expressed in a dimensionaless form relative to the reference elastic power, given by the ratio between the energy scale of the system, κ, and the elastic relaxation time of the membrane, $t_\kappa = \eta_0 a^3/\kappa$, leading to $W_\kappa^0 = \kappa^2/\eta_0 a^3$.

9.3.1 External power

From the definition of the external power, it is obvious that fluid suspensions with a higher flow rate require of higher external power than those with lower flow rates, if the external forcing is maintained constant. As expected, the comparison between the external power for asymmetric and axisymmetric shapes, Figure 9.4, shows that high powers are required for asymmetric cells over the entire range of C_κ, but specifically in the slipper regime when the different behaviour of each configuration is more accentuated.

In Figure 9.4 B, we test the energy balance of (9.6) in our simulations, comparing the external power with the sum of the contributions to the energy dissipation. We observe a good agreement between both terms at low capillaries, but a consistent though slight deviation at high C_κ, with an overestimation of the external power of roughly 7%. We associate this error with the numerical precission due to the mesh discretization. We check this hypothesis by comparing (9.3) and (9.4) for a single fluid (in the absence of membrane), in which the newtonian flow is given by the Poiseuille profile and it is straightforward to prove that both expressions coincide. In this case, we still observe a deviation of 4%, which must be necessarily due to numerical precission. The difference of 3% in the presence of the cell might be explained by errors in the estimation of the membrane force.

9.3.2 Elastic membrane power

The elastic power, ploted in Figure 9.5 A, shows a markedly different behaviour between the asymmetric and axisymmetric RBCs. In both cases the power is negative, reflecting its reactive nature. At low C_κ, the power is similar in both configurations and increases in magnitude as the cell bends. For asymmetric shapes, however, the power peaks in the transition to the slipper at $C_\kappa \sim 5$, meaning that the relaxation of the elastic energy of the membrane has anologously associated a strong reduction of the dissipated energy of the membrane. During the entire slipper regime the elastic energy remains below 5% of the total power. The evolution of the elastic power for axisymmetric cells is more complex. At low C_κ, it increases similarly to the asymmetric case, but this increasing continues up to $C_\kappa \sim 7$, when it peaks and starts to decay towards values similar to that of the slipper, at high $C_\kappa \sim 100$. The change in the tendency is accompanied

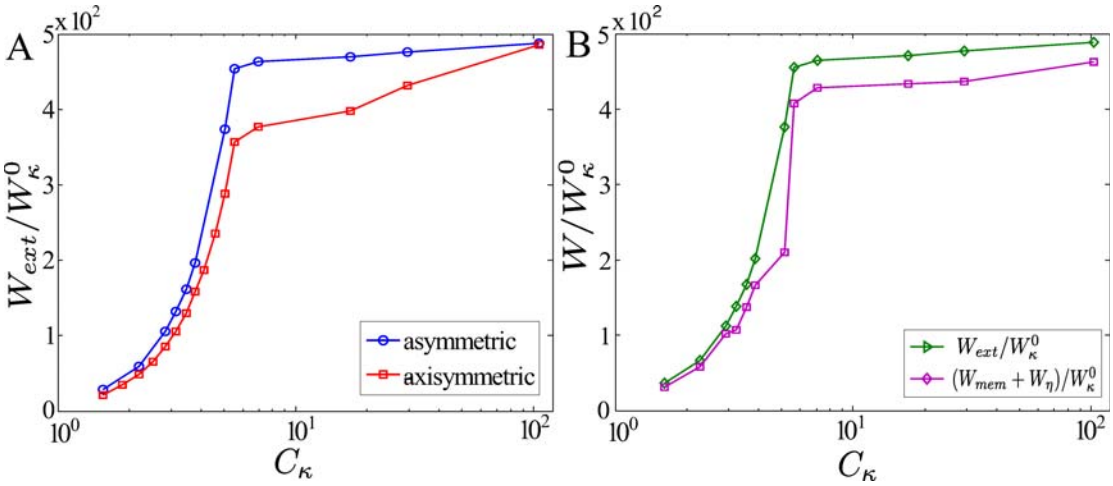

Figure 9.4: (A) External power introduced to the system, (9.3), as a function of C_κ, for both the asymmetric and axisymmetric case. The power is higher for asymmetric shapes due to its higher flow rate, and therefore differences are more pronounced at the slipper regime. (B) Energy balance given by equation (9.6). The external power as defined in (9.3) is compared to the sum of the contributions of the viscous dissipation 9.4 and the elastic power (9.5). Differences around 7% are observed at high capillary number, which we associate to numerical precission (see main text).

by a subtle morphological transition. For $C_\kappa < 7$, axisymmetric shapes show weak deformations, bending their profile but maintaining parallel leading and trailing edges, reminiscent of a *boomerang* shape. For $C_\kappa > 7$, centered cells lose this symmetry, their edges are no longer parallel and deform into more cup-like shapes, with a central core at the center region of the disk, eventually assuming the classic parachute shape. Examples of these morphologies are shown in the inset of Figure 9.5; cell *a*, still weakly bent and with parallel edges, shows a high dissipation. Parachutes *b, c,* and especially *d*, with a subtle different profile, present lower dissipation. Although, a priori, it is difficult to understand how this change in the morphology triggers the decay in the dissipated elastic energy, the regime of real parachutes shows a very different behaviour than the boomerang-like shapes. Indeed, the regime at high C_κ in which centered cells equate their dissipated energy with that of the slippers, agrees when free cells return to the center and assume parachute shapes.

The elastic power presents a different behaviour if expressed relative to the total power, instead of in absolute value, as shown in Figure 9.5 B. In this case, centered vesicles present a homogeneous decay in the elastic power from the maximum value at low C_κ. Asymmetric shapes, on the contrary, present a marked reduction of the dissipation at low C_κ, and the contribution to the total dissipation is low (almost negligible) at intermediate and high values of the capillary number.

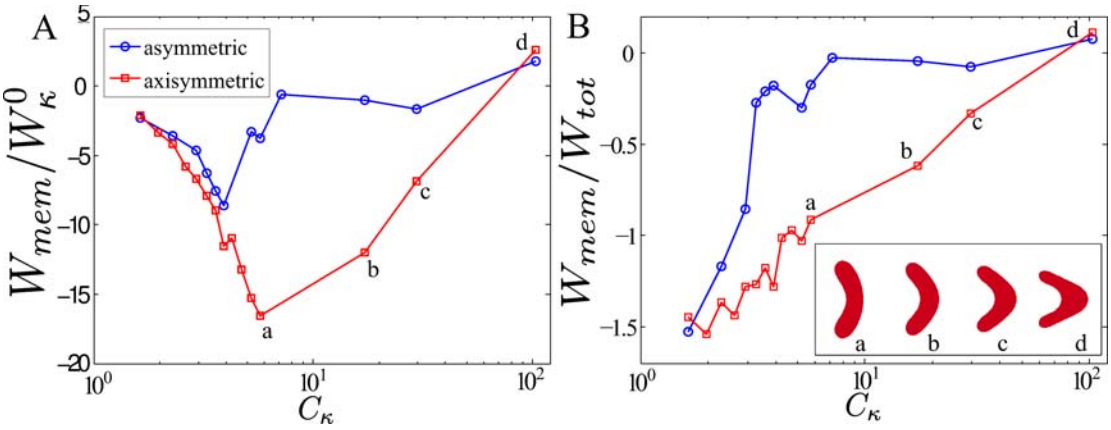

Figure 9.5: (A) Elastic power as a function of C_κ for asymmetric and axisymmetric RBCs. Both contributions are negative, reflecting that it represents a reactive term. For asymetric shapes, the formation of the slipper is associated to a strong reduction of the elastic power. In the case of axisymmetric cells, the reduction of the power is more difficult to identify in terms of the cell behaviour, but we find the peak corresponds to the transition from the *boomerang* to the real *parachute* morphologies (as can be seen in the inset of (B)). (B) Elastic power relative to the total power $W_{mem} + W_\eta$.

9.3.3 Viscous dissipation

The total viscous dissipation corresponds to the remaining term of (9.6), and is shown in Figure 9.6 A. Dissipation increases homogeneously in both cases, but the increment is much sharper for asymmetric shapes as a result of the damping observed in the elastic power. Hence, once the elastic power is minimum, most of the external energy introduced is dissipated by the fluid. For axisymmetric shapes, however, the balance is more homogeneous and the viscous dissipation shows a smoother increase. In addition to the total viscous dissipation, it is interesting to study where this energy is preferentially dissipated. In Figure 9.6 B, we plot the dissipation in the inner fluid of the cell. Thus, the integral of (9.4) is reduced to the region $\{\phi > 0\}$, and expressed relative to W_{tot}. The results suggest that at low C_κ dissipation is concentrated in the interior of the cell (note that the volume fraction is low ~ 0.08 but the inner dissipation corresponds to a 0.7 of the total). The inner dissipation, however, decreases reducing to 0.1 at high C_κ. The comparison between symmetric and axisymmetric shapes does not show substantial differences in their behaviour, suggesting that the distribution of the viscous dissipation is not a relevant mechanism driving RBC migration towards asymmetric position.

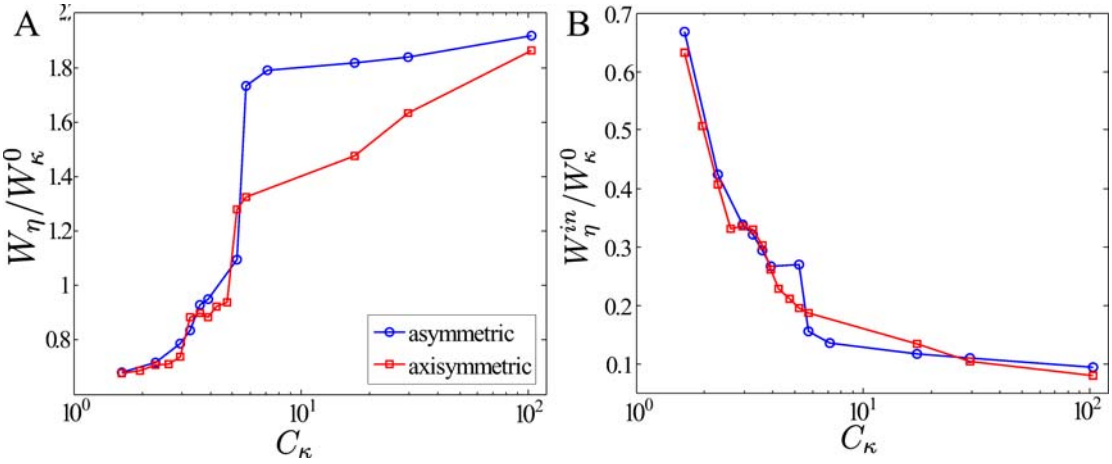

Figure 9.6: (A) Viscous dissipation as a function of C_κ. (B) Viscous dissipation of the internal fluid of the cell, relative to the total viscous dissipation.

9.4 Conclusions

There has been an intense debate about the significance and advantages of the asymmetric shapes and positions that RBCs acquire while flowing in narrow tubes. Secomb (2011) attributed this phenomenon to the reduction of the flow resistance, as demonstrated in Figure 9.2. Kaoui et al. (2009), on the contrary, proposed that the formation of slippers responds to a reduction of the velocity lag between the cell and the flow. Although we agree with these observations, it is difficult to recognize them as driving mechanisms of the migration. There is a number of other aspects, of similar physical meaning, that distinguish the behaviour of symmetric and slipper shapes. For instance, as shown in Chapter 8, slippers also benefit from a low vorticity. The formation of vortices can prelude a flow instability, and hence slippers can be understood as more stable configurations against hydrodynamic instabilities.

The results presented in this Chapter suggest that the minimization of the viscous dissipation does not play a key role in driving the migration of cells towards off-center positions. However, the cell benefits from this lateral position by a strong relaxation of its deformation energy and the reduction of the elastic power. Minimization of the elastic stresses induced by the flow deformation seems to be a strong advantage of the slipper morphology.

Chapter 10

RBC focusing

The manipulation of single cells in microfluific devices requires of a sutile control of the flow behaviour, as exposed in Chapter 7. Among others, the lateral position of cells and particles can be exploited to separate objects of different characteristics (*eg* shape, rigidity) in pressure-driven flow without the need of any other agent, such as an electromagnetic field.

The equilibrium position of a particle in the tube depends on several factors such as flow velocity or confinement (Matas et al., 2004). It is well known that isolated particles flowing in thick tubes move laterally (*ie* cross stream migration) towards a specific off center position, as first observed by Segré and Silberberg (1962) for rigid spheres in a Poiseuille flow, and extended later on to other objects (Jeffrey and Pearson, 1965; Han et al., 1999), and different channel geometries (Tachibana, 1973). This effect, however, is driven by an inertial drift which forces the object to leave the center (Wang and Skalak, 1969). The dynamics of the object is not critically determined by its specific properties and the off center focusing has been also observed for red blood cells and other soft entities (Carlo et al., 2007). At very narrow microchannels, when inertial effects are negligible, the absence of this drift should prevent from a lateral migration during the downstream evolution, and hard spheres and spherical vesicles does not focalize. At this regime, however, the deformability and geometry of the object arise as crucial mechanisms of symmetry breaking (Olla, 1999), and RBCs are known to present a much more complex behaviour than spherical objects (Abkarian et al., 2008). Whilst the dynamics of particles and RBCs in the presence of inertia has been extensively studied in the literature, the limit of low Reynolds number, which requires of a more accurate description of the geometry and elasticity of the object, has been scarcely tackled in spite of its relevance in microfluidics.

In this Chapter, we explore the effect of channel geometry and flow velocity to control RBC focusing and lateral position. The formation of regular trains, an in-

teresting problem in microfluidic engineering, is also studied in detail. Finally, the relevance of the object shape is also analyzed, in order to identify the differences in the dynamic behaviour between RBCs and other cells or particles.

10.1 Effective viscosity and focusing

Our results show that η_{eff} depends on the initial condition of the RBC, especially at low C_κ when the dispersion $\Delta\eta_{eff} = (\eta_{eff} - \bar{\eta}_{eff})/\bar{\eta}_{eff}$, where $\bar{\eta}_{eff}$ is the average viscosity, can be as high as 25%. The dispersion of the effective viscosity is shown in Fig 10.1 A, for a number of different configurations. In experiments, the effect of thermal noise, that allows random exploration of different orientations, may lead to a more uniform measurement. Therefore, in order to obtain a robust measurement of the viscosity, we average over a set of 7 different inclinations and 3 different lateral positions. The dispersion of each configuration is shown in Figure 10.1 B (inclinations) and C (lateral positions). According to their particular position and alignment with the flow, RBCs will offer variable resistance to flow. RBCs aligned parallel to the incoming flow and flowing close to the walls (where the shear stress decreases) present smaller contribution to the viscosity than those centered and with normal orientation, which induce a severe perturbation of the surrounding flow. Remarkably, in this region RBCs oriented symmetrically with respect to the normal flow direction (*eg*, orientation of $\theta = 45°$ and $135°$) show a similar viscosity. This could suggest that the relevant parameter controlling the value of the viscosity, within this rigid limit, is the ratio between the section occupied by the cell with the respect to the total section of the channel. The dispersion reduces for intermediate C_κ and it is negligible at high values.

The memory of the RBC to its initial configuration can be separated into two different contributing phenomena: alignment of the RBC with the flow and focusing to a final position. Due to the channel symmetry with respect to its axis, RBCs focus at two symmetric lateral bands, depending on which channel region was the cell located with respect to the axis at the initial condition. Initially centered RBCs migration is determined by numerical noise. Henceforth, we concentrate in one of the channel regions (*ie* from the axis to one of the walls), bearing in mind that symmetric phenomena occur in the opposite region. At very low C_κ, RBCs do not orient their axis with the flow, and they flow maintaining the initial position, without showing migration across streamlines. The increasing external flow forces the cell to rotate and align with the flow, but still showing a dependence with the initial position along the channel section. The dispersion of the viscosity decreases as the range of cell inclinations is reduced, but still maintaing the contribution due to the different position along the tube Further increase in-

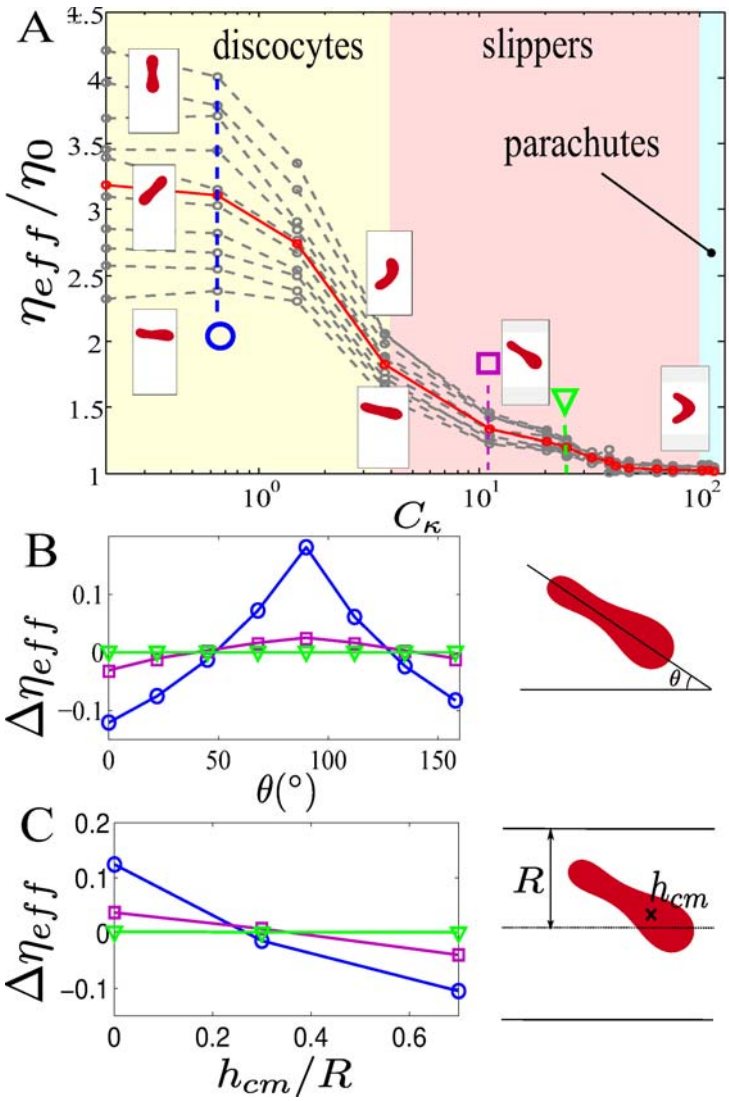

Figure 10.1: Effective viscosity of a suspension of RBCs as a function of the capillary number, C_κ. Examples of the RBC morphology, as well as the steady position and orientation for different initial configurations, are shown in the snapshots. (A) The viscosity presents a certain sensitivity to the initial conditions of the RBC, especially at low capillary numbers. Each dashed line represents the viscosity for a specific initial configuration. The mean effective viscosity, $\bar{\eta}_{eff}$ (red line), is therefore averaged over the different configurations, covering: (B) initial inclinations (with respect to the channel axis), with normal RBCs presenting a higher resistance to flow compared to aligned RBCs; (C) initial heights in the channel, with centered RBCs opposing more resistance than RBCs flowing close to the walls. The viscosity dispersion is defined as $\Delta\eta_{eff} = (\eta_{eff} - \bar{\eta}_{eff})/\bar{\eta}_{eff}$, where η_{eff} is the effective viscosity for each particular initial configuration. In all cases, within the slipper regime ($\triangledown$) the final configuration is nearly independent from the initial one. The dependence is stronger at intermediate ($\square$) and especially low ($\circ$) capillaries. The schemes on the right represent the RBC inclination θ and center of mass height h_{cm}.

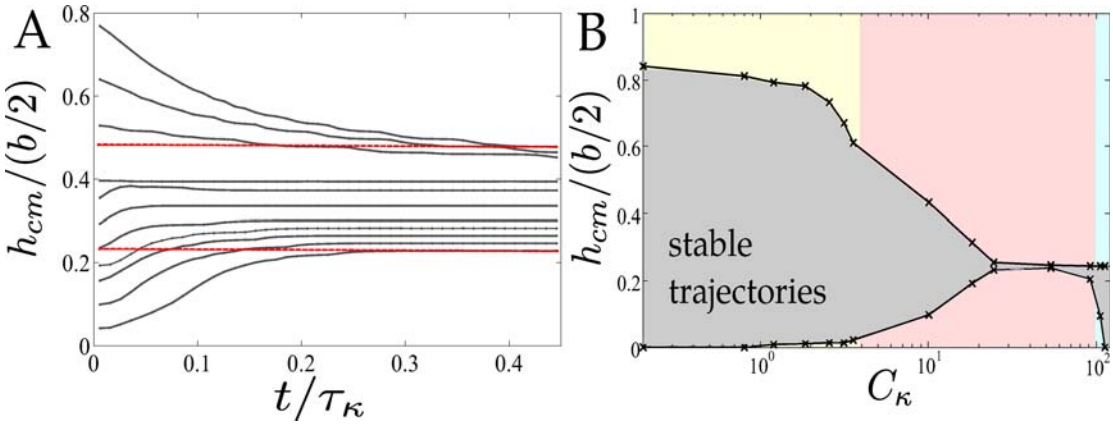

Figure 10.2: (A) Evolution during the downstream flow of the center of mass height, h_{cm}, of RBCs initially placed at different lateral positions, within the slipper regime, $C_\kappa = 13.2$. RBCs close to the wall are repulsed and migrate towards the center; likewise, centered RBCs migrate towards the walls. All RBCs stabilize at intermediate positions, forming a band of stable trajectories. In this case the confinement has been increased with respect to the standard one, here being $a/b = 0.49$, in order to observe larger and more perceptible migrations. (B) Width of the band of stable trajectories as a function of C_κ. The width of the band can be controlled by increasing the flow velocity (confinement $a/b = 0.71$). High velocities induce a narrowing of the band until the RBC eventually occupies a unique position in the channel. Within the parachute regime, RBCs develop parachute and slipper morphologies at fixed flow conditions depending on their initial position: RBCs initially placed close to the wall are repulsed and assume a slipper shape, whereas cells placed at the channel core deform into a parachute.

duces a migration towards an off center region, then the RBC distribution narrows forming a thin band. The viscosity dispersion decreases with the focusing and, for sufficiently high flow velocities, the final position and orientation of the RBC is unique regardless of its initial condition, leading to a well-defined value of the effective viscosity.

10.2 RBC focusing and alignment

RBC focusing has been extensively studied in the inertial regime, but it is not well understood in the viscous one. In this section we study how the focusing of RBCs to a defined, off center position can be obtained by tuning the capillary number and the distance between the channel walls.

10.2.1 Focusing

At low C_κ, RBCs flow occupying the entire channel section, without any favoured position. If the external forcing increases, however, RBCs concentrate on a narrow

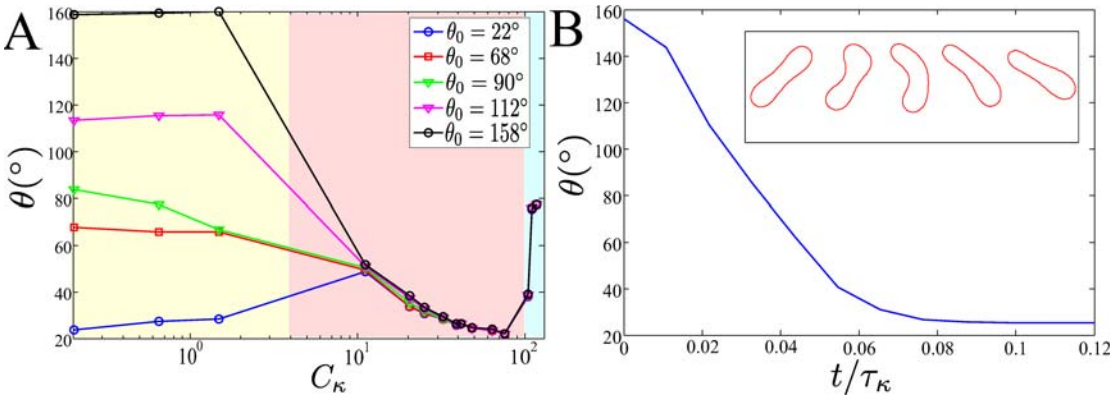

Figure 10.3: (A) Orientation of the RBC as a function of the capillary number for different initial conditions, θ_0. Within the discocyte regime, the RBC maintains its initial orientation, with slight deformation. For $C_\kappa > 2$, all RBCs rotate and orient their axis with the imposed flow profile. (B) Temporal evolution of the inclination of a RBC at $C_\kappa = 4.5$. The rotation towards the equilibrium inclination occurs in a fast time scale compared to the migration and relaxation time of the cell. In the inset some snapshots of the evolution are shown.

band off the channel axis, as shown in Figure 10.2. In Figure 10.2A, at $C_\kappa = 10$, the height in the channel during the downstream flow for RBCs placed at different initial position is shown. RBCs initially placed close to the wall experience a repulsion and migrate towards the center, stabilizing at $h_{cm}/R = 0.5$. RBCs initially placed in the channel axis also migrate from the center and reach a equilibrium position at $h_{cm}/R = 0.25$. The rest of RBCs stabilize at intermediate positions, forming a band of stable trajectories. The channel width has been increased to $a/b = 0.49$ to allow larger and more perceptible migrations. The time scale of the migration is typically half of the deformation time τ_κ. The increase in C_κ induces a narrowing of the band of stable trajectories, as shown in Figure 10.2B, and eventually RBCs are found in a unique lateral position regardless of their initial condition, for $C_\kappa > 40$.

10.2.2 Alignment

RBCs at very low capillary $C_\kappa < 2$ flow maintaining their initial orientation, as can be seen in Figure 10.3A. However, beyond the critical value $C_\kappa = 2$ RBCs lose this dependence and rotate towards a fixed orientation, which in turn depends on the lateral position along the channel. RBCs flowing close to the wall assume slightly higher inclinations than those more centered, as a result of the non uniform curvature of the flow profile. The focusing of RBCs takes place for higher capillaries. The sensitivity to the initial conditions of the orientation and the lateral position is seemingly uncoupled. Accordingly, the dispersion on the final configurations

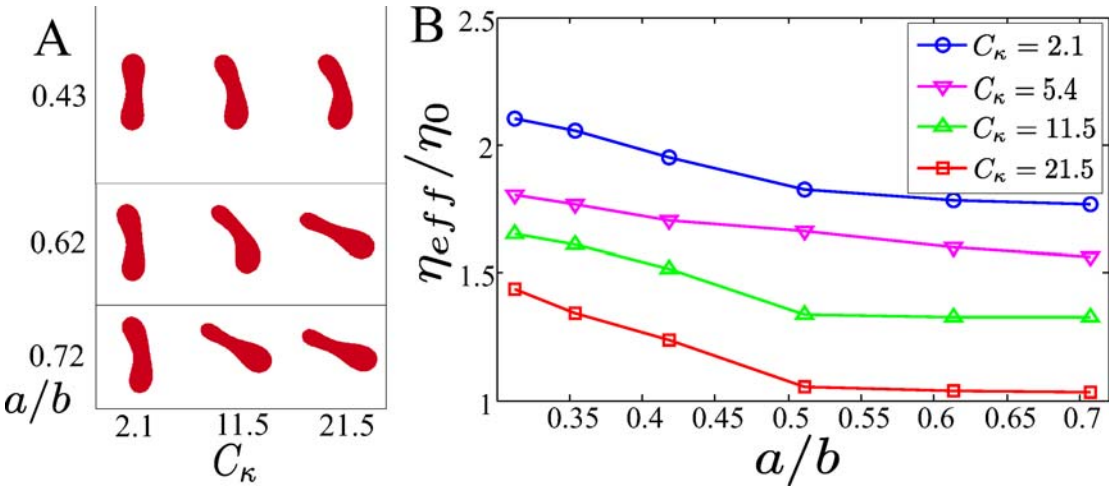

Figure 10.4: Effect of channel confinement in the RBC behaviour at different C_κ. All the RBC are initially placed at the channel axis. (A) RBC morphologies found at different confined channels; cells shown here are initially placed at the channel axis, normal to the flow direction. The shear rate is maintained constant for each value of C_κ. The effect of the walls is important to induce lateral migration, as confined RBCs exhibit the characteristic slipper morphology whereas the RBC flowing at the thicker tube still retain a discocytic shape. Less confined RBCs, which may present weaker interactions with the walls, require of higher C_κ to deform and migrate. (B) Effective viscosity η_{eff} for a suspension of RBCs as a function of the channel confinement and capillary number, at constant volume fraction. η_{eff}, specially at high capillaries, strongly depends on the confinement. For confined RBCs which have migrated, the viscosity is low and uniform. However, if the channel is thick enough the RBC does not migrate and its center position and normal orientation imply a higher viscosity.

can be separated into three different situations: *(i)* for $C_\kappa < 2$, RBCs flow maintaining their initial distribution and orientation, deforming its shape to the local flow profile; *(ii)* for $2 < C_\kappa < 7$, RBCs show a fixed orientation aligned with the flow, but they still retain their memory to the initial position along the channel section; and *(iii)* $C_\kappa > 7$ RBCs focalize to two symmetric lateral positions in the channel, aligned with the flow. The temporal characterization of the rotation of the RBC towards its stable orientation is shown in Figure 10.3B. RBCs rotate in a much shorter timescale than the migration, typically $\sim 0.1\tau_\kappa$. In the inset, some snapshots of the process are depicted.

10.2.3 Effect of walls confinement

The focusing of RBCs can be achieved by both increasing the flow velocity or the degree of confinement of the channel. By varying the distance between the walls b, but maintaining a constant shear rate $\dot{\gamma}$, we identify how the closer presence of the walls affects to the RBC morphology. We focus on intermediate and high

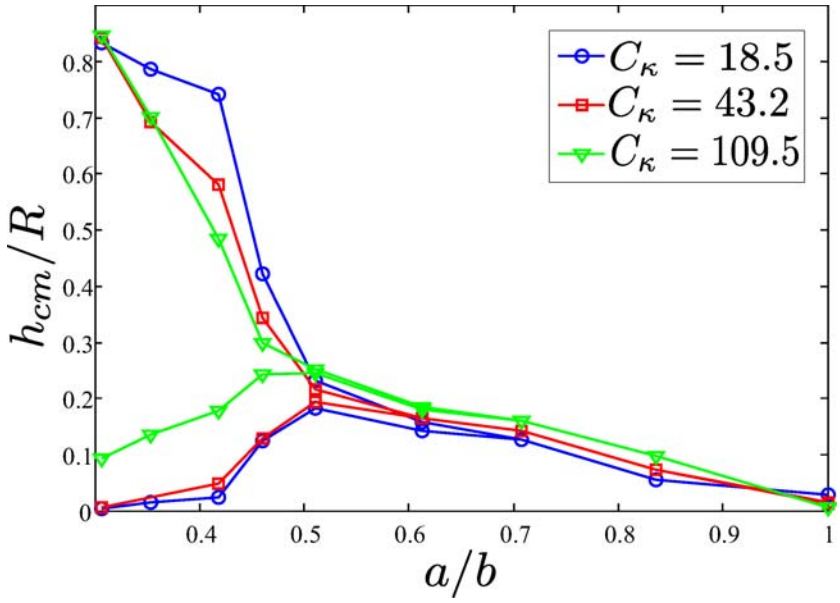

Figure 10.5: Focusing of RBCs as a function of the wall confinement and the capillary number. For each C_κ, the up and bottom values correspond, respectively, to the outermost (*ie* closest to the wall) and innermost (closest to the center) equilibrium positions; all the rest possible positions are found in between these two. The wall confinement favours the focusing and typically the effect is reduced below $a/b < 0.5$. The lateral position of the RBC is found further away from the axis in thicker channels, and in the limit in which the width of the channel is equal to the cell diameter, RBCs flow nearly centered. The capillary number also induces an increasing focusing (especially in the case $C_\kappa = 109.5$), though its effect is weaker.

capillaries in which the presence of the walls is more relevant. In Figure10.4A, a phase diagram for different capillaries and confinements is presented. Moving along a row of constant capillary number, the increasing confinement induces higher migrations and lower inclinations. This effect is especially noticeable at intermediate capillaries, in which high confined RBCs have migrated and acquired the slipper morphology whereas less confined RBCs still remain centered and retain a discocyte shape. The relative distance to the wall arises as an important factor to trigger the migration, and at thick channels the capillary required to observe slippers and parachutes might be extremely high. Interestingly, the diagram highlights the similar effect of moving along the vertical and horizontal axis. This suggests a coupling between the effect of confinement and capillary, implying that increasing shear rates induce stronger interactions between the cell and the walls, leading to a larger repulsive force from the axis, and this effect can be emphasized by a closer distance of the RBC to the walls. The lateral position and focusing of RBCs for different wall confinements is shown in Figure 10.5. The confinement positively affects focusing, and for all capillaries $C_\kappa > 20$ RBCs are localized at a defined lateral position if $a/b > 0.5$. The distance from the axis of this position increases for thicker channels, from $h_{cm} = 0.05R$ to $0.3R$ in the range of channels studied. At the narrowest channels, the RBC is placed close to the center, likely due to the geometrical constraints but also to the strong wall repulsion. The increase in C_κ reinforces the focusing effects, and especially for $C_\kappa = 109.5$ focusing has extended to thicker channels and RBCs are localized at positions further from the channel axis. Note, however, that the effect is relatively weak for the two other cases $C_\kappa = 18.5$ and 43.2.

The larger inclination and migration observed in RBCs flowing along the narrowest channels is accompanied by lower values of the effective viscosity, as shown in Figure10.4 B. In the case of high capillary, the viscosity is similar for all the channels in which the RBC has been forced to migrate and align. However, if the confinement is low and the RBC still flows along the centerline, it will displace a larger amount of external fluid and therefore its viscosity will be also larger. For decreasing confinements the effective viscosity increases, until it eventually stabilizes when the wall influence is negligible and the RBC behaviour is similar to that in an unbounded flow. The confinement necessary to recover this unbounded behaviour also depends on the capillary number, as expected given the existing coupling between confinement and capillary number. At lower values of the capillary, all the RBCs exhibit a less marked migration and alignment, and the differences between the viscosity of each initial condition are less accentuated.

10.3 Vesicle shape

We explore the relevance of the object geometry by studying the case of three vesicles with different reduced volume and compare with the RBC case. The relaxed shapes of the vesicles are obtained from minimizing several initial ellipsoids with different area an perimeter, $\nu_{red} = 0.97, 0.69, 0.55, 0.48$, corresponding to the equilibrium shapes from a circular to a discocyte shape. This minimization is performed in the absence of fluid. The vesicles are then placed in the channel and the fluid is switched on. Due to its symmetric shape, circular vesicles present less degrees of freedom to adapt and orient with the external flow, showing slight deformations even at high forcements. They do not migrate out of the axis, remaining at the center line, but their center of mass moves to a more forward position at high capillaries, acquiring at intermediate capillaries an almost triangular shape which reminds a parachute, the so-called bullet, as shown in Figure 10.6 A. We check the evolution of a circular vesicle when initially placed close to the wall, finding that it rapidly migrates towards the center recovering the symmetric shape, as opposed to the discocytes. Deflated vesicles present an intermediate behaviour between the circular and the discocyte vesicles. For all the cases studied the equilibrium position is strictly asymmetric and therefore the vesicles eventually deform and migrate, but lower values of the capillary require of more deflated vesicles to acquire asymmetric shapes. The off center position of objects in the inertial regime does not depend on their specific geometry, and hard spheres, soft beads and cells behave similarly migrating towards roughly the same equilibrium position. The repulsive force from the axis does not manifest a critical dependence on the specific properties of the object. A potential explanation could be that deflated shapes present an asymmetric distribution of normal stresses, implying a effective repulsive drift, which is on the contrary balanced in circular vesicles because of their symmetry.

In the rigid limit, discocytes present a considerably higher resistance to flow than circular vesicles, in spite of its lower volume. This may respond to the smoother streamlines of the flow when passing round the object, whereas the flatter face of the discocyte impose a sharper change in the flow direction. However, the capability to deform, migrate and orient implies that discocytes present a larger gap in the effective viscosity (Figure 10.6 B). The mechanism of migration and orientation permits a sharp relaxation and at high shear rates the circular vesicle has higher effective viscosity than the discocyte. All the deflated vesicles behave very similarly, especially at high capillaries, with a marked shear-thinning behaviour which increases for lower reduced volumes. Conversely, the viscosity of the spherical vesicle is rather constant at high capillaries, when the vesicle has adopted the so-called bullet shape (*ie* the equivalent of the parachute for spherical

shapes).

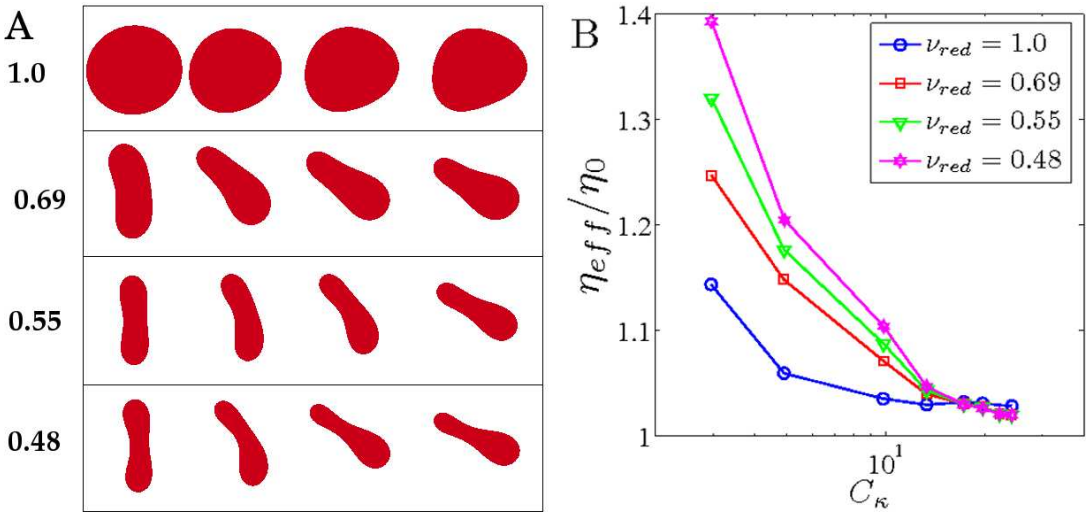

Figure 10.6: Effect of the reduced volume on vesicles and RBCs behaviour and suspension rheology. (A) Vesicle morphologies for different reduced volumes. Circular vesicles, which are symmetric, do not migrate and remain centered flowing at the channel center line. The increasing deflation of the vesicles (*ie*, lower reduced volumes) induces a higher degree of migration and asymmetry. Discocytes exhibit the largest degree of migration towards the wall and orientation with the flow profile. (B) Effective viscosity as a function of the capillary number for different reduced volumes. The ability to migrate and orient of deflated vesicles enables them to reduce their resistance to flow, and this property implies a sharper shear-thinning behaviour than in the case of circular vesicles.

10.4 Discussion and conclusions

The results presented in this Chapter describe the extensive phenomenology of the circulation of RBCs at microchannels, highlighting the subtle dependence of the cell dynamics with the flow velocity, wall confinement and intracell distance. The focusing and alignment of RBCs play an important role in the rheological behaviour of the suspension. At low C_κ, when RBCs flow with variable orientation and position, the effective viscosity of the suspension shows high sensitivity to the particular configuration. RBCs flowing normal to the flow direction oppose higher resistance than those flowing paralel to the flow. Additionally, RBCs flowing close to the walls are also characterized by lower contributions to the viscosity. The dispersion of the effective viscosity may be prevented by an average measure over RBCs with different positions and orientations, to reproduce a more homogeneous suspension.

We have verified that the dependence of the RBC morphology to its initial condition is not due either to a small relaxation process or to an underlying finite

size correlation between cells. Figure 10.7 shows the effective deformation time, t_κ^{eff}, computed as the effective relaxation time of the membrane energy[1], as a function of C_κ. The relaxation time increases when decreasing C_κ, but it is not diverging in the regime of small C_κ where we observe strong memory effects. We have carried out simulations 20 times longer than the highest t_κ^{eff} measured, thus largely exceeding the expected relaxation time scale, and observed the same dependence on the RBC initial configuration. Additionally, we have checked that increasing the channel length from $L = 4a$ to $12a$ we do not observe any change in the final RBC morphology at small C_κ, ruling out that the memory reported is due to finite size effects. Therefore, the origin of the sensitivity of RBCs to their initial configuration at small C_κ remains unclear. It could be due to the elastic nature of the RBC and its ability to slightly deform, adapting to the position dependent flow.

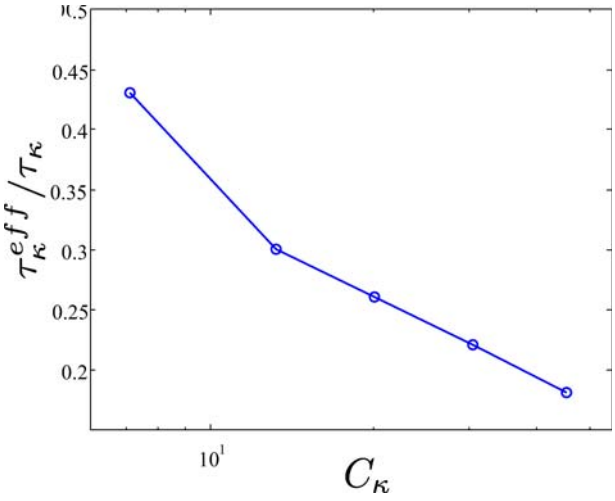

Figure 10.7: Effective deformation time τ_κ^{eff}, measured from the evolution of the deformation energy, as a function of C_κ. We consider that the RBC has reached a steady shape when the energy achieves a value at 1% of the final value. The curve is restricted to the regime in which RBCs rotate and orient with the flow, not presentig dependence with the initial inclination. The evolution of the typical time scale of evolution is smooth and unlikely to diverge at lower C_κ. Deviations between the theoretical deformation time τ_κ and the effective value measured may respond to the definition of the relevant length of the cell, which we have fixed for simplicity as the cell diameter a.

The focusing of RBCs in two narrow bands at symmetric lateral positions of the channel is primarily controlled by the capillary number. At low C_κ, RBCs maintain their initial height in the channel during the flow, and thus cross stream migration is not observed. Supposing a suspension in which initially RBCs are

[1]We have verified that this relaxation time is comparable to the characteristic time in which the RBC migrates laterally in the channel or reorients, corresponding to the quantities plotted in Figure 10.3.A and Figure 10.2 B, respectively.

uniformly distributed along the channel section, the downstream evolution does not change the cell distribution. For $C_\kappa > 10$, RBCs exhibit a marked migration until they reach an equilibrium off center position. In terms of the RBCs spatial organization, the flow gives rise to a converging distribution of cells, an effect often known as *tubular pinch*. The off-center migration of particles and cells in the inertial regime results from a balance between the wall repulsion and a drift from the axis towards the wall, as demonstrated analytically for rigid spheres (Ho and Leal, 1974; Asmolov, 1999). This drift is caused by inertial effects, so that the physical origin of the migration observed in the viscous regime must be different, and may be found in the asymmetry and deformable properties of the object, explaining the diverging behaviour observed for RBCs and spherical vesicles. These results highlight the relevance of the specific properties of the deformable object, as opposed to the inertial regime in which RBCs, vesicles and particles are known to share a similar behaviour (Carlo et al., 2007).

The channel confinement determines the off center equilibrium position of the RBC within the slipper regime: cells flowing in thick channels (*eg* $a/b \sim 0.5$) migrate towards a position of $\sim 0.3R$, whereas vesicles flowing at the narrowest channels (*eg* $a/b \sim 0.9$) are constrained to positions closer to the axis $\sim 0.1R$. This lateral position is considerably lower than the classic Segré & Silverberg inertial result of $0.6R$, but the difference with our results might not relate with the hydrodynamic regime but it is likely explained by the geometric constraints imposed by the large size of the cell in comparison with the channel width, since recent experimental results at large confinements in the inertial regime also found equilibrium positions in the range $0.2 - 0.4R$ (Carlo et al., 2009).

The wall effect on the RBC is, additionally, coupled to the flow velocity. Less confined cells require of higher C_κ (even if the shear rate is maintained constant) to show lateral migration. Therefore, focusing at thick channels is achieved for increasingly higher C_κ, implying that slipppers and especially parachutes are rarely found. The coupling between capillary and confinement has been experimentally observed for single RBCs. Abkarian et al. (2008) present a phase-diagram in which advanced parachutes are obtained at the highest confinements and flow velocities, whilst slippers are restricted to lower values of confinement and velocity. For a fixed thick channel, they also observe more sparse positions of the RBC at low flow velocities. Their results might be interpreted as a transition from parachutes to slippers when the channel width is increased up to $a/b < 0.4$, suggesting that they are at the high C_κ limit.

Chapter 11

Collective flow of RBCs

Thus far, we have studied the elastic behaviour of a single cell flowing in a very narrow channel. This system captures the physics of RBCs suspensions at very confined channels, when cells flow aligned in a single row and the dynamics of the cell is dominated by its interaction with the wall rather than with its neighbours. This case facilitates the identification of the physics driving the single-cell behaviour. However, while flowing in thicker channels, where cells typically flow at higher concentrations, RBCs do interact, and collective effects substantially change the flow properties. In this Chapter we explore the transition between the single cell case to situations in which cells present hydrodynamic interactions, although still far from the high concentration limit of 45% hematocrit characteristic of blood in large arteries, when the bulk properties of blood are also different. The study is oriented to understand the basic principles that govern important macroscopic properties of blood flow, such as the Faehreus-Lindqvist effect. The Chapter is structured in two parts. In the first, we specifically investigate the relevance of interactions between cells with respect to the interactions with the walls. We exploit the periodic boundary conditions in the flow direction to study the case of regular arrays, when the domain length is short and the cell interacts with its image. Besides, we study the effect on cell deformation when an isolated group of three closely placed cells are exposed to a parabolic flow. In the second part we explore different aspects of RBC flow at moderately narrow channels (of roughly 15 and 30μm width,) when several RBCs are interacting, focusing on the spatial ordering of cells when both confinement and shear rate are modified, and the subsequent effects in the suspension rheology. Most results are conducted towards the comparison with the isolated case, in order to separate the physics of the single cell situation from the regime dominated by collective effects.

Although RBCs are known to aggregate and cluster due to electrochemical attractions mediated by membrane composition (Merrill et al., 1966), we restrict

our analysis to purely hydrodynamic interactions. However, a weak short-range repulsion is included in order to avoid cell fussion, as described in Chapter 6.

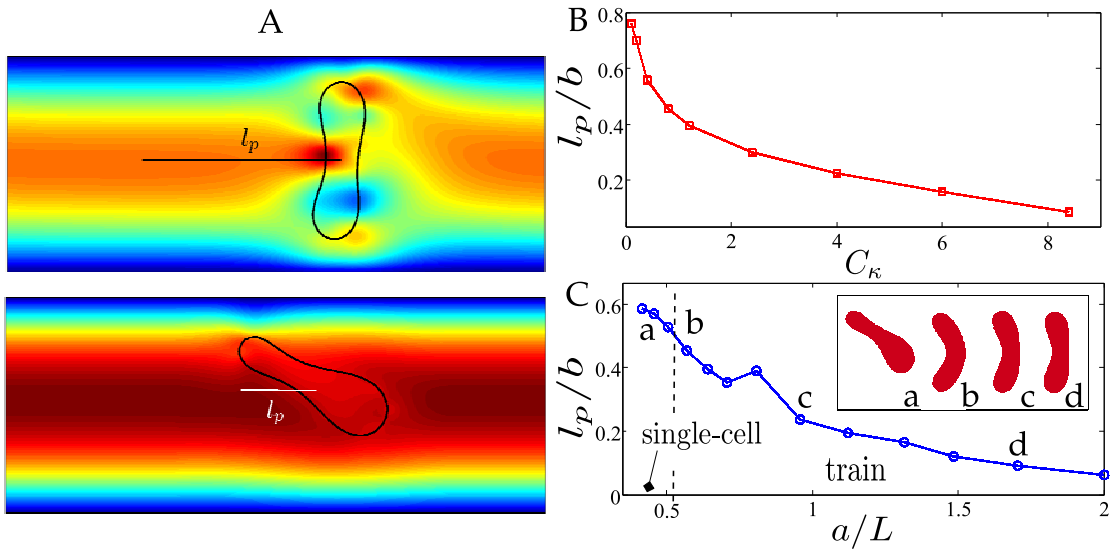

Figure 11.1: (A) Flow disruption induced by a RBC in a Poiseuille flow. The colormap represents the value of the velocity component v_z. C_κ affects the flow disturbance that the cell induces: rigid RBCs (up, $C_\kappa = 0.8$) disturb a larger region of the surrounding flow than flexible RBCs (bottom, $C_\kappa = 15.1$). (B) Penetration length, l_p of the flow disruption caused by the RBC for different C_κ. l_p is the typical length of the flow distortion caused by the cell in the surrounding flow with respect to the unperturbed Poiseuille, but see the main text for a explicit definition. l_p decreases rapidly with C_κ. For $C_\kappa > 10$ it falls down to $l_p < 0.1a$, meaning that RBCs induce a limited perturbation of the flow at intermediate and high capillaries. (C) Penetration distance l_p for closely placed RBCs, as a function of the distance between cells L. Even if the flow disruption shows a strong decay at high capillaries, RBC behaviour is highly sensitive to the presence of neighbour cells. The dashed line separates the single-cell behaviour (when RBCs are able to migrate off center and assume slipper morphologies) from the train configuration (when they order in regular arrays of centered, symmetric cells). For $C_\kappa = 19.5$, RBCs only recover the single-cell behaviour if the distance between them is higher than $1.5a$ (inset). For lower values, RBCs are hydrodynamically coupled and migration is inhibited. The penetration length l_p shows that the coupling between RBCs is large if the distance is much lower than the length of the channel (wall confinement here is $a/b = 0.71$).

11.1 Hydrodynamic interactions between RBCs

11.1.1 Regular arrays

While flowing along confined channels at high concentrations, RBCs often order in regular trains, as first noted by Gaehtgens et al. (1980). The formation of these

ordered configurations is important in the designing of microfluidic devices as it increases the control of cell manipulation. From the theoretical point of view, the organization in trains also offers an interesting way to study the hydrodynamic interactions between neighbouring cells, and how it affects to the RBC dynamics. To study these trains of RBCs, we take advantage of the periodic boundary conditions in the $\hat{z}$ direction that, if the length scale of the hydrodynamic interactions is below the length of the channel L_z, induce a interaction of the cell with its image. Effectively, the system reproduces a regular array of identical RBCs separated by a distance L, which agrees with the domain length L_z. In this section the competition between the wall-induced effects and interactions between RBCs is analyzed.

The membrane stiffness dictates the flow disruption induced by the RBC. Rigid cells induce stronger perturbations of the incoming flow than softer ones, as seen in Figure 11.1 A. We define the flow amplitude $A(z) = \sum(a_n a_n^0 + b_n b_n^0)/\sum[(a_n^0)^2 + (b_n^0)^2]$ of the imposed Poseuille, where (a_n, b_n) and (a_n^0, b_n^0) are the coefficients of the Fourier decomposition of the actual $v_z(x, z_0)$ and imposed $v_{z0}(x, z_0)$ velocity profiles, respectively, for the first $n = 20$ modes, $v(x, z_0) = \sum[a_n \sin(2\pi n x/b) + b_n \cos(2\pi n x/b)]$. By fitting the flow amplitude to a Gaussian decay $A(z) = A_0 \exp(-((z - z_{cm})/l_p)^2)$, a typical distance of the flow distortion is obtained, the penetration length l_p. Figure 11.1 B displays the penetration legth for different C_κ, at very long tubes $L_z \gg a$ when RBCs do not interact. The results show that the flow disruption decay is strong and for $C_\kappa > 10$ the flow deviates from the reference one only at very close distances from the RBC, $\sim 0.1b$. This could suggest that the coupling between RBCs is only relevant if they are placed extremely close.

However, even if deviations from the imposed flow are small when RBCs are distant, interactions strengthen for lower distances between cells, favouring RBC collective behaviour. If RBCs are initially placed very close to each other, even at high C_κ, they do not migrate towards the walls but flow maintaining a centered position, forming an ordered array of RBCs aligned normal to the channel axis, as shown in Figure 11.1 C (inset, RBCs on the right) for $C_\kappa = 19.5$. RBCs bend, coupling their surface to the flow profile. If the distance between cells is increased, eventually slippers are recovered, initally showing a slight distortion and then fully exhibiting the single-cell behaviour. The distance necessary to separate this ordered train configuration from the single-cell behaviour depends on the capillary number, low C_κ requiring of larger cell-to-cell distances. For $C_\kappa = 19.5$, the RBC behaves as hydrodynamically isolated for $l_p > 1.4a$, but the critical distance decays to 0.5 for $C_\kappa = 97$. The formation of the trains originates on the transversal confinement that the RBC feels due to the presence of its neighbours. The flow disturbance generated by the RBC is symmetrically compressed by both

the preceding and the rear cells of the train, inhibiting the symmetry breaking of the flows generated around the RBC that prelude the migration in the case of isolated cells. The transversal confinement thereby constraint the RBC shape to a centered, symmetric morphology.

Figure 11.1 C presents the dependence of the penetration length with the separation between RBCs L, at wall confinement $a/b = 0.71$. The results suggest that the penetration length for isolated RBCs is typically of the order of the channel width, though it depends on C_κ. For $C_\kappa = 19.5$, at distances L much lower than the channel width the wall effect is subdominant and the RBC behaviour is controlled by the transversal confinement, forming trains of RBCs. Only for $a/L > 0.66$ RBCs behave as hydrodynamically isolated, recovering the single-cell behaviour, exhibiting lateral migration and assuming slipper shapes.

The formation of trains of RBCs has important implications in the rheology of the suspension. The normal orientation of the cells implies a larger resistance to flow than aligned RBCs (*ie* slippers), and the solvent is repelled from the channel core towards the walls where it flows free of cells disturbance. This however implies that the effective viscosity of the suspension increases, as shown in Figure 11.2 A, where the effective viscosity of the suspensions shown in Figure 11.1 C at constant C_κ is plotted. A sweep in C_κ reveals that the differences in the viscosity are accentuated at lower values, as a direct consequence of the stronger interactions between more rigid cells. This effect is shown in Figure 11.2 B, where the effective viscosity as a function of C_κ is shown for three different distances between RBCs. At high C_κ, the distance between RBCs in all cases is larger than the critical distance of the single-cell regime. For lower values of C_κ, the differences of the viscosity is primarily due to the different volume fraction. At some point, marked by the dashed line, the distance between RBCs is lower than the increasing critical length and RBCs switch to the train configuration, inducing a considerable increase of the effective viscosity. Accordingly, the presence of collective behaviour between RBCs critically determines both the morphological and rheological behaviour of the suspension.

11.1.2 Screening between cells

The study of the cell morphologies in ordered trains demonstrates the relevance of the screening between RBCs. The close distance between cells disrupts the Poiseuille flow in the entire domain, and thereby cells interact with an attenuated flow and they are not forced to migrate. An alternative case of interest is to consider a channel in which a few RBCs are placed close enough to ensure that they will interact, but at the same time the tube is sufficiently large so that the Poiseuille flow is recovered. The analysis of the morphologies adopted by the RBCs

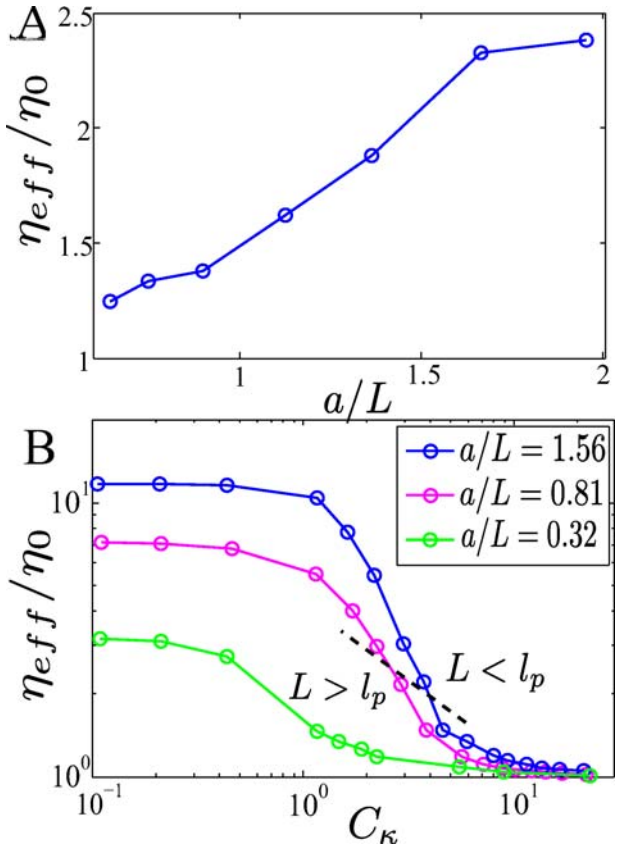

Figure 11.2: (A) Effective viscosity for a regular array as a function of the intracell distance, a/L, at constant capillary number $C_\kappa = 18$. Each value of the viscosity corresponds here to the shapes shown in Figure 10.2, for initially centered RBCs. The increase in the viscosity can be decomposed into two different contributions: *(i)* the change in the volume fraction, from 0.40 to 0.13, *(ii)* the effect of the interactions between RBCs at low L, which allow the formation of train of cells at the channel core that present higher flow resistance. (B) Effective viscosity as a function of C_κ for different cell-to-cell distances. If the channel is not sufficiently long, at some point, marked with a dashed line, the penetration length l_p exceeds the distance between cells L and the RBC interact with its image (forming an array of RBCs due to the periodic boundary conditions) and this fact triggers a considerable increase in the effective viscosity. The change between the single-cell and train like configurations is marked by a dashed line, and the specific cell shapes are shown in the inset. At low distances between RBCs, they maintain a centered position but bending their surface. Only for large distances between cells slippers are observed, RBC on the left.

will provide information about the screening effect between them in response to the external, unperturbed, flow. We fix the initial configuration as a group of three aligned RBCs with orientation $\theta_0 = 45°$, separated by a distance d. At the imposed flow conditions, an isolated RBC shows the usual slipper-bowl shape. Examples of steady state conditions are shown in Figure 11.3, for $d/a = 0.45$ and 0.95, and capillary numbers $C_\kappa = 16$ and 31. Cells flow maintaining a nearly constant distance, but their morphological response differs from that of isolated cells.

The results show that only the leading cell (in the flow direction) deforms into a slipper, as it interacts with a pure Poiseuille flow. The two following cells present a different deformation, more curved and distorted. The interpretation of these shapes is not straightforward, as they could represent both advanced or retarded morphologies with respect to the slipper (*ie* parachutes or discocytes, respectively), depending on which cell is undergoing a stronger deformation due to the flow. However, Figure 11.3 d offers interesting information, as large d and C_κ correspond to the single-cell limit, and all the cells indeed show slipper shapes. Hence, in the other plots screening might be larger, and cells interact with a disrupt flow which present a lower effective capillary number. Thus, one could hypothesize that cell morphologies subjected to the screening of a neighbour cell represent retarded stages of the morphological sequence of Figure 11.3. Accordingly, if more RBCs are added to the trailing end of the group, they will sequentially deform into shapes closer to the discocyte (*ie* less distorted). In the limit of infinite number of cells, all of them are expected to show only slightly distorted shapes, and this is the idea behind the results presented in the previous section.

The morphologies depicted in Figure 11.3 intuitively show that the capillary number reduces the screening effect. Whilst at the lower C_κ the two non-leading cells are highly deformed, at $C_\kappa = 31$ the flow-induced deformation is more dominant and the three RBCs adopt a slipper morphology (d) or only the trailing one is deformed for closer cells (c). The distance between cells is obviously also important, as the screening range is related with the penetration length, and cells separated a larger distance will be exposed to a lower screening. This effect is quantified in Figure 11.4, where the shape distance (as defined in section 8.2) is shown for different distances and C_κ. We only consider the morphological deformation of the trailing cell. Note that shape distance for a typical slipper is roughly $\Delta_s \sim 0.2$. The results show that at low C_κ, RBCs are remarkably distorted (far from the slipper value characteristic of the single-cell regime) with a weak attenuation with the separation between cells, suggesting that screening is present even for cells separated a distance $\sim a$, and thus interactions between cells are dominant. At higher C_κ, on the contrary, there is a strong decay of the shape distance,

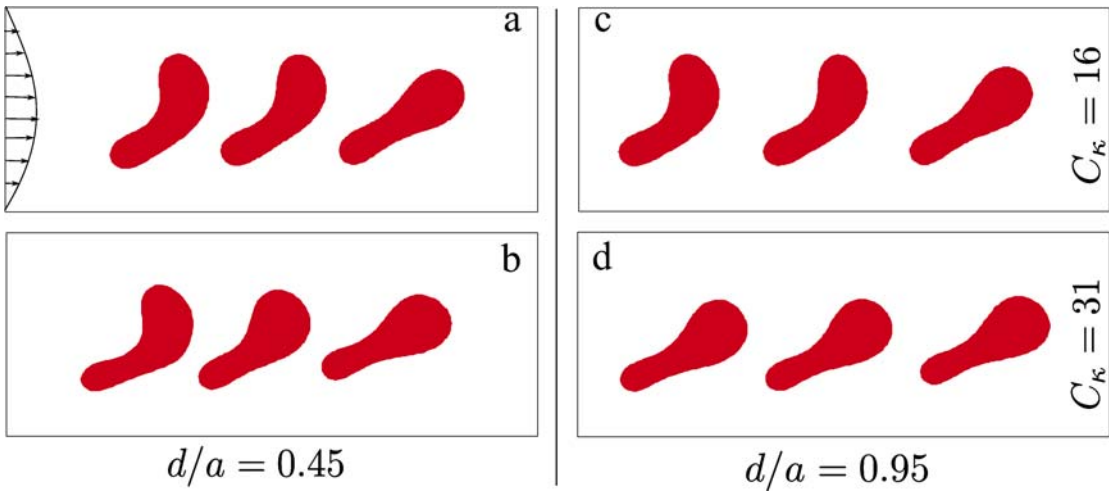

Figure 11.3: RBCs flowing in a channel at confinement $a/b = 0.71$. In all cases three cells where initially placed at the channel axis with a distance d between cells and orientation $\theta_0 = 45°$. Both the distance and the capillary number minimize the interactions between cells, and in (d) all the cells develop a slipper morphology, converging to the single-cell limit. In b, the screening is of the leading cell is low and the middle cell shows and intermediate shape, whereas the trailing cell benefits from the combined screening and it assumes a shape similar to those found at lower C_κ.

converging to the isolated slipper value. This transformation suggests that at this capillary, for separation between cells $\sim 0.5a$, wall effect is still subdominant with respect to interactions between cells, but for separations $\sim 1a$ the wall influence completely overcomes the hydrodynamic interactions between cells.

11.2 Several RBCs in flow

The analysis performed in the previous sections highlights the sensitivity of cell behaviour to hydrodynamic interactions with other cells, and the competition between these interactions and the wall effects dictates a different RBC flow properties when several cells are flowing at high and moderate concentration. For instance, in the inertial regime, the limit of single-cell behaviour is characterized by the Segré-Silverberg effect, when cells migrate towards a specific lateral position, whereas at higher concentrations the collective behaviour dominates and cells are located at the tube core, the Faehereus-Lindqvist effect. The transition between both regimes is not well understood, in spite of its relevance for chip-design as cell focusing will be severely affected. In the subsequent sections we explore the interactions between RBCs in parabolic flow at relatively low concentrations, identifying the new mechanisms introduced that explain the main differences with the single-cell case in terms of spatial ordering and focusing.

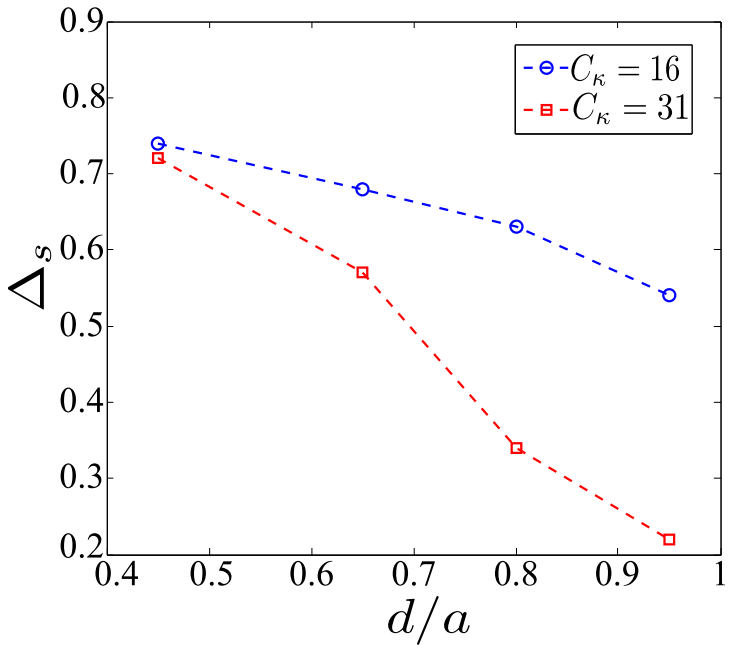

Figure 11.4: Shape distance of the trailing RBC (the left one of the group in Figure 11.3) as a function of the distance between cells. Whereas for $C_\kappa = 16$ results suggest that screening is relevant in all the cases, for $C_\kappa = 32$ there is a clear switch from the screened to single-cell configurations, indicated that wall effect has became dominant for distances $\sim a$.

We carry out simulations with the same parameters as in Chapters 8, 9, and 10. Several RBCs (ranging from 3 to 12 cells, depending on the simulations) are initiliazed in the domain, with different configurations (*eg* all the cells with the same orientations, disordered center positions, etc) as discussed below. We explore the same range of capillaries as the previous section, but extend the confinement including thicker tubes.

11.2.1 Order vs disordered configurations

Our simulations show that RBCs in flow, especially at low capillaries, depend on the initial condition, especially if this corresponds to a very symmetric configuration. This fact might be expected according to the results of section 10.1, and it has been reported elsewhere in the literature (McWhirter et al., 2008). Examples of a very symmetric and a disordered configurations are given in Figure 11.5. We quantify the equivalence between configurations by means of the pairwise correlation function and the orientation of the cells. The pairwise correlation function in the x-direction, $G(d_x)$, for n RBCs, reads

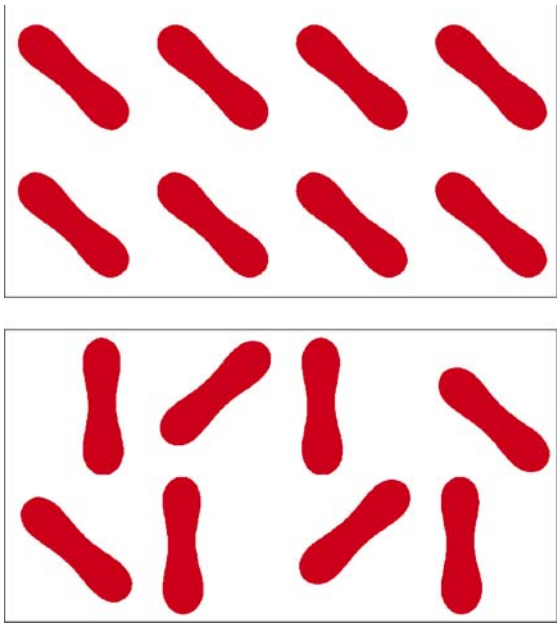

Figure 11.5: *(Top)* Initial condition with an ordered configuration, at $a/b = 0.53$, for $n = 8$ RBCs. *(Bottom)* Initial condition with a disordered configuration, at $a/b = 0.53$, for $n = 8$ RBCs. RBCs are placed at random position and orientation within a local domain.

$$G(d_x) = \frac{1}{n\rho} \left\langle \sum_i \sum_j \delta(d_x - d_{cm}^{i,j}) \right\rangle . \tag{11.1}$$

where $\rho = (n-1)/Lx$, and d_x expresses distances in the x-direction, so that $d_{cm}^{i,j} = x_{cm}^i - x_{cm}^j$ is the projection onto x of the distance between the center of mass of cells i and j, and $\delta(x)$ is a function that takes the value $\delta(x) = 1/\Delta x$ if $x \in [-\Delta x/2, \Delta x/2]$, and 0 otherwise. We fix $\Delta x = 0.05a$. This function provides information about the structuring and spatial organization of the cells in the channel section.

In Figure 11.6 A we compare both quantities for the symmetric and two disordered configurations. The pairwise correlation function shows a significant different behaviour between both cases: the symmetric configuration orders in two homogeneous rows, and the peaks of the correlation function are well defined at distance 0 (corresponding to the cells of the same row) and $\sim 1.1a$ (corresponding to the axisymmetric row at the opposite side of the channel). For disordered configurations, however, the profile is not as well defined and presents a third peak at an intermediate position, corresponding to cells at the axis or with higher inclination, which are therefore off the row and contribute to the correlation function at intermediate distances. The curves are, however, considerably similar between both disordered configurations. In fact, in our simulations we observe

that an ordered initial configuration in which cells are initiallized at three different heights is enough to break the symmetry, and results are consistent with more disordered configurations. The ordered configuration is particular because the system presents a long-term memory at high confinement, and therefore it is not representative of the general behaviour of other configurations. Accordingly, one must be concerned of avoiding initially symmetric configurations, but results are expected to be homogeneous for any other initial configuration.

The cell orientation shows similar values, as shown in Figure 11.6 B. The orientation dispersion is defined as,

$$< (\Delta\theta)^2 >= \frac{1}{N}\sum_{i=1}^{N}(\theta_i - < \theta >)^2. \tag{11.2}$$

where N is the number of cells in the domain. The orientation dispersion is negligible in the case of ordered configurations, because the symmetry implies that all cells behave very similarly. Disordered cells, as expected, present a much higher dispersion which reduces with C_κ with the gradual alignment of the cells. Both disordered configurations present similar values of the dispersion. The mean orientation (inset) shows that the value of the mean orientation is more similar between disordered and ordered configurations than the dispersion, though still the symmetric configuration presents a lower orientation as a result of the perfect alignment of all the cells, whereas disordered configurations are characterized by higher absolute value as well as dispersion in the measure of the orientation, as a result of the limited ordering that the flow induces.

11.2.2 Migration and orientation in ordered configurations

Although ordered configurations, such as the one shown in Figure 11.5, represent just a particular and very specific case of RBC circulation, their homogeneity can be exploited to understand some basic mechanisms introduced by interactions between RBCs. We study the mean orientation and lateral position of the cells in ordered configurations as a function of the capillary number and separation between cells, as plotted in Figure 11.7 A, where the value in the single-cell limit is also provided for comparison. RBC orientation presents two different behaviours depending on the capillary. At $C_\kappa = 12.3$, RBCs orient their axis with the flow, assuming planar slippers. Depending on the distance between cells, they are free to completely orient with the profile (in the single-cell limit), or they present higher orientations if the spatial constraints do not permit a complete alignment. For higher values of $C_\kappa = 30.8$ and 43.40, RBCs acquire a very horizontal inclination (around 15°), and assume a more curved shape, coupling their profile.

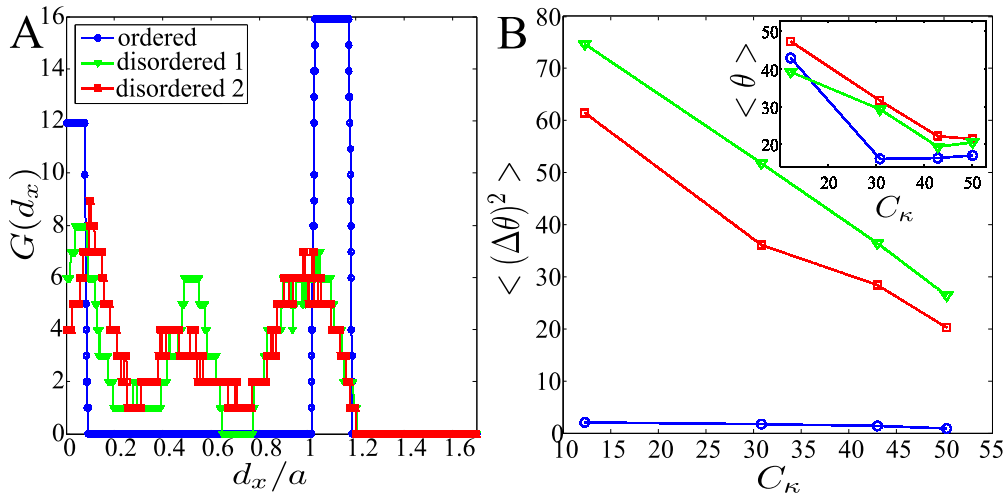

Figure 11.6: (A) Steady pairwise correlation function, $G(d_x)$, for an ordered and two disordered initial configurations, at $C_\kappa = 30.5$. The ordered initial condition forces a symmetric ordering of the cells during flow. Initially disordered configurations show as more homogeneous profile, with the development of a third peak at a intermediate position. (B) Dispersion in RBC orientation $< (\Delta\theta)^2 >$ (see main text) for both ordered and disordered configurations as a function of C_κ. The dispersion is negligible for ordered configurations, as all cells orient simultaneously showing the same behaviour; as expected, disordered orientations present a much higher dispersion, though it reduces for high C_κ when a certain alignment is induced. (Inset) Mean value of the RBC orientation, averaged over the whole suspension. Although ordered and disordered configurations still differ, the measure is mean value is more similar between both cases than the dispersion.

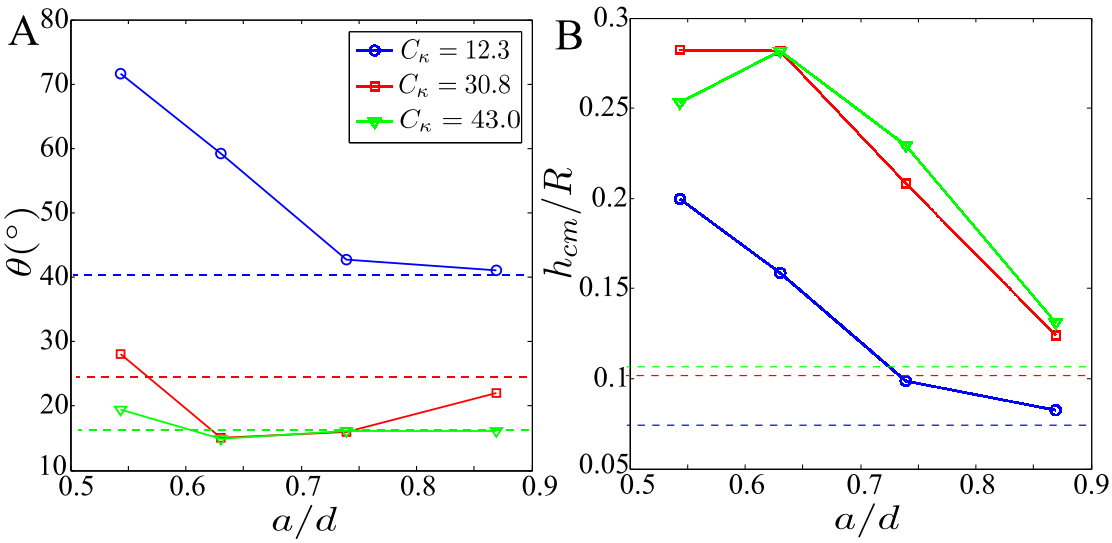

Figure 11.7: (A) Mean orientation of RBCs in an ordered configuration as a function of the distance d in the z-direction. At low C_κ, RBCs show a higher orientation when are placed closed, but the orientation is nearly constant, regardles of the intercell distance, for higher capillary number. Dashed lines represent the single-cell behaviour. (B) Mean position of the center of mass of RBCs in an ordered configuration, as a function of the distance d in the z-direction. Although the lateral position in the channel is not affected for $d/a \sim 1$, at closer distances RBCs experience a substantial repulsion and they are found closer to the walls.

This configuration is similar to the slipper-zigzag described in McWhirter et al. (2008). The orientation of the cells is nearly independent of the distance between them. This zig-zag configuration is stable over an extensive range of C_κ, and at the conditions described we did not found parachutes even for $C_\kappa = 120$. Only at configurations of larger confinement, $a/b > 0.65$, and relatively symmetric initial conditions (in which the center of mass of the RBCs is placely at similar heights), parachute trains are observed. If these conditions are not fullfilled, RBCs prefer to order in the zig-zag phase. Remarkably, both configurations (slippers zig-zag and trains of parachutes) are observed for the same flow conditions, depending on the symmetry of the initial condition.

The mean lateral position of the RBCs, Figure 11.7 B, shows that the closer presence of neighbour cells induces a repulsion towards the walls, and RBCs are located considerably outer than at sinle-cell conditions. For instance, at $C_\kappa = 30.8$, the lateral position displaces from 0.1 to 0.27.

11.2.3 Spatial ordering

The spatial organization of RBCs during downstream flow shows several differences with respect to the single-cell behaviour. We explore the effect of confine-

ment by comparing two channels, of confinement $a/b = 0.53$ and $a/b = 0.40$. Note that they correspond to widths slightly lower than $2a$ and $3a$. The initial condition was a disordered configuration in which cells are initialized at three different channel heights (one at the axis and two symmetric lateral positions). Examples of typical steady configurations are shown in Figures 11.8 and 11.9, for distances between cells $d/a = 0.54$ and $d/a = 0.735$. In both cases, cells show a considerable horizontal inclination, although at the closer distance the geometrical constraints do not permit a perfect alignment, as already described in the previous section. RBCs organize forming a well defined structure, with two rows formed in the narrower channel and three rows in the broader one, in spite of the three-row structure of the initial condition in both cases. The presence of cells at the channel core is interesting, as in the single-cell regime this position is unstable. However, cells that during the downstream flow are located in the intermediate region cannot migrate outwards due to the presence of other cells, and they remain trapped close to the axis. The analysis of the lateral pairwise correlation function demonstrates that both channels present a different organization, as shown in Figure 11.10 (only shown for the case $d/a = 0.40$). For $a/b = 0.53$, the system presents two well defined peaks at $d_x = 0$ and $d_x = 1.2a$, confirming the formation of two rows. For $a/b = 0.40$, however, the profile of the correlation function suggests the formation of four stable positions, the two expected external rows as well as two intermediate positions which are symmetric with respect to the axis. Accordingly, RBCs trapped in the core region also seem to avoid the axis. The position of these intermediate rows is slightly closer to the outer rows than to the axis. We have also analyzed the pairwise correlation function in the transversal direction z, $G(d_z)$ (not shown here). The profile of the correlation function is relatively homogeneous, suggesting that transverse ordering is weak or subdominant with respect to the wall-induced lateral organization.

11.2.4 Focusing

The focusing and alignment of cells have been studied for a single cell throughout the Part III of this Thesis, showing that an increase of the capillary number provides a more defined localization of the particle lateral distribution. This observation is due to a stronger repulsion from the wall and off-center drift, leading to a fine band of equilibrium lateral positions. In addition, in previous sections the different dynamics of RBCs at higher concentration has been described. Concerning spatial organization, two phenomena have been described: *(i)* RBCs can be located at the core axis, showing a more regular distribution of cells along the channel profile; and *(ii)* interaction between cells forces lateral positions closer to the wall than in the case of isolated cells. The competition between these

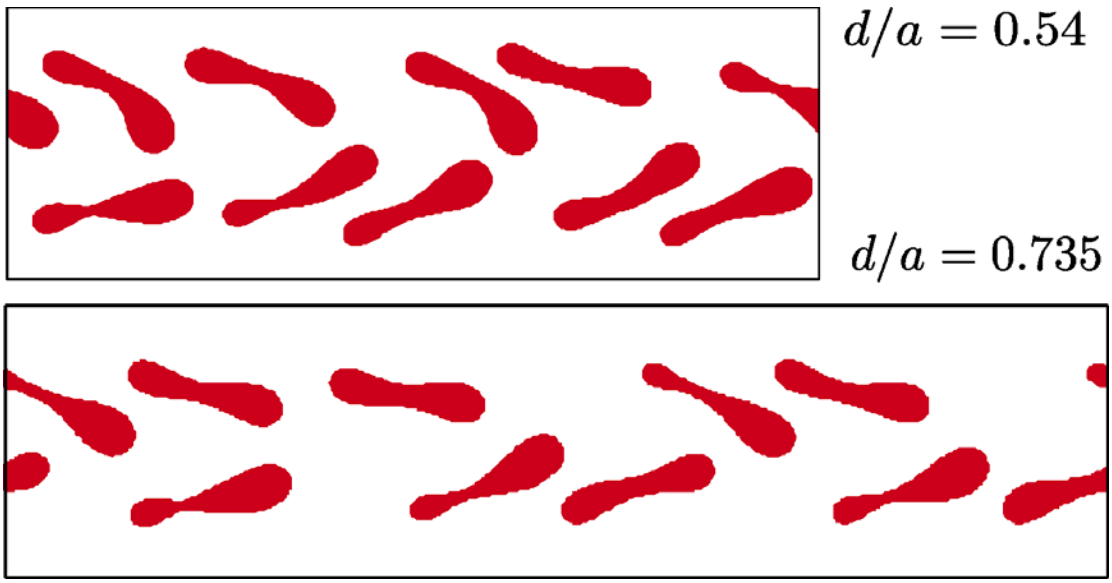

Figure 11.8: RBC during flow in a channel of confinement $a/b = 0.53$, at $C_k = 41$, for distances $d/a = 0.54$, (top) and $d/a = 0.735$ (bottom). n=10 RBCs are simulated in each domain with periodic boundary conditions in the flow direction. RBCs are more disordered (*ie* showing more variation in orientation and position) for lower intercell distants, as the result of less degrees of freedom to orient and accomodate.

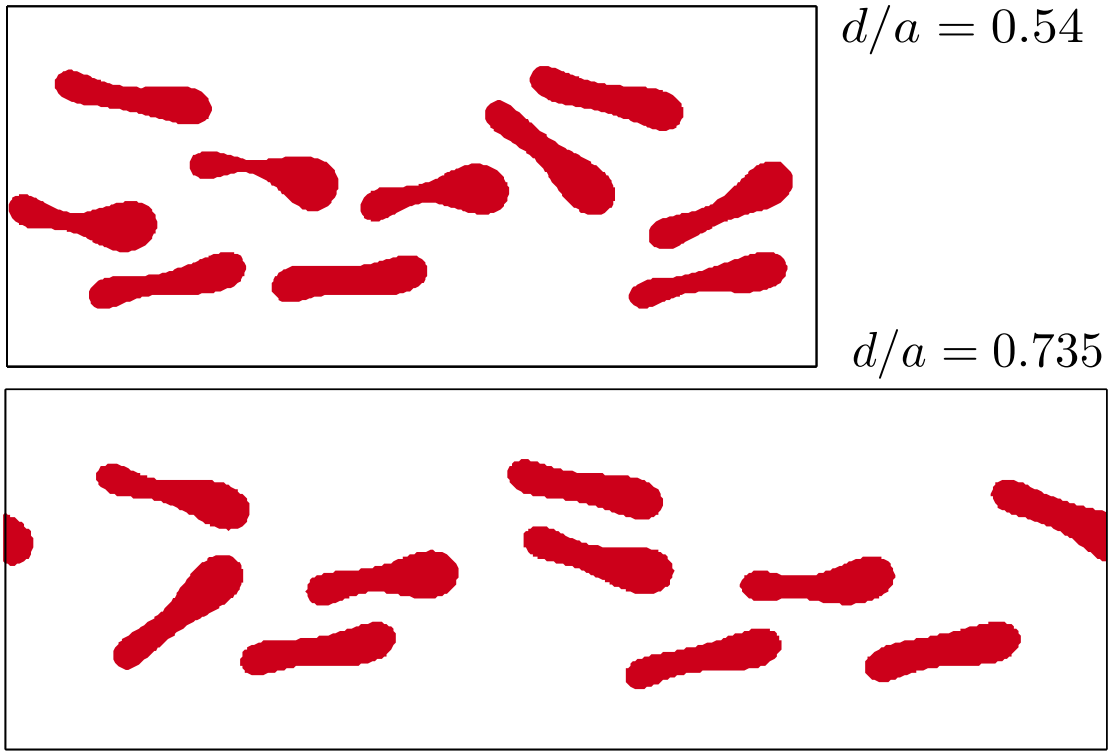

Figure 11.9: RBC during flow in a channel of confinement $a/b = 0.40$, at $C_k = 40.8$, for distances $d/a = 0.54$ (top) and $d/a = 0.735$ (bottom). n=10 RBCs are simulated in each domain with periodic boundary conditions in the flow direction.

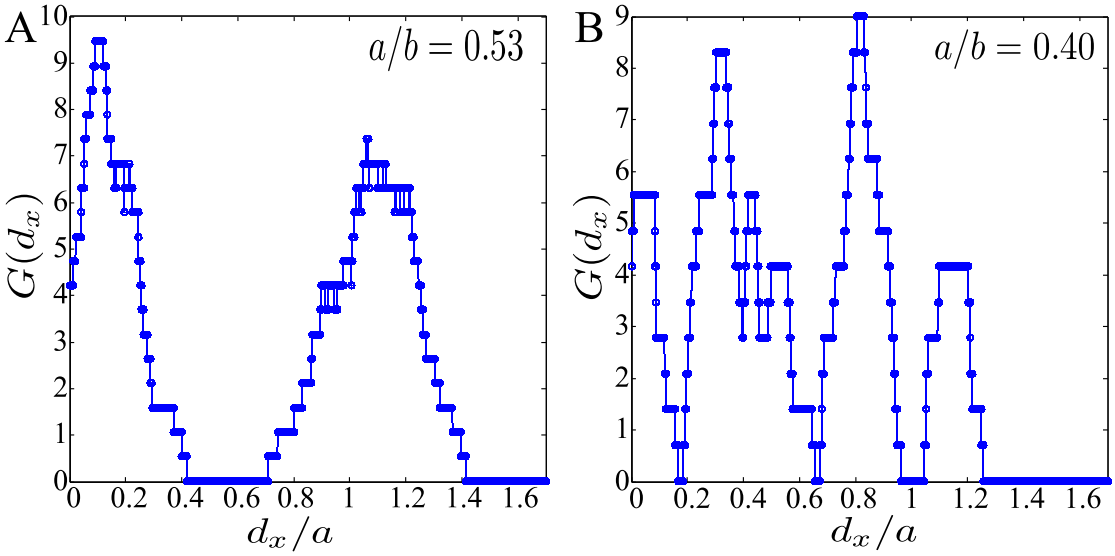

Figure 11.10: Pairwise correlation function $G(d_x)$ for RBCs flowing at channels at confinement $a/b = 0.53$ (A) and $a/b = 0.40$ (B), for $C_k = 40.8$ and distance between cells $d/a = 0.735$. The correlation function clearly describes the organization in two rows in the narrow channel, whereas in the broad channel intermediate positions at the channel core are permitted, although the channel axis is avoided.

mechanisms will dictate the overall organization of RBCs in channel flow.

Figure 11.11 shows three steady configurations of RBC flow at confinement $a/b = 0.40$ for three increasing capillary numbers, C_κ =25.3, 30.4, and 40.8. For the lower capillary, RBCs are found with low but not strictly horizontal orientations, and distributed along the channel. For the higher values of C_κ RBCs flow with its axis oriented with the channel and more ordered in three different positions.

Figure 11.12 A compares the focusing effect for single-cell and several cells. Isolated cells focus to two lateral positions, symmetric with respect to the axis. The focusing results from the balance between the increasingly stronger repulsion from the wall and drift off the axis. Cells interacting with neighbours are found at the core channel and also at regions close to the wall which are forbidden in the previous case. This change is understood from the repulsion between cells, given that some of them are forced to remain in the center by the outer ones, which in turn are pushed towards the center by the wall drift; at the same time, cells from the center force the outer cells towards the wall, a drift not present in the single-cell case. The balance of these interactions explains the RBC distribution and the different behaviour from the single-cell case. If C_κ is increased, the stronger repulsion from the wall forces the outer cells towards more centered positions, and hence the width of the RBC distribution narrows. A band of fluid free of cells is formed close to the walls.

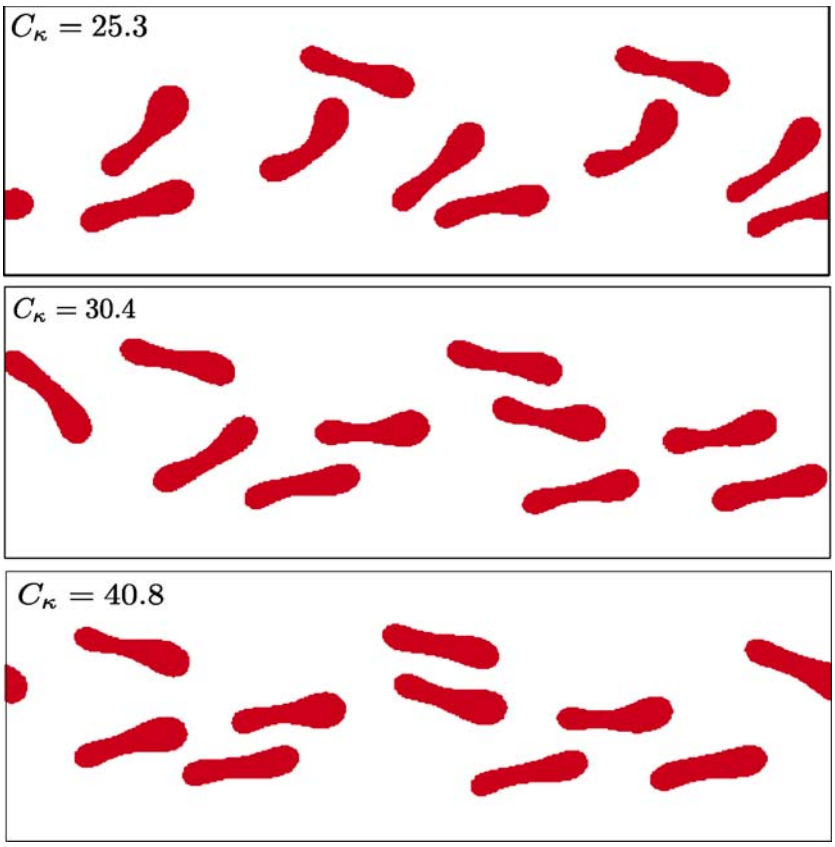

Figure 11.11: RBC during flow in a channel of confinement $a/b = 0.40$, intercell distance $d/a = 0.75$, and C_κ =25.3, 30.4, and 40.8, from top to bottom, respectively. n=10 RBCs are simulated in each domain with periodic boundary conditions in the flow direction.

Figure 11.12 B shows that the presence of neighbour cells also induces a more horizontal inclination of the cells compared to the isolated case. This effect is difficult to explain and further research is required to understand this more pronounced orientation. However, a plausible hypothesis is that the lateral interactions between cells promote the ordering in parallel rows, and thus this horizontal inclination is governed by the lateral confinements induced between the cells rows. Compare these configurations with that shown in Figure 7.3 D, where cells are also found to flow downstream with an horizontal inclination located at the channel core.

11.2.5 Rheology

The dynamics of several RBCs at moderate concentrations have proven to differ in several aspects from the single-cell case, and this should affect the rheological behaviour of the suspension. We compute the effective viscosity for three configurations (one ordered and two disordered), at volume fraction $\phi_v = 0.14$ and

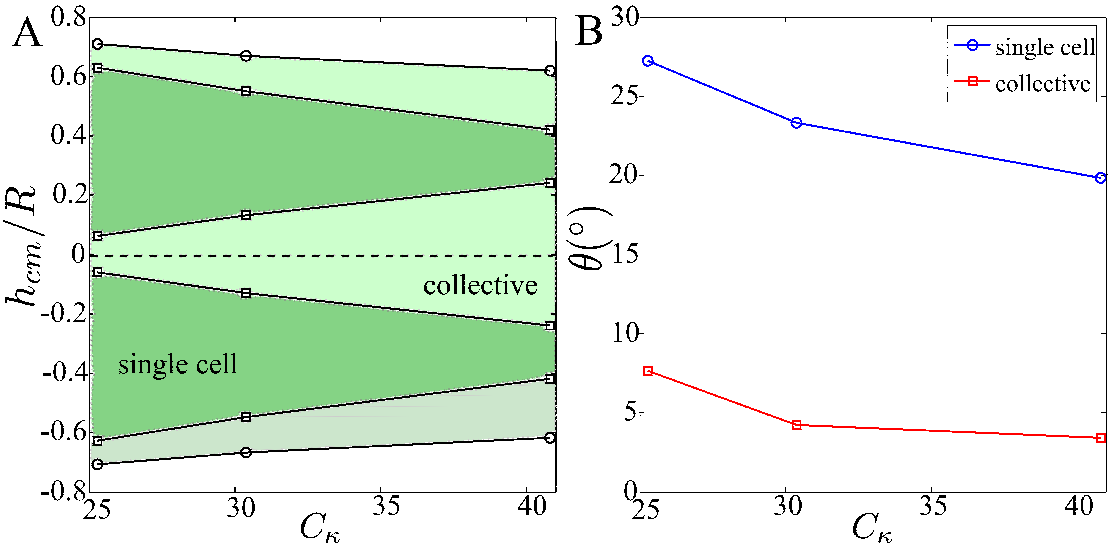

Figure 11.12: (A) Focusing of RBCs in a channel of confinement $a/b = 0.40$, intercell distance $d/a = 0.75$, and $C_\kappa = 40.8$. The shading areas represent the permitted trajectories in the case of single-cell (dark shading) and when collective effects are present (light shading). In the case of several cells, each point represents the outermost position for the n=10 cells in the domain. The increasing C_κ induces the focusing towards more centered positions, giving rise to the formation of a layer free of cells close to the walls. (B) Mean orientation of RBCs at the flow conditions described for (A). Cells flowing at higher concentrations exhibit more horizontal inclinations that those flowin isolated.

confinement $a/b = 0.45$. The viscosity measures, shown in Figure 11.13, are similar for the three cases. The viscosity curves recover the expected shear-thinning behaviour, though two main differences are found with respect to the single-cell case: the magnitude of the effective viscosity obtained and the C_κ required to observe the shear-thinnig decay.

On one hand, the effective viscosity value obtained is larger than that at the single-cell case, and several contributions are expected to explain this difference. The presence of several cells, at least at low C_κ, leads reduces the alignment capability of the cells, and therefore they oppose higher resistance to flow than aligned isolated cells. Additionally, the higher concentration may play a relevant role here.

On the other hand, the shear-thinning decay is found at considerable larger C_κ than in the isolated case. This suggests that the relevant mechanisms that induce the viscosity decay, such as lateral ordering and orientation, require of higher flow velocities than in the single-cell case. The presence of neighbour cells reduces the alignment with the flow, as shown in *eg* (Figure 11.11) at $C_\kappa = 25$, where cells are found with a diversity of orientations. At this C_κ, a single cell flows completely aligned, as can be checked in Figure 10.3. The capillary required to align all the cells in the conditions of Figure 11.11 is ~ 50, indicating that the stronger flow

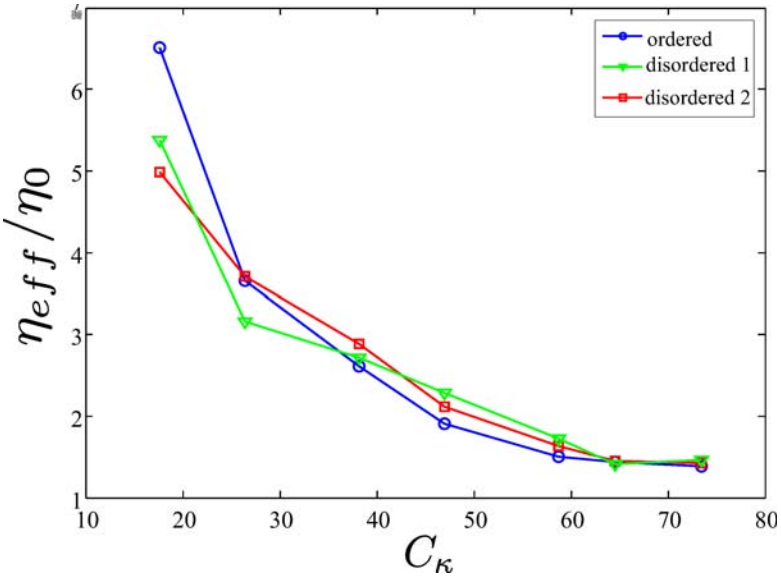

Figure 11.13: Effective viscosity for a RBC suspension at concentration $\phi_v = 0.14$ and confinement $a/b = 0.45$, as a function of the capillary number. Three initial conditions, one ordered and two disordered, are calculated, obtaining similar results. The curve shows the expected shear-thinning behaviour.

perturbation when severall cells are present attenuates the alignment induced by the flow. Hence, only high flow rates are able to induce complete alignment and the viscosity decay is drifted towards higher C_κ.

11.3 Discussion and conclusions

Hydrodynamic interactions between cells modify several aspects of RBC flow in confined channels. Even when just a few cells are flowing, if they are closely placed, the flow disruption introduced by the leading cell implies a different morphological response of the rest of the cells of the group, and this screening is critically determined by the distance between cells (an increase of $0.5a$ in the distance between cells is enough to switch from the single-cell to the interacting regimes) and the capillary number (for higher C_κ the screening effect is subdominant as the flow disruption of the cells is attenuated).

The study of regular arrays of RBCs, when a single row of flowing cells is formed, allows to compare the influence of the wall and the neighbouring cells in a controlled manner. Results show that at intermediate C_κ, at the slipper regime, the typical distance for which RBCs behave as hydrodynamically isolated is of the order of the channel width, whereas for distances below this threshold value the characteristic migration and asymmetric shapes are not observed and cells prefer to order in the center of the channel.

For thicker channels, several cells can occupy the channel section and thus lateral interactions between cells also compete with the wall. We study the flow of RBCs at moderate concentrations $\sim 10-20\%$. At low C_κ, RBCs flow with a disordered distribution, showing a variety of orientations. Further increasing C_κ cells orient and flow with very aligned, horizontal inclinations. We observe that parachute shapes only develop in very confined channels and with initial conditions in which cells are situated at similar heights. Otherwise, cells prefer to order in two rows of slippers that is known in the literature as slipper zig-zag. The collective disruption of the incoming flow allows cells to retain slipper shapes even at extremely high capillaries, in detritment of parachute deformations which are penalized by higher elastic energies.

The channel width determines the lateral ordering of the RBCs. In narrow channels $\sim 2a$ RBCs order in two symmetric rows, similar to the single-cell behaviour, although the repulsion between cells typically force an outer lateral position of the cell center of mass. In channels of width $\sim 3a$, RBCs order in 3-4 rows; some cells are trapped at the channel core, repulsed towards the axis by those flowing along outer streamlines. Therefore, at these conditions, RBCs can be found flowing close to the channel axis, and the cell distribution is more homogeneous along the channel section than in the low concentration regime. Lateral focusing is hence lose, although high C_κ have been shown to nduce a higher repulsion from the wall, so that the outer position of the cell displaces inwards. The width of the band of cell distribution is then given by the competition betwen the wall repulsion, which drifts cells towards the axis, and the repulsion between the cells in the core and those flowing at the lateral. This principle likely represents the basis of the Faehreus-Lindqvist effect, and further increase of C_κ will lead to a cell focusing in the channel central region.

The transition from the single-cell to the collective behaviour is found here at volume fractions ~ 0.1, in contrast to the results at thicker tubes where it is typically found at ~ 0.2 (Han et al., 1999), but the much higher Reynolds and capillary numbers might attenuate the interactions between RBCs, implying that collective effects become dominant for closer distances between cells.

The different elastic and flow behaviour of RBCs at the collective regime has important consequences in the rheology of the suspension. In addition to the expected increase of the effective viscosity as a consequence of the higher volume fraction, the shear-thinning decay requires of higher flow velocities. The collective disruption and retarded alignment and ordering of the cells at these conditions might be fundamental to explain this drift in the viscosity curve.

Part V

Conclusions

Chapter 12

Conclusions and future perspectives

12.1 Conclusions

Understanding the elastic response of RBCs under certain situations that they experience during their functional live span is the guiding thread throughout this Thesis. From a theoretical perspective, and based on both analytical and numerical calculations, we have studied the role of membrane microstructure (*ie* the internal balance between the lipid bilayer and the spectrin cytoskeleton) in RBC shape control. Besides, we have developed a phase-field model for membrane modeling, accounting for both the membrane elasticity and hydrodynamics of the surrounding fluid, and explaining in detail its derivation from the classic theory of elasticity of membranes. This model can be applied to a number of problems related with membrane elasticity. In particular, we have made use of this model to study the deformability of RBCs in channel flow, and the importance of RBC elasticity in the rheological properties of blood.

In Part I, we have established the biophysical framework on which this Thesis is based on. Due to their simplicity an anucleated nature, RBCs have been the scope of most studies about membrane elasticity. Appart from their intrinsic interest in the field of membranes, RBCs are also the main component of blood, and the understanding of their deformability and flow behaviour is fundamental in different biomedical areas. Our research is based on the Helfrich theory of membranes, which assumes that the membrane elasticity is characterized by its resistance to bend. Although the Helfrich model is the reference theory within the membrane field, it fails to explain some phenomena observed in the experiments, such as the formation of echinocytes. The model has been extended to account for the effect of the coupling between the leaflets of the bilayer, in the so-called ADE

model, and the elastic contribution of the underlaying cytoskeleton. Nevertheless, the importance of each membrane component in the macroscopic response of the cell is still an open subject of active debate.

Membrane elasticity and the disco-echinocyte transition

In Part II we concentrate on the disco-echinocyte morphological transition that RBCs undergo when exposed to certain agents, such as incubation in the presence of amphiphiles, or ATP depletion. In these conditions, RBCs lose their healthy biconcave shape and develop numerous spicules and bumps along their contour, becoming more spherical. The observed altered shapes result from the imbalance of the conformational structure of the membrane, and for instance the formation of bumps is driven by the expansion of the outer leaflet with respect to the inner one.

We have carried out a theoretical study in which we consider the elastic contributions of the lipid bilayer and the cytoskeleton, which allows us to identify the role of each microstructure in the disco-echinocyte transition. We consider a gradual increase of the internal asymmetry of the membrane, and by means of numerical calculations we obtain the minimal shape for each membrane asymmetry. We can then specify the equilibrium shapes of the RBCs as a function of the membrane structure. The study is based on a Cassini oval parametrization of the cell profile.

Our results show that the expansion of the outer leaflet triggers the development of bumps, since higher membrane curvatures allow the relaxation of the bilayer energetic storage. In the absence of the cytoskeleton, the discocyte desestabilizes for minute deviations of the membrane asymmetry. The cytoskeleton presents a strong resistance to the formation of bumps, as it is severely deformed and its elastic energy increases sharply. The balance between both contributions dictates the development of undulations and bumps, as well as the specific shape of these structures. The results provide an energetic scale of the shape transition, showing that the separation between each morphology is of the order of hundreds of k_BT, ensuring a high stability of the altered shapes. The study also highlights the importance of the relaxed state of the cytoskeleton. We have compared the area expansion required to induce each morphological stage from our results (assuming a discocytic shape) with previous from the literature (in which a elliptic relaxed shape is considered). The discocytic conformation leads to a gradual transition, with crenated shapes developed for a homogeneous increase of the asymmetry. For elliptic relaxed shapes, the transition is sharper, and a considerable increase of the asymmetry is necessary to desestabilize the discocyte

whereas the development of spicules require of minute changes. We can state that the main conclusions of this Part are:

- The interplay between the bilayer and the cytoskeleton determines the stable shape of the RBC. When subjected to a expansion of the outer leaflet, the bilayer tends to curve and develop bumps, and the cytoskeleton opposes resistance to these deformations, preserving compact shapes.
- The cytoskeleton is a key ingredient in the stabilization of the discocyte structure against changes in the membrane internal asymmetry, even if discocytic relaxed shapes are considered. In the absence of the cytoskeleton the discocyte is unstable under very small increases of the asymmetry.
- The morphological transition has a marked hierarchy, with a considerable energetic separation between the shapes sequentially found. In this picture, the discocyte represents a ground state of the morphologies ensemble.
- The quantitative comparison of the development of the different morphologies with respect to the area expansion supports the hypothesis of a discocytic relaxed shape of the cytoskeleton, in detritment of an elliptic reference conformation.

The theoretical study allows us to explain the experiments of AFM-induced shape transformations carried out by Kathryn A. Melzak and José Luis Toca-Herrera. A series of experiments shows that echinocytes can be perturbed by a AFM tip, and the cells deform into less crenated shapes or discocytes. The method allows to control and modify the shape of altered cells at the single-cell scale. Supported by our theoretical results, we hypothesize that the AFM tip punctures the lipid bilayer, breaking locally the hydrophobic potential around the tip perimeter and hence permitting the rearrangement of lipids from the inner to the outer leaflet, relaxing the shape stress energy towards lower-energy configurations.

Membrane phase-field model

Part III is devoted to the derivation of a phase-field model for membrane modeling. Phase-field methods have been widely used to the study of interfaces, an their robust physical basis has served to explain a wealth of dynamic instabilities. The classic framework focuses on tension-driven interfaces, in which the only elastic contribution is the surface tension. The modelization of more complex interfaces, such as membranes, in which different elastic effects potentially contribute, requires of further and detailed analysis.

We have first connected phase field models with the theory of elasticity, deriving the general expressions for the chemical potential and stress tensor in terms of the order parameter. We have identified the elastic modulii of the interface in terms coefficients of the phase-field energy and equilibrium profile of the order parameter, showing that the elastic parameters are sequentially found as moments of the lateral stress profile, in accordance with the Helfrich theory. These calculations allow us to consider a specific phase-field model which indeed captures the physics of a membrane, with vanishing surface tensions and thus obtaining a bending-driven interface.

We have incorporated the phase-field model to a dynamic formalism. We consider a diffusive dynamics in the form of a Cahn-Hilliard equation. We have extended this theory to account for the hydrodynamics of the surrounding fluid, presenting a complete phase-field Navier-Stokes model. The equation describing the membrane dynamics is coupled to the Navier-Stokes equation. Besides, we have performed a sharp-interface limit analysis which provides us the macroscopic equations of the phase-field model. The hydrodynamics has not been considered in this study. On one hand, we recover the well-known Ou Zhang-Helfrich equilibrium equation for a symmetric membrane. On the other hand, we obtain the complete macroscopic dynamic model. From the set of equations of obtained, we have studied the relaxation of a flat membrane subjected to a sinusoidal perturbation, and this procedure provides information about the elasticity of the interface. We have used this method to test the accuracy of both the PF and PF-NS models, performing numerical simulations. The results serve to validate the model, obtaining a good agreement with the relaxational behaviour predicted by the theory.

In Chapter 6, we have described the numerical method implemented to perform simulations of the model. We make use of a lattice-Boltzmann method for integrating the Navier-Stokes equation, coupled to a standard finite-differences method for the integration of the phase-field equation. Given the particularities of bending interfaces and their delicate control, we have explained the main numerical problems that must be adressed to correctly simulate these interfaces.

We thus might point that

- We have derived a phase-field model for membrane modeling, proving its consistency with the classic theory of membranes and obtaining the expressions of the elastic stress tensor and lateral stress profile.

- The model recovers the equilibrium equation of the membrane, as proved by means of a sharp-interface limit analysis. The method also allows us to obtain the macroscopic equations of the model.

- We have tested numerically our model by means of a linear stability analysis of a flat interface, obtaining the desired membrane dynamics.

- The complete method is numerically integrated by a lattice-Boltzmann scheme, which must be tunned carefully in order to capture the delicate behaviour dictated by bending interfaces.

RBC flow

In Part IV of this Thesis, we have studied the elastic behaviour of RBCs flowing in confined microchannels, both at low concentrations in very thin channels, when they display single-cell behaviour, and at higher concentrations at intermediate channels, when collective effects dominate the dynamics. The study has been conducted to understand and identify the elastic mechanisms that contribute to the rheological behaviour of blood. We have performed simulations making use of the phase-field Navier-Stokes model derived in Part III.

In Chapters 8 and 9, we have focused on the deformability and rheological properties of single RBCs. The parameter control is the capillary number, which balances the elastic forces of the membrane and the fluid forcing. Our results show that for increasing capillary, RBCs develop a sequence of different morphologies, namely discocytes, slippers and parachutes. The shapes obtained show a nice agreement with experimentally observed RBCs at similar conditions. The deformability and capability to orient of the cell modulates the rheological behaviour of the suspension. We obtain a shear-thinning behaviour of the effective viscosity. The viscosity decay is mainly associated with the transition to the slipper, highlighting the importance of cell deformation and orientation. The analysis of the energetic contributions has shown that membrane incompressibility is crucial for preserving compact shapes, and at intermediate and high capillary RBCs are subjected to strong membrane tensions. We have investigated the origins of the slipper morphology, showing that the RBC benefits from a relaxation of its deformation energy in comparison with cells flowing at the channel axis. The fluidity of the suspension also benefits from this lateral positioning. The main conclusions of this study therefore are,

- RBCs present a rich behaviour determined by the interplay between their elastic membrane and the flow. Sequentially, discocytes, slippers and parachutes are found for increasing capillary number.

- The suspension presents a characteristic shear-thinning behaviour, originated on the elasticity and orientation of the cell with the flow.

- Asymmetric shapes are low-energy configurations which also enhance the fluidity of the suspension compared to cells flowing at the channel axis.

- The similar shapes obtained by our model, which lacks an in-plane contribution of the cytoskeleton, and previously observed morphologies both in experimental and numerical studies in which the cytoskeleton was considered, suggests that the cyskeleton does not play a key role in this type of deformations.

In Chapter 10, we have investigated the control of RBC focusing and spatial organization, motivated by the enormous interest of this subject in lab-on-a-chip devices and microfluidics. We have shown that for low capillary numbers RBCs flow along the entire section, but increasing the capillary number the cell distribution narrows to a lateral band. We have explored the effect of capillary number and confinement, showing that both effects are coupled and reinforce the focusing. For sufficiently high capillary, the band converges towards a unique lateral position. For thicker channels, larger values of the capillary are required to induce focusing. However, in these channels the stable lateral position is found further from the axis. This position is likely determined by the balance between the repulsive force from the wall and a drift from the axis. Additionally, we have studied the dependence of cell shape, obtaining that more spherical vesicles prefer the channel axis.

- RBC focusing is controlled by the flow velocity and confinement of the channel, and both effects are coupled. Higher flow velocities and narrower channels induce the focalization of cells towards a more defined position in the lateral channel.

- The shape of the object is a key parameter controlling the object flow. RBCs and deflated vesicles flow at different lateral positions along the channel section, with more spherical vesicles prefering the center and RBCs occupying outer positions.

In Chapter 11, we have explored the effect of hydrodynamic interactions between RBCs when they flow maintaining short distances between cells, and the competition of these interactions with the wall effect. If cells are sufficiently distant, wall-effects dominate and the cell exhibits single-cell behaviour, such as the lateral migration and orientation. The presence of a close neighbour could inhibit this effect and then RBCs behave collectively. Afterwards, we have studied the behaviour of several cells flowing in a channel. RBCs are found flowing close to the axis, as they are repulsed by the neighbour flowing at an outer position, and at the same time the cells situated in the center push the outer ones towards the walls. The focusing effect described in Chapter 9 dissapears. However, we have

found that increasing the flow velocity also induces a focusing, now towards a more concentrated distribution of cells in the channel core as wall repulsion increases. As a summing-up of this study, we can state that

- Hydrodynamic interactions between RBCs strongly modify the flow behaviour of the cell, as the screening between cells attenuates cell deformation andit can inhibit lateral migrations. Which effect is dominant is determined by the distance between cells and the capillary number.
- When several cells are present, parachutes are only found at very confined channels and close distances between cells. For thicker channels and higher distance between cells, they prefer to organize in paralel rows of slippers, a configuration stable even at very high flow velocities.
- For channels of typical width three times the cell length, cells order forming several rows of RBCs with horizontal inclination, parallel to the walls, and exhibit weak deformation from the discocyte.
- The collective effect forces the occupation of the channel core, and the characteristic lateral focusing of the single-cell behaviour is not observed. However, the higher repulsion from the walls for higher capillaries forces the narrowing of the band of trajectories occupied, as cells are repulsed towards the axis.

12.2 Future perspectives

The complexity of cell membranes invariably causes that in the process of ellucidating a certain aspect of their functioning, many other questions arise, of similar complexity and importance. Some of these questions can be actually studied with the phase-field method developed in this Thesis.

Stability of cell membranes

In Chapter 5, we have carried out a stability analysis for the simplest membrane configuration, a symmetric flat membrane. This method, however, can be extended to more complex geometries and membranes. For instance, the relaxation of membranes at cylindric or spherical morphologies is a subject of interest as it is not completely understood (Shiba and Noguchi, 2011). The effect of a non zero spontaneous curvature is also a problem of complex analytical treatment, and the phase-field model offers the appropriate framework to study and adress these problems.

Phase-field modelization of the cytoskeleton

One of the major limitations of the phase-field model presented here is that it does not account for the in-plane contribution of the cytoskeleton. Ideally, the model could be refined to incorporate terms of shear and stretching, as has been developed in other fields, such as fracture dynamics (Pons and Karma, 2010). Although the derivation of such a model seems, a priori, a considerable challenge, it would represent a formidable tool for studying numerous new problems. For instance, the disco-echinocyte transition could be study even introducing dynamic effects, such as the competition in the time scales of membrane asymmetry change and cell deformation. This study could clarify important aspects of membrane damage during blood storage. A different problem would be to study the rheological behaviour of echinocytes in flow, as blood under crenation is known to present a considerable different behaviour.

New aspects of RBC flow

The study of RBCs flow presented in this Thesis has adressed the main aspects at the cell scale or the effects when a few RBCs are interacting. However, many other problems of interest can be potentially study. The convergence to the high concentration limit, at hematocrit $\sim 45\%$, could reveal new mechanisms and aspects of RBC deformability. At high concentration, cells often aggregate due to the presence of certain molecules on their membrane, forming new structures that severely alter the suspension rheology (Fedosov et al., 2011). In addition, new components of blood can be added, such as hard spheres of small size, roughly $4 - 5\mu$m, which mimic the behaviour of platalets or beams. This system is interesting because it is known that during blood flow, these objects avoid the arteriole core when RBCs concentrate, and flow at the layer close to the wall. This effect, known as cell-margination, is of great interest due to its applications for drug delivery (Kumar and Graham, 2012).

Chapter 13

Resumen en castellano

Las membranas celulares son estructuras de una enorme complejidad, compuestas por un gran número de lípidos y proteínas. La membrana tiene un papel fundamental en la vida celular, pues separa el interior de la célula del medio externo y define un gran número de funciones y actividad proteínica. Es, además, responsable de la respuesta celular frente a perturbaciones mecánicas, y por ello las membranas poseen una propiedades elásticas únicas entre los materiales. Por todo ello, el estudio de las membranas ha atraído a los físicos desde hace muchos años, y un gran numero de fenómenos en este campo han sido explicados gracias a la contribución de modelos fisicos.

En este contexto, los glóbulos rojos son células muy particulares entre las diferentes especies de células humanas, por ser las únicas que carecen de núcleo y orgánulos internos, de forma que sus propiedades morfológicas y mecánicas están completamente determinados por su membrana. Por este hecho, el estudio de membranas celulares se ha centrado a menudo en glóbulos rojos. Estas células, además, tienen un papel muy importante en el funcionamiento del cuerpo humano, pues son el componente principal de la sangre y son los encargados del transporte de oxígeno al resto de células del cuerpo. En concreto, cuando los glóbulos atraviesan los capilares más finos, de sección menor que su propia área, se ven forzados a deformarse fuertemente y alargarse. La capacidad para realizar estas deformaciones y poder atravesar los capilares muestra una extrema sensibilidad a las propiedades elásticas de la membrana.

Esta Tesis está centrada en el estudio teórico de las propiedades mecánicas y elásticas de los glóbulos rojos. Nuestro estudio abarca desde la respuesta morfológica de la célula ante cambios en la microestructura de la membrana, hasta el estudio del flujo de glóbulos en canales donde las células se deforman e interaccionan con células vecinas.

13.1 Introducción

13.1.1 Introducción biológica

La membrana celular está formada por dos componentes principales: una bicapa lipídica y un citosqueleto de espectrina que se encuentra bajo la bicapa. La bicapa lipídica está formada por dos películas de lípidos, que se ensamblan en dirección contraria, dejando las colas lipídicas (de naturaleza hidrofóbica) en la región interna, y las cabezas (hidrofílicas) en contacto con el líquido externo. La bicapa es fluída en el plano de la membrana, debido a una rápida difusión lateral de los lípidos, y contiene un gran número de proteínas transmembrana que se encuentran *flotando*, en el llamado mosaico fluído (Singer and Nicolson, 1972). El citoesqueleto, por el contrario, es una malla de espectrina que presenta resistencia a realizar esfuerzos laterales. Se trata de una estructura de dos dimensiones que se encuentra anclada a la cara interna (citosólica) de la membrana. La interacción de ambas estructuras determina la respuesta elástica de la membrana celular.

Esta membrana es, por tanto, el elemento principal de los glóbulos rojos. La célula se compone además de un citosol rico en proteínas, donde la hemogoblina se concentra. Los glóbulos presentan una forma característica, conocida como discocito, similar a un disco plano pero con una zona cóncava en el centro. El perfil de esta célula es, por tanto, un eliptocito bicóncavo. El diámetro de la célula es de unas 8 micras, y el grosor varía entre las 1 y 2 micras entre sus valores máximo y mínimo.

La sangre es un fluído formado por una gran variedad de componentes, pero su elemento principal son los glóbulos rojos, llegando a constituir un 95% de las células sanguíneas. Otros componentes de importancia son las plaquetas y los leucocitos. La concentración de células es típicamente del 45%, siendo el resto un fluído llamado plasma sanguíneo similar al agua, aunque con abundantes proteínas y otras moléculas. La elasticidad y deformabilidad de los glóbulos confiere a la sangre unas complejas propiedades reológicas.

13.1.2 Modelos físicos de membranas

La fuerte separación entre la escala del grosor de la membrana, de unos 4nm, y la longitud típica de la célula, unas 8 micras, sugiere que un tratamiento apropiado es considerar la membrana como una lámina de dos dimensioneso. Así, su elasticidad puede aproximarse por la de una lámina elástica, de acuerdo con la teoría general de la elasticidad. Fueron Canham (1970) y Helfrich (1973) los primeros en proponer una energía elástica para describir las membranas celulares. En concreto, su teoría asume que la única contribución relevante proviene de la resistancia a

doblarse. Además, la bicapa lipídica presenta una fuerte incompresibilidad lateral, de forma que el área se mantiene constante. Por último, la membrana es impermeable al paso de agua, de forma que para membranas el volúmen es constante. Teniendo esto en cuenta, propusieron una energía de la forma

$$\mathcal{F}_b = \frac{\kappa}{2}\int (C - c_0)^2 dA + \kappa_G \int G dA + \int \gamma dA + \int \Delta p dV, \tag{13.1}$$

donde C y G son la curvatura total y Gaussiana, respectivamente, κ y κ_G son los módulos de flexión y Gaussiano. c_0 es la curvatura espontánea, que refleja una posible asimetría interna de la membrana. Este modelo, sin embargo, no tiene en cuenta algunas particularidades de la arquitectura de las membranas. Por un lado, no considera que la bicapa está formada por dos hojas separadas y acopladas. Por otro, no tiene en cuenta la contribución a la elasticidad en el plano de la membrana por parte del citoesqueleto, que se descompone en una contribución de esfuerzo normal y otro de cizalla (Evans and Skalak, 1980). La teoría de Helfrich ha sido extendida, incorporando estas nuevas contribuciones, de forma que un modelo de membrana general sería

$$\begin{aligned} E_{mem} = \frac{\kappa}{2}\int_S (C - c_0)^2 dS + \frac{\kappa_{NL}\pi}{A_{RBC} d^2}\left(\Delta A - \Delta A_0\right)^2 \\ + \int_{S_0} \left[\frac{K}{2}(\lambda_1\lambda_2 - 1)^2 + \mu\frac{(\lambda_1 - \lambda_2)^2}{2\lambda_1\lambda_2}\right] dS_0. \end{aligned} \tag{13.2}$$

donde el primer término se corresponde al modelo de Helfrich y la contribución de diferencia de área (Seifert et al., 1991; Waugh et al., 1992), dada por la diferencia entre las áreas de la capa exterior y la interior, ΔA_0. Los paramétros elásticos del citoesqueleto vienen dados por el módulo de cizalla, μ, y el de compresión, K.

13.2 Resultados

13.2.1 Elasticidad de la membrana y transición del discocito al equinocito

En los Capítulos 3 y 4, nos hemos centrado en el estudio de la transición discocito-equinocito. Se trata de una secuencia de formas que los glóbulos rojos desarrollan cuando se ven afectados por la acción de diferentes agentes. Entre otros muchos, es bien sabido que al ser expuestos a la presencia de ciertos lípidos, o bien a la reducción de ATP, los globulos se deforman y adquieren morfologías más esféricas,

con numerosas espículas y protuberancias en su superficie. Estas deformaciones se deben a cambios conformacionales en la microestructura de la membrana. Por ejemplo, en el caso en el que las células se incuban en presencia de lípidos, estos son incorporados a la membrana, y se sitúan en la capa externa. En estas condiciones, la capa externa acumula una mayor concentración de lípidos y trata de expandir su área para poder acomodarlos. Por eso tiende a curvarse y formar esa protuberancias, posibilitando la expansión de la capa externa con respecto a la interna. La transición ha sido estudiada experimentalmente y un gran número de agentes y mecanismos han sido identificados. Sin embargo, la transición no ha sido caracterizada cuantitativamente y ciertos aspectos de las transiciones no son bien comprendidos.

En el Capítulo 4 hemos presentado un estudio teórico en el que analizamos la respuesta mecánica y morfológica de los globulos cuando son sujetos a un incremento en su asimetría de la membrana. Consideramos el modelo de membrana (13.2), basándonos en una parametrización de la superficie de la célula en términos de los óvalos de Cassini, una familia de curvas que son conocidas por presentar una sección biconcava muy similar a la del discocito. La expresión analítica de estas curvas viene dada por

$$(x^2 + z^2 + a^2)^2 - 4a^2x^2 = c^4. \tag{13.3}$$

de donde se define la biconcavidad, $\epsilon \equiv a/c$. Para $\epsilon = 1$ la curva se corresponde con un lemniscato de Bernuilli, mientras que para $\epsilon = 0$ se recupera un círculo. En nuestro caso, recuperamos la forma de una célula aplicando simetría axial en torno a $x = 0$. La modelización de las espículas y protuberancias se realiza superponiendo superficies específicas.

Nuestros resultados prueban que la morfología de la célula muestra una sensibilidad extraordinaria al equilibrio entre la bicapa lípidica y el citoesqueleto. Para asimetrías bajas, el discocito es la forma de energía mínima, pero cuando cuando la asimetría se va incrementando, la célula prefiere adquirir formas más convexas, con las que poder acomodar el exceso de área en la capa externa. El citoesqueleto, por el contrario, se opone a este tipo de deformaciones y prefiere mantener formas más cercanas al discocito. La competición de ambas estructuras dictamina la forma de equilibrio. Si la asimetría de la membrana induce suficiente almacenamiento de energía en la bicapa, finalmente el citoesqueleto se verá forzado a deformarse y las protuberancias van apareciendo sequencialmente. Primero, aparecen ondulaciones en el contorno de la célula, lo que se denomina discoequinocito I. Después, protuberancias aparecen también en la cara principal del disco, distribuídas a lo largo de la superficie. Simultáneamente el glóbulo se va volviendo más esferico. Nuestro estudio se limita a estos primeros estadios de

la transición.

Nuestro estudio permite cuantificar la cantidad de exceso de área en la capa externa necesaria para inducir el cambio morfológico. Obtenemos valores cercanos al 0.63% para desestabilizar el discocito, pero este valor se reduce al 2.0% en la ausencia del citoesqueleto. Por tanto, el citoesqueleto es una estructura básica para controlar la estabilidad del discocito con respecto a cambios en la asimetría de la membrana. Las escalas energéticas de la transición muestran que las diferencias entre las diferentes morfologías son del orden de cientos de k_BT, evidenciando la gran estabilidad de estas formas. En concreto, el discocito representa el estado fundamental de la transicón, y está muy favorecido energéticamente respecto a los equinocitos, que presentan un alto grado de estrés del citoesqueleto.

El estudio teórico explicado previamente nos permite interpretar los resultados realizados por Kathryn A. Melzak y José Luis Toca-Herrera. En estos experimentos, se utiliza la punta de un AFM para inducir una transición morfológica en glóbulos rojo. En concreto, se seleccionan equinocitos que han sido formados mediante reducción de los niveles de ATP, y tras la perturbación con el AFM se observa la transición hacia el discocito. Proponemos que en los experimentos el AFM perfora la bicapa lipídica, y el contacto con la punta del AFM rompe la barrera hidrofóbica permitiendo el salto de algunos lípidos de la cara externa, donde están en alta concentración, a la interna, donde se encuentran más relajados. El mecanismo permite la relajación de la energía de curvatura y la célula vuelve hacia el discocito, que representa una morfología de mucha menor energía.

13.2.2 Métodos de interfase difusa para modelado de membranas

Los métodos de interfase difusa (en inglés usualmente conocidos como *phase-field models*) son muy útiles a la hora de tratar problemas dinámicos de interfases. Se han aplicado ampliamente al estudio, entre otros, de inestabilidades entre dos fluídos, en los que la interfase está caracterizada por la tensión superficial. Sin embargo, las membranas son objetos complejos en los que la tensión superficial es insignificante y la dinámica de la membrana está dominada por la flexión. Los modelos de interfase difusa se basan en utilizar un parámetro de orden, ϕ, que tiene dos fases estables ± 1 y varia suavemente de una a otra. La interfase viene caracterizada por un grosor ϵ. El método se basa en resolver directamente la dinámica de la membrana, y de ahi extraer la forma y evolución de la interfase. Así, se evita el problema de aplicar condiciones de contorno para una interfase móvil.

Hemos desarollado un modelo de interfase difusa que captura las propiedades

elásticas de las membranas. Para ello, se propone un modelo de energía libre de la forma

$$\mathcal{F}_b[\phi] = \frac{\kappa^*}{2}\int(\phi^2 - 2\phi^4 + \phi^6 + (3\phi^2-1)\epsilon^2(\nabla\phi)^2 + \epsilon^4(\nabla^2\phi)^2)dV. \tag{13.4}$$

La incompresibilidad de la membrana se introduce mediante un multiplicador de Lagrange que fija el área de la célula. Hemos probado que esta energía converge a la de Helfrich (13.1) para los valores particulares de $\gamma = c_0 = \kappa_G = 0$. Hemos derivado, a partir de la energía libre, las expresiones para el potencial químico $\mu = \delta\mathcal{F}/\partial\phi$ y el tensor de esfuerzos en función del parámetro de orden. Esta última adquiere la forma,

$$\sigma_{\alpha\beta} = \left(\mathcal{F} - \phi\frac{\delta\mathcal{F}}{\delta\phi}\right)\delta_{\alpha\beta} - \nabla_\alpha\phi\frac{\partial\mathcal{F}}{\partial(\nabla_\beta\phi)} + \nabla_\alpha\phi\nabla_\beta\frac{\partial\mathcal{F}}{\partial(\nabla^2\phi)} + \nabla_\alpha\nabla_\beta\phi\frac{\partial\mathcal{F}}{\partial(\nabla^2\phi)}. \tag{13.5}$$

y permite demostrar que la densidad de fuerza elástica de la membrana, en términos del parámetro de orden, viene dada por la expresión

$$\mathbf{f_{mem}} = \nabla\cdot\sigma_{\mathbf{mem}} = -\phi\nabla\mu_{mem}. \tag{13.6}$$

Hemos incorporado la energía libre a un modelo dinámico de tipo Cahn-Hilliard, incluyendo también los efectos hidrodinámicos del fluído que rodea a la membrana. La hidrodinámica viene dada por la ecuación de Navier-Stokes, de forma que tenemos dos ecuaciones acopladas, una que describe la dinámica de la membrana y otra para el fluído. El modelo completo es, por tanto,

$$\frac{\partial\phi}{\partial t} + \mathbf{v}\cdot\nabla\phi = M\nabla^2\mu_{mem}. \tag{13.7}$$

$$\rho\left[\frac{\partial\mathbf{v}}{\partial t} + (\mathbf{v}\cdot\nabla\mathbf{v})\right] = -\nabla P + \mathbf{f_{mem}} + \eta\nabla^2\mathbf{v} + \mathbf{f_{ext}}. \tag{13.8}$$

Un estudio del límite de interfase abrupta, $\epsilon \to 0$, nos permite obtener las ecuaciones del modelo macroscópico. En equilibrio, el modelo recupera la ecuación clásica para una membrana asimétrica, $c_0 = 0$, que viene dada por

$$\Delta p = \gamma C + (1/2)\kappa C(C^2 - 4G) - \kappa\Delta_s C. \tag{13.9}$$

Fuera del equilibrio, obtenemos la ecuación que describe la dinámica de la membrana, (5.55). A partir de estas ecuaciones, hemos realizado un análisis de estabilidad lineal que nos permite estudiar el comportamiento relajacional de la membrana, y sirve a su vez como test para comprobar que nuestro modelo captura la dinámica correcta predicha por la teoría, como se muestra en la Figura 5.3.

13.2.3 Flujo de glóbulos rojos en canales confinados

El modelo de interfase difusa presentado en el Capítulo 5 ofrece las herramientas necesarias para simular el comportamiento de glóbulos rojos fluyendo en canales. Este problema es de enorme interés en biomedicina por diversas razones. Por un lado, entender el comportamiento reológico de la sangre es clave para mejorar nuestro conocimiento sobre el funcionamiento de la microcirculación, así como mejoras en el almacenamiento y manejo de sangre para transfusiones o análisis médicos. Por otro, gracias al reciente desarollo en microfluídica, el manejo de una única célula posibilita la diagnosis de enfermedades en pequeños dispositivos.

Nuestro modelo de interfase difusa es utilizado para realizar simulaciones por medio de un método conocido como *lattice-Boltzmann*. El esquema y la implementación numérica se han descrito en detalle en el Capítulo 6, concentrándonos en las particularidades de la simulación de membranas.

En los Capítulos 8 y 9, nos hemos centrado en el estudio de las propiedades elásticas y reológicas de un glóbulo fluyendo aislado en un canal confinado. Asumimos que en este régimen, de baja concentración de células, los efectos inducidos por las paredes son dominantes con respecto a las interacciones hidrodinámicas entre células. El sistema está caracterizado por el número capilar, que define el balance entre las fuerzas viscosas del fluído y las elásticas de la membrana de la célula,

$$C_\kappa = \frac{\tau_\kappa}{\tau_\eta} = \frac{\eta_0 \bar{v}_z a^2}{\kappa} \left(\frac{a}{b}\right). \tag{13.10}$$

Situando un glóbulo en el canal, y para un incremento del número capilar, obtenemos una secuencia de morfologías bien diferenciadas. A bajos capilares $C_\kappa < 4$, las células fluyen mostrando formas muy similares al discocito de referencia, que denominamos discocitos (*discocytes*). Una célula inicializada en el centro se mantendrá en esa posición, mostrando un pequeño acoplamiento con el flujo y una ligera asimetría. Para capilares mayores, $C_\kappa > 10$, las células migran hacia una posición lateral en el canal, estabilizándose en una posición intermedia entre el canal y la pared. En ésta posición adquieren una forma que se denomina *slipper*. Esta configuración es muy estable y se observa en el rango de capilares 10-90. Por

encima de ese valor, el *slipper* se vuelve inestable y la célula vuelve a una posición axial, donde adquiere una forma característica denominada *parachute*. El estudio de las contribuciones elásticas en cada régimen muestra que la migración lateral y el desarrollo del *slipper* supone una relajación en la energía de deformación con respecto a las configuraciones más centradas. Así mismo, muestra que el término de incompresibilidad es dominante a altos capilares, evidenciando que las células están sujetas a altas tensiones en la membrana. Así mismo, hemos estudiado el comportamiento reológico de la suspensión. La viscosidad efectiva muestra un comportamiento de *shear-thinning*, en el que la viscosidad decae al aumentar el ritmo de cizalla. Este decaimiento, asociado a una mayor fluidez de la suspensión. Este cambio se debe a la posición lateral y consiguiente alineamiento del glóbulo durante el régimen de *slipper*, así como la gradual pérdida de rigidez de la membrana que provoca una menor distorsión del flujo.

En el Capítulo 9, hemos estudiado explicítamente las ventajas de la posición asimétrica del *slipper* con respecto a posiciones simétricas en el canal. El por qué los glóbulos prefieren posiciones y formas asimétricas cuando fluyen en flujos simétricos es una cuestión abierta y de gran interés en la comunidad. Nuestros resultados muestran que la posición asimétrica permite una relajación de la energía de deformación, y una impotante reducción de los esfuerzos en las membrana. En este sentido, las posiciones centrales se ven mucho más penalizadas. Además, la vorticidad se cuando la célula se encuentra en una posición lateral disminuye drásticamente y se focaliza en el lóbulo trasero del glóbulo.

En el Capítulo 10, nos hemos centrado en el estudio de la focalización de los glóbulos hacia ciertas posiciones específicas a lo largo de la sección del canal, motivados por su interés a la hora de separar células en pequeños chips o la posibilidad de diagnosticar enfermedades. Nuestros resultados muestran que la focalización de las células a una posición específica se puede controlar mediante el acoplamiento del flujo y el confinamiento. De esta forma, mientras que para bajos capilares las células pueden encontrarse fluyendo a lo largo de toda la sección del canal, para capilares intermedios y altos, las células se concentran en dos bandas laterales (simétricas respecto al eje), que con el aumento del capilar se van haciendo más finas hasta que, eventualmente, todas las células fluyen en una misma trayectoria, independientemente de si su configuración inicial es cercana a la pared o al eje. El confinamiento es también relevante: en canales anchos, es necesario un capilar mayor para inducir este efecto de focalización, pero a la vez las células miran hacia posiciones más exteriores, cercanas a la pared. Finalmente, hemos estudiado la dependencia de este comportamiento con la forma, comparando el caso de glóbulos rojos con vesículas más esféricas. Los resultados muestran que las vesículas esféricas migran hacia posiciones centradas, fluyendo a lo largo del eje. Por tanto, la asimetría es un factor importante a la hora de explicar la posición lateral.

En el Capítulo 11, nos hemos centrado en el estudio del comportamiento de glóbulos fluyendo a concentraciones mayores, en los que la interacción con células vecinas puede jugar un factor relevante y dominar respecto a la interacción con la pared. Estudiando el efecto de apantallamiento entre células, observamos que la perturbación que una célula ejerce sobre el flujo entrante hace que la célula vecina interaccione de forma efectiva con un flujo caracterizado por fuerzas viscosas menores, de forma que sufre un menro deformación. Por esta razón, celulas fluyendo en formaciones alineadas o a pequeñas distancias muestran deformaciones mucho menores que aquellas fluyendo aisladas, y la migración lateral se ve parcialmente inhibida. Solo cuando la distancia entre células aumenta lo suficiente, el efecto de apantallamiento de atenúa y se recupera el comportamiento de célula aislada. Este cambio de comportamiento marca el régimen en el que los efectos de la pared son dominantes respecto a las interacciones entre celulas.

Finalmente, hemos estudiado estos efectos cuando muchos glóbulos fluyen en un canal. Los resultados muestran que el comportamiento de los glóbulos cambia significativamente. Para canales de anchura tres veces la de la célula, los glóbulos se concentran en el centro del canal, formando 3-4 filas. Las células situadas cerca del eje se ven atrapadas por las más externas, y están forzadas a fluir en el centro (una posición inestable para el caso de una célula aislada). A su vez, las células internas repelen hacia la pared a las externas, y estas se encuentran localizadas más cerca de la pared que en el caso de una célula aislada. Así, la focalización lateral se pierde, y las células se concentran ahora en el núcleo del canal. Aumentando el capilar, la repulsión de las paredes también aumenta y la localización de las células focaliza a una distribución más centrada.

13.3 Conclusiones

El objetivo principal de esta Tesis ha sido estudiar desde una perspectiva teórica el comportamiento mecánico de los glóbulos rojos en diferentes situaciones, concentrándonos en el entendimiento de las propiedades elásticas macroscópicas a partir de la microestructura de la membrana celular.

La investigación original de esta Tesis se ha divido en tres partes. En la Parte II hemos estudiado la respuesta morfológica de los glóbulos cuando se ven afectados por cambios en la asimetría de la bicapa lipídica. Hemos encontrado que el desarrollo de protuberancias que dan pie a la formación del equinocito responde a la relajación de la bicapa cuando se ve sometida a un exceso de área en su capa externa. El citoesqueleto, en cambio, opone resistencia a la formación de estas estructuras, manteniendo un forma más compacta y siendo por tanto un elemento clave en la estabilización del discocito.

En la Parte III, nos hemos centrado en la derivación de un modelo de interfase difusa para el modelado de membranas. Hemos demostrado que nuestro modelo captura la física relevante de las membranas y recupera las ecuaciones de equilibrio y el comportamiento relajacional predichos por la teoría.

Finalmente, en la Parte IV, hemos utilizado el método de interfase difusa para estudiar el comportamiento de glóbulos rojos en flujos en canales. Inicialmente nos hemos centrado en el caso de una célula a alto confinamiento, observando que las células prefieren posiciones asimétricas a lo largo del canal, donde se orientan con el flujo, y que se ven sujetas a fuertes tensiones en la membrana. Después hemos estudiado también el caso en el que muchas células esán presentes, comprobando la fuerte dependencia en las interacciones con otras células y como los efectos de migración y alineación se ven atenúados.

Appendix A

Notes on differential geometry

In this Appendix we include some basic concepts of differential geometry of surfaces that could be useful for the understanding of some of the calculations in the main text.

A.1 Mean curvature

The curvature and area element of a shape can be obtained from the first and second fundamental forms of the manifold. Considering the parametrization:

$$\vec{r} = (rcos(\theta), rsin(\theta), z(r,\theta)) \tag{A.1}$$

and defining $\vec{r}_r = d\vec{r}/dr$, $\vec{r}_\theta = d\vec{r}/d\theta$, then

$$\begin{aligned} E &= \vec{r}_r \cdot \vec{r}_r, \\ F &= \vec{r}_r \cdot \vec{r}_\theta, \\ G &= \vec{r}_\theta \cdot \vec{r}_\theta, \end{aligned} \tag{A.2}$$

using standard notation. The first fundamental form reads:

$$I = Edr^2 + 2Fdrd\theta + Gd\theta^2. \tag{A.3}$$

In a similar way, for the second fundamental form,

$$\begin{aligned} L &= \vec{r}_{rr} \cdot \hat{n}, \\ M &= \vec{r}_{r\theta} \cdot \hat{n}, \\ N &= \vec{r}_{\theta\theta} \cdot \hat{n}, \end{aligned} \tag{A.4}$$

where $\hat{n}$ is the normal to the surface, and from here:

$$II = Ldr^2 + Mdrd\theta + Nd\theta^2. \tag{A.5}$$

The total curvature and surface area element can be easily obtained:

$$C = \frac{NE - 2MF + LG}{(EG - F^2)}, \tag{A.6}$$

$$dA = \sqrt{EG - F^2} drd\theta. \tag{A.7}$$

Unfortunately, even if these expressions are analytical (note that they only depend on the derivatives $z_r, z_\theta, z_{rr}, z_{r\theta}, z_{\theta\theta}$), the surface integral of eqn (4.2) has no analytical solution and the integration must be numerically computed.

A.2 Extension ratios

The extension ratios represent the normal strain of a line element. Within the finite strain theory framework, they characterize the deformation of a manifold from the reference $S_0(\vec{x})$ to the current $S(\vec{X})$ state. They are obtained from the Green's strain tensor,

$$\epsilon_{\alpha\beta} \equiv \frac{1}{2}\left(\frac{\partial X^\gamma}{\partial x_\alpha}\frac{\partial X_\gamma}{\partial x_\beta} - \delta_{\alpha\beta}\right), \tag{A.8}$$

and from the eigenvalues of this tensor ϵ_i ,

$$\lambda_i = \sqrt{2\epsilon_i + 1}. \tag{A.9}$$

The Green's strain tensor can be easily calculated if the current state can be analytically expressed in terms of the reference state. Once the extension ratios are obtained, eqn (4.4) is numerically computed. In a isotropic dilation $\lambda_1 = \lambda_2$ and the second term vanishes; alternatively, if the area element is conserved $\lambda_1 = 1/\lambda_2$, the first term of the energy is null.

A non-trivial issue concerns the mapping from the reference to the actual state $S_0 :\to S$. In our model, the connection between manifolds is determined by the condition $A(r) = A_0(r_0)$, thus equaling the areas from the polar axis in both configurations. This implies that the central point is less sensitive to deformations than the external region, a reasonable hypothesis at these early stages of the transition. Obviously, this method is only valid as far as the area of the reference state is equal to that of the cell.

A.3 Differential operators in curvilinear coordinates

In Part III of this Thesis, we introduce the curvilinear coordinates in order to deal with the sharp-interface limit of a slightly curved interface. These coordinates represent a naïve parametrization of the membrane surface, but they are rarely used in the literature and hence it is convenient to specify its metrics and differential operators. The vector basis is chosen as follows. At each position of the surface, the normal vector $\mathbf{n}$ is defined. From the tangential plane we choose two vectors forming an orthonormal trihedron, $\mathbf{t_2} = \mathbf{n} \times \mathbf{t_1}$. We define a vector position $\mathbf{n}$ that can be decomposed into the vector position in the surface and the normal projection, $\mathbf{r} = \mathbf{R}(s,u) + r\mathbf{n}(s,u)$, where r is the coordinate in the direction of $\mathbf{n}$ and (s,u) are the coordinates in the directions of $\mathbf{t_1}$ and $\mathbf{t_2}$, respectively. Hence, (r,s) are orthogonal coordinates on the membrane surface, and describe arclengths of the curve formed by the intersection of the membrane surface and the planes $(r,s) = const$ and $(r,u) = const$. From here, we obtain $|\partial\mathbf{R}/\partial u| = |\partial\mathbf{R}/\partial s| = 1$, and $\mathbf{t_1} = \partial\mathbf{R}/\partial u$ and $\mathbf{t_2} = \partial\mathbf{R}/\partial s$ by definition. The particular choice of this coordinates reduces the classic Bonnet-Kowalewski trihedron to the Frenet formulas (do Carmo, 1976; Biben et al., 2005), obtaining

$$\begin{aligned} \frac{\partial \mathbf{n}}{\partial s} &= -c_1\mathbf{t_1} - \tau_1\mathbf{t_2}, \\ \frac{\partial \mathbf{t_1}}{\partial s} = c_1\mathbf{n}, \qquad \frac{\partial \mathbf{t_2}}{\partial s} &= \tau_1\mathbf{n}, \\ \frac{\partial \mathbf{n}}{\partial u} &= -c_2\mathbf{t_2} - \tau_2\mathbf{t_1}, \\ \frac{\partial \mathbf{t_1}}{\partial s} = -\tau_2\mathbf{n}, \qquad \frac{\partial \mathbf{t_2}}{\partial u} &= c_2\mathbf{n}. \end{aligned} \tag{A.10}$$

where c_1 and c_2 are the curvatures and τ_1 and τ_2 the torsions in the (u,s) directions, respectively.

Combining the expressions given before, the base vector can be calculated,

$$\begin{aligned} \mathcal{E}_r &\equiv \frac{\partial \mathbf{r}}{\partial r} = \mathbf{n}, \\ \mathcal{E}_s \equiv \frac{\partial \mathbf{r}}{\partial s} &= \frac{\partial \mathbf{R}}{\partial s} + r\frac{\partial \mathbf{n}}{\partial s} = (1 - rc_1)\mathbf{t_1} - r\tau_1\mathbf{t_2}, \\ \mathcal{E}_u \equiv \frac{\partial \mathbf{r}}{\partial u} &= \frac{\partial \mathbf{R}}{\partial u} + r\frac{\partial \mathbf{n}}{\partial u} = (1 - rc_2)\mathbf{t_2} + r\tau_2\mathbf{t_1}. \end{aligned} \tag{A.11}$$

From this basis the metric can be readily computed as $g_{\alpha\beta} = \mathcal{E}_\alpha\mathcal{E}_\beta$, leading to

$$g_{\alpha\beta} = \begin{pmatrix} 1 & 0 & 0 \\ 0 & (1+rc_1)^2 + r^2\tau^2 & -2r\tau + r^2(c_1+c_2)\tau \\ 0 & -2r\tau + r^2(c_1+c_2)\tau & (1+rc_1)^2 + r^2\tau^2 \end{pmatrix}. \tag{A.12}$$

We have introduced $\tau = \tau_1 = \tau_2$ as can be easily proved from $\partial_s \mathcal{E}_u = \partial_u \mathcal{E}_s$. From here, the determinant of the metric reads

$$g = \det g_{\alpha\beta} = [(1-rc_1)(1-rc_2) - r^2\tau^2]^2. \tag{A.13}$$

We are interested in the expression of the differential operators, in particular, those which appear in the phase-field free energy, *ie* the gradient and the laplacian. The gradient can be computed from its formal definition $\nabla = \mathcal{E}^\alpha \partial_\alpha$, obtaining

$$\nabla = \mathbf{n}\partial_r + \frac{1}{1-rC+r^2G}\{[\mathbf{t_1}[(1-rc_1)\partial_s + r\tau\partial_u] + \mathbf{t_2}[r\tau\partial_s + (1+rc_1)\partial_u]\}. \tag{A.14}$$

where we have introduced the total curvature $C = c_1 + c_2$, and the Gaussian curvature $G = c_1c_2 - \tau^2$. Analogously, the general expression of the Laplacian is given by

$$\nabla^2 = \frac{1}{\sqrt{g}}\partial_\alpha \sqrt{g} g^{\alpha\beta}\partial_\beta. \tag{A.15}$$

Introducing (A.12) and (A.13) in (A.15), the final expression of the Laplacian in curvilinear coordinates reads

$$\begin{aligned} \nabla^2 = \partial_r^2 - \left[\frac{C-2Gr}{1-Cr+Gr^2}\right]\partial_r + \frac{(1-rc_2)^2 + r^2\tau^2}{[(1-rc_1)(1-rc_2) - r^2\tau^2]^2}\partial_u^2 \\ + \frac{(1-rc_1)^2 + r^2\tau^2}{[(1-rc_1)(1-rc_2) - r^2\tau^2]^2}\partial_u^2\partial_s^2 + \cdots, \end{aligned} \tag{A.16}$$

where, for the sake of clarity, we have neglected the contribution of terms of the form $\partial_u C \partial_u$, $\partial_s \partial_u$,..., as they are irrelevant for the purposes of this Thesis.

Appendix B

The sharp-interface limit

The sharp-interface limit is a classic method for determining the macroscopic equations of diffuse interface models (Folch et al., 1999). It exploits the separation between the length scale of the interface, given by ϵ, and the typical length of the interface, which can be defined from the total curvature as $l \sim 1/C$. The limit applies only in the low-curvature limit, $\epsilon C \ll 1$.

B.1 The inner and the outer region

The interface is described by the curvilinear coordinate (r, s, u), described in Appendix A. r is normal to the interface at each point (s, u) on the surface. The space is separated into two different regions. The interfacial region, called here *inner* region, is described by a fast coordinate $\omega = r/\epsilon$. Thus, the interfacial region is zoomed up in order to resolve the details of the smooth interface, although in the *outer* region the interface is effectively sharp in the limit $\epsilon \to 0$. The starting point is a flat interface in equilibrium, with relaxed profile ϕ_0. If a small perturbation is induced, the deviations from the equilibrium profile can be expanded in terms of ϵ,

$$\begin{aligned} a(\omega, s, u) &= a_0(\omega, s, u) + \epsilon a_1(\omega, s, u) + \epsilon^2 a_2(\omega, s, u) + ..., \\ A(r, s, u) &= A_0(r, s, u) + \epsilon A_1(r, s, u) + \epsilon^2 A_2(r, s, u) + ..., \end{aligned} \tag{B.1}$$

where capital letters denote variables in the outer region, and lower case letters indicate variables in the inner region. In the limit $\omega \to \pm\infty$ both regions meet, and the matching conditions read:

$$\begin{gathered} a_0(\omega, s, u) = A_0(0^{\pm}, s, u), \\ a_1(\omega, s, u) = a_1(0^{\pm}, s, u) + \omega \partial_r a_0(0^{\pm}, s, u), \\ a_2(\omega, s, u) = a_2(0^{\pm}, s, u) + \omega \partial_r a_1(0^{\pm}, s, u) + \tfrac{\omega^2}{2} \partial_{rr}^2 a_1(0^{\pm}, s, u), \\ \cdots . \end{gathered} \tag{B.2}$$

The dynamic equation (5.34) is analogously decomposed in the two regions, with the corresponding inner and outer variables. The differential operators must be also expanded in terms of ϵ. We also assume that the interface motion is much larger than the characteristic times of order parameter diffusion, and hence the time is also rescaled $\tau = \epsilon t$, where τ is the time in the inner region. Hence, in this quasiestatic approximation we can write,

$$\partial_t \phi(r) = \epsilon \partial_\tau \phi(\omega) - \frac{1}{\epsilon} \partial_\tau \omega \partial_\omega \phi(\omega), \tag{B.3}$$

and defining the normal velocity of the interface $v = -\partial_\tau \omega$ the dynamic equation reads

$$\epsilon \partial_\tau \phi - \frac{1}{\epsilon} v \partial_\omega \phi = M \nabla^2 \mu, \tag{B.4}$$

where the laplacian must be expanded, as shown below. The method does not allow for finding explicit solutions of the fields, but provide a set of equations that in the limit $\epsilon \to 0$ represent the macroscopic equations of the model.

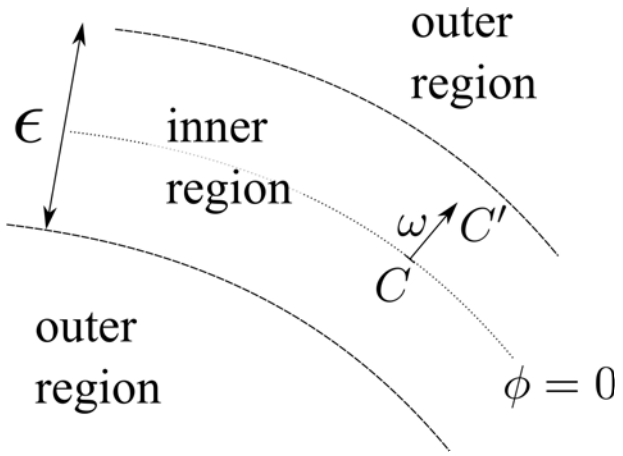

Figure B.1: Scheme of the sharp interface method. The interface has a normal direction at each point given by the coordinates r in the outer region and the fast coordinate $\omega = r/\epsilon$ in the inner region. In the inner region, each isosurface $\phi = const$ has an associated mean curvature $C'(u, s)$, whereas the isosurface $\phi = 0$ is associated to C.

B.2 Differential operators

The differential operators in curvilinear coordinates have been derived in Appendix A. However, here we follow a different procedure which provides a more intuitive understanding of the sharp-interface methodology. An scheme of the interfacial isosurfaces and curvatures is provided in Figure B.1. As previously stated, the differential operators must be also expanded in terms of ϵ. In the inner coordinates, $\nabla\phi = (\epsilon^{-1}\partial_\omega\phi, \partial_s\phi, \partial_u\phi)$, and thus at leading order only the normal coordinate contributes. This means that the variations of ϕ along the coordinate directions (s, u) are disregardable with respect to variations in ω. For simplicity, in the subsequent calculations we deliverately neglect some derivatives of the tangential coordinates, which do not contribute after the expansion, in order to simplify the expressions obtained. Some useful identities are (Du et al., 2005)

$$\hat{n} = \nabla r,$$

$$C = -\nabla \cdot \hat{n} = -\nabla^2 r, \tag{B.5}$$

$$G = -(1/2)[2\mathrm{tr}((\nabla_\alpha \nabla_\beta r)^2) - (\mathrm{tr}(\nabla_\alpha \nabla_\beta r))^2].$$

for the normal vector and total curvature, respectively. Note that, because the normal vector is unitary, $(\nabla r)^2 = 1$, and consequently

$$n_\alpha \nabla_\beta n_\alpha = (1/2)\nabla_\beta (n_\alpha n_\alpha) = 0. \tag{B.6}$$

We suppose that at each point of the isosurface $\phi = const$, there is a local coordinate system given by the coordinate $r(\mathbf{x})$, normal to the surface, and the tangential coordinates $(u(\mathbf{x}), s(\mathbf{x}))$. We suppose that there exists a solution for the order parameter profile of the form $\phi = \phi(r, u, s)$. We can write the gradient and laplacian as

$$\begin{gathered}\nabla\phi = \partial_r\phi\nabla r + \partial_s\phi\nabla s + \partial_u\phi\nabla u. \\ \nabla^2\phi = \partial_r^2\phi(\nabla r) + \partial_r\phi\nabla^2 r + \partial_s^2\phi(\nabla s)^2 + \partial_s\phi\nabla^2 s + \partial_u^2\phi(\nabla u)^2 + \partial_u\phi\nabla^2 u.\end{gathered} \tag{B.7}$$

In this expression, the normal vector $\hat{n}$ and total curvature C can be directly identified. The terms related with the tangential derivatives are more difficult to interpret, though for instance ∇s is given by

$$\nabla s = \frac{1}{\sqrt{g}}[(1 - rc_1)\mathbf{t_1} + r\tau\mathbf{t_2}]. \tag{B.8}$$

It can be proved that these terms correspond to those appearing in the last terms of (A.16), although it will not be derived here. For simplicity, we only consider the terms associated to the higher derivative, *eg* ∂_s^2 in the Laplacian. Introducing these considerations, the expression for the Laplacian can be rewritten as

$$\nabla^2\phi = \partial_r^2\phi - C'\partial\phi + \partial_s^2\phi + \partial_u^2\phi + \cdots . \tag{B.9}$$

Here, C' corresponds to the local total curvature of the isorfuce at each point of the space (r, s, u). However, in the interface region it is convenient to write the local curvature of the isosurface $\phi = const$ expressed in terms of the curvature of the isosurface $\phi = 0$, which we denote C, given that in the sharp interface limit $C' \to C$. The relation between the curvature of two surfaces is given by

$$C' = C\left[\frac{2rG/C - 1}{1 - rC + r^2G}\right]. \tag{B.10}$$

Introducing this expression in (B.9), the expression for the Laplacian is given by

$$\nabla^2\phi = \partial_r^2\phi - \left[\frac{2rG - C}{1 - rC + r^2G}\right]\partial\phi + \partial_s^2\phi + \partial_u^2\phi + \cdots . \tag{B.11}$$

Note that this expression agrees with that found in Appendix A, (A.16). At low curvatures, the function associated to ∂_r can be expanded, obtaining

$$\nabla^2\phi = \partial_r^2\phi - \left[C + r(C^2 - 2G) + r^2(C^3 - 3GC + ...)\right]\partial\phi + \partial_s^2\phi + \partial_u^2\phi + \cdots . \tag{B.12}$$

If the fast coordinate ω is introduced, the expression reads

$$\nabla^2\phi = \epsilon^{-2}\partial_r^2\phi - \epsilon^{-1}\left[C + \epsilon r(C^2 - 2G) + \epsilon^2 r^2(C^3 - 3GC + ...)\right]\partial\phi + \partial_s^2\phi + \partial_u^2\phi + \cdots . \tag{B.13}$$

The derivation of the fourth derivative, $\nabla^4 = \nabla^2\nabla^2$, is more complicated. By taking the derivative of the expression of the Laplacian (B.7), one obtains

$$\nabla^2\nabla^2\phi = \partial_r^4 + 2\nabla^2 r\partial_r^3 + 2\nabla_\alpha r\nabla_\alpha\nabla^2 r\partial_r^2\phi + (\nabla^2 r)^2\partial_r^2\phi + \nabla^2\nabla^2 r\partial_r\phi. \tag{B.14}$$

In this expression, several terms can be readily identified in terms of the total curvature (*eg* $C^2 = (\nabla^2 r)^2$), but particularly the physical meaning of $\nabla_\alpha r \nabla_\alpha \nabla^2 r$ is not straightforward.

For convenience, we perform below some algebraic manipulations that will be useful in the derivation of the equilibrium condition in Section 5.6. Let us consider first the fourth term in the right hand side of (B.14). Multiplying by $\partial_r \phi$ and $(\nabla_\alpha r)(\nabla_\alpha r) = 1$, and integrating by parts

$$\begin{aligned} &\int \nabla_\alpha r \nabla_\alpha r \partial_r \phi \partial_r^2 \phi (\nabla^2 r)^2 dx \\ &\qquad = -\frac{1}{2} \int [(\nabla^2 r)^3 + 2\nabla_\alpha r \nabla_\alpha \nabla^2 r \nabla^2 r](\partial_r \phi)^2 dx. \end{aligned} \tag{B.15}$$

The interpretation of this expression requires to consider the identity $C'^2 - 4G' = 2\mathrm{tr}(\nabla^2 r)^2 - (\nabla^2 r)^2$, as can be obtained from identities (B.5). Then, it is straightforward to show the equivalence:

$$\begin{aligned} &C'(C'^2 - 4G') = -\nabla^2 r (2\mathrm{tr}(\nabla_\alpha \nabla_\beta r)^2 - (\nabla^2 r)^2) = \\ &- 2\nabla_\alpha (\nabla^2 r \nabla_\beta r \nabla_\alpha \nabla_\beta r) + 2(\nabla_\alpha \nabla^2 r \nabla_\beta r \nabla_\alpha \nabla_\beta r) \\ &+ 2\nabla^2 r \nabla_\alpha r \nabla_\alpha r \nabla^2 r + (\nabla^2 r)^3 = (\nabla^2 r)^3 + 2\nabla_\alpha r \nabla^2 r \nabla_\alpha \nabla^2 r, \end{aligned} \tag{B.16}$$

where in the last equality we have used (B.6). The comparison between equations (B.15) and (B.16) demonstrates that the fourth term in (B.14) relates with $-(1/2)C'(C'^2 - 4G')$.

Considering now the third term in the right hand side of (B.14), multiplying by $\partial_r \phi$ and $(\nabla_\beta r)(\nabla_\beta r) = 1$,

$$\begin{aligned} \int \nabla_\beta r \nabla_\beta r \nabla_\alpha r \nabla_\alpha \nabla^2 r \partial_r^2 \phi \partial_r \phi dx = -\frac{1}{2} \int [\nabla_\beta r \nabla_\beta \nabla^2 r \nabla^2 r + \\ \nabla_\beta r \nabla_\alpha \nabla_\beta r \nabla_\alpha \nabla^2 r + \nabla_\beta r \nabla_\alpha r \nabla_\alpha \nabla_\beta \nabla^2 r](\partial_r \phi)^2 dx. \end{aligned} \tag{B.17}$$

Note that the second term in the expression in brackets vanishes by (B.6). From the expression for the gradient operator projected over the surface S, $\nabla_\alpha^S = \nabla_\alpha - n_\alpha n_\beta \nabla_\beta$, the Laplace-Beltrami operator over the surface reads

$$\Delta_S = \nabla_\alpha^S \nabla_\alpha^S = \nabla^2 + C' n_\alpha \nabla_\alpha - n_\alpha n_\beta \nabla_\alpha \nabla_\beta. \tag{B.18}$$

Manipulating this expression, and using $n_\alpha = \nabla_\alpha r$, leads to,

$$\begin{aligned}\Delta_S C' &= \nabla^2 C' + C' n_\alpha \nabla_\alpha C' - n_\alpha n_\beta \nabla^\alpha \nabla^\beta C' \\ &= -\nabla^2\nabla^2 r + \nabla^2 r \nabla_\alpha r \nabla_\alpha \nabla^2 r + \nabla_\alpha r \nabla_\beta r \nabla_\alpha \nabla_\beta \nabla^2 r.\end{aligned} \tag{B.19}$$

Hence, our calculations show that the third and fifth terms of (B.14) are equivalent to the surface variations of the curvature, $\Delta_S C'$. As a summing up, introducing the fast coordinate ω and multiplying equation (B.14) by $\partial_\omega \phi$ we obtain the relation

$$\begin{aligned}\int \partial_\omega \phi \nabla^2 \nabla^2 \phi dx = \int \{&\epsilon^{-4} \partial_\omega^4 \phi \partial_\omega \phi \\ &+ 2[C + \omega(2G - C^2) + \omega^2(C^3 - 3GC) + ...]\partial_\omega^3 \phi \partial_\omega \phi \\ &- \frac{1}{2}\epsilon^{-1} C(C^2 - 4G)(\partial_\omega \phi)^2 - \epsilon^{-1}\Delta_S C (\partial_\omega \phi)^2\} dx.\end{aligned} \tag{B.20}$$

Note that the terms associated with the first derivative, $\partial_\omega \phi$, correspond to the highest order considered in the expansion and at this order $C = C'$.

Appendix C

List of publications

- K. A. Melzak, G. R. Lázaro, A. Hernández-Machado, I. Pagonabarraga, J. M. Cárdenas Díaz de Espada, and J. L. Toca-Herrera. AFM measurements and lipid rearrangements: evidence from red blood cell shape changes. *Soft Matter*, 8:7716–7726, 2012.
- G. R. Lázaro, K. A. Melzak, J. L. Toca-Herrera, I. Pagonabarraga, and A. Hernández-Machado. Elastic energies and morphologies of the first stages of the discoechinocyte transition. *Soft Matter*, 9:6430–6441, 2013.
- G. R. Lázaro, I. Pagonabarraga and A. Hernández-Machado. Phase field-theories for mathematical modeling of biological membranes. *Membrane mechanics: from the molecular to the cellular scale*, Special Issue of *Chemistry and Physics of Lipids*.
- G. R. Lázaro, A. Hernández-Machado, and I. Pagonabarraga. Rheology of red blood cells under flow in highly confined microchannels: I. Effect of elasticity. *Soft Matter* 2014.
- G. R. Lázaro, A. Hernández-Machado, and I. Pagonabarraga. Rheology of red blood cells under flow in highly confined microchannels: II. Effect of focusing and confinement. *Soft Matter* 2014 b.
- G. R. Lázaro, I. Pagonabarraga and A. Hernández-Machado. Mechanical and dynamic properties of membrane phase-field models. (submitted)
- G. R. Lázaro, A. Hernández-Machado and I. Pagonabarraga. Asymmetric shapes and lateral position of red blood cells in confined channels. (in prep.)

References

M. Abkarian, C. Lartigue, and A. Viallat. Tank treading and unbinding of deformable vesicles in shear flow: Determination of the lift force. *Phys. Rev. Lett.*, 88:068103, 2002.

M. Abkarian, M. Faivre, and A. Viallat. Swinging of red blood cells under shear flow. *Phys. Rev. Lett.*, 98:188302, 2007.

M. Abkarian, M. Faivre, R. Horton, K. Smistrup, C. A. Best-Popescu, and H. A. Stone. Cellular-scale hydrodynamics. *Biomed. Mater.*, 3(3):034011, 2008.

B. Alberts, D. Bray, M. Raff, K. Roberts, and J. D. Watson. *Molecular Biology of the Cell*. Garland Science, New York, 1994.

J. Alcaraz, L. Buscemi, M. Grabulosa, X. Trepat, B. Fabry, R. Farré, and D. Navajas. Microrheology of human lung epithelial cells measured by atomic force microscopy. *Biophys. J.*, 84(3):2071–2079, 2003.

J. A. Allen, R. A. Halverson-Tamboli, and M. M. Rasenick. Lipid raft microdomains and neurotransmitter signalling. *Nature Rev. Neurosci.*, 8:128–140, 2007.

B. Angelov and I. Mladenov. *On the Geometry of the Red Blood Cell, Geometry, Integrability and Quantization*. Coral Press Scientific Publishing, Sofia, 2000.

G. M. Artmann, K.-L. Paul Sung, T. Horn, D. Whittemore, G. Norwich, and S. Chien. Micropipette apiration of human erythrocytes induces echinocytes via membrane phospholipid translocation. *Biophys. J.*, 72:1434–1441, 1997.

E. S. Asmolov. The inertial lift on a spherical particle in a plane poiseuille flow at large channel reynolds number. *J. Fluid. Mech.*, 381:63–87, 1999.

O. K. Baskurt and H. J. Meiselman. Blood rheology and hemodynamics. *Seminars in Thrombosis and Hemostasis*, 29(5):435–450, 2003.

O. K. Baskurt, M. Hardeman, M. W. Rampling, and H. J. Meiselman. *Handbook of Hemorheology and Hemodynamics*. IOS Press., Amsterdam, Netherlands., 2007.

T. Baumgart, S. Hess, and H. Webb. Imaging coexisting fluid domains in biomembrane models coupling curvature and line tension. *Nature*, 425:821824, 2003.

V. Bennett. The spectrin-actin junction of erythrocyte membrane skeletons. *Biochim. Biophys. Acta*, 988(1):107–121, 1989.

R. Benzi, M. Sbragaglia, S. Succi, M. Bernaschi, and S. Chibbaro. Mesoscopic lattice boltzmann modeling of soft-glassy systems: theory and simulations. *J. Chem. Phys.*, 131:104903, 2009.

M. Besis. *Living Blood Cells and Their Ultrastructure*. Springer, New York, 1973.

T. Betz, M. Lenz, J.-F. Joanny, and C. Sykes. Atp-dependent mechanics of red blood cells. *Proc. Nat. Acad. Sci. USA*, 106(36):15312–15317, 2009.

P. L. Bhatnagar, E. P. Gross, and M. Krook. A model for collision processes in gases. i. small amplitude processes in charged and neutral one-component systems. *Phys. Rev.*, 94:511–525, 1954.

T. Biben and C. Misbah. Tumbling of vesicles under shear flow within an advected-field approach. *Phys. Rev. E*, 67:031908, 2003.

T. Biben, K. Kassner, and C. Misbah. Phase-field approach to three-dimensional vesicle dynamics. *Phys. Rev. E*, 72:041921, 2005.

J. Brannick, C. Liu, T. Qian, and H. Sun. Diffuse interface methods for multiple phase materials: an energetic variational approach. *arXiv:1402.5375*, page 1, 2014.

F. Brochard and J.-F. Lennon. Flicker spectrum of the flicker phenomenon in erythrocytes. *J. Phys. France*, 11:1035, 1975.

J. E. Cahn and J. E. Hilliard. Free energy of a nonuniform system: Ii. nucleation in a two-component incompressible fluid. *J. Chem. Phys.*, 31:688–699, 1959.

F. Campelo and A. Hernández-Machado. Dynamic model and stationary shapes of fluid vesicles. *Eur. Phys. J. E*, 20(1):37–45, 2006.

F. Campelo and A. Hernández-Machado. Model for curvature–driven pearling instability in membranes. *Phys. Rev. Lett.*, 99:088101, 2007a.

F. Campelo and A. Hernández-Machado. Shapes instabilities in vesicles: A phase-field model. *Eur. Phys. J. Special Topics*, 143:101–108, 2007b.

F. Campelo and A. Hernández-Machado. Polymer-induced tubulation in lipid vesicles. *Phys. Rev. Lett.*, 100:158103, 2008.

F. Campelo, A. Cruz, J. Pérez-Gil, L. Vázquez, and A. Hernández-Machado. Phase-field model for the morphology of monolayer lipid domains. *Eur. Phys. J. E Soft Matter*, 35(6):49, 2012.

P. B. Canham. The minimum energy of bending as a possible explanation of the biconcave shape of the human red blood cell. *J. Theor. Biol.*, 26:6181, 1970.

R. Capovilla and J. Guven. Stresses in lipid membranes. *J. Phys. A: Math. Gen.*, 35:6233, 2002.

D. Di Carlo, D. Irimia, R. G. Tompkins, and M. Toner. Continuous inertial focusing, ordering, and separation of particles in microchannels. *Proc. Nat. Acad. Sci. U.S.A.*, 104(48):18892–18897, 2007.

D. Di Carlo, J. F. Edd, K. J. Humphry, H. A. Stone, and M. Toner. Particle segregation and dynamics in confined flows. *Phys. Rev. Phys.*, 102:094503, 2009.

M. E. Cates, J.-C. Desplat, P. Stansell, A. J. Wagner, K. Stratford, and I. Pagonabarraga. Physical and computational scaling issues in lattice boltzmann simulations of binary fluid mixtures. *Phil. Trans. R. Soc.*, 363:1917–1935, 2005.

M. E. Cates, O. Henrich, D. Marenduzzo, and K. Stratford. Lattice boltzmann simulations of liquid crystalline fluids: active gels and blue phases. *Soft Matter*, 5:3791, 2009.

B. M. Cooke, N. Mohandas, and R. L. Coppel. Malaria and the red blood cell membrane. *Seminars in Hematology*, 48(2):173–188, 2004.

G. M. Cooper and R. E. Hausman. *The Cell. A Molecular Approach*. Sinauer Associates, Sunderland, USA., 5th edition, 2009.

G. Coupier, B. Kaoui, T. Podgorski, and C. Misbah. Noninertial lateral migration of vesicles in bounded poiseuille flow. *Phys. Fluids*, 25:111702, 2008.

G. Degré, P. Joseph, P. Tabeling, S. Lerouge, M. Cloitre, and A. Ajdari. Rheology of complex fluids by particle image velocimetry in microchannels. *Appl. Phys. Lett.*, 89:024104, 2006.

J. Deschamps, V. Kantsler, and V. steinberg. Phase diagram of single vesicle dynamical states in shear flow. *Phys. Rev. Lett.*, 102(11):118105, 2009.

M. Deserno. Mesoscopic membrane physics: concepts, simulations, and selected applications. *Macromol. Rapid. Commun.*, 30:752–771, 2009.

J.-C. Desplat, I. Pagonabarraga, and P. Bladon. Ludwig: A parallel latticeboltzmann code for complex fluids. *Comput. Phys. Comms.*, 134:273–290, 2001.

P. F. Devaux, A. Herrmann, N. Ohlwein, and M. M. Kozlov. How lipid flippases can modulate membrane structure. *Biochim. Biophys. Acta*, 1778:1591–1600, 2008.

P. Dimitrakopoulos. Analysis of the variation in the determination of the shear modulus of the erythrocyte membrane: Effects of constitutive law and membrane modeling. *Phys. Rev. E*, 85:041917, 2012.

I. K. Dimov, L. Basabe-Desmonts, J. L. Garcia-Cordero, B. M. Ross, A. J. Riccoa, and L. P. Lee. Stand-alone self-powered integrated microfluidic blood analysis system (simbas). *Lab Chip*, 11:845–850, 2011.

R. Dimova, K. A. Rieske, S. Aranda, N. Bezlyepkina, R. L. Knorr, and R. Lipowsky. Giant vesicles in electric fields. *Soft Matter*, 3:817–827, 2007.

D. E. Discher, D. H. Boal, and S. K. Boey. Phase transitions and anisotropic responses on planar triangular nets under large deformation. *Phys. Rev. E*, 55: 4762–4772, 1997.

M. P. do Carmo. *Differential Geometry of Curves and Surfaces*. Prentice-Hall, New Jersey, U.S.A., 1976.

A. M. Dondorp, P. A. Kager, J. Vreeken, and N. C. White. Abnormal blood flow and red blood cell deformability in severe malaria. *Parasitology Today*, 16(6): 228–232, 2000.

Q. Du and M. Li. On the stochastic immersed boundary method with an implicit interface formulation. *Discrete and Continuous*, 15(2):373–389, 2011.

Q. Du, C. Liu, , and X. Wang. *J. Comput. Phys.*, 198:450, 2004.

Q. Du, C. Liu, R. RYham, and X. Wang. A phase-field formulation of the willmore problem. *Nonlinearity*, 18:1249–1267, 2005.

B. Duenweg and A. J. C. Ladd. Lattice boltzmann simulations of soft matter systems. *Adv. Polym. Sci.*, 221:89, 2009.

D. M. Engelman. Membranes are more mosaic than fluidic. *Nature*, 438:578–580, 2005.

E. Eremina, J. Hellmers, Y. Eremin, and T. Wriedt. Different shape models for erythrocyte: Light scattering analysis based on the discrete sources method. *Jour. Quan. Spec. & Rad. Trans.*, 102:3–10, 2006.

E. Evans and D. Needham. Physical properties of surfactant bilayer membranes: Thermal transitions, elasticity, rigidity, cohesion, and colloidal interactions. *J. Phys. Chem.*, 91:42194228, 1987.

E. A. Evans. Bending resistance and chemically induced moments in membrane bilayers. *Biophys. J.*, 14(12):923, 1974.

E. A. Evans and R. Skalak. *Mechanics and Thermodynamics of Biomembranes*. CRC Press, Boca Raton, 1980.

R. Fahraeus and T. Lindqvist. The viscosity of the blood in narrow capillary tubes. *Am. J. Physiol.*, 96:562–568, 1931.

D. A. Fedosov, W. Pan, B. Caswell, G. Gompper, and G. E. Karniadakis. Predicting human blood viscosity in silico. *Proc. Nat. Acad. Sci. U.S.A.*, 108(29): 11772–11777, 2011.

J. E. Ferrell, K.J. Lee, and W. H. Huestis. *Biochemistry*, 24:2849–2857, 1985.

T. M. Fischer. Shape memory of human red blood cells. *Biophys. J.*, 86(5): 3304–3313, 2004.

R. Folch, J. Casademunt, A. Hernández-Machado, and L. Ramírez-Piscina. Phase-field model for hele-shaw flows with arbitrary viscocity contrast. i. theoretical approach. *Phys. Rev. E*, 60:1724, 1999.

A. M. Forsyth, J. Wan, W. D. Ristenpart, and H. A. Stone. The dynamic behavior of chemically stiffened red blood cells in microchannel flows. *Microvas. Res.*, 80:37–43, 2011.

Y. C. Fung. *Biomechanics: Circulation*. Springer, New York, 1997.

J. Gachelin, G. Mi no, H. Berthet, A. Lindner, A. Rousselet, and E. Clément. Non-newtonian viscosity of escherichia coli suspensions. *Phys. Rev. Lett.*, 110: 268103, 2013.

P. Gaehtgens, C. Duhrssen, and K. H. Albrecht. Motion, deformation, and interaction of blood cells and plasma during flow through narrow capillary tubes. *Blood Cells*, 6:799–812, 1980.

P. G. Gallagher. Red blood cell membrane disorders. *Hematology AM. Soc. Hematology Educ. Program*, 13:8, 2005.

G. Gompper and M. Schick. *Self assembling amphiphilic systems*. Academic Press Limited, London, 1994.

G. Gompper and S. Zschocke. Elastic properties of interfaces in a ginzburg–landau theory of swollen micelles, droplet crystals and lamellar phases. *Europhys. Lett.*, 16:731, 1991.

G. Gompper and S. Zsckocke. Ginzburg-landau theory of oil-water-surfactant mixtures. *Phys. Rev. A*, 46(8):4836, 1992.

G. Gonnella, E. Orlandini, and J. M. Yeomans. Spinodal decomposition to a lamellar phase: effects of hydrodynamic flow. *Phys. Rev. Lett.*, 78:1695, 1997.

N. S. Gov. Active elastic network: Cytoskeleton of the red blood cell. *Phys. Rev. E*, 75:011921, 2007.

N. S. Gov and S. A. Safran. Red blood cell membrane fluctuations and shape controlled by atp-induced cytoskeletal defects. *Biophys. J.*, 88:1859–1874, 2005.

P. Guillot, P. Panizza, J.-B. Salmon, M. Joanicot, A. Colin, C.-H. Bruneau, and T. Colin. Viscosimeter on a microfluidic chip. *Langmuir*, 22:6438–6445, 2006.

J. E. Hall. *Guyton and Hall: Textbook of Medical Physiology*. Elsevier Saunders, Philadelphia, U.S.A., 11th edition, 2011.

M. Han, C. Kim, M. Kim, and S. Lee. *J. Rheol.*, 43:1157–1174, 1999.

W. Helfrich. Elastic properties of lipid membranes: theory and possible experiments. *Z. Naturforsch. C*, 28:693703, 1973.

J. Hellmers, E. Eremina, and T. Wriedt. Simulation of light scattering by biconcave cassini ovals using the nullfield method with discrete sources. *Jour. Opt. A: P and Appl. Opt.*, 8:1–9, 2006.

A. Hernández-Machado and D. Jasnow. Stability of a nonequilibrium steady-state interface. *Phys. Rev. A*, 37(2):656, 1988.

A. Hernández-Machado, A. M. Lacasta, E. Mayoral, and E. Corvera Poiré. Phase-field model of hele-shaw flows in the high-viscosity contrast regime. *Phys. Rev. E*, 68:046310, 2003.

B. P. Ho and L. G. Leal. Inertial migration of rigid spheres in two-dimensional unidirectional flows. *J. Fluid. Mech.*, 65:365–400, 1974.

J. Hoffman. Further musings on some red blood cell problems for perspicacious physiologists. *Blood Cells. Mol. Dis.*, 27:57, 2001.

M. Hu, D. H. de Jong, S. J. Marrink, and M. Deserno. Gaussian curvature elasticity determined from global shape transformations and local stress distributions: a comparative study using the martini model. *Faraday Discuss.*, 161:365–382, 2013.

A. Ikai and R. Afrin. Toward mechanical manipulations of cell membranes and membrane proteins using an atomic force microscope. *Cell Biochem. Biophys.*, 39:257–277, 2003.

K. Jacobson, O. G. Mouritsen, and R. G. Anderson. Lipid rafts: at a crossroad between cell biology and physics. *Nature Cell Biol.*, 9:7–14, 2007.

R. C. Jeffrey and J. R. A. Pearson. Particle motion in laminar vertical tube flow. *J. Fluid. Mech.*, 22:721–735, 1965.

B. Kaoui, G. Biros, and C. Misbah. Why do red blood cells have asymmetric shapes even in a symmetric flow? *Phys. Rev. Lett.*, 103:188101, 2009.

B. Kaoui, T. Krueger, and J. Harting. How does confinement affect the dynamics of viscous vesicles and red blood cells? *Soft Matter*, 8:9246–9252, 2012.

S. R. Keller and R. Skalak. Motion of a tank-treading ellipsoidal particle in a shear flow. *J. Fluid Mech.*, 120:27, 1982.

V. M. Kendon, M. E. Cates, I. Pagonabrraga, J.-C. Desplat, and P. Blandon. Inertial effects in three–dimensional spinodal decomposition of a symmetric binary fluid mixture: a lattice boltzmann study. *J. Fluid Mech.*, 440:147–203, 2001.

K. Khairy and J. Howard. Minimum-energy vesicle and cell shapes calculated using spherical harmonics parameterization. *Soft Matter*, 7:2138–2143, 2011.

K. Khairy, J. Foo, and J. Howard. Shapes of red blood cells: Comparison of 3d confocal images with the bilayer-couple model. *Cell. Mol. Bioeng.*, 1:173–181, 2010.

M. M. Kozlov. Membrane shape equations. *J. Phys. Cond. Matt.*, 18:1177–1190, 2006.

A. Kumar and M. D. Graham. Margination and segregation in confined flows of blood and other multicomponent suspensions. *Soft Matter*, 8:10536, 2012.

T. Kuriabova and A. J. Levine. Nanorheology of viscoelastic shells: applications to viral capsids. *Phys. Rev. E*, 77:031921, 2008.

T. G. Kuznetsova, M. N. Starodubtseva, N. I. Yegorenkov, S. A. Chizhik, and R. I. Zhdanov. Atomic force microscopy probing of cell elasticity. *Micron*, 38: 824–833, 2007.

A. J. C. Ladd. Numerical simulations of particulate suspensions via a discretized boltzmann equation. part 2. numerical results. *J. Fluid Mech.*, 271:285–309, 1994.

A. J. C. Ladd and R. Verberg. Lattice-boltzmann simulations of particle-fluid suspensions. *J. Stat. Phys.*, 104:1191–1251, 2001.

C. A. Lamontagne, C. M. Cuerrier, and M. Grandbois. Afm as a tool to probe and manipulate cellular processes. *Pflugers Arch.*, 456(1):61–70, 2008.

L. D. Landau and E. M. Lifshitz. *Theory of Elasticity.* Butterworth – Heinmann, Oxford, 1999.

Y. Lange and J. Slayton. Interaction of cholesterol and lysophosphatidylcholine in determining red cell shape. *J. Lipid Res.*, 23:1121–1127, 1982.

J. C. M. Lee, D. T. Wong, and D. E. Discher. Direct measures of large, anisotropic strains in deformation of erythrocyte cytoskeleton. *Biophys. J.*, 77:853–864, 1999.

M. Leslie. Do lipid rafts exist? *Science*, 334:1046–1047, 2011.

A. Lewalle and K. H. Parker. Axisymmetric optical-trap measurement of red blood cell membrane elasticity. *J. Biomech. Eng.*, 133:011007, 2011.

J. Li, M. Dao, C. T. Lim, and S. Suresh. Spectrin-level modeling of the cytoskeleton and optical tweezers stretching of the erythrocyte. *Biophys. J.*, 88: 3707–3719, 2005.

J. Li, G. Lykotrafitis, M. Dao, and S. Suresh. Cytoskeletal dynamics of human erythrocyte. *Proc. Nat. Acad. Sci. USA*, 104:4937–4942, 2007.

P. Li, Z. S. Stratton, M. Dao, J. Ritz, and T. J. Huang. Probing circulating tumor cells in microfluidics. *Lab on a chip*, 13:602–609, 2013.

Y. Li. Wavenumber-extended high-order upwind-biased finite-difference schemes for convective scalar transport. *J. Comp. Phys.*, 133(2):235–255, 1997.

G. H. W. Lim, M. Wortis, and R. Mukhopadhyay. Stomatocyte–discocyte–echinocyte sequence of the huan red blood cell: Evidence for the bilayer couple hypothesis from membrane dynamics. *Proc. Nat. Acad. Sci. USA*, 99(26): 16766–16769, 2002.

R. Lima, M. Nakamura, T. Omori, T. Ishikawa, S. Wada, and T. Yamaguchi. *1st ECCOMAS Thematic Conference on Computational Vision and Medical Image Processing. Advances in Computational Vision and Medical Image Processing: Methods and Applications.*, chapter Microscale flow dynamics of red blood cells in microchannels: an experimental and numerical analysis. Springer, 2009.

Q. H. Liu, Z. Haijun, J. X. Liu, and O. Y. Zhong-Can. Spheres and prolate and oblate ellipsoids from an analytical solution of the spontaneous-curvature fluid-membrane model. *Phys. Rev. E*, 60:3227–3233, 1999.

S. C. Liu, L. H. Derick, and J. Palek. Alteration of the erythrocyte-membrane skeletal ultrastructure in hereditary spherocytosis, hereditary elliptocytosis, and pyropoikilocytosis. *Blood*, 76:198–205, 1990.

I. López-Montero, N. Rodríguez abd S. Cribier, A. Pohl, M. Vélez, and P. F. Devaux. Rapid transbilayer movement of ceramides in phospholipid vesicles and in human erythrocytes. *J. Biol. Chem.*, 280(27):25811–25819, 2005.

A. Malevanets and R. Kapral. Mesoscopic model for solvent dynamics. *J Chem. Phys.*, 110:8605–8613, 1999.

S. Manno, Y. Takakuwa, and N. Mohandas. Modulation of erythrocyte membrane mechanical function by protein 4.1 phosphorylation. *J. Biol. Chem.*, 280(9): 7581–7587, 2005.

J. F. Marko and E. D. Siggia. Stretching dna. *Macromolecules*, 28(26):8759–8770, 1995.

S. J. Marrink and D. P. Tieleman. Perspective on the Martini Model. *Chem. Soc. Rev.*, 42:6801–6822, 2013.

S. J. Marrink, H. J. Risselada, S. Yefimov, D. P. Tieleman, and A. H. de Vries. The MARTINI Force Field: Grained Model for Biomolecular Simulations. *J. Phys. Chem. B*, 111:7812–7824, 2007.

R. Martino and P. Zampirollo. A mathematical analysis of the disk-sphere transition of the human red cell. *Experientia*, 34(4):466–467, 1978.

J.-P. Matas, J. F. Morris, and E. Guazzelli. Inertial migration of rigid spherical particles in poiseuille flow. *J. Fluid. Mech.*, 515:171–195, 2004.

E. D. Matayoshi. Distribution of shape-changing compounds across the red cell membrane. *Biochemistry*, 19:3414–3422, 1980.

J. L. McWhirter, H. Noguchi, and G. Gompper. Flow-induced clustering and alignment of vesicles and red blood cells in microcapillaries. *Proc. Nat. Acad. Sci. USA*, 106(15):6039–6043, 2008.

J. L. McWhirter, H. Noguchi, and G. Gompper. Flow-induced clustering and alignment of vesicles and red blood cells in microcapillaries. *Proc. Nat. Acad. Sci. U.S.A.*, 106(15):6039–6043, 2009.

G. R. Lázaro K. M. Melzak, J. L. Toca-Herrera, I. Pagonabarraga, and A. Hernández-Machado. Elastic energies and morphologies of the frst stages of the discoechinocyte transition. *Soft Matter*, 9:6430–6441, 2013.

K. A. Melzak, G. R. Lázaro, A. Hernández-Machado, I. Pagonabarraga, J. M. Cárdenas-Díaz de Espada, and J. L. Toca-Herrera. Afm measurements and lipid rearrangements: evidence from red blood cell shape changes. *Soft Matter*, 8:7716–7726, 2012.

E. W. Merrill, E. R. Gilliland, T. S. Lee, and E. W. Salzman. Blood rheology: effect of fibrinogen decuded by addition. *Circ. Res.*, 18:437–446, 1966.

H. Mohamed, L. D. McCurdy, D. H. Szarowski, S. Duva, J. N. Turner, and M. Caggana. Development of a rare cell frationation device: application for cancer detection. *IEEE Trans. Nanobiosci.*, 3(4):251–256, 2004.

R. Mukhopadhyay, G. Lim H. W., and M. Wortis. Echinocyte shapes: bending, stretching, and shear determine spicule shape and spacing. *Biophys. J.*, 82: 1756–1772, 2002.

M. Nakao, N. Nakao, and S. Yamazoe. Adenosine triphosphate and maintenance of shape of the human red cells. *Nature (London)*, 187:945–946, 1960.

V. Narsimhan, H. Zhao, and E. S. G. Shaqfeh. Coarse-grained theory to predict the concentration distribution of red blood cells in wall-bounded couette flow at zero reynolds number. *Phys. Fluids*, 25:061901, 2013.

P. Nghe, P. Tabeling, and A. Ajdari. Flow-induced polymer degradation probed by a high throughput microfluidic set-up. *J. Non-Newtonian FLuid Mech.*, 165: 313–322, 2010.

H. Noguchi and G. Gompper. Shape transitions of fluid vesicles and red blood cells in capillary flows. *Proc. Nat. Acad. Sci. U.S.A.*, 102(40):14159–14164, 2005.

M. Oishi, H. Kinoshita, T. Fuiji, and M. Oshima. Continuous and simultaneous measurement of the tank-treading motion of red blood cels and the surrounding flow using translational confocal micro-particle image velocimetry (micro-piv) with sub-micron resolution. *Meas. Sci. Technol.*, 23:035301, 2012.

P. Olla. The lift on a tank treading ellipsoidal cell in a shear flow. *J. Phys. II France*, 7:1533–1540, 1997.

P. Olla. Simplified model for red blood cell dynamics in small blood vessels. *Phys. Rev. Lett.*, 82(2):453, 1999.

Z. Ou-Yang and W. Helfrich. Instability and deformation of a spherical vesicle by pressure. *Phys. Rev. Lett.*, 59:2486–2488, 1987.

Y. Park, C. A. Best, T. Auth, N. S. Gov, S. A. Safran, G. Popescu, S. Suresh, and M. S. Feld. *Proc. Nat. Acad. Sci. USA*, 107(4):1289–1294, 2010a.

Y. Park, C. A. Best, K. Badizadegan, R. R. Dasari, M. S. Feld, T. Kriabova, M. L. Henle, A. J. Levine, and G. Popescu. Measurements of red blood cell mechanics during morphological changes. *Proc. Nat. Acad. Sci. USA*, 107(15):6731–6736, 2010b.

Z. Peng, R. J. Asaro, and Q. Zhu. Multiscale simulation of erythrocyte membranes. *Phys. Rev. E*, 81:031904, 2010.

Z. Peng, X. Li, I. V. Pivkin, M. Dao, G. E. Karniakidis, and S. Suresh. Lipid bilayers and cytoskeletal interactions in a red blood cell. *Proc. Nat. Acad. Sci. USA*, 110:13356–13361, 2013.

C. S. Peskin. The immersed boundary method. *Acta Numerica*, 11:1–39, 2002.

A. G. Petrov and J. Bivas. Elastic and flexoelectric aspects of out-of-plane fluctuations in biological and model membranes. *Progress. Surf. Sci.*, 18:389, 1984.

J. C. Pinder, D. Bray, and W. B. Gratzer. Control of interaction of spectrin and actin by phosphorylation. *Nature*, 270:752–754, 1977.

M. S. Pommer and C. D. Meinhart. *Proceedings of the 6th International symposium on particle image velocimetry PIV'05.*, chapter Shear-stress distribution surrounding individual adherent red cells in a microchannel measures using micro-PIV. 2005.

A. J. Pons and A. Karma. Helical crack-front instability in mixed-mode fracture. *Nature*, 464:85–89, 2010.

C. Pozrikidis. *Boundary Integral & Singularity Methods for Linearised Viscous FLow*. Cambridge University Press, New York, 1992.

C. Pozrikidis. Finite deformation of liquid capsules enclosed by elastic membranes in simple shear flow. *Soft Matter*, 297:123–152, 1995.

W. Rawicz, K. C. Olbrich, T. McIntosh, D. Needham, and E. Evans. Effect of chain length and unsaturation on elasticity of lipid bilayers. *Biophys. J.*, 79(1): 328–339, 2000.

H. R. Reinhart and S. Chien. Red cell rheology in stomatocyte-echinocyte transformation: roles of cell geometry and cell shape. *Blood*, 67:1110–1118, 1986.

S. B. Schwarz, B. Deuticke, and C. W. Haest. Adenosine triphosphate and maintenance of shape of the human red cells. *Mol. Membr. Biol.*, 16:247–255, 1999.

T. W. Secomb. Mechanics and computational simulation of blood flow in microvessels. *Med. Eng. Phys.*, 33(7):800–804, 2011.

T. W. Secomb, B. Styp-Rekowska, and A. R. Pries. Two-dimensional simulation of red blood cell deformation and lateral migration in microvessels. *Ann. Biomed. Eng.*, 35:755–765, 2007.

G. Segré and A. Silberberg. Behavior of macroscopic rigid spheres in poiseuille ïňĆow. *J. Fluid. Mech.*, 14:136–157, 1962.

U. Seifert and R. Lipowsky. *Structure and Dynamics of Membranes, Handbook of Biological Sciences, vol. 1*, chapter The morphology of vesicles. Elsevier, Amsterdam, 1995.

U. Seifert, K. Berndel, and R. Lipowsky. Shape transformations of vesicles: phase diagram for spontaneous-curvature and bilayer-couple models. *Phys. Rev. A*, 44(2):11821202, 1991.

J. Y. Shao, C. Shu, and Y. T. Chew. Development of an immersed boundary phase field-lattice boltzmann method for neumann boundary condition to study contact line dynamics. *J. Comp. Phys.*, 234:8–32, 2013.

M. P. Sheetz and S. J. Singer. Biological membranes as bilayer couples. a molecular mechanism of drug-erythrocyte interactions. *Proc. Nat. Acad. Sci. USA*, 71: 4457–4461, 1974.

L. Shi, T.-W. Pan, and R. Glowinski. Numerical simulation of lateral migration of red blood cells in poiseuille flows. *Phys. Rev. E*, 85:016307, 2012.

H. Shiba and H. Noguchi. Estimation of the bending rigidity and spontaneous curvature of fluid membranes in simulations. *Phys. Rev. E*, 84:031926, 2011.

J. C. Shillcock and R. Lipowsky. The computational route from bilayer membranes to vesicle fusion. *J. Phys.: Condens. Matter*, 18:1191–1219, 2006.

K. Simons and W. Vaz. Model systems, lipid rafts, and cell membranes. *Annu. Rev. Biophys. Biomol. Struct.*, 33:269–295, 2004.

S. J. Singer and G. L. Nicolson. The fluid mosaic model of the structure of cell membranes. *Science*, 175:720–731, 1972.

N. Srivastava, R. D. Davenport, and M. A. Burns. A nanoliter viscometer for analyzing plasma and other liquid samples. *Annal. Chem.*, 77:383–392, 2005.

I. Steinbach. Phase-field models in materials science. *Mod. Simul. Mater. Sci. Eng.*, 17:073001, 2009.

B. T. Stokke, A. Mikkelsen, and A. Elgsaeter. Spectrin, human erythrocyte shapes, and mechanical properties. *Biophys. J.*, 49:319–327, 1986.

K. Stratford and I. Pagonabarraga. Parallel simulation of particle suspensions with the lattice boltzmann method. *Comput. Math. Appl.*, 55:1585–1593, 2008.

S. Succi. *The Lattice Boltzmann Equation: For Fluid Dynamics and Beyond*. Oxford University Press, Norfolk, 2001.

S. Svetina, D. Kuzman, R. E. Waugh, P. Ziherl, and B. Zeks. The cooperative role of membrane skeleton and bilayer in the mechanical behaviour of red blood cells. *Bioelectrochemistry*, 62:107–113, 2004.

K. Svodoba, C. F. Schmidt, D. Branton, and S. M. Block. Conformation and elasticity of the isolated red blood cell membrane skeleton. *Biophys. J.*, 63: 784–793, 1992.

M. Tachibana. On the behaviour of a sphere in the laminar tube flows. *Rheol. Acta*, 12:58–69, 1973.

N. Tahiri, T. Biben, H. Ez-Zahraouy, and C. Misbah. On the problem of slipper shapes of red blood cells in the microvasculature. *Microvasc. Res.*, 85:40–45, 2013.

O. Theissen, G. Gompper, and D. M. Kroll. Lattice-boltzmann model of amphiphilic systems. *Europhys. Lett.*, 42(4):419–424, 1998.

G. B. Thurston. Viscoelasticity of human blood. *Biophys. J.*, 12(9):1205–1217, 1972.

G. B. Thurston. *Advances in Hemodynamics and Hemorheology*, chapter Viscoelastic properties of blood and blood analogs. JAI Press. INc., 1996.

G Tomaioulo, M. Simone, V. Martinelli, B. Rotoli, and S. Guido. Red blood cell deformation in microconfined flow. *Soft Matter*, 5:3736–3740, 2009.

G. Tomaiuolo and S. Guido. Start-up shape dynamics of red blood cells in microcapillary flow. *Microvasc. Res.*, 82:35–41, 2011.

M. Toner and D. Irimia. Blood-on-a-chip. *Annu. Rev. Biomed. Eng.*, 7:77–103, 2005.

I. Tsafrir, D. Sagi, T. Arzi, M. A. Guedeau-Boudeville, V. Frette, D. Kandel, and J. Stavans. Pearling instabilities of membrane tubes with anchored polymers. *Phys. Rev. Lett.*, 86:1138–1141, 2001.

I. Tsafrir, Y. Caspi, M. A. Guedeau-Boudeville, T. Arzi, and J. Stavans. Budding and tubulation in highly oblate vesicles by anchored amphiphilic molecules. *Phys. Rev. Lett.*, 91:138102, 2003.

C. Uzoigwe. The human erythrocyte has developed the biconcave disc shape to optimise the flow properties of the blood in the large vessels. *Medical Hypotheses*, 67(5):1159–1163, 2006.

G. van Meer, D. R. Voelker, and G. W. Feigenson. Membrane lipids: where they are and how they behave. *Nature Rev. Mol. Cell Biol.*, 9:112–124, 2008.

P. M. Vlahovska, T. Podgorski, and C. Misbah. Vesicles and red blood cells in flow: From individual dynamics to rheology. *C. R. Physique*, 10:775–789, 2009.

H. Wang and R. Skalak. Viscous flow in a cylindrical tube containing a line of spherical particles. *J. Fluid. Mech.*, 38:75–96, 1969.

X. Wang and Q. Du. Modeling and Simulations of Multi-Component Lipid Membranes and Open Membranes via Diffuse Interface Approaches. *J. Math. Biol.*, 56(3):347–371, 2008.

R. Waugh. Elastic energy of curvature-driven bump formation on red blood cell membrane. *Biophys. J.*, 70:1027–1035, 1996.

R. E. Waugh, J. Song, and B. Zeks. Local and nonlocal curvature elasticity in bilayer membranes by tether formation from lecithin vesicles. *Biophys. J.*, 61: 974–982, 1992.

J. G. White. Effects of an lonophore, a23187, on the surface morphology of normal erythrocytes. *Am. J. Pathol.*, 77:507–518, 1974.

P. Wong. A basis of echinocytosis and stomatocytosis in the disc-sphere transforations of the erythrocyte. *J. Theor. Biol.*, 196:343–361, 1999.

P. L. Yeagle. *The Membranes of Cells.* Academic Press, San Diego, CA, USA., 2nd edition, 1993.

J. Yu, D. A. Fischman, and T. L. Steck. Selective solubilization of proteins and phospholipids from red blood cell membranes by nonionic detergents. *J. Supramol. Struct.*, 1:233–248, 1973.

P. R. Zarda, S. Chien, and R. Skalak. Elastic deformations of red blood cells. *J. Biomech.*, 10:211–281, 1977.

K. Zeman, H. Engelhard, and E. Sackman. Bending undulations and elasticity of the erythrocyte membrane: Effects of cell shape and membrane organization. *Eur. Biophys. J.*, 18:203–219, 1990.